# Synthesis and Characterizations of $SrBi_2Ta_2O_9$ Modified NBT-BT and NBT-KNN Ferroelectric Ceramics near Morphotropic Phase Boundary

**Sridevi Swain**

Department of Physics and Astronomy
**National Institute of Technology Rourkela**

# Synthesis and Characterizations of $SrBi_2Ta_2O_9$ Modified NBT-BT and NBT-KNN Ferroelectric Ceramics near Morphotropic Phase Boundary

*Dissertation submitted to the*
***National Institute of Technology Rourkela***
*in partial fulfilment of the requirements*
*of the degree of*
***Doctor of Philosophy***
***in***
***Physics***
*by*
***Sridevi Swain***
(Roll Number: 510PH301)
*under the supervision of*
***Prof. Pawan Kumar***

December 2015
Department of Physics and Astronomy
**National Institute of Technology Rourkela**

Physics and Astronomy
**National Institute of Technology Rourkela**

---

# Certificate of Examination

**Roll Number:** 510PH301

**Name:** Sridevi Swain

**Title of Dissertation:** Synthesis and Characterizations of $SrBi_2Ta_2O_9$ Modified NBT-BT and NBT-KNN Ferroelectric Ceramics near Morphotropic Phase Boundary.

We the below signed, after checking the dissertation mentioned above and the official record book (s) of the student, hereby state our approval of the dissertation submitted in partial fulfillment of the requirements of the degree of Doctor of Philosophy in Physics and Astronomy at National Institute of Technology Rourkela. We are satisfied with the volume, quality, correctness, and originality of the work.

**Dr. Pawan Kumar**
Supervisor

**Prof. J. Bera**
Member (DSC)

**Dr. S. Jena**
Member (DSC)

**Dr. D. K. Pradhan**
Member (DSC)

**Dr. D. K. Bisoyi**
Chairman (DSC)

**Dr. Muhammad Shahid Anwar**
Examiner

Physics and Astronomy
**National Institute of Technology Rourkela**

***Dr. Pawan Kumar***
Associate Professor

December 28, 2015

# Supervisor's Certificate

This is to certify that the work presented in this dissertation entitled "*Synthesis and Characterizations of* $SrBi_2Ta_2O_9$ *Modified NBT-BT and NBT-KNN Ferroelectric Ceramics near Morphotropic Phase Boundary*", Roll Number 510PH301, is a record of original research carried out by her under my supervision and guidance in partial fulfilment of the requirements for the degree of *Doctor of Philosophy* in *Physics*. Neither this dissertation nor any part of it has been submitted for any degree or diploma to any institute or university in India or abroad.

*Pawan Kumar*
*Supervisor*

*Dedicated to*

***My Loving Parents***

# Declaration of Originality

I, Sridevi Swain, Roll Number 510PH301 hereby declare that this dissertation entitled *“Synthesis and Characterizations of* $SrBi_2Ta_2O_9$ *Modified NBT-BT and NBT-KNN Ferroelectric Ceramics near Morphotropic Phase Boundary”* represents my original work carried out as a doctoral student of NIT Rourkela and, to the best of my knowledge, it contains no material previously published or written by another person, nor any material presented for the award of any other degree or diploma of NIT Rourkela or any other institution. Any contribution made to this research by others, with whom I have worked at NIT Rourkela or elsewhere, is explicitly acknowledged in the dissertation. Works of other authors cited in this dissertation have been duly acknowledged under the reference section. I have also submitted my original research records to the scrutiny committee for evaluation of my dissertation.

I am fully aware that in the case of any non-compliance detected in future, the Senate of NIT Rourkela may withdraw the degree awarded to me on the basis of the present dissertation.

December 28, 2015 *Sridevi Swain*

NIT Rourkela

# Acknowledgments

It is with immense gratitude that I acknowledge the support and help of my advisor Dr. Pawan Kumar, who is the most influential person in my academic life. He was always available for assisting me and provided with all kinds of facilities for carrying out this research work. According to me, he seems to have the magnetic power to convert complicated things simple. I am grateful to him for his guidance, motivation and for so much I have learned from him.

It gives me great pleasure to acknowledge my DSC committee members, Dr. D. K. Bisoyi, Dr. S. Jena, Prof. J. Bera and Dr. D. K. Pradhan for their valuable suggestions and encouragements during the course of this work.

I share the credit for my work with Prof. S. K. Sarangi, Director, NIT Rourkela for allowing me to utilize all the relevant facilities available in the Institute in general and Department of Physics & Astronomy in particular**.**

I express my gratitude to all the faculty members of the Department of Physics & Astronomy for their great support and motivation.

I am extremely thankful to all the supporting and technical staff of the Department of Physics & Astronomy, Department of Materials and Metallurgical Engineering and Department of Ceramic Engineering for their valuable help without which I could not have completed my work.

I am grateful to the Department of Science and Technology, New Delhi, India for the financial support provided under the INSPIRE scheme that encouraged me to pursue my research work successfully.

I am extremely thankful to my laboratory members: Dr. Naresh Kumar, Dr. Prakash K. Palei, Dr. Subrat K. Kar, Dr. Punyatoya Mishra, Mausumi didi, Chandrasekhar, Rashmi, Dipika and Buddhadeb for their timely cooperation and encouragements to finish my work.

My thanks also go to all the research scholars of the Department of Physics & Astronomy, NIT Rourkela.

A special thank goes to my MHRD funded school, Jawahar Navodaya Vidyalaya, without which I would not have been here today. And also for providing free education and teaching me all the values of life during those precious seven years. Moreover, the encouragement of my school teachers: Mr. Nepal Roy, Mr. H.K. Giri and Dr. Banamali Jena, is highly valuable to me till date.

I would be happy to share the support of all my school and college friends especially Shagufta, Sushant Roul, Neha, Sushant Baral, Rinki, Gita, Soni, Ranjita, Sugyani, Santosh, Swapnadip and Sashi as a constant source of encouragement and their confidence in me to complete this work. It also gives me a great pleasure to thank my friends particularly, Krishna, Sweta, Smruti, Arunima, Dr. Bhabani, Asish who supported, encouraged and helped me directly or indirectly during this dissertation.

Finally, I would like to express my deepest appreciation to my beloved parents, Mr. Rabi Narayan Swain and Mrs. Pratima Swain who have never stopped giving me unconditional love, affection and hope that held me through all the difficulties throughout my Ph.D. tenure. Then, I owe a deep sense of indebtedness to my sisters Rupa dei and Lucky, my brother Alok and brother-in-laws Prakash bhaina and Ajay for their much needed love and continuous support all the time. I am happy to share the love for my nephews, Ayush & Piyush, also for my cute little niece Ayesha, whose voice always refreshed my mind whenever I was stressed during my dissertation writing.

I express my whole hearted gratitude to the Almighty God, for giving me all protection and ability to complete this work.

# Abstract

In the scientific community, ferroelectric ceramics have attracted great attention because of their unique dielectric, piezoelectric, pyroelectric and ferroelectric properties. These properties of ferroelectric ceramics make them suitable for various multifunctional device applications. Till date, owing to excellent dielectric, piezoelectric, pyroelectric and ferroelectric properties, the $Pb(Ti,Zr)O_3$(PZT) based ferroelectric ceramics, near morphotropic phase boundary (MPB), are widely used in applications such as actuators, sensors, etc. However, the toxicity, problems in recycling and disposal are the major environmental concerns against the use of lead-based ferroelectric materials. Therefore, there is an urgent need for searching effective lead-free ferroelectrics, whose properties are comparable to those of the well-known PZT based materials. Among the effective lead-free ferroelectrics, the $(Na_{0.5}Bi_{0.5})TiO_3$(NBT) system has drawn great attention in recent years. Although, the NBT system shows a strong ferroelectric behavior, yet it has some critical limitations such as (i) high coercive field, (ii) high conductivity, (iii) high dielectric loss and (iv) high leakage current, which goes against the use of this system in various device applications. Efforts have been made to overcome these limitations by doping or synthesizing solid solutions with other systems. The solid solution of the (1-x)NBT-xBT system exhibits an MPB at $x\approx0.07$. Similarly, in the solid solution of the (1-x)NBT-xKNN system there exist an MPB at $x\approx0.07$ between the rhombohedral FE phase and a tetragonal AFE phase. Therefore, it is imperative to study structural, dielectric, piezoelectric, ferroelectric, polarization fatigue and leakage current density properties of the (1-x)NBT-xBT and (1-x)NBT-xKNN systems near their respective MPBs.

**Selected Perovskite Materials**

- $(1-x)Na_{0.5}Bi_{0.5}TiO_3$-$xBaTiO_3$/NBT-xBT
- $(1-x)Na_{0.5}Bi_{0.5}TiO_3$-x $K_{0.5}Na_{0.5}NbO_3$/NBT-xKNN
  (Where x=0.05, 0.06, 0.07, 0.08)

Solid solutions of the NBT-xBT and NBT-xKNN (where x=0.05, 0.06, 0.07, 0.08) systems were prepared by solid state reaction route. The XRD study confirmed the single perovskite phase in both the NBT-xBT and NBT-xKNN systems at 1000$^o$C and 800 $^o$C calcination temperatures, respectively. No remarkable change in the grain size (average grain size ~2.5µm) was observed with the variation of BT content in the NBT–xBT system. Whereas, in the NBT–xKNN system, the average grain size first increases with the increase of KNN content up to x=0.07 and then starts decreasing for x=0.08. Highest experimental density was found to be ~5.89g/cc (98.30% of the theoretical density ($\rho_{th}$)) and 5.77g/cc (97.81% of the $\rho_{th}$) for x=0.07 compositions of the NBT-xBT and NBT-xKNN systems, respectively. Dielectric study showed existence of both $T_d$ (depolarization temperature) and $T_m$ (temperature corresponding to maximum dielectric constant) in all the systems with diffusive phase transition behavior. Dielectric constant ($\boldsymbol{\varepsilon_r}$) (at 1 kHz frequency) at room temperature (RT) and at $T_m$ were found to be ~2275 and ~5067, respectively for the x=0.07 ceramic samples of the NBT-xBT system. Whereas, for the x=0.07 ceramic samples of the NBT-xKNN system, $\boldsymbol{\varepsilon_r}$ (at 1 kHz frequency) at RT and at $T_m$ were found to be ~2787 and ~4438, respectively. Leakage current density was found to be between $10^{-7}$-$10^{-6}$A/cm$^2$ and

$\sim 10^{-6}$A/cm$^2$ for all the NBT-xBT and NBT-xKNN ceramics, respectively. In the NBT-xBT system, optimum values of remnant polarization ($P_r$) ~ 31.71μC/cm$^2$, piezoelectric coefficient ($d_{33}$) ~105pC/N, electromechanical coupling coefficient ($k_p$) ~0.21 and maximum induced strain% ~0.45 at RT were obtained in the x=0.07 composition. Whereas, optimum values of $P_r$ ~20.61μC/cm$^2$, $d_{33}$ ~78pC/N, $k_p$ ~0.12 and maximum induced strain% ~0.36 were obtained at RT in the x=0.07 composition of the NBT-xKNN system. Bipolar polarization fatigue study confirmed the degradation of all the NBT-xBT and NBT-xKNN ceramics after $10^7$ cycles. Excellent dielectric, piezoelectric and ferroelectric properties confirmed the MPB nature of x=0.07 composition of both the systems. Still, both these systems lack the reliability issues such as polarization fatigue, high coercive field, high leakage current, etc.

On the other hand, bismuth layered structure ferroelectrics (BLSF) such as $SrBi_2Ta_2O_9$, $SrBi_2Nb_2O_9$, $Bi_4Ti_3O_{12}$, $SrBi_4Ti_4O_{15}$, etc., are the natural anti-fatigue materials which can withstand $10^{12}$ erase/rewrite operations. A detail structural, dielectric, piezoelectric, ferroelectric, leakage current density and polarization fatigue properties of the effective BLSFs systems were carried out.

**Selected BLSF Materials**

- $SrBi_2Ta_2O_9$/SBT,
- $Sr_{0.8}Bi_{2.15}Ta_2O_9$/SB$_{ex}$T and
- $SrBi_2(Ta_{0.925}W_{0.075})_2O_9$/SBTW

2-layered SBT, SB$_{ex}$T, and SBTW ceramics were synthesized in single phase by solid-state reaction technique. SEM micrographs showed the development of plate-like grains with maximum experimental density ~8.87 g/cc (98 % of the $\rho_{th}$) of the SB$_{ex}$T ceramic samples, sintered at 1200$^o$C/4hr. Enhanced transition temperature ($T_c$), and better $\varepsilon_r$ and ferroelectric properties were observed in both the SB$_{ex}$T and SBTW ceramic samples compared to the SBT ceramic samples. The dielectric study also showed the sharp transition in both the SB$_{ex}$T and SBTW ceramic samples, whereas a diffused phase transition was observed in the SBT system. From dielectric measurements, highest $T_c$ was obtained in the SB$_{ex}$T system. P-E hysteresis loop study confirmed the ferroelectric nature of all the SBT based ceramic samples. The maximum $P_r$ ~ 8.07μC/cm$^2$ with minimum coercive field ($E_c$) ~ 15.18kV/cm were obtained in the SB$_{ex}$T ceramic samples. Optimum RT value of $d_{33}$ ~24pC/N and $k_p$ ~ 0.098 were obtained in the SB$_{ex}$T ceramic samples. Reduced leakage current density ~3.14x10$^{-9}$A/cm$^2$ was obtained in the SB$_{ex}$T ceramic samples. Bipolar polarization fatigue study confirmed the negligible degradation of all the BLSF materials even after $10^9$ cycles.

Though, the MPB compositions of the NBT-xBT and NBT-xKNN systems exhibit high dielectric, piezoelectric and ferroelectric properties but they show high leakage current density and large degradation of polarization value after repeated cycles. On the contrary, SB$_{ex}$T ceramic samples showed lower leakage current density and better polarization fatigue resistance after repeated cycles. But, the $P_r$ value of the SB$_{ex}$T samples is lower compared to the MPB compositions of the NBT-xBT and NBT-xKNN systems. Therefore, for retaining comparably higher value of $P_r$ and improving the polarization fatigue resistance, these MPB compositions were further modified by SB$_{ex}$T system.

**Selected Perovskite-BLSF Materials**

- (1-ϕ)(0.93 $Na_{0.5}Bi_{0.5}TiO_3$-0.07 $BaTiO_3$/NBT-BT)-ϕ$Sr_{0.8}Bi_{2.15}Ta_2O_9$
- (1-ϕ)(0.93 $Na_{0.5}Bi_{0.5}TiO_3$-0.07 $K_{0.5}Na_{0.5}NbO_3$/NBT-KNN)-ϕ $Sr_{0.8}Bi_{2.15}Ta_2O_9$
  (Where ϕ= 2, 4, 8, 12, 16 wt. %)

(1-ϕ)(NBT-BT)-ϕ$SB_{ex}T$ and (1-ϕ)(NBT-KNN)- ϕ$SB_{ex}T$ (where ϕ= 2, 4, 8, 12, 16 wt. %) ceramic composites were prepared by solid state reaction route. XRD studies showed the co-existence of individual phases in both the ceramic composite series. SEM study showed the development of plate-like grains for higher content of $SB_{ex}T$ phase in both the composite systems. RT $\varepsilon_r$ and tanδ values decreased and diffuse phase transition nature increased with the increase of $SB_{ex}T$ content in both the ceramic composite systems. In both the ceramic composite systems, the leakage current density was found to be ~$10^{-7}$ to $10^{-8}$ A/$cm^2$, which is one to two order less than the NBT-BT and NBT-KNN systems. Maximum induced strain% decreased with the increase of $SB_{ex}T$ content in both the ceramic composite systems. P-E hysteresis loops of the $SB_{ex}T$ modified NBT-KNN ceramics showed the retention of good $P_r$ values. Polarization fatigue studies showed the improvement of polarization fatigue resistance with the increase of $SB_{ex}T$ content in both the ceramic composite systems. Improvement in leakage currents density, fatigue resistance, retention of high $\varepsilon_r$, $P_r$, $d_{33}$ and $k_p$ for $\phi \leq$ 4wt. % of (1-ϕ) (NBT-KNN)-ϕ$SB_{ex}T$ ceramic composites suggested its usefulness in capacitor, piezoelectric and NVRAM applications.

***Keywords**: XRD; SEM; MPB; Perovskite; BLSF; Dielectric; Piezoelectric; Ferroelectric; Polarization Fatigue.*

**The present work is reported in the following chapters**

**Chapter I** presents a short introduction to the phenomenon of general ferroelectricity, piezoelectricity, the significance of lead-free perovskite materials with MPB, ceramic-ceramic composite materials, and their applications. The motivation and objective of this thesis work is also included in this chapter.

**Chapter II** describes the experimental details and the investigated parameters.

**Chapter III** presents the detail description of the synthesis of ceramics and ceramic-ceramic composites. The experimental techniques used to characterize the synthesized materials are also presented in this chapter.

**Chapter IV** describes the dielectric, piezoelectric and ferroelectric studies of NBT-xBT and NBT-xKNN ceramics near their respective MPB.

**Chapter V** describes the dielectric, piezoelectric and ferroelectric properties of SBT based ceramics.

**Chapter VI** describes the dielectric, piezoelectric and ferroelectric properties of $SB_{ex}T$ modified NBT-xBT (x=0.07) and NBT-xKNN (x=0.07) ceramic composites.

**Chapter VII** presents the major conclusions of the present work with future work recommendations.

# Contents

## 1. Introduction and Literature Survey

## 2. Synthesis Route and Investigated Parameters

## 3. Experimental Details

## 4. Dielectric, Piezoelectric, and Ferroelectric Properties of NBT-xBT and NBT- xKNN Ceramics near MPB

## 5. Dielectric, Piezoelectric, and Ferroelectric Properties of the 2-Layered $SrBi_2Ta_2O_9$ based Ceramics

## 6. Dielectric, Piezoelectric and Ferroelectric Properties of $SB_{ex}T$ modified NBT-xBT and NBT-xKNN (x=0.07) Ceramics

## 7. Conclusions and Future Work

# LIST OF FIGURES

## Chapter 1

## Chapter 2

## Chapter 3

## Chapter 4

## Chapter 5

## Chapter 6

# LIST OF TABLES

# List of symbols and abbreviations

| | |
|---|---|
| $\varepsilon_r$ | Dielectric constant |
| Tan$\delta$ | Dielectric loss |
| $\varepsilon_0$ | Permittivity of free space |
| $\varepsilon'$ | Real part of permittivity |
| $\varepsilon''$ | Imaginary part of permittivity |
| X | Dielectric susceptibility |
| $P_r$ | Remnant polarization |
| $E_c$ | Coercive field |
| J-E | Current density-Electric field |
| S-E | Induced strain- Electric field |
| P-E | Polarization-Electric field |
| $\rho_{th}$ | Theoretical density |
| $\rho_{ex}$ | Experimental density |
| $d_{33}$ | Piezoelectric coefficient |
| $k_p$ | Electromechanical coupling factor |
| $f_a$ | Antiresonance frequency |
| $f_r$ | Resonance frequency |
| a, b, c | Lattice parameters |
| $T_c$ | Curie temperature |
| $T_d$ | Depolarization temperature |
| $T_m$ | Temperature at maximum dielectric constant |
| RT | Room temperature |
| PNR | Polar nano region |
| DPT | Diffused phase transition |
| NVFRAM | Non-Volatile Ferroelectric Random Access Memories |
| PZT | $(Pb_{0.52}Zr_{0.48})TiO_3$ |
| BT | $BaTiO_3$ |
| PMN-PT | $Pb(Mg_{1/3}Nb_{2/3})O_3$-$PbTiO_3$ |

|  |  |
|---|---|
| NBT | $Na_{0.5}Bi_{0.5}TiO_3$ |
| KNN | $K_{0.5}Na_{0.5}NbO_3$ |
| SBT | $SrBi_2Ta_2O_9$ |
| $SB_{ex}T$ | $Sr_{0.8}Bi_{2.15}Ta_2O_9$ |
| SBTW | $SrBi_2(Ta_{0.925}W_{0.075})_2O_9$ |
| $(1-\phi)$(NBT-BT)-$\phi SB_{ex}T$ | $(1-\phi)(0.93\ Na_{0.5}Bi_{0.5}TiO_3-0.07\ BaTiO_3)-\phi Sr_{0.8}Bi_{2.15}Ta_2O_9$ |
| $(1-\phi)$(NBT-KNN)-$\phi SB_{ex}T$ | $(1-\phi)(0.93\ Na_{0.5}Bi_{0.5}TiO_3-0.07\ K_{0.5}Na_{0.5}NbO_3)-\phi Sr_{0.8}Bi_{2.15}Ta_2O_9$ |
| MPB | Morphotropic phase boundary |
| BLSF | Bismuth layered structure ferroelectrics |
| SSRR | Solid state reaction route |
| PVA | Polyvinyl alcohol |
| DSC | Differential scanning calorimetry |
| TGA | Thermo gravimetric analysis |
| XRD | X-ray diffraction |
| SEM | Scanning electron microscope |
| SCLC | Space charge limited currents |
| FE | Ferroelectric |
| AFE | Antiferroelectric |
| PE | Paraelectric |

# Chapter 1

# *Introduction and Literature Survey*

## 1.1 Introduction

In the present era of device miniaturization, smart ceramic materials are technologically significant particularly in sensor, actuator, transducer, memory and capacitor devices. Smart ceramic materials change their chemical or physical properties under the influence of external stimuli. These materials are also known as electroceramics because of their extraordinary electrical properties. A parallel development of various subclasses of electroceramics with piezoelectric properties has also taken place along with the development of new technologies. Consequently, since more than half a century, the piezoelectric ceramics have been getting considerable recognition. In addition, polycrystalline ceramics (ferroelectric in nature) with high dielectric constant were initially used in the capacitors. In the early 1950's, only $BaTiO_3$ (BT) based ceramics were used in capacitor and piezoelectric transducer device applications. Subsequently, many other ferroelectric ceramics including lead titanate ($PbTiO_3$), lead zirconate titanate (PZT), lead lanthanum zirconate titanate (PLZT) and relaxor ferroelectrics like lead magnesium niobate (PMN) have been developed and utilized in various device applications [1]. Among the limited choice of lead-free ferroelectric ceramics, $Na_{0.5}Bi_{0.5}TiO_3$ (NBT) system with perovskite structure has remained as the prototype material due to its better ferroelectric properties. However, some critical issues associated with NBT system propel the researchers to modify the system either by doping/substitution or by preparing solid solution with other ceramic materials. By the choice of a suitable ferroelectric system, NBT based solid solutions, possessing a morphotropic phase boundary (MPB) can easily be realized. Although, through these modifications major critical issues associated with the NBT system are resolved, still the reliability problems such as polarization fatigue and high leakage current are not yet addressed. On the other hand, though the ferroelectric properties of bismuth layered structure ferroelectrics (BLSFs) are weak compared to their perovskite counterparts, yet they possess the superior polarization fatigue endurance property. In this connection, emphasis was given to NBT based systems near their MPBs, which were further modified by suitable BLSF systems for improving the reliability issues.

# 1.2 Background of Ferroelectric Phenomena and Related Definitions

## 1.2.1 Dielectric Materials

Dielectrics are a class of insulating materials, which have virtually no free charge carriers and find their use in capacitor applications. Induction of polarization under an applied external electric field is the special characteristic of dielectrics, which separates them out from other class of insulating materials. This polarization in a dielectric material can occur by several mechanisms through limited charge rearrangements. Dielectrics are generally described by the dielectric constant or relative permittivity ( $\varepsilon_r$ ) and dielectric loss ( $\tan\delta$ ) parameters. And, the total capacitance, $C$ of a capacitor is given by

$$C = \frac{\varepsilon_o \varepsilon_r A}{d} \qquad (1.1)$$

Where, ‘ $\varepsilon_o$ ’ is the permittivity of the free space, ‘ $\varepsilon_r$ ’ is the dielectric constant (‘ $\varepsilon_o\varepsilon_r$ ’ is the permittivity of dielectric material), ‘ $d$ ’ is the distance between the parallel plates, and ‘ $A$ ’ is the area of the plates. Moreover, the material parameter ‘ $\chi$ ’, which is known as dielectric susceptibility relates the applied external electric field ( $E$ ) and electrical polarization ( $P$ ) by the relation

$$P = \chi \varepsilon_o E \qquad (1.2)$$

Also, $\varepsilon_r$ of an isotropic medium is defined by the relation

$$\varepsilon_r = {(\varepsilon_0 E + P)}/{\varepsilon_0 E} = 1 + \chi \qquad (1.3)$$

where, $\varepsilon_0 E + P = D$ is the electric displacement field [2].

The mechanisms related to polarization, occurring in a dielectric material, depend on the frequency of the applied external electric field. Following are the different contributions to the total polarization in a dielectric material [3]:

- Electronic polarization (displacement of the negatively charged electron shell against the positively charged nucleus).
- Ionic polarization (mutual displacement of the positive and negative sub lattices under the influence of an applied electric field).
- Orientation polarization (alignment of permanent dipoles).
- Space charge polarization (polarization effect in a dielectric material showing spatial inhomogeneity of charge carrier densities).

Each polarization contribution originates from the short-range movement of the charges, which responds to the applied electric field with different time scales. Schematic dispersion of the real and imaginary parts of the dielectric function is shown in Fig.1.1. Each of the polarization contributions has its own characteristic frequency, which is the reciprocal of the characteristic time/relaxation time and where a maximum of the dielectric loss appears (shown in lower part of Fig.1.1). Depending on whether the oscillating masses experience a restoring force or not, one can distinguish between resonance and relaxation effects, respectively. Resonances are observed for the ionic (molecular vibrations and ionic lattices in the infrared (IR) region, $10^{11}$-$10^{13}$ Hz) as well as electronic polarization (above $10^{13}$ Hz), while relaxation effects are found for the orientational polarization (electric dipoles from $10^{8}$-$10^{10}$ Hz) as well as interface or space charge polarization (below 10Hz) [4].

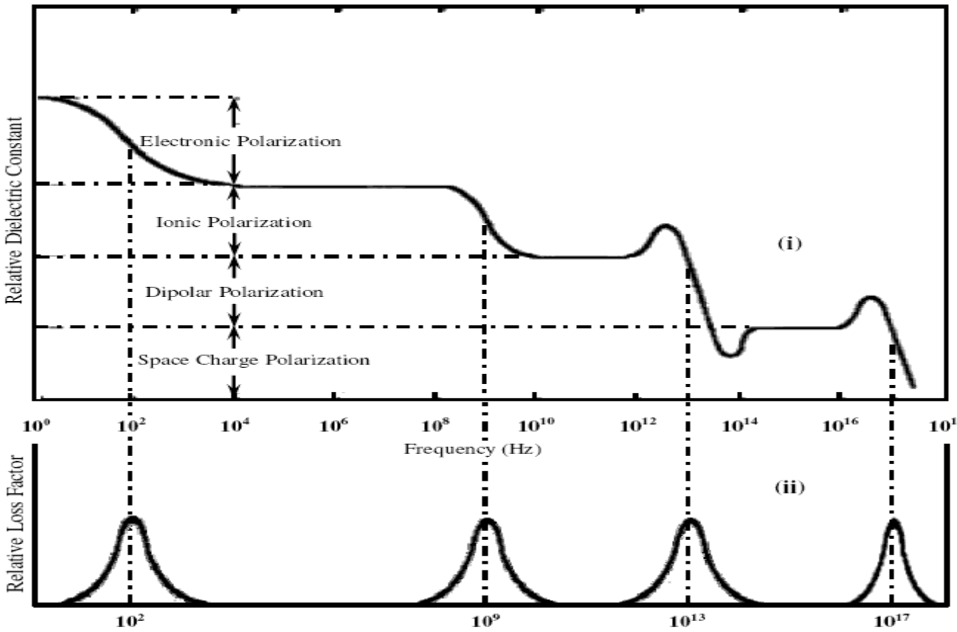

**Fig. 1.1**: Frequency dependence of different polarizations in a dielectric material [5].

## 1.2.2 Classification of Materials based on Symmetry Principle

The physical properties of crystals, thin films, polycrystalline or an amorphous material are affected by their symmetry. According to Neumann's principle, the symmetry of a crystal's internal structure is reflected in the symmetry of its external properties [6]. To explain symmetry about a point in space, crystallographers employ four symmetry operations; (1) a center of symmetry, (2) axes of rotation, (3) mirror planes and (4) combinations of these [7], which leads to a total of 32 point groups. Dielectric materials may belong to any one of the 32 point groups (or crystal classes) among which twenty groups are piezoelectric, where the polarization can be induced by an applied electric field. Half of the piezoelectric class of materials, (i.e. 10 point groups) are called polar materials, which exhibit spontaneous polarization in the absence of any applied electric field or stress. Such dielectrics are called pyroelectrics, since the detection of spontaneous polarization is carried out by heating the specimens. The spontaneous polarization of a polar material results from an inherent asymmetry within the basic crystal cell. Polar materials whose direction of spontaneous polarization can be changed by an applied electric field are known as ferroelectrics or Siegnette electrics occasionally. The term ferroelectricity is derived from the analogy with ferromagnetic materials, since ferroelectric materials also possess domains, exhibit hysteresis loops and show Curie-Weiss type behavior near their phase transition temperatures [8]. Fig.1.2 shows the classification of materials on the basis of crystal symmetry and Fig.1.3 shows the relationship between dielectric, ferroelectric, pyroelectric and piezoelectric materials.

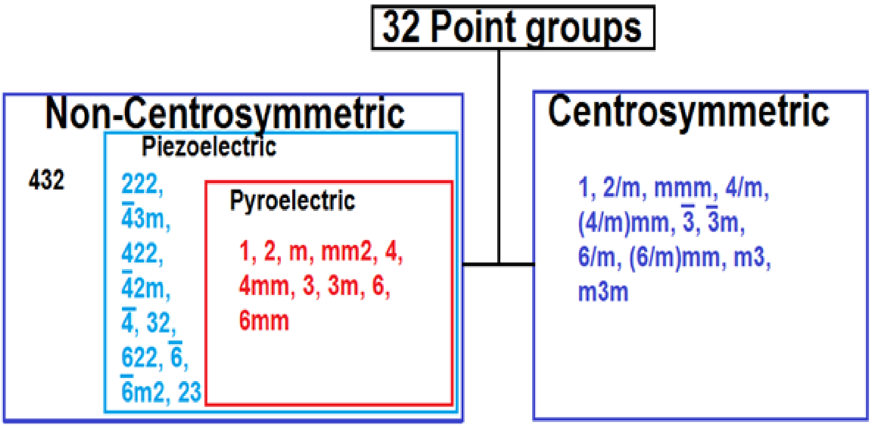

**Fig. 1.2:** Crystal classification based on symmetry principle [9].

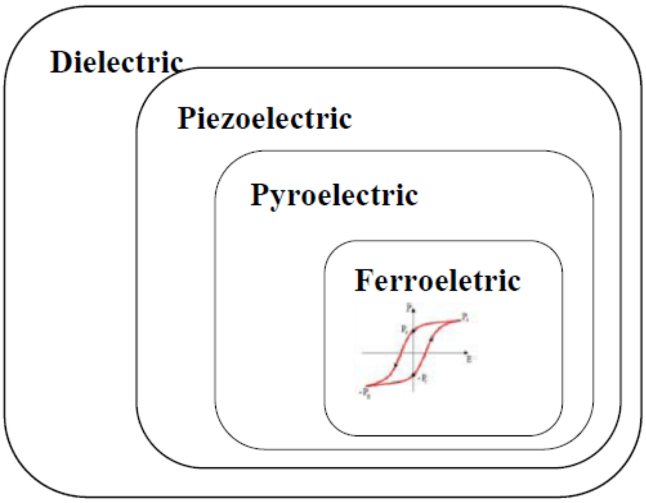

**Fig. 1.3:** Diagrammatic representations of the relationship between ferroelectrics, pyroelectrics and piezoelectrics.

### 1.2.3 Piezoelectric Materials

Piezoelectric materials possess the coupling between electrical and mechanical energies, i.e. an applied mechanical stress results in the generation of polarization. Over hundred years ago, Jacques and Pierre Curie discovered that the unit cells of piezoelectric materials lack center of crystallographic symmetry. This asymmetrical configuration of atoms in the unit cell creates an asymmetric charge distribution, which results in the formation of an electric dipole in the crystal as a whole. This macroscopic charge displacement or polarization is proportional to the applied mechanical stress. It was observed that the converse is also true where the voltage applied to the surface of a piezoelectric crystal creates a small change in its dimensions, which is proportional to the applied voltage. Although the attainable strain is relatively small, it can impart sufficient force to displace objects; many times more massive than the crystal itself, which makes these materials suitable for actuator applications [10].

The direct and converse piezoelectric effects, as shown in Fig.1.4, can be expressed in tensor notation as,

$$D_i = d_{ijk}\sigma_{jk} \qquad (1.4) \quad \text{(Direct Effect)}$$

$$S_{ij} = d_{kij}E_k \qquad (1.5) \quad \text{(Converse Effect)}$$

where, $D_i$ is the polarization generated along the $i$- axis in response to the applied stress $\sigma_{jk}$. For the converse effect, $S_{ij}$ is the strain generated in a particular orientation of the crystal by the application of electric field $E_k$ along the $k$-axis [6]. $d_{ijk}$ and $d_{kij}$ are the piezoelectric coefficients for direct and converse effects, respectively.

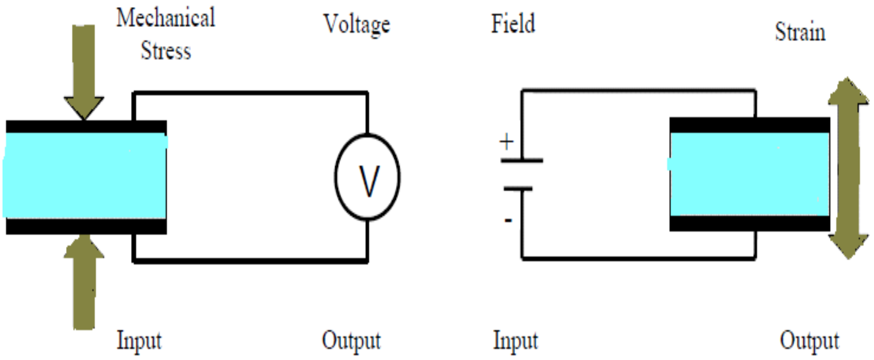

**Fig. 1.4:** Schematic diagram of direct and converse piezoelectric effects [11].

### 1.2.4 Pyroelectric Materials

Pyroelectrics are subclasses of piezoelectrics, which possess spontaneous polarization. Generally, this spontaneous polarization in pyroelectric materials is not necessarily switchable by an external electric field. This inherent dipole moment within each unit cell induces a net polarization, which can be manipulated by temperature. The pyroelectric coefficient ( $p_i$ ) is described as the change in the spontaneous polarization with temperature [7] as,

$$p_i = \frac{\partial P_s}{\partial T} \qquad (1.6)$$

where, $p_i$ ($\mathrm{Cm^{-2}K^{-1}}$) is the pyroelectric coefficient. Alternatively, ‘ $p_i$ ’ is calculated using the relation,

$$p_i = \frac{I}{A\frac{dT}{dt}} \qquad (1.7)$$

Where, ‘ $I$ ’ is the pyroelectric current, measured during the heating cycle, ‘ $A$ ’ is the area of the electrode and ‘ $dT/dt$ ’ is the rate of heating. The spontaneous polarization disappears above the Curie temperature ( $T_c$ ), the temperature above which a pyroelectric unit cell transforms into the centrosymmetric paraelectric phase. In the centrosymmetric paraelectric phase, there exist no dipole moment within the unit cell, and thus exhibits a reduced piezoelectric effect [1].

### 1.2.5 Ferroelectric Materials

Ferroelectrics are subclasses of pyroelectrics, in which the spontaneous electric polarization can be reversed by the application of an external electric field. The effect of the application of an electric field and cycling through negative and positive directions to a ferroelectric material, results in a hysteretic behavior, shown in Fig.1.5. With the increase of electric field, the polarization initially increases from zero to a saturation polarization, $P_{sat}$ , and then upon decreasing the electric field, it reduces to a remnant polarization, $P_r$ . The electric field required to reduce the polarization back to zero value, is called coercive field $E_c$ . A ferroelectric material has the following characteristics [7] :

- Ferroelectric hysteresis loop
- Spontaneous polarization
- Reversible polarization
- Ferroelectric transition temperature.

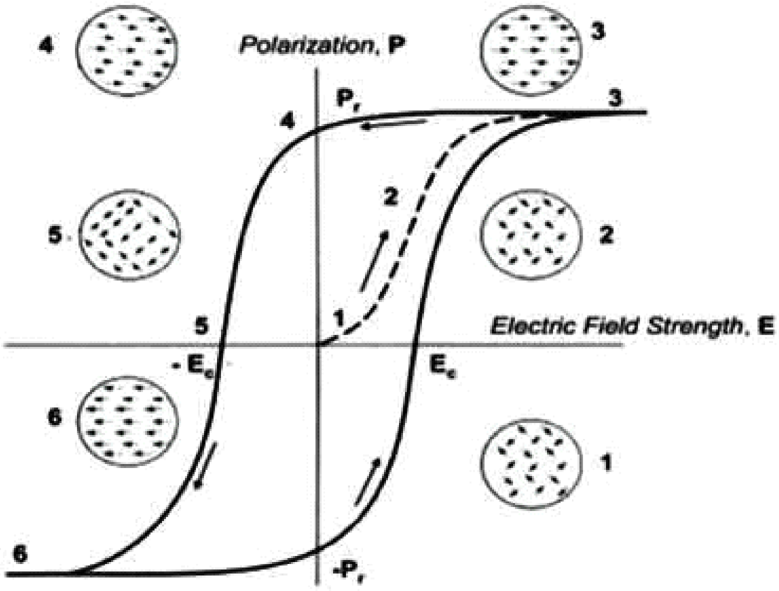

**Fig.1.5:** Polarization hysteresis in a ferroelectric material [12].

### 1.2.5.1 Ferroelectric Domains and Domain Walls

Ferroelectric materials consist of regions, called domains, within which spontaneous polarization is uniformly oriented. This polarization orientation differs from an adjacent domain and the region which separates the two adjacent domains is called the domain wall. The walls between domains with opposite orientation and mutually perpendicular polarizations are called 180$^o$ and 90$^o$ walls, respectively [13]. More often, spontaneous polarization is generated by cooling the ferroelectric material below the Curie point. As the temperature is reduced down to the Curie point, the generation of spontaneous polarization leads to the formation of surface charges, which produce a depolarizing field, $E_d$, directed opposite to the spontaneous polarization. In principle, ferroelectric domains are formed to minimize the electrostatic energy of the depolarizing fields, $E_d$, and elastic energy associated with mechanical strain generated in the ferroelectric material when it is cooled through paraelectric to ferroelectric state [14]. A combination of electric and elastic boundary conditions to which a ferroelectric material is subjected when it is cooled down through the ferroelectric phase transition temperature, usually leads to a complex domain structure with many 90$^o$, 180$^o$ and many other walls. This is schematically shown in Fig.1.6.

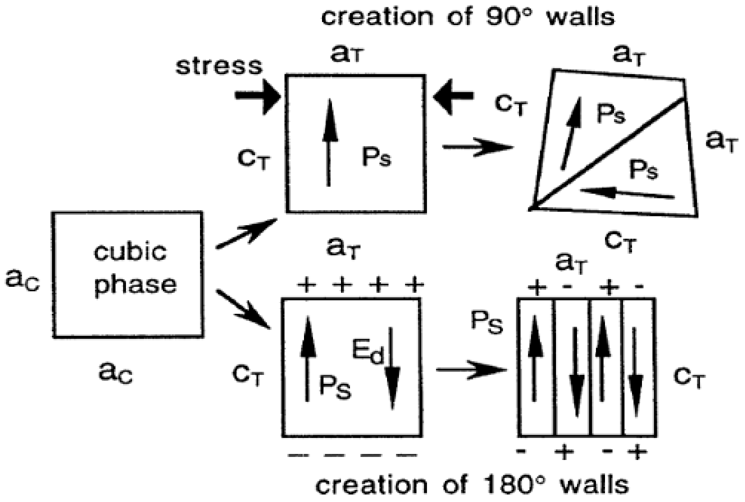

**Fig.1.6:** Creation of ferroelectric domains [15].

### 1.2.5.2 Ferroelectrics for Electronic Applications

After the discovery of $BaTiO_3$ ceramics, ferroelectric crystals and ceramics have been studied for a variety of electronic device applications, including actuators, filters, sensors and capacitors. Most extensive research in various ferroelectric materials which have been carried out till date is related to the field of utilization of switchable polarization under the application of an external electric field. Therefore, the concept of utilizing the reversible spontaneous polarization of ferroelectric materials as a non-volatile ferroelectric random access memory (NVFRAM) state is one of the key research interests of the present time. A concise description of the ferroelectric non-volatile memories, followed by a discussion on polarization fatigue, one of the major reliability issues, which limits the applicability of ferroelectrics in memory devices, has been summarized in the successive two sections.

### 1.2.5.3 Non-Volatile Ferroelectric Random Access Memories (NVFRAM)

The hysteresis behavior of ferroelectric polarization vs. applied external electric field (*P*-*E*) of ferroelectric material makes it useful for the non-volatile memory applications. In these materials, there exists a nominal threshold electric field (called coercive field), above which the polarization changes its sign and we get two zero field values i.e. the $\pm P_r$, which are equally stable. Either of these two states of the polarization can be encoded as “1” or “0” in the memory devices and since no external electric field is required to maintain these states, the memory is termed as non-volatile [16]. Due to their following advantages such as (i) fast access speed, (ii) low power consumption, (iii) extended read/write endurance and (iv) ability to store data without the need for battery backup power, the bistable states of the ferroelectric makes them ideal replacements for the standard random access memory (RAM), erasable programmable read-only memory (EPROM) and flash memories. Following the first NVFRAM demonstrations in 1989, NVRAMs have been extensively developed [17]. Moreover, current applications of these ferroelectric materials include in smart cards, data collection and storage (e.g., power meters), configuration storage and buffer devices.

### 1.2.5.4 Fatigue in Ferroelectric Ceramics

As per definition, ferroelectric (polarization) fatigue is the loss of the switchable remnant polarization in a ferroelectric material, undergoing unipolar/bipolar pulses. Fig. 1.7 shows a schematic representation of the polarization decay vs. the number of cycles in a ferroelectric material. Fatigue is generally accepted as the result of charge injection and the accumulation of space charges, which pin the domain switching. The microscopic models for explaining the origins of the fatigues are the formation of charged defect pairs, such as lead vacancies, bismuth vacancies, oxygen vacancies [18] and space-charge accumulation at or near the electrode-ferroelectric interfaces [19]. Defect charges play important role in all these models [20].Though both bulk and thin film ferroelectric materials are susceptible to polarization fatigue, the mechanism of polarization fatigue is presently not well understood. Yet, in the early studies, mostly in single crystals, considerable research on ferroelectric fatigue has produced a large quantity of experimental data. The influence of various conditions i.e., temperature, ambient atmosphere, choice of electrode, composition of the ferroelectric material, and the characteristics of the external electric field on fatigue has been studied previously [21-23].

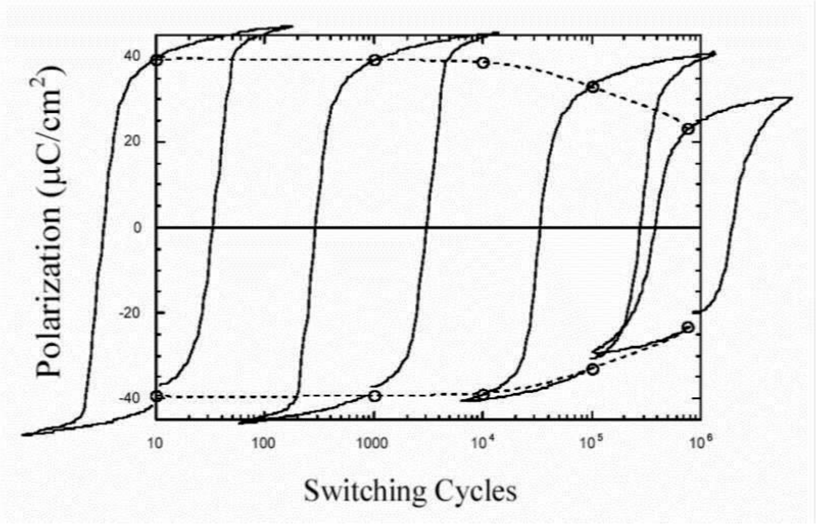

**Fig.1.7**: A schematic illustration of polarization decay as a function of the number of switching cycles [18].

## 1.3 Classification of Ferroelectrics

According to the nature of chemical bonds, crystalline ferroelectrics may be classified into four types [24]: (i) Perovskite e.g.: $BaTiO_3$, $K_{0.5}Na_{0.5}NbO_3$, $Na_{0.5}Bi_{0.5}TiO_3$ (ii) Layer structure e.g.: $SrBi_2Ta_2O_9$, $Bi_4Ti_3O_{12}$ (iii) Tungsten bronze e.g.: $PbNb_2O_6$, and (iv) Pyrochlore e.g.: $Cd_2Nb_2O_7$.

### 1.3.1 Ferroelectrics with Perovskite Structure

Perovskite is a family name of a group of materials having a prototype $ABO_3$ type of structure. Here, the A-site cations (e.g. $Ba^{2+}$, $Sr^{2+}$, $Ca^{2+}$, $Pb^{2+}$) are normally larger than the B-site cations (e.g. $Ti^{4+}$, $Zr^{4+}$, $Sn^{4+}$) and O represents the oxygen atoms. Fig. 1.8 (a) shows the three-dimensional corner sharing $O^{2-}$ ions octahedral network. The A-site cations are surrounded by twelve anions in cube-octahedral coordination and the B site cations are surrounded by six anions in octahedral coordination.

Fig.1.8 (b) shows the ideal perovskite with cubic unit cell [25]. Most of the materials belonging to the perovskite structure are ionic compounds. In perovskites, the chemical composition related to its stability can be measured by their tolerance factor '$t$', also known as Goldschmidt tolerance factor, which is given below:

$$t = \frac{R_A + R_O}{\sqrt{2}(R_B + R_O)} \tag{1.8}$$

where, $R_A$, $R_B$ and $R_O$ are the ionic radii of A, B and O ions, respectively [26]. For ideal cubic structure $t$ =1.0, however, perovskite structures with 0.95< $t$ < 1.0 are cubic in nature. The perovskite structures with $t$ > 1.0 tend to be ferroelectric and with $t$ < 0.95, leads to non-ferroelectric nature and results in distorted perovskite structure. In addition to '$t$', the polarizability of the ions also plays a significant role in determining the nature of the material [27].

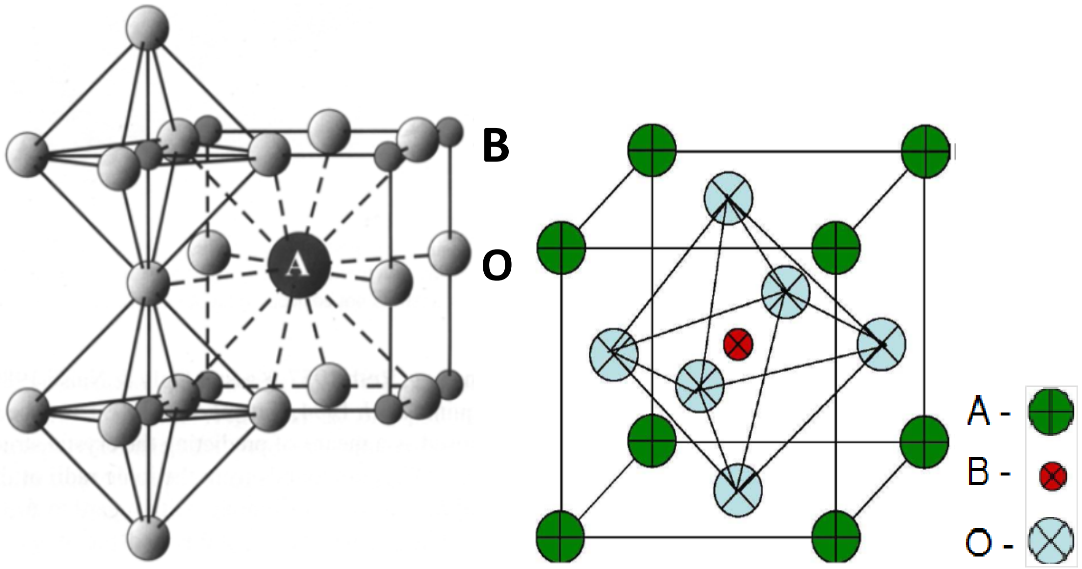

(a) (b)

**Fig.1.8: (a)** Three-dimensional network of the corner-sharing octahedra of $O^{2-}$ ions, **(b)** A cubic $ABO_3$ perovskite-type unit cell [28].

In few materials, the A site becomes complex by comprising more than one cation in the $ABO_3$ structure, which is denoted as $(A_1A_2)BO_3$ and known as complex perovskite structure. Generally, in this complex perovskite structure, $A_1$ and $A_2$ are relatively large size mono-, di- or tri-valent cations such as $Na^+$, $K^+$ , $Ba^{2+}$, $Ca^{2+}$, $Sr^{2+}$, $Pb^{2+}$, $Bi^{3+}$ etc. and B site is a small size, highly charged tera-, penta- or hexa-valent cations, such as $Ti^{4+}$, $Nb^{5+}$, $W^{6+}$, etc. Compositional heterogeneities due to the A-site cations in these complex perovskite structures make the nature of the phase transition in these ferroelectrics as diffused type.

## 1.3.2 Ferroelectrics with Bismuth Layer Structure

Bismuth layer-structured ferroelectrics (BLSFs) were first synthesized by Aurivillius in 1949 and hence they are also known as Aurivillius compounds [29]. Fig.1.9 shows the structure of BLSF, which comprises the intergrowth of fluorite-like $(Bi_2O_2)^{2+}$ units and pseudo-perovskite slabs $(A_{n-1}B_nO_{3n+1})^{2-}$ . 'n' indicates the number of perovskite layers stacked along the c-axis between the $(Bi_2O_2)^{2+}$ layers and generally its value lies between $1 \leq n \leq 8$. In $(A_{n-1}B_nO_{3n+1})^{2-}$, B is a small size, highly charged tetra-, penta- or hexa-valent cation, such as $Ti^{4+}$, $Ta^{5+}$, $Nb^{5+}$, $V^{5+}$, $W^{6+}$ etc. $(A_{n-1}B_nO_{3n+1})^{2-}$ perovskite slabs are sandwiched between the $Bi_2O_2$ layers and gives a characteristic layer structure. Ferroelectricity in these compounds is generally attributed to the cationic displacement along the polar a-axis and the tilting of octahedra around the 'a' and 'c' axes [29-32].

Some typical examples of BLSFs are: $Bi_2WO_6$ (n = 1), $SrBi_2Ta_2O_9$ (n = 2), $Bi_4Ti_3O_{12}$ (n = 3), $MBi_4Ti_4O_{15}$ (M = Ca, Sr, Pb, Ba) (n=4), $Ba_2Bi_4Ti_5O_{18}$ (n=5) etc. These BLSFs possess some exclusively attractive electrical properties such as excellent fatigue endurance, fast switching speed, good polarization retention, relatively high Curie temperature, low aging rate and low operating voltage [33-36]. The mentioned electrical properties of BLSFs make them suitable for ferroelectric non-volatile random access memory (NVRAM) storage devices, high-temperature piezoelectric device, sensor and photo-catalysts applications [37, 38].

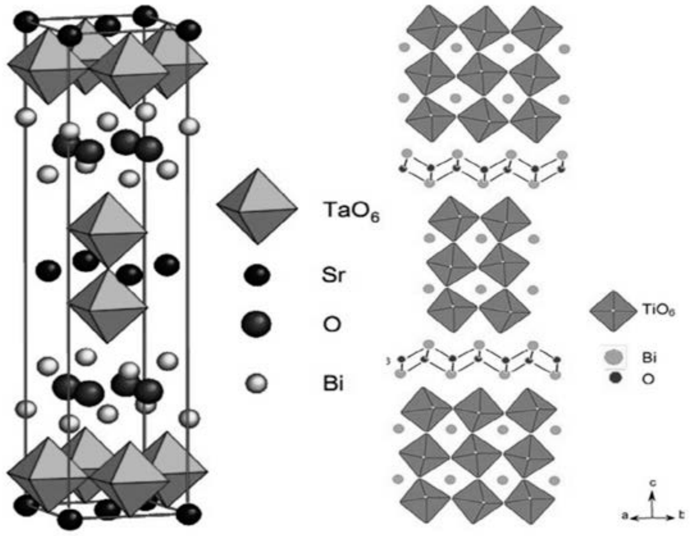

**Fig.1.9**: Typical structure of two layered [39], and three layered [40] BLSFs.

### 1.3.3 Ferroelectrics with Tungsten Bronze Structure

The “Tetragonal Tungsten Bronze” (TTB) structural type is related to the potassium tungstate ($K_{0.475}WO_3$) like structure [41]. Interconnected corner-sharing oxygen octahedral with three types of pseudo-symmetric open channels i.e. three-, four-, and five-fold is the characteristic feature of the TTB crystal structure, as shown in Fig.1.10 [42]. The site occupancy formula for TTB structure is given by $(A1)_2(A2)_4(C)_4(B1)_2(B2)_8O_{30}$. The three open channels (A1, A2 and C sites) and the space encapsulated by oxygen octahedron (B1 and B2) can accommodate a wide range of cations and anions, leading to modified materials with different tailored properties. Lead niobate ($PbNb_2O_6$) was the first crystal of the tungsten bronze type structure to show useful ferroelectric properties [1]. Various substitutions in the TTB structure have led to the discovery of many new normal, and relaxor type ferroelectrics [43]. At present, there are more than hundred ferroelectric materials which belong to tungsten bronze family.

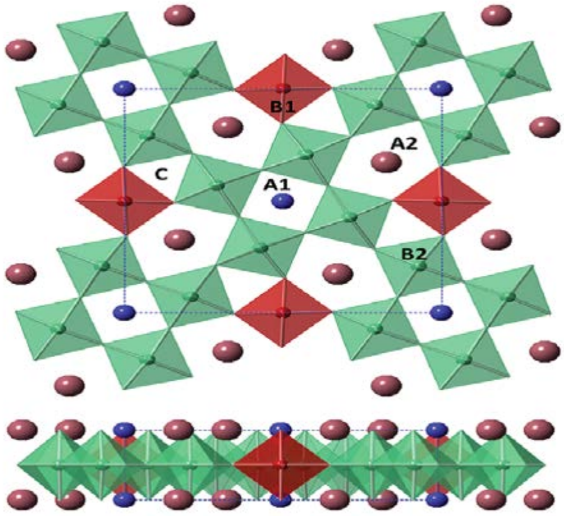

**Fig.1.10**: Schematic diagram showing a projection of the tetragonal tungsten bronze structure on the (001) plane [42].

## 1.3.4 Ferroelectrics with Pyrochlore Structure

The pyrochlore structure is shown by materials having a stoichiometric formula of $A_2B_2O_7$ [44], where A is a trivalent or divalent cation and B is a tetra- or pentavalent cation. Fig.1.11 shows the one octant part of pyrochlore structure [45]. Due to a wide compositional range of A and B site cations, pyrochlore compounds show interesting properties useful for solid electrolytes, anodes and cathodes for fuel cells and sensors, catalysts, dielectrics and materials for the encapsulation of actinides and other nuclear wastes [46].

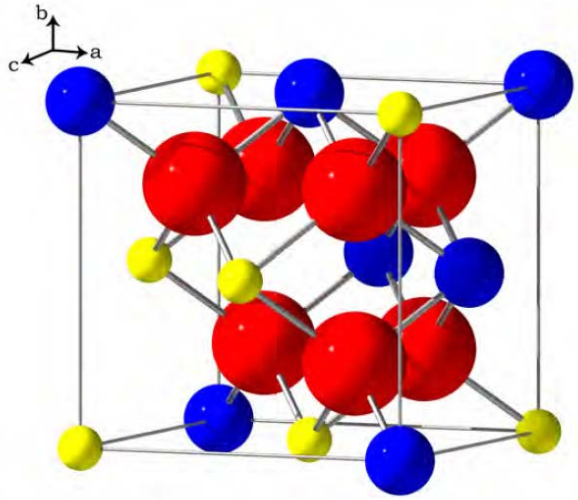

**Fig.1.11:** One octant part of the pyrochlore structure ($A_2B_2O_7$). Blue spheres are $A^{3+}$ ions, yellow spheres are $B^{4+}$ ions, and red spheres are $O^{2-}$ ions [44].

Ferroelectric materials, such as $Ce_2Ti_2O_7$, $Sr_2Nb_2O_7$, $La_2Ti_2O_7$ (LTO), and $Nd_2Ti_2O_7$ (NTO), with a pseudo-pyrochlore structure, exhibit a high coercive field, good thermal stability and a low dielectric constant [47].

# 1.4 Literature Review

In the following sections, literature review about the potential lead-free perovskite and BLSF ceramics is presented.

## 1.4.1 Lead-Free Ferroelectric Ceramics

Lead(Pb)-containing ferroelectric ceramics such as $(Pb_{0.52}Zr_{0.48})TiO_3$ (PZT), $Pb(Mg_{1/3}Nb_{2/3})O_3$–$PbTiO_3$ (PMN-PT) etc. find their use in the modern sensors, actuators and transducers applications due to their superior dielectric, ferroelectric and piezoelectric properties. These excellent properties appear due to the special electronic configuration as well as the peculiar crystal chemistry of $Pb^{2+}$ ions in the Pb-based systems. Specifically, the stereochemically active $6s^2$ lone pair of $Pb^{2+}$ ions causes a strong structural distortion, which leads to highly polarizable and electrically active materials in the Pb-based systems [48, 49]. Furthermore, the exceptionally superior properties in these PZT, PMN-PT etc. systems are obtained near the respective morphotropic phase boundary (MPB) regions [27]. The MPB describes the boundary that separate regions of different symmetries and can be crossed through a change in composition [50]. At MPBs, the crystal structure of these system changes abruptly and the electromechanical properties are optimum. Despite the excellent properties of PZT based systems, regulatory agencies worldwide began putting restrictions on the use of lead over the past few years, due to its toxicity, and currently research is focused mostly on Pb-free materials [51]. Many research groups around the globe are actively involved to find out the effective alternative to lead-free ferroelectric systems. In this search, a special attention has been given to the materials with perovskite phase. This is because materials with perovskite phase are easy to synthesize and suitable modifications in these systems can be incorporated easily. $BaTiO_3$ (BT), $Na_{0.5}Bi_{0.5}TiO_3$ (NBT), $K_{0.5}Bi_{0.5}TiO_3$ (KBT), $KNbO_3$ (KN), $K_{0.5}Na_{0.5}NbO_3$ (KNN), $BaZrTiO_3$ (BZT), $BaSrTiO_3$ (BST) etc. are the various effective lead-free perovskite ferroelectrics [52]. Among them, NBT based systems are more searched from past few years as the effective lead-free ferroelectric systems [53].

In contrast, bismuth layered structure ferroelectrics (BLSF) such as $Bi_4Ti_3O_{12}$ (BIT), $SrBi_2Nb_2O_6$ (SBN), $SrBi_2Ta_2O_9$ (SBT), $SrBi_4Ti_4O_{15}$ etc. have also attracted the attention of the research community because of promising ferroelectric properties [29]. Despite weak piezoelectric properties, these BLSFs find their use in piezoelectric resonators [54].

Although the use of perovskite ferroelectrics in various applications is widespread but they do not find their due promising use because of polarization fatigue and imprint related problems in dielectric, ferroelectric and piezoelectric properties [55]. On the other hand, BLSFs materials show polarization fatigue-resistance up to ~$10^{12}$ cycles, which is comparatively ~ 5-6 order higher than their perovskite counterparts. A key feature is that the devices are typically read destructively, which leads to the requirement that the ferroelectric materials should endure large numbers of switching cycles. However, polarization fatigue is one of the major issues limiting the applicability of ferroelectrics in memory device applications. NBT is a promising ferroelectric material and possesses strong ferroelectricity,

### 1.4.2 $Na_{0.5}Bi_{0.5}TiO_3$ (NBT) System

Sodium bismuth titanate (NBT) was first discovered in 1960 by Smolenskii *et al.* [53]. This system is an A-site distorted perovskite material, in which both the $Bi^{3+}$ and $Na^{+}$ ions occupy the same A-site positions, shown in Fig. 1.12. Furthermore, this system belongs to $ABO_3$ perovskite category with a rhombohedral (R3c) crystal structure at room temperature (RT). However, preliminary structural studies of the NBT system did not provide a conclusive structural understanding [56, 57]. Jones and Thomas reported that this system exhibits rhombohedral *R3c* space group at RT and upon heating changes to tetragonal and subsequently to cubic structure [58]. NBT is a promising ferroelectric material with excellent ferroelectric properties with a relatively large $P_r$ (~ 38μC/$cm^2$) and a high $E_c$ (~ 73 kV/cm), high Curie temperature ~320°C with diffuse phase transition (DPT) and a moderate piezoelectric coefficient ($d_{33}$) ~73pC/N [59]. The peculiar phase transition behavior with different dielectric anomalies of the NBT system has attracted considerable attention [60]. The Rietveld analysis of neutron diffraction data has revealed the coexistence of rhombohedral-tetragonal and tetragonal-cubic phases over the 250-400°C, and 500-540°C temperature ranges, respectively [58]. Yet, two other characteristic transition temperatures were obtained from the dielectric studies, indicated by $T_d$ and $T_m$, known to be depolarization temperature and temperature of the maximum dielectric constant, respectively [61]. At the same time, the high-temperature phase transition viz. tetragonal-cubic has been verified through differential scanning calorimetry (DSC) [62]. Furthermore, the phase transition, at low temperature especially between $T_d$ and $T_m$ has been reported as $T_{R-T}$, which is partially questionable [63, 64]. Vakhrushev *et al.* [65] reported that there is co-existence of rhombohedral-tetragonal phases with the rhombohedral clusters dispersed within a tetragonal matrix in between $T_d$ and $T_m$. The investigation of phase transition behavior between $T_d$ and $T_m$ using transmission electron microscopy (TEM) by Dorcet *et al.* [66] reported rhombohedral-orthorhombic phase transition through the formation of an intermediate modulated phase. The antiferroelectric and relaxor behaviour are reported in the NBT based systems [66]. The interpretation of the behavior of phase transition between $T_d$ and $T_m$ is still quite open to discussion and needs further study in the NBT based systems.

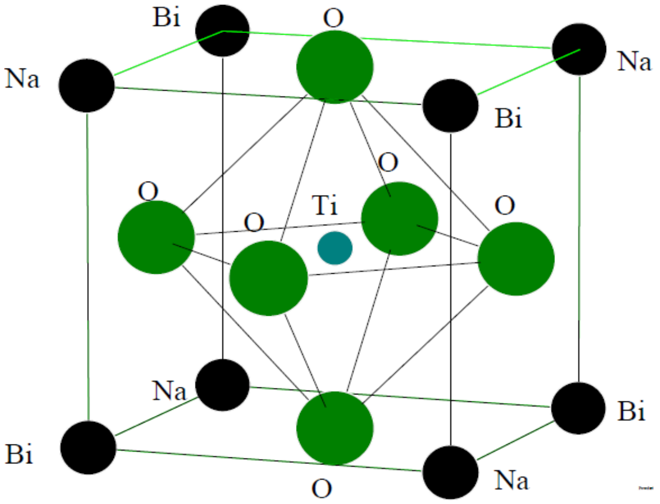

**Fig. 1.12:** Cubic perovskite phase of the NBT system [67]

Besides all the properties and phase transition behaviour of NBT material, it has been noticed from the preliminary literature survey that although the pure NBT material shows a strong ferroelectric behaviour, but it has some critical limitations such as: (i) high coercive field, (ii) high conductivity, (iii) high dielectric loss, (iv) high leakage current, and (v) prone to polarization fatigue. The issue of high conductivity was attributed to volatilization of $Bi^{3+}$ ions during sintering process. Hiruma *et al.* reported the increase in resistivity with the addition of excess bismuth in this system [59]. $Bi^{3+}$ doped NBT system was studied by Wang *et al.*[68] and they reported that it reduces the leakage current, enhances the piezoelectric properties, and increases the dielectric constant and the dielectric loss.

Despite numerous studies on NBT based systems with various substitutions, solid solutions of NBT with some other perovskite-based systems exhibit desired improved properties, and only few of them shows the MPBs in certain compositional ranges. These systems near their MPBs exhibits piezoelectric, ferroelectric and electromechanical properties comparable with the Pb-based ferroelectric materials.

### 1.4.2.1 NBT based Solid-Solutions with MPB

Kounga *et al.* reported an MPB ~6-7 mol% addition of KNN in the NBT system [69]. Although, the addition of KNN system in the NBT system made the solid solution more antiferroelectric in its behavior, it also led to a much higher unipolar strain [69]. However, in the solid solution of $(1-x)(Bi_{0.5}Na_{0.5})TiO_3-(x)(K_{0.5}Na_{0.5})NbO_3$ ceramics, Laoratanakul *et al.* [70] reported an MPB near the composition between x = 0.03 and x = 0.05. Takenaka *et al.* [71] have reported the MPB for $x$ = 0.06-0.07 in the $(1-x)(Bi_{0.5}Na_{0.5})TiO_3$-$xBaTiO_3$ system. The structure of $(Na_{0.5}Bi_{0.5})_{1-x}Ba_xTiO_3$ system showed an MPB between rhombohedral–tetragonal phase in the composition range of 0.04<x<0.08 at RT [72]. The composition of $(Bi_{0.5}N_{0.5})TiO_3$-$Ba(Zr_{0.05}Ti_{0.95})O_3$ system shows an MPB and improved piezoelectric properties in the 3-12 mol% doping of the Ba $(Zr_{0.05}Ti_{0.95})O_3$ ceramics. Chen *et al.* studied the electrical properties of $(1-x)(Bi_{0.5}N_{0.5})TiO_3$-$xBa(Zr_{0.04}Ti_{0.96})O_3$ solid solutions and reported an MPB with the addition of 6 mole % of $Ba(Zr_{0.04}Ti_{0.96})O_3$ ceramics in the NBT system [73]. Zhou *et al.* reported an MPB in the $(Bi_{1/2}Na_{1/2})Ti_{1-x}(Zn_{1/3}Nb_{2/3})_xO_3$ system within the $0.5\% \leq x \leq 2.0\%$ compositional range [74].

Since NBT, BT, and KNN are typical end members for developing lead-free piezoelectric materials [75] their binary as well as ternary solid solutions have been widely studied for ferroelectric and piezoelectric properties [76]. This concept is visualized in Fig. 1.13, where a quasi-ternary phase diagram between the NBT, BT and KNN is constructed [76-78]. From these combinations, seven binary MPBs are constructed (shown in Fig. 1.13) where, MPB-1 and MPB-2 are the NBT rich MPBs owing to binary solid solutions.

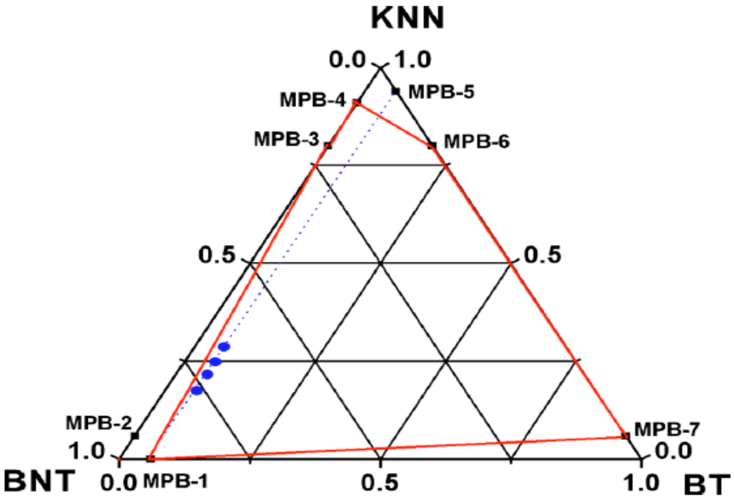

**Fig. 1.13:** Phase diagram of the NBT–BT–KNN ternary system [79].

Nevertheless, in the binary solid solutions of NBT-BT and NBT-KNN, still there is ambiguity regarding the presence of MPB at an exact composition [69-71, 80]. Therefore, the solid solutions of the (1-x) NBT- xBT and (1-x) NBT-xKNN systems near

MPBs have captured our attention for achieving better dielectric, ferroelectric and piezoelectric properties.

## 1.4.3 BLSF Systems

Ferroelectric bismuth-layer perovskite materials are recognized as promising materials for FeRAM applications due to their high polarization fatigue resistance, satisfactory electrical and retention characteristics compared to Pb-based and Pb-free perovskite ferroelectrics [81]. Two families of materials, lead zirconate titanate (PZT) and strontium bismuth tantalate (SBT), have been widely investigated for memory applications. Since the current research is an effort to choose material with excellent ferroelectric behaviour with fatigue-resistant behaviour for NVRAM applications, $SrBi_2Ta_2O_9$ (SBT) has been chosen among numerous BLSFs. This is because of its distinguished properties, which are briefly discussed in the following section.

### 1.4.3.1 $SrBi_2Ta_2O_9$ (SBT) based Systems

SBT system, shown in Fig. 1.9, is an n=2 member of the Aurivillius family of layered compounds, considered to be a versatile material for multifarious applications. The crystal structure of this system has orthorhombic distortion with space group $A2_1am$ and a=0.5306 nm, b=0.55344 nm, and c=2.49839 nm as the lattice parameters [82]. The $P_r$ value of pristine SBT system is ~10μC/cm$^2$ which is much higher than other BLSFs and hence focussed for this research. Araujo *et al.* [83] have first reported the fatigue-free behavior of SBT system. They recognized the inherent advantage of BLSFs over other ferroelectric materials on account of the fact that the former have intermediate bismuth oxide layers between the ferroelectric units. This Pb-free system has a great importance in ferroelectric memory application devices. But, the $\varepsilon_r$ and $P_r$ values of the SBT based systems are lower compared to the perovskite-based counterparts. Therefore, many attempts have been made to improve the dielectric and ferroelectric properties of the SBT based systems with different modifications [84-86]. Moreover, most of the studies on SBT based system are related to their thin film forms. Shimakawa *et al.* [87] have reported that the calculated polarization of Sr-deficient-and-Bi-excess $Sr_{0.8}Bi_{2.2}Ta_2O_9$ ($T_c$ ~ 400 °C) system is larger than their counterpart stoichiometric system. Substitution of Bi and the cation vacancies at the Sr sites helps in enhancing the structural distortion of the $TaO_6$ octahedra, which lead to larger spontaneous polarization and higher Curie temperature. Takemura *et al.* [88] observed that excess Bi and/or Sr deficient SBT thin films showed stronger dielectric anomaly near $T_c$. In particular, the $T_c$ values of the Sr deficient SBT thin films were higher than that of the corresponding bulk ceramics. Simultaneously, creating Sr deficiency and doping excessive Bi can improve the crystallinity and promote the grain growth in the SBT based systems. On the contrary, Wu *et al.* [89] studied $V^{5+}$ doped $SrBi_2Ta_2O_9$ and reported an increased $T_c$ ~360 °C as compared to 305 °C for pure SBT. Coondoo *et al.* [90] studied donor ($W^{6+}$, $Eu^{3+}$) substituted SBT system and reported the decreased electrical conductivity with both the donor substituent. The substitution of the smaller $W^{6+}$ ions for $Ta^{5+}$ ions in the SBT system is reported to be effective in improving its dielectric properties [90]. Moreover, $W^{6+}$ has been investigated as a substituent for bismuth titanates ($Bi_4Ti_3O_{12}$/BIT) in which the $P_r$ is reported to enhance when a small amount of $Ti^{4+}$ was replaced by $W^{6+}$. This has been explained by considering the fact that the substitution introduces cation vacancies that suppress oxygen vacancies in the structure. This is especially relevant for SBT, where the degradation in ferroelectric properties and fatigue is widely believed to originate from the existence of oxygen vacancies[91]. In the present work, the hexa valent ion $W^{6+}$ has been chosen as a donor cation for substituting the pentavalent $Ta^{5+}$ sites in SBT and its influence on the microstructure, dielectric and ferroelectric properties that have been expected. From the literature, we further observed that Coondoo *et al.* studied the series of $SrBi_2(Ta_{1-x}W_x)_2O_9$ (SBTW) samples and the ferroelectric properties was maximum for x = 0.075 [91]. Therefore, simultaneously doped Bi-excess and Sr-deficient non-stoichiometric $Sr_{0.8}Bi_{2.15}Ta_2O_9$ as studied by Aoyagi *et al.* [92], and the donor ($W^{6+}$) doped $SrBi_2(Ta_{0.925}W_{0.075})_2O_9$/SBTW system, as studied by Coondoo *et al.* [91] have caught the attention of the author as promising candidates among the BLSFs.

### 1.4.4 Ferroelectric Ceramic-Ceramic Composites

As discussed in the previous sections, the ferroelectrics can be classified based on their structures. Several researchers have put efforts to prepare composites using different structured ferroelectrics to improve the required properties. In this section, a few examples of such efforts are briefly outlined. N. Zhang *et al.* [93] have investigated the electric fatigue properties of traditional perovskite structured $Pb_{0.94}La_{0.04}(Zr_{0.70}Ti_{0.30})O_3$/PLZT ceramics incorporated with layered structured ferroelectric material, $SrBi_2Nb_2O_9$. Enhancement of grain strength of the PLZT ceramics and increase in the value of dielectric constant due to incorporation of $SrBi_2Nb_2O_9$/SBN was reported. Ceramic composites of $Pb_{0.94}La_{0.04}$ $(Zr_{0.70}Ti_{0.30})O_3$ and $SrBi_2Nb_2O_9$ with almost no deterioration in the value of switchable polarization and hysteresis as compared to 60% deterioration observed in pure PLZT ceramic after $10^6$ cycles was reported. The mechanism of improvement in the fatigue properties was attributed to the specific structure of the bismuth oxide layer in SBN, which could alleviate piled-up oxygen vacancies, nearby ferroelectric domain walls, and facilitate the movement of the ferroelectric domain walls in the process of the ferroelectric domain reorientation. N. Zhang *et al.* [94] again investigated the influences of $SrBi_2Ta_2O_9$ (SBT) on the dielectric and ferroelectric properties of $Pb_{0.94}La_{0.04}(Zr_{0.70}Ti_{0.30})O_3$ ceramics. A substantial increase of dielectric constant was observed with the increase of SBT content in the PLZT–SBT composites. While only 40% value of original switchable polarization could be kept in pure PLZT ceramics after $10^6$ polarization switching, almost no deterioration of switchable polarization and hysteresis loop of the PLZT–SBT composites was observed. Thongmee *et al.* [95] investigated the $Pb(Zr_{0.52}Ti_{0.48})O_3$–$Bi_{3.25}La_{0.75}Ti_3O_{12}$/PLZT-BLT ceramics and observed higher remnant polarization values of the PZT–BLT ceramics than that of the pure PZT (~11.12 μC /$cm^2$) and pure BLT (~10 μC /$cm^2$) ceramics. The coercive field ~4.04 kV/mm, lower than that of pure BLT ceramics, was also obtained in the PZT–BLT ceramics. BLT addition reduced the tendency to depolarize, induced higher endurance to switching field as well as better fatigue resistance to the PZT-BLT samples. This literature study suggests that we can combine an effective Pb-free perovskite with suitable Bi-layered material for improving its fatigue properties.

## 1.5 Motivation

NBT-based solid solutions near MPBs possess high remnant polarization, excellent ferroelectric, piezoelectric and dielectric properties. However, polarization fatigue and leakage current behaviors of these NBT based compounds restrict their use in various device applications. Combination of perovskite-based material with SBT based materials can lead to the improvement in polarization fatigue endurance nature and lower the leakage current density effectively. Hence, we are motivated to choose the NBT based solid solutions near MPB and further modify them with suitable SBT based materials for improving polarization fatigue endurance nature and lower the leakage current density.

## 1.6 Objectives and Scope of the Present Work

Ferroelectric materials find a notable position in the field of material research because of their unique and superior properties, which make them suitable for various electronic, optoelectronic, computer memory etc. device applications. The objectives of the present work have been defined on the basis of the existing problems, challenges and current status in the field of NBT based ferroelectric materials. The main objectives of the present thesis are listed below:

[1] To select the potential lead-free ferroelectric materials with perovskite type structure near their MPBs.

[2] To select the potential lead-free ferroelectrics with bismuth layer structure, possessing excellent polarization fatigue resistant and low leakage current properties.

[3] To optimize the synthesis process for single phase formation of these selected systems by solid state reaction route.

[4] To carry out the detailed structural, microstructural, dielectric, ferroelectric, piezoelectric, leakage current and polarization fatigue studies of the selected lead free perovskite and bismuth layer structure based systems.

[5] To synthesize ferroelectric ceramic-ceramic composites using effective perovskite and effective bismuth layer structure ceramics for improving the polarization fatigue and lower the leakage current behaviors.

[6] To carry out the detailed structural, microstructural, dielectric, ferroelectric, piezoelectric, leakage current and polarization fatigue studies of these ceramic composite systems.

## 1.7 Materials under Present Investigation

In the present work, a systematic investigation of the dielectric, leakage current, piezoelectric, ferroelectric and polarization fatigue properties of the solid solutions of NBT with BT and KNN ceramics was carried out. SBT based ceramics were also synthesized and their various properties were also characterized and analyzed. Finally, the ceramic-ceramic composites using effective perovskite and effective bismuth layer structure ceramics were synthesized, characterized and analysed. Following are the selected materials for the above mentioned objectives:

**Perovskite Material Series**

- $(1-x)Na_{0.5}Bi_{0.5}TiO_3-xBaTiO_3$/NBT-xBT
- $(1-x)Na_{0.5}Bi_{0.5}TiO_3-x\ K_{0.5}Na_{0.5}NbO_3$/NBT-xKNN

(Where x=0.05, 0.06, 0.07, 0.08)

**BLSF Materials**

- $SrBi_2Ta_2O_9$/SBT
- $Sr_{0.8}Bi_{2.15}Ta_2O_9$/$SB_{ex}T$
- $SrBi_2(Ta_{0.925}W_{0.075})_2O_9$/SBTW

**Perovskite-BLSF Series**

- $(1-\phi)(0.93\ Na_{0.5}Bi_{0.5}TiO_3-0.07\ BaTiO_3$/ NBT-BT$)-\phi\ Sr_{0.8}Bi_{2.15}Ta_2O_9$
- $(1-\phi)(0.93\ Na_{0.5}Bi_{0.5}TiO_3-0.07\ K_{0.5}Na_{0.5}NbO_3$/ NBT-KNN$)-\phi\ Sr_{0.8}Bi_{2.15}Ta_2O_9$

(Where $\phi$= 2, 4, 8, 12, 16 wt. %)

# References

[1] A. Safari, R.K. Panda, V.F. Janas, Ferroelectricity: Materials, Characteristics & Applications, Key Engineering Materials, 122-124 (1996) 35-70.

[2] C. Kittel, Introduction to Solid State Physics, John Wiley & Sons, New York, 2005.

[3] A.J. Moulson , J.M. Herbert, Electroceramics: Materials, Properties, Applications, John Wiley & Sons 2003.

[4] B.S. Prakash, Investigations into the microstructure-property correlation in doped and undoped giant dielectric constant material $CaCu_3Ti_4O_{12}$, Materials Research Centre, Indian Institute of Science, Bangalore, 2007.

[5] A.M. Badr, H.A. Elshaikh, I.M. Ashraf, Impacts of Temperature and Frequency on the Dielectric Properties for Insight into the Nature of the Charge Transports in the Tl2S Layered Single Crystals, Journal of Modern Physics, 2 (2011) 12-25.

[6] J.F. Nye, Physical Properties of Crystals: Their Representation by Tensors and Matrices, Clarendon Press1985.

[7] D. Damjanovic, Ferroelectric, dielectric and piezoelectric properties of ferroelectric thin films and ceramics, Reports on Progress in Physics, 61 (1998) 1267.

[8] J.C. Burfoot, G.W. Taylor, Polar Dielectrics and Their Applications, University of California Press 1979.

[9] S.N. Kumar, Synthesis and Characterization of $Sr_{0.53}Ba_{0.47}Nb_2O_6$ based Ferroelectric Composites for Pyroelectric Applications, Department of Physics and Astronomy, National Institute of Technology, Rourkela, 2012.

[10] T.L. Jordan, Z. Ounaies, Piezoelectric Ceramics Characterization, ICASE NASA Langley Research Center Hampton, Virginia, 2001.

[11] P. Dineva, D. Gross, R. Müller, T. Rangelov, Dynamic Fracture of Piezoelectric Materials: Solution of Time-Harmonic Problems via BIEM, Springer International Publishing 2014.

[12] D. Askeland, P. Fulay, W. Wright, The Science and Engineering of Materials, Cengage Learning 2010.

[13] S. Stemmer, S. Streiffer, F. Ernst, M. Ruuhle, Atomistic structure of 90 domain walls in ferroelectric PbTiO3 thin films, Philosophical Magazine A, 71 (1995) 713-724.

[14] R.E. Newnham, Structure-Property Relations, Springer Science & Business Media 2012.

[15] M.A. Torghabeh, Development of lead-free piezoelectric thin films by pulsed laser deposition, Materials Science and Engineering, Rutgers, The State University of New Jersey, 2010.

[16] S.B. Desu, Minimization of fatigue in ferroelectric films, physica status solidi (a), 151 (1995) 467-480.

[17] G.R. Fox, F. Chu, T. Davenport, Current and future ferroelectric nonvolatile memory technology, Journal of Vacuum Science &amp; Technology B, 19 (2001) 1967-1971.

[18] M. Ozgul, Polarization Switching and Fatigue Anisotropy in Relaxor-Lead Titanate Ferroelectric Single Crystals, Department of Materials Science and Engineering, The Pennsylvania State University 2003.

[19] R. Landauer, Electrostatic Considerations in $BaTiO_3$ Domain Formation during Polarization Reversal, Journal of Applied Physics, 28 (1957) 227-234.

[20] H. Blattner, W. Kanzig, W. Merz, H. Sutter, Domain structure of barium titanate crystals Helv Phys Acta 21(1948) 207–209.

[21] G.W. Taylor, Electrical Properties of Niobium-Doped Ferroelectric $Pb(Zr, Sn, Ti)O_3$ Ceramics, Journal of Applied Physics, 38 (1967) 4697-4706.

[22] Q.Y. Jiang, E.C. Subbarao, L.E. Cross, Effect of composition and temperature on electric fatigue of La-doped lead zirconate titanate ceramics, Journal of Applied Physics, 75 (1994) 7433-7443.

[23] C.P. de Araujo, J.F. Scott, G.W. Taylor, Ferroelectric Thin Films: Synthesis and Basic Properties, Gordon and Breach 1996.

[24] G.H. Haertling, Ferroelectric Ceramics : History and Technology, Journal of American Ceramic Society, 82 (1999) 797–818.

[25] B.G. Hyde, S. Andersson, Inorganic crystal structures, John Wiley and Sons, New York, 1989.

[26] H.D. Megaw, Crystal structures: a working approach, Saunders Co., Philadelphia, 1973.

[27] B. Jaffe, W.R. Cook Jr., H. Jaffe, Piezoelectric Ceramics, Academic Press, London and New York 1971.

[28] R.S. Roth, Classification of perovskite and other $ABO_3$-type compounds, Journal of Research of the National Bureau of Standards, 58 (1957) 75-88.

[29] B. Aurivillius, Mixed Bismuth Oxides with Layer Lattices: I. The Structure Type of $CaNb_2Bi_2O_9$, Arkiv for Kemi, 1 (1949) 463-480.

[30] B. Aurivillius, Mixed Bismuth Oxides with Layer Lattices: II. Structure of $Bi_4Ti_3O_{12}$ Arkiv For Kemi, 1 (1949) 499-512

[31] E.C. Subbarao, Crystal Chemistry of Mixed Bismuth Oxides with Layer-Type Structure, Journal of the American Ceramic Society, 45 (1962) 166-169.

[32] R.E. Newnham, R.W. Wolfe, J.F. Dorrian, Structural basis of ferroelectricity in the bismuth titanate family, Materials Research Bulletin, 6 (1971) 1029-1039.

[33] F. Chu, D. Damjanovic, O. Steiner, N. Setter, Piezoelectricity and Phase Transitions of the Mixed-Layer Bismuth Titanate Niobate $Bi_7Ti_4NbO_{21}$, Journal of the American Ceramic Society, 78 (1995) 3142-3144.

[34] H.S. Shulman, M. Testorf, D. Damjanovic, N. Setter, Microstructure, Electrical Conductivity, and Piezoelectric Properties of Bismuth Titanate, Journal of the American Ceramic Society, 79 (1996) 3124-3128.

[35] J.A. Horn, S.C. Zhang, U. Selvaraj, G.L. Messing, S. Trolier-McKinstry, Templated Grain Growth of Textured Bismuth Titanate, Journal of the American Ceramic Society, 82 (1999) 921-926.

[36] S.K. Rout, E. Sinha, A. Hussian, J.S. Lee, C.W. Ahn, I.W. Kim, S.I. Woo, Phase transition in $ABi_4Ti_4O_{15}$(A=Ca,Sr,Ba) Aurivillius oxides prepared through a soft chemical route, Journal of Applied Physics, 105 (2009) 024105.

[37] S.O. Alfaro, A. Martinez-de la Cruz, Synthesis, characterization and visible-light photocatalytic properties of $Bi_2WO_6$ and $Bi_2W_2O_9$ obtained by co-precipitation method, Applied Catalysis A: General, 383 (2010) 128-133.

[38] H. Yan, H. Zhang, M.J. Reece, X. Dong, Thermal depoling of high Curie point Aurivillius phase ferroelectric ceramics, Applied Physics Letters, 87 (2005) 082911.

[39] H.C. Gupta, Archana, V. Luthra, A lattice dynamical investigation of the Raman and the infrared wavenumbers of SBT ($SrBi_2Ta_2O_9$), Journal of Molecular Structure, 984 (2010) 204-208.

[40] M. Tripathy, R. Mani, J. Gopalakrishnan, New substitutions and novel derivatives of the Aurivillius phases, $Bi_5TiNbWO_{15}$ and $Bi_4Ti_3O_{12}$, Materials Research Bulletin, 42 (2007) 950-960.

[41] A. Magneli, Arkiv for Kemi, 1 (1949) 213.

[42] C. Elias, J. Michael, M. Dominique, M. Mario, Flexible relaxor materials: $Ba_2Pr_xNd_{1-x}FeNb_4O_{15}$ tetragonal tungsten bronze solid solution, Journal of Physics: Condensed Matter, 21 (2009) 452201.

[43] J. Ravez, A. Simon, Lead-free relaxor ferroelectrics with 'TTB' structure, Comptes Rendus Chimie, 5 (2002) 143-148.

[44] M.A. Subramanian, G. Aravamudan, G.V. Subba Rao, Oxide pyrochlores - A review, Progress in Solid State Chemistry, 15 (1983) 55-143.

[45] E.E. Erickson, D. Gray, K. Taylor, R.T. Macaluso, L.A. LeTard, G.S. Lee, J.Y. Chan, Synthesis, structure and dielectric characterization of $Ln_2Ti_{2-2x}M_{2x}O_7$(Ln=Gd, Er; M=Zr, Sn, Si), Materials Research Bulletin, 37 (2002) 2077-2083.

[46] A.R. Cleave, Atomic Scale Simulations for Waste Form Applications, Department of Materials Imperial College of Science, Technology and Medicine, London, 2006.

[47] W.S. Kim, J.-K. Yang, C.-K. Lee, H.-S. Lee, H.-H. Park, Synthesis and characterization of ferroelectric properties of $Ce_2Ti_2O_7$ thin films with $Ce^{3+}$ by chemical solution deposition, Thin Solid Films, 517 (2008) 506-509.

[48] A.R. West, Basic solid state chemistry, John Wiley & Sons, New York, 1999.

[49] R.E. Cohen, Origin of ferroelectricity in perovskite oxides, Nature, 358 (1992) 136-138.

[50] M. Ahart, M. Somayazulu, R.E. Cohen, P. Ganesh, P. Dera, H.-k. Mao, R.J. Hemley, Y. Ren, P. Liermann, Z. Wu, Origin of morphotropic phase boundaries in ferroelectrics, Nature, 451 (2008) 545-548.

[51] M. Pecht, Y. Fukuda, S. Rajagopal, The impact of lead-free legislation exemptions on the electronics industry, Electronics Packaging Manufacturing, IEEE Transactions, 27 (2004) 221-232.

[52] T. Takenaka, Piezoelectric properties of some lead-free ferroelectric ceramics, Ferroelectrics, 230 (1999) 87-98.

[53] G.A. Smolenskii, V.A. Isupv, A.I. Afranovskaya, N.N. Krainik, New ferroelectrics of complex composition, Soviet Physics Solid State, 2 (1961) 2651.

[54] S. Zhang, H.J. Lee, C. Ma, X. Tan, Sintering Effect on Microstructure and Properties of $(K,Na)NbO_3$ Ceramics, Journal of the American Ceramic Society, 94 (2011) 3659-3665.

[55] S. Poykko, D.J. Chadi, Dipolar Defect Model for Fatigue in Ferroelectric Perovskites, Physical Review Letters, 83 (1999) 1231-1234.

[56] J. Suchanicz, J. Kwapulinski, X-ray diffraction study of the phase transitions in $Na_{0.5}Bi_{0.5}TiO_3$, Ferroelectrics, 165 (1995) 249-253.

[57] V.A. Isupov, T.V. Kruzina, Some physical-properties of $Na_{0.5}Bi_{0.5}TiO_3$ ferroelectric Izv. Akad. Nauk Sssr Fiz, 47 (1983) 616-618.

[58] G.O. Jones, P.A. Thomas, Investigation of the structure and phase transitions in the novel A-site substituted distorted perovskite compound $Na_{0.5}Bi_{0.5}TiO_3$, Acta Crystallographica Section B, 58 (2002) 168-178.

[59] Y. Hiruma, H. Nagata, T. Takenaka, Thermal depoling process and piezoelectric properties of bismuth sodium titanate ceramics, Journal of Applied Physics, 105 (2009) 084112.

[60] J. Suchanicz, Behaviour of $Na_{0.5}Bi_{0.5}TiO_3$ ceramics in the a.c. electric field, Ferroelectrics, 209 (1998) 561-568.

[61] Z. Yang, Y. Hou, B. Liu, L. Wei, Structure and electrical properties of $Nd_2O_3$-doped $0.82Bi_{0.5}Na_{0.5}TiO_3$-$0.18Bi_{0.5}K_{0.5}TiO_3$ ceramics, Ceramics International, 35 (2009) 1423-1427.

[62] I.P. Pronin, P.P. Syrnikov, V.A. Isupov, V.M. Egorov, N.V. Zaitseva, Peculiarities of phase transitions in sodium-bismuth titanate, Ferroelectrics, 25 (1980) 395-397.

[63] X.X. Wang, X.G. Tang, H.L.W. Chan, Electromechanical and ferroelectric properties of $(Bi_{1/2}Na_{1/2})TiO_3$-$(Bi_{1/2}K_{1/2})TiO_3$-$BaTiO_3$ lead-free piezoelectric ceramics, Applied Physics Letters, 85 (2004) 91-93.

[64] Y. Hiruma, K. Yoshii, H. Nagata, T. Takenaka, Phase transition temperature and electrical properties of $(Bi_{1/2}Na_{1/2})TiO_3$-$(Bi_{1/2}A_{1/2})TiO_3$ (A=Li and K) lead-free ferroelectric ceramics, Journal of Applied Physics, 103 (2008) 084121.

[65] S.B. Vakhrushev, V.A. Isupov, B.E. Kvyatkovsky, N.M. Okuneva, I.P. Pronin, G.A. Smolensky, P.P. Syrnikov, Phase transitions and soft modes in sodium bismuth titanate, Ferroelectrics, 63 (1985) 153-160.

[66] V. Dorcet, G. Trolliard, P. Boullay, Reinvestigation of Phase Transitions in $Na_{0.5}Bi_{0.5}TiO_3$ by TEM. Part I: First Order Rhombohedral to Orthorhombic Phase Transition, Chemistry of Materials, 20 (2008) 5061-5073.

[67] C.J. Walsh, Bond Valence Structure Analysis of Doped Bismuth Sodium Titanate Faculty of Ceramic Engineering. Kazuo Inamori School of Engineering, Alfred University, 2004.

[68] X.X. Wang, K.W. Kwok, X.G. Tang, H.L.W. Chan, C.L. Choy, Electromechanical properties and dielectric behavior of $(Bi_{1/2}Na_{1/2})_{(1-x)}Bi_xTiO_3$ lead-free piezoelectric ceramics, Solid State Communications, 129 (2004) 319-323.

[69] A.B. Kounga, S.-T. Zhang, W. Jo, T. Granzow, J. Rodel, Morphotropic phase boundary in (1-x) $Na_{0.5}Bi_{0.5}TiO_3$-$xK_{0.5}Na_{0.5}NbO_3$ lead-free piezoceramics, Applied Physics Letters, 92 (2008) 222902.

[70] P. Laoratanakul, R. Yimnirun, S. Wongsaenmai, Phase formation and dielectric properties of bismuth sodium titanate-potassium sodium niobate ceramics, Current Applied Physics, 11 S161-S166.

[71] T. Tadashi, M. Kei-ichi, S. Koichiro, $(Bi_{1/2}Na_{1/2})TiO_3$-$BaTiO_3$ System for Lead-Free Piezoelectric Ceramics, Japanese Journal of Applied Physics, 30 (1991) 2236.

[72] Q. Xu, S. Chen, W. Chen, S. Wu, J. Lee, J. Zhou, H. Sun, Y. Li, Structure, piezoelectric properties and ferroelectric properties of $(Na_{0.5}Bi_{0.5})_{1-x}Ba_xTiO_3$ system, Journal of Alloys and Compounds, 381 (2004) 221-225.

[73] Z. Chen, A. Shui, Z. Lu, P. Liu, Piezoelectric and Dielectric Properties of $(Bi_{0.5}Na_{0.5})TiO_3$-$Ba(Zr_{0.04}Ti_{0.96})O_3$ Lead-Free Piezoelectric Ceramics, Journal of the Ceramic Society of Japan, 114 (2006) 857-860.

[74] C. Zhou, X. Liu, Effect of B-site substitution of complex ions on dielectric and piezoelectric properties in $(Bi_{1/2}Na_{1/2})TiO_3$ piezoelectric ceramics, Materials Chemistry and Physics, 108 (2008) 413-416.

[75] S. Zhang, R. Xia, T.R. Shrout, Lead-free piezoelectric ceramics vs. PZT?, J Electroceram, 19 (2007) 251-257.

[76] S.-T. Zhang, A.B. Kounga, E. Aulbach, H. Ehrenberg, J. Rödel, Giant strain in lead-free piezoceramics $Bi_{0.5}Na_{0.5}TiO_3$–$BaTiO_3$–$K_{0.5}Na_{0.5}NbO_3$ system, Applied Physics Letters, 91 (2007) 112906.

[77] S.-T. Zhang, A.B. Kounga, E. Aulbach, T. Granzow, W. Jo, H.-J. Kleebe, J. Rödel, Lead-free piezoceramics with giant strain in the system $Bi_{0.5}Na_{0.5}TiO_3$–$BaTiO_3$–$K_{0.5}Na_{0.5}NbO_3$. I. Structure and room temperature properties, Journal of Applied Physics, 103 (2008) 034107.

[78] S.-T. Zhang, A.B. Kounga, E. Aulbach, W. Jo, T. Granzow, H. Ehrenberg, J. Rödel, Lead-free piezoceramics with giant strain in the system $Bi_{0.5}Na_{0.5}TiO_3$–$BaTiO_3$–$K_{0.5}Na_{0.5}NbO_3$. II. Temperature dependent properties, Journal of Applied Physics, 103 (2008) 034108.

[79] S.-T. Zhang, F. Yan, B. Yang, W. Cao, Phase diagram and electrostrictive properties of $Bi_{0.5}Na_{0.5}TiO_3$–$BaTiO_3$–$K_{0.5}Na_{0.5}NbO_3$ ceramics, Applied Physics Letters, 97 (2010) 122901.

[80] G. Picht, J. Topfer, E. Hennig, Structural properties of $(Bi_{0.5}Na_{0.5})_{1-x}Ba_xTiO_3$ lead-free piezoelectric ceramics, Journal of the European Ceramic Society, 30 (2010) 3445-3453.

[81] J.F. Scott, C.A. Paz de Araujo, Ferroelectric Memories, Science, 246 (1989) 1400-1405.

[82] C.-H. Lu, Y.-C. Chen, Sintering and decomposition of ferroelectric layered perovskites: Strontium bismuth tantalate ceramics, Journal of the European Ceramic Society, 19 (1999) 2909-2915.

[83] C.A.P. de Araujo, J.D. Cuchiaro, L.D. McMillan, M.C. Scott, J.F. Scott, Fatigue-free ferroelectric capacitors with platinum electrodes, Nature, 374 (1995) 627-629.

[84] I. Seiji, U. Ichiro, Piezoelectricity in Ceramics of Ferroelectric Bismuth Compound with Layer Structure, Japanese Journal of Applied Physics, 13 (1974) 1572.

[85] I. Coondoo, A.K. Jha, Investigations of structural, dielectric and ferroelectric behavior of europium substituted $SrBi_2Ta_2O_9$ ferroelectric ceramics, Solid State Communications, 142 (2007) 561-565.

[86] A. Li, H. Ling, D. Wu, T. Yu, M. Wang, X. Yin, Z. Liu, N. Ming, Investigation of the structural and electrical properties of $Sr_{1-x}Bi_{2.2}Ta_2O_9$ thin films with deficient Sr contents, Applied Surface Science, 173 (2001) 307-312.

[87] Y. Shimakawa, Y. Kubo, Y. Nakagawa, T. Kamiyama, H. Asano, F. Izumi, Crystal structures and ferroelectric properties of $SrBi_2Ta_2O_9$ and $Sr_{0.8}Bi_{2.2}Ta_2O_9$, Applied Physics Letters, 74 (1999) 1904-1906.

[88] K. Takemura, T. Noguchi, T. Hase, Y. Miyasaka, Dielectric anomaly in strontium bismuth tantalate thin films, Applied Physics Letters, 73 (1998) 1649-1651.

[89] Y. Wu, M.J. Forbess, S. Seraji, S.J. Limmer, T.P. Chou, G. Cao, Oxygen-vacancy-related dielectric relaxation in $SrBi_2Ta_{1.8}V_{0.2}O_9$ ferroelectrics, Journal of Applied Physics, 89 (2001) 5647-5652.

[90] I. Coondoo, N. Panwar, Enhanced Dielectric and Ferroelectric Properties of Donor ($W^{6+}$, $Eu^{3+}$) Substituted SBT Ferroelectric Ceramics, INTECH Open Access Publisher, 2010.

[91] I. Coondoo, N. Panwar, A.K. Jha, Effect of sintering temperature on the structural, dielectric and ferroelectric properties of tungsten substituted SBT ceramics, Physica B: Condensed Matter, 406 (2011) 374-381.

[92] R. Aoyagi, H. Takeda, S. Okamura, T. Shiosaki, Ferroelectric and piezoelectric properties of bismuth layered-structure ferroelectric $(Sr,Na,Bi)Bi_2Ta_2O_9$ ceramics, Materials Science and Engineering: B, 116 (2005) 156-160.

[93] N. Zhang, L. Li, Z. Gui, Improvement of electric fatigue properties in $Pb_{0.94}La_{0.04}(Zr_{0.70}Ti_{0.30})O_3$ ferroelectric capacitors due to $SrBi_2Nb_2O_9$ incorporation, Materials Research Bulletin, 36 (2001) 2553-2562.

[94] N. Zhang, L. Li, B. Li, D. Guo, Z. Gui, Improvement of electric fatigue properties in PLZT ferroelectric ceramics due to $SrBi_2Ta_2O_9$ incorporation, Materials Science and Engineering: B, 90 (2002) 185-190.

[95] N. Thongmee, A. Watcharapasorn, M. Hoffman, S. Jiansirisomboon, Ferroelectric properties of $Pb(Zr_{0.52}Ti_{0.48})O_3$-$Bi_{3.25}La_{0.75}Ti_3O_{12}$ ceramics, Ceramics International, 38, Supplement 1 (2012) S205-S209.

# Chapter 2

## *Synthesis Route and Investigated Parameters*

### 2.1 Introduction

The basic steps of the solid state reaction route, used in the present work, are presented in the following sections. Structural, microstructural, dielectric, piezoelectric, leakage current, ferroelectric and polarization fatigue characterization techniques are used in the present study. The basic principles of these experimental methods and techniques are also briefly explained in this chapter.

### 2.2 Synthesis Procedure

Processing technique plays a vital role in determining the purity, microstructure and density, which ultimately decides the electrical properties of the synthesized product [1-3]. The ever increasing demand of advanced ceramics with specific properties has led to the improvement and optimization of existing synthesis techniques as well as development of new ones. Some of the most interesting methods/techniques, used to prepare the ferroelectric ceramic materials, are solid-state reaction route, sol-gel, polymer-sol-gel, hydrothermal, micro emulsion, combustion, thermal pyrolysis spray, molten salt synthesis route etc. Each of these synthesis routes has their own advantages and disadvantages. In order to achieve a quality product with respect to purity, homogeneity, reactivity, particle sizes etc., one has to select the most desirable synthesis route. In the present study, solid state reaction route has been selected for the processing of the selected materials. Though, the solid state reaction route has some inherent shortcomings like: chances of contamination and non-homogeneity, yet it has its own specific advantages over other synthesis routes. Solid state reaction route, mostly used for a large-scale production of the ceramics, is also most convenient for laboratory scale preparation of the ceramics. It is a convenient, easier and a low-cost technique among other available synthesis methods in terms of performance, reliability and reproducibility [4].

## 2.2.1 Solid State Reaction Route (SSRR)

Solid state reaction route is the most extensively used processing method for the synthesis of polycrystalline bulk ceramics. This method involves large range of selection of starting materials viz. carbonates, oxides, etc. Since solids do not react with each other at room temperature (RT), it is necessary to heat them at elevated temperatures as high as up to ~1500°C for the proper reaction to take place at significant rate. Thus, both kinetic and thermodynamic factors are important in this method. Here, the solid reactants react chemically without the presence of any solvent at high temperatures yielding a product which is stable. The major advantage of this method is that the final compound is in the solid form, which is structurally pure and with the desired properties. The various steps of solid-state reaction synthesis route are given in the flow chart, shown in Fig.2.1.

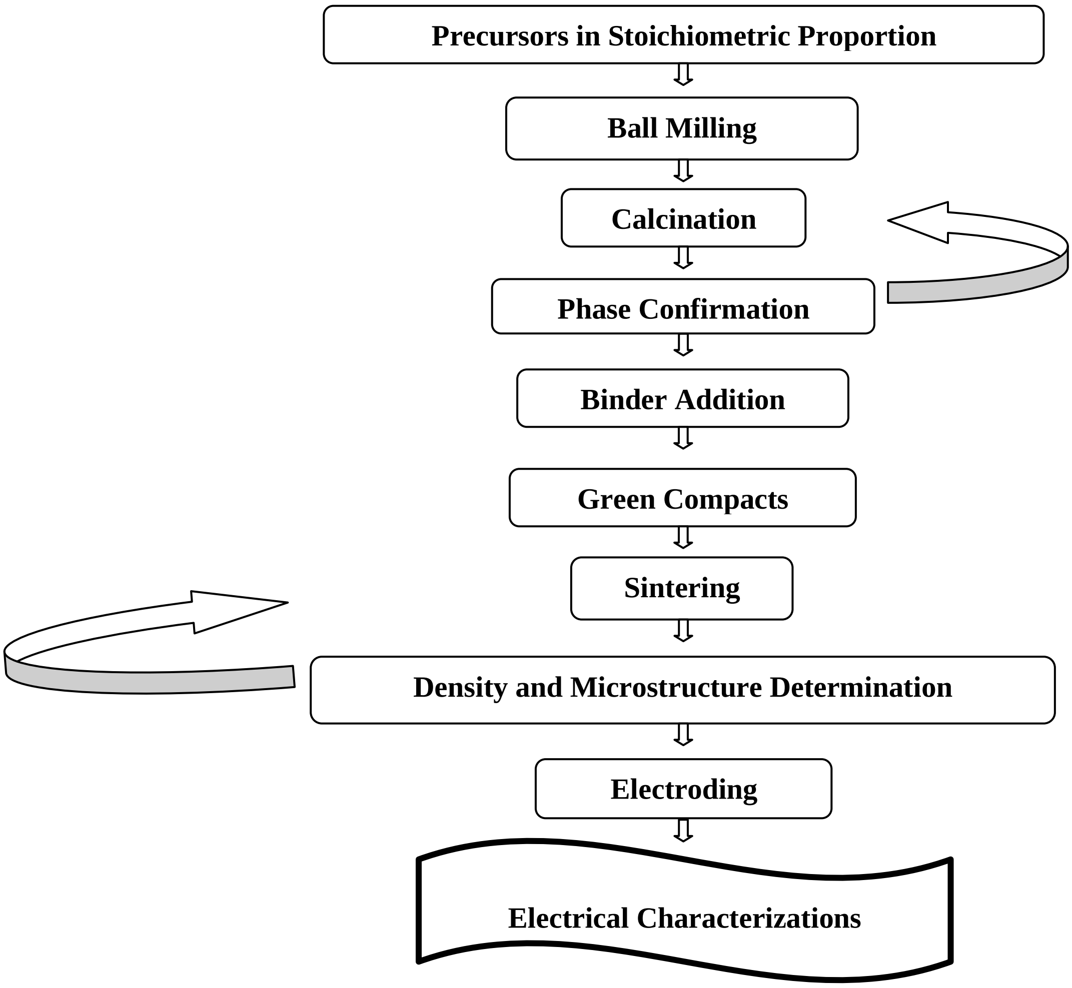

**Fig.2.1:** Synthesis steps involved in a conventional solid state reaction route.

#### 2.2.1.1 Precursors in Stoichiometric Proportion

Precursors are the starting raw materials also called as reagents. The nature of the raw materials has a major effect on the properties of the final ceramic material. The quality of the starting raw materials depends upon the purity% and the particle size. The starting reagents are dried thoroughly before weighing to remove the moisture and are selected on the basis of reaction conditions. The surface area of the reagents influences the reaction rate for which fine-grained materials should be used. If the raw materials contain some impurities, it affects the physical properties of the final product material [5].

#### 2.2.1.2 Ball Milling and Grinding

Ball milling is a process of grinding the raw materials into fine powder for uniform mixing when different materials are grinded together. The rate of grinding depends on particle size of raw materials, grinding media, container and the medium used [6]. Rate of grinding is inversely proportional to particle size of the materials. As the particles become fairly fine, further reduction in size becomes more and more difficult. The size and density of grinding media plays an important role for deciding the rate of milling. In the milling process, the particles experience mechanical stress at their contact points due to compression, impact, or shear with the milling medium or with other particles. Size and density of the particles play an important role in the formation of desired product; therefore proper care should be taken in the milling and grinding steps.

#### 2.2.1.3 Calcination

The calcination temperature can be estimated by thermal analysis techniques (DSC/TGA characterization techniques, discussed in later sections) of the dried precursor mixture, obtained after milling process. During calcination, the phase formation of the compound takes place by solid-phase reaction, which involves the chemical reaction through atomic diffusion at temperature below the melting points of the precursors [7]. Four physical processes are involved in the calcination process, viz. (i) linear expansion of the particles (ii) contraction of the product (iii) solid phase reaction and (iv) grain growth. Generally, calcination process is an endothermic decomposition reaction, which results in the final single phase with the liberation of gases [8].

#### 2.2.1.4 Binder Addition

Binder holds the granules of the powder together during the preparation of the green compacts, required for sintering. Addition of binder also reduces the brittleness of the green compacts. The binder should decompose at much lower temperature, compared to the calcination temperature of the compound. Generally, polyvinyl alcohol (PVA) is used as the binder which is a water soluble synthetic polymer with a monomer of (-CH2-CHOH-) with excellent adhesive property.

### 2.2.1.5 Sintering

Green compacts are densified through the sintering process. The various mechanisms of sintering of polycrystalline materials take place through bonding and growth of necks between the particles. Various sintering mechanisms are: lattice diffusion from the surface, surface diffusion, vapor transport, lattice diffusion from the grain boundary, grain boundary diffusion, and plastic flow [9]. Grain boundary diffusion and lattice diffusion are the most important densifying mechanisms in the polycrystalline ceramics. The diffusion from grain boundary to the pore permits neck growth as well as contribute to the densification process. Besides these mechanisms, different ionic species forming the compound are coupled to preserve the stoichiometry and electroneutrality. In sintering process, the green compacts are heated to a temperature, which is approximately ~50-80% of the melting temperature [10], as a result the pellet does not melt and the particles join to reduce the porosity of the compact by ionic diffusion, shown in Fig.2.2. The sintered pellets are ready for any type of characterizations succeeded by proper optimization or/else sintering temperature is varied for better densification and is optimized again.

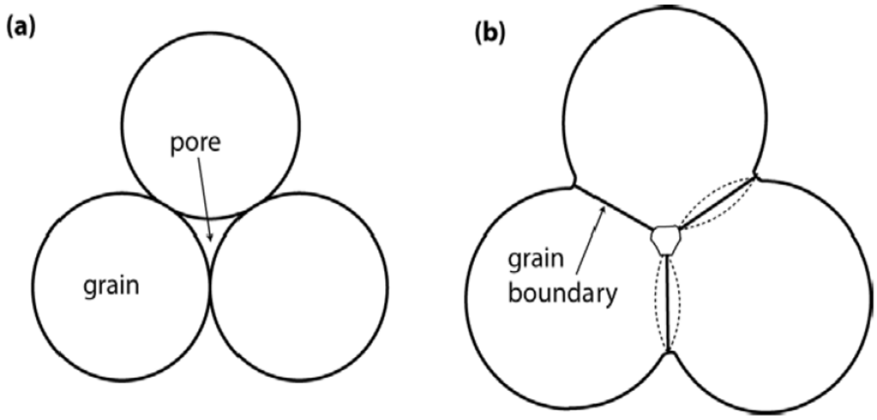

**Fig. 2.2:**Schematics of sintering process: (a) three grains before solid-state sintering, and (b) after sintering[11].

### 2.2.1.6 Electroding

Electroding on insulating ceramics is required for testing the electrical properties of the ceramic materials. The selection of suitable conducting electrodes for electrical measurements of a non-conducting sample is very important. There are two types of parallel plate measurement methods: contacting and non-contacting electrodes. The contacting thin film electrode method is adopted widely. This is because it causes minimum error, caused by the air gap between the electrodes and the surface of the test material. Secondly, the procedure to measure dielectric constant under this method is simple as compared to non-contacting electrode method.

## 2.3 Characterization Techniques

Advanced ceramics demonstrate specific properties, and they are characterized by various experimental techniques with a specific aim. Some of the characterizations are related with the synthesis process and others are related with the characterizations of the final product for the purpose of analyzing their utility for a specific device application. In the present study, following experimental techniques are used:

- Thermogravimetric analysis and differential scanning calorimetry
- X-Ray diffraction study
- Density measurements
- Scanning electron microscope
- Dielectric characterizations
- Leakage current study
- Piezoelectric study
- Ferroelectric P-E loop study
- Polarization fatigue study

### 2.3.1 Thermo Gravimetric Analysis and Differential Scanning Calorimetry

Thermo Gravimetric Analysis (TGA) is one of the thermal analysis techniques in which the substance undergoes a mass change when subjected to a controlled temperature rise. The specimen powder and the reference material are placed on refractory pans (Alpha alumina or platinum) and suspended from high precision balances. A thermocouple is in close proximity to the specimen though not in contact, so as not to interfere with the free float of the balances. The balances are electronically compensated to ensure the specimen pan does not move whenever the specimen gains or losses weight. The measurement is normally carried out in air or in an inert atmosphere, such as He/Ar, and the changes in weight are recorded as a function of temperature of the testing samples. Sometimes the measurement is performed in neon oxygen atmosphere to slow down the oxidation process [12, 13].

Differential scanning calorimetry (DSC) is also one of the thermal analysis techniques in which the difference in the amount of heat required to increase the temperature of a sample and that of the reference is measured as a function of temperature. The sample and reference are enclosed in the same furnace and are maintained at nearly the same temperature throughout the experiment. The temperature program is designed in such a way that the temperature of sample holder increases linearly as a function of time. The reference sample has a well-defined heat capacity over the range of temperatures to be scanned and does not undergo a physical or chemical change during the measurement. The basic principle underlying this technique is that the sample undergoes a physical transformation namely phase transitions, melting, decomposition, crystallization etc. and heat will flow into or out of the specimen (endothermic or exothermic process) in order to maintain both the specimen and the reference at the same temperature. When the specimen undergoes a phase transition from solid to liquid phase it requires more heat to be supplied than the reference to maintain the same temperature. This absorption of heat corresponds to an endothermic peak in the DSC curve. Similarly when the sample becomes crystallized, heat energy is liberated from the specimen and hence corresponds to an exothermic peak in the DSC curve. By observing the difference in heat flow between the specimen and reference, it is possible to measure the amount of heat absorbed or released during such transitions [12-14].

### 2.3.2 X-Ray Diffraction Study

X-ray diffraction (XRD) is a powerful nondestructive tool for determining the structure, phase, crystal orientations (texture), and other structural parameters, such as average crystallite size, strain, crystallinity, and crystal defects. Physical properties of the solids (e. g., electrical, optical, magnetic, ferroelectric, etc.) depend on atomic arrangements of materials; therefore the determination of the crystal structure is an important part in the characterizations of the materials. XRD peaks are formed by constructive interference of a monochromatic beam of X-rays scattered at specific angles from each set of lattice planes in a sample [15]. The peak intensities are determined by the atomic arrangements within the lattice plane. Consequently, the XRD pattern is a fingerprint of periodic atomic arrangements in the given material [16]. The XRD pattern is governed by the Bragg’s law. The Bragg condition of diffraction is defined as

$$n\lambda = 2d\sin\theta \qquad (2.1)$$

where, n is the order of diffraction, $\lambda$ is the wavelength of the X-rays, $d$ is the interplanar spacing, and $\theta$ is the scattering angle. The wavelength of the X-rays should be of the order of lattice spacing of the sample in order to produce diffraction peaks at specific angles. Fig 2.3 shows the schematic interaction of X-rays with the crystal planes.

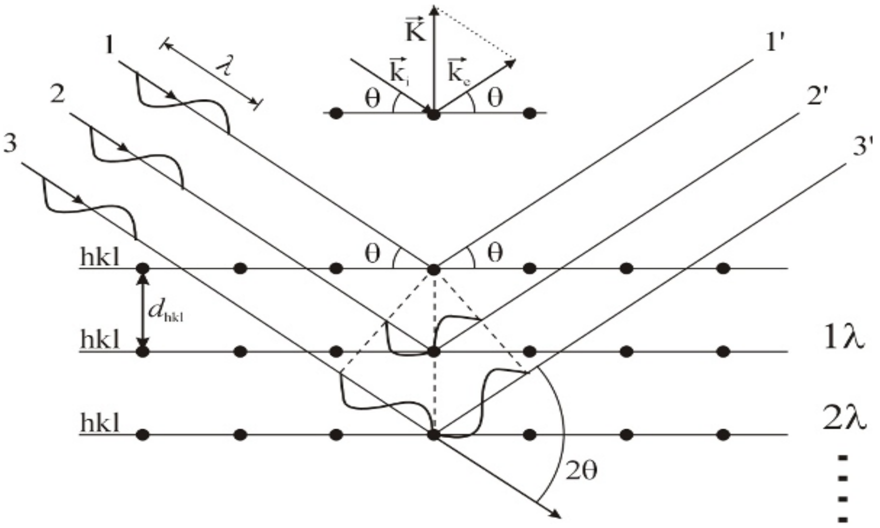

**Fig.2.3**: Schematic representation of interaction of X-rays with crystal planes [17].

Various properties of the materials can be analyzed by determining the lattice parameters accurately. The calculation of the lattice parameters from the $2\theta$ positions or $d$-spacing values can be done using the following formula:

$$\frac{1}{d_{hkl}^{2}} = V^2[h^2b^2c^2\sin^2\alpha + k^2c^2a^2\sin^2\beta + l^2a^2b^2\sin^2\gamma]$$

$$= abc(1-\cos^2\alpha - \cos^2\beta - \cos^2\gamma + \cos\alpha\cos\beta\cos\gamma)^{1/2} \qquad (2.2)$$

where, $V$ is the volume of the unit cell, $a$, $b$, $c$, $\alpha$, $\beta$, and $\gamma$ are the lattice parameters and $h, k, l$ are the Miller indices of the lattice planes. The following information can be obtained from the XRD analysis: (i) quality and phase confirmation of the synthesized samples, (ii) the interplanar spacing (d), (iii) the intensities of the reflections, (iv) the unit cell parameters and the type of lattice [18].

### 2.3.3 Density Measurements

Density of the synthesized materials is an important experimental parameter for specifying their use in various device applications. The synthesized materials having experimental density near to that of the theoretical density exhibits better properties. The theoretical density can be determined by knowing the lattice parameters. The theoretical density '$\rho_{th}$' can be determined by using the following equation,

$$\rho_{th} = \frac{nM}{NV} \qquad (2.3)$$

where, $n$ is the number of atoms per unit cell and $M$ is the atomic weight. '$N$' is Avogadro's number and '$V$' is the volume of the unit cell. The experimental density ($\rho_{ex}$) of the synthesized materials is measured by using the Archimedes principle:

$$\rho_{ex} = \left[ \frac{Dry\ weight}{Soaked\ weight - Suspended\ weight} \right] \times Density\ of\ the\ liquid \qquad (2.4)$$

Relative density (RD) of the synthesized materials is defined as the ratio of experimental density to the theoretical density and calculated by using the following relation,

$$RD = (\frac{\rho_{ex}}{\rho_{th}}) \times 100\% \qquad (2.5)$$

## 2.3.4 Scanning Electron Microscope

Scanning electron microscope (SEM) is a type of electron microscope that images a sample surface by scanning it with a high-energy beam of electrons. This technique is widely used to characterize the surface topography and morphology of the sintered samples. The fundamental principle of scanning electron microscopy (SEM) is mainly based on the kinetic energy of the accelerated electrons. This energy is dissipated in the form of a variety of signals due to the electron-sample interactions. These signals include secondary electrons, backscattered electrons (BSE) (used for SEM images), diffracted backscattered electrons (used to determine crystal structures and orientations), photons (characteristic X-rays, used for elemental analysis), visible light (cathode luminescence), and heat. Secondary electrons and backscattered electrons are commonly used in studying the morphology of the sintered samples and illustrating the contrasts in the composition of the multiphase samples (i.e. for rapid phase discrimination). The characteristic X-rays are generated by inelastic collisions of the incident electrons with electrons in discrete orbitals (shells) of the atoms of the investigated samples, thus the characteristic X-rays are produced for each element of the samples. SEM analysis is considered to be "non-destructive"; because the X-rays generated by electron interactions do not lead to volume loss of the sample [19, 20]. Fig 2.4 shows the schematic diagram of different signals coming out from the interaction of electron beam with the matter.

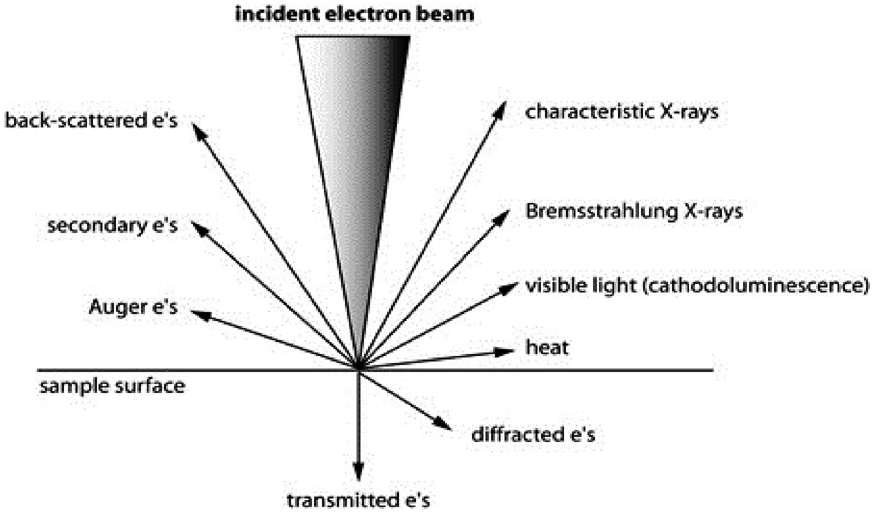

**Fig. 2.4:** Interaction of electron beam with matter [21]

The specimen under scanning electron microscope must be electrically conductive at least at the surface and electrically grounded to prevent the accumulation of electrostatic charge at the surface. The nonconductive specimen tends to get charged when scanned by the electron beam and especially in the secondary electron imaging mode; which causes scanning faults and other imaging artifacts. Therefore, it is usually coated with an ultrathin layer of electrically conducting material like platinum or gold; using low vacuum sputter coating or by high vacuum evaporation [20, 22].

## 2.3.5 Dielectric Characterizations

Ferroelectric materials very often show interesting dielectric properties like high dielectric constant (**$\varepsilon_r$**) and low dielectric loss (tanδ), which are important for practical capacitor device applications. Study of **$\varepsilon_r$** and tanδ provides a great deal of information about the utility of the ferroelectric materials in various dielectric applications.

### 2.3.5.1 Dielectric Constant

The dielectric constant (**$\varepsilon_r$**) of a material is the ratio of the charge stored on a pair of electrodes, separated by a slab of material, at a given voltage and the charge stored on a set of identical electrodes, separated by vacuum. It is defined as;

$$\varepsilon_r = 1 + \frac{P}{\varepsilon_0 E} \qquad (2.6)$$

where, $\varepsilon_r$ : Dielectric constant or relative permittivity of the material

$E$ : Net electric field in the presence of dielectric material

$P$ : Induced dipole moment / volume under an applied electric field $E$

$\varepsilon_0$ : Permittivity of the free space

And, for an alternating electric field, the dielectric constant can be written as

$$\varepsilon_r = \varepsilon' - i\varepsilon'' \qquad (2.7)$$

where, $\varepsilon'$ and $\varepsilon''$ are the real and imaginary components of the dielectric constant, respectively. The real component is in phase and imaginary component is in $90^o$ out of phase with the applied external electric field. The $\varepsilon''$ is caused either by resistive leakage or dielectric absorption.

For ordinary substances, the value of $\varepsilon_r$ is low, usually under 5 for organic materials and under 20 for most inorganic solids. Ferroelectric ceramics, however generally have much higher $\varepsilon_r$, typically several hundred to several thousand [23, 24].

LCR meter measures the various electrical parameters at low frequencies employing auto-balancing bridge. Fig.2.5 shows the schematic diagram of auto-balancing bridge. Z is the impedance of the material (in the form of electrode pellet), $Z_1$ and $Z_2$ are known impedance and $Z_x$ is variable impedance. $Z_x$ is varied until no current flows through G. Underbalanced condition, Z can be calculated as,

$$Z = (\frac{Z_2}{Z_1})Z_\times \qquad (2.8)$$

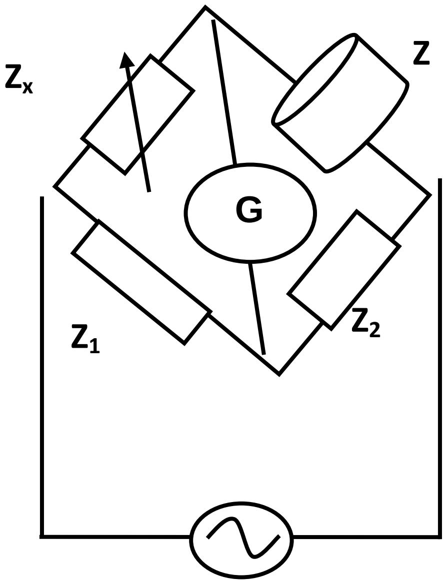

**Fig. 2.5:** Schematic diagram of auto-balancing bridge [25].

Knowing the value of $Z$, the resistance component ($R$) and reactance component ($X$) can be calculated. Capacitance ($C$) and dielectric loss ($\tan\delta$) can be calculated using the following formula $C = 1/2\pi fX$ where $f$ is frequency and $\tan\delta = R/X$. Knowing the capacitance $C$, dielectric constant can be calculated as,

$$\varepsilon_r = \frac{C \times d}{\varepsilon_o \times A} \qquad (2.9)$$

where, $\varepsilon_o$ : Permittivity of free space in farad per meter (8.854 x $10^{-12}$F/m)

$\varepsilon_r$ : Dielectric constant or relative permittivity of the sample.

$A$ : Area of each plane electrode in square meters ($m^2$)

$d$ : Thickness of the electrode ceramic sample in meters (m)

### 2.3.5.2 Dielectric Loss

The charging current in an ideal dielectric leads the applied voltage by $\pi/2$ radians ($90^o$). However, in real dielectrics, in addition to the charging current, associated with the storage of electric charge by the dipoles, a loss current must be considered, which arises from the long-range migration of charges, e.g., DC ohmic conduction and the dissipation of energy associated with the rotation or oscillation of dipoles [24]. As the dielectric always possesses a loss, it is generally represented by a complex dielectric constant, defined in equation 2.10. The total current in the real dielectric is a complex quantity which leads the voltage by an angle (90-δ), where δ is called the loss angle. The tangent loss is given by

$$\tan\delta = I_l/I_c = \frac{\varepsilon''}{\varepsilon'} \qquad (2.10)$$

The total current $I$ through the capacitor can be resolved into two components, a charging current ($I_c$) in quadrature with voltage and conduction current $I_l$ in phase with the voltage. The vector resolution of the total current is shown in Fig. 2.6.

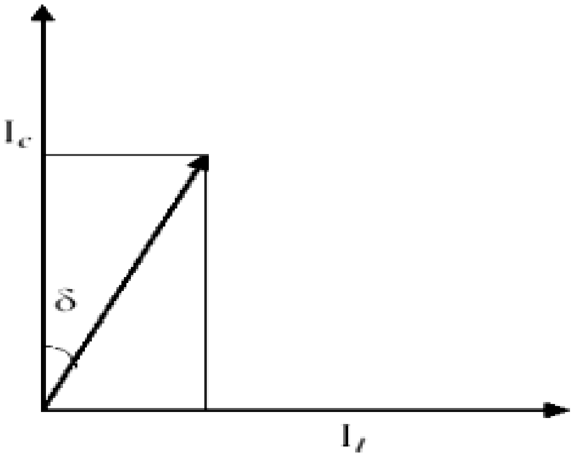

**Fig. 2.6:**The vector resolution of ac current in a capacitor [4].

Dielectric loss ( $\tan\delta$ ) is also commonly known as the dissipation factor, $D$. The inverse of the loss tangent, $Q = 1/\tan\delta$, is used as a figure of merit in high-frequency applications [24].

### 2.3.6 Leakage Current Study

Leakage current is primarily associated with the dielectric capacitors, used in the electronic devices, and refers to the conduction of a small amount of current even when they are electrically turned off. Even though this off current is of the order of magnitude less than that of the current through the device when it is on, this leakage current still slowly discharges through the capacitor. The leakage current through a capacitor relate to the imperfection within the used dielectric materials and hence also known as dielectric leakage. In most of the applications, the ferroelectrics are used as capacitors, either as bulk ceramics or single crystals or as thin films of polycrystalline or of epitaxial nature [26]. Also, most of the device applications are related with the external voltage, applied on the ferroelectric capacitors, which leads to the unavoidable occurrence of a leakage current. Traditionally, the possible conduction mechanisms in ferroelectric materials are divided in two major classes [27]:

1. Bulk limited: ohmic-type conduction; space charge limited currents (SCLC); Pool-Frenkel emission (PFE) from the deep traps; hopping.
2. Interface limited: thermionic emission over the potential barrier at the electrode interface, also known as Schottky emission (SE); electric field assisted tunneling or Fowler-Nordheim tunneling (FNT).

If the leakage is controlled by the PFE, which originates from the field assisted thermal ionization of trapped carriers into the conduction band of the materials; then the leakage current density can be expressed as [28].

$$J = AE\exp\left[\frac{-\left(\phi_t - e\sqrt{\frac{eE}{\pi\varepsilon_{opt}\varepsilon_0}}\right)}{kT}\right] \qquad (2.11)$$

where, $A$ is a constant, $E$ is applied electric field, $\phi_t$ is the trap ionization energy, $e$ is the elementary charge, $T$ is the temperature, $k$ is the Boltzmann's constant, $\varepsilon_{opt}$ is the optical dielectric constant, and $\varepsilon_o$ is the permittivity of free space. On the other hand, if the leakage is dominated by SCLC, which originates from the density of free electrons when carrier injection overcomes density of thermally stimulated free electrons, then the leakage current density can be expressed as [29]

$$J = \frac{9}{8}\varepsilon_r \varepsilon_0 \mu \frac{E^2}{L} \qquad (2.12)$$

Where, μ is the mobility of charge carriers, $\varepsilon_r$ is the dielectric constant, and L is the material thickness. Furthermore, if the leakage is controlled by the FN tunneling, then the leakage current density can be expressed as [30]

$$J = BE^2 \exp\left(-\frac{C\phi_i^{3/2}}{E}\right) \qquad (2.13)$$

Where, B and C are constants and $\phi_i$ is the potential barrier height.

The J-E characteristics of FN tunneling, PF emission, and SCLC can be characterized by the linear relationships $J$ $vs.$ $E$ in the form $\ln(J/E^2) - \ln(1/E)$, $\ln(J/E) - E^{1/2}$ and $\log(J) - \log(E)$, respectively, based on their slope which is around two.

## 2.3.7 Piezoelectric Study

### 2.3.7.1 Strain vs. Electric Field Behavior

In ferroelectric materials, polarization switching by an applied external electric field leads to strain–electric field ($S - E$) hysteresis loop. Generally, the $S - E$ hysteresis loops in the ferroelectrics resemble the shape of a butterfly and arises due to the three types of effects. One is the converse piezoelectric effect and the other two are due to switching and movement of domain walls. Here, the converse piezoelectric effect is known to be a primary electromechanical coupling effect in solid-state theory i.e. the strain is linearly proportional to the electric field, whereas electrostriction is a secondary coupling effect in which the strain is proportional to the square of the electric field and is independent of the direction of the applied electric field. Some ferroelectric materials (relaxor) show the electrostrictive effect, shown in Fig. 2.7(a) [31], and expressed as:

$$x = ME^2 \qquad (2.14)$$

Where, $x$ is the strain induced with the application of applied electric field $E$, and $M$ is electrostrictive constant.

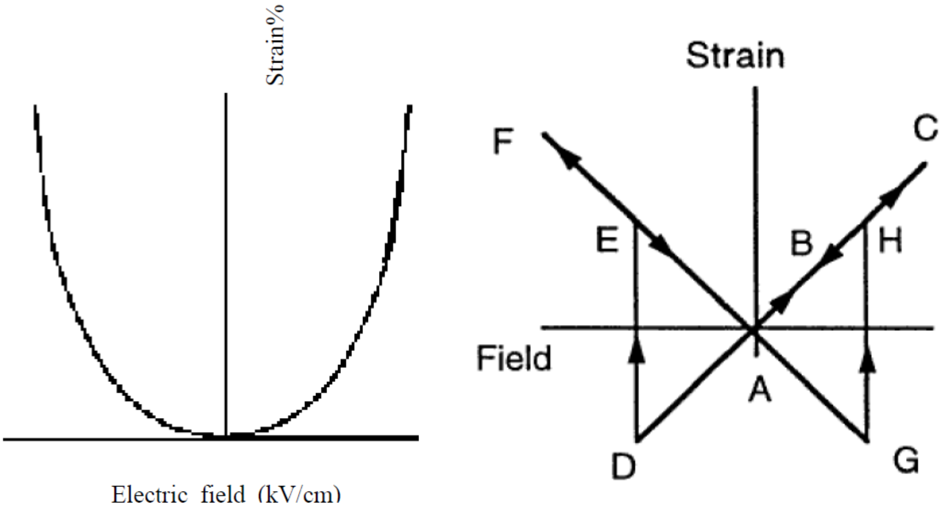

**Fig. 2.7: (a)** Strain induced by electric field in an electrostrictive material [32]**,** and **(b)** butterfly loop in a piezoelectric material [33]**.**

Fig. 2.7(b) shows the strain vs. electric field ($S-E$) hysteresis loop of a ferroelectric material. At zero fields (point A), the strain of the crystal is taken to be zero. The electric field is then applied in the direction of the spontaneous polarization. As the field is increased, the crystal expands due to piezoelectric effect and the induced strain traces the path A–B–C. The expansion continues until the maximum field reaches to point C. At point C, the field starts to decrease, but it is still parallel to $P_s$. The strain of the sample traces the same line but in the opposite direction (from C to A). At point A the strain is again zero. The field then changes its direction, becoming antiparallel to $P_s$. As the field strength increases in the negative direction, the crystal contracts with respect to point A. At point D, the field is large enough to switch the direction of polarization. After switching, the polarization becomes parallel to the field and the strain becomes positive again (point E). During further increase of the field in the negative direction, strain increases to point F and then decreases back to point A as the field is decreased [33]. The reversal of the polarization and sudden change of the strain happens again at point G. The strain–field curve is linear, indicating that the strain is purely piezoelectric except at the switching points D and G.

Practically, the $S-E$ curve for a piezoelectric material has a hysteresis loop, which resembles the shape of a butterfly, shown in Fig. 2.8. This results because of the combined effect of electrostrictive and piezoelectric phenomenon, switching and movement of domain walls in a ferroelectric material. Moreover, ceramic samples usually contain a number of non-180$^{o}$ domain walls. The movement and switching of non-180$^{o}$ domain walls may involve a significant change in the dimensions [34]. During the field cycling process, a residual (or remnant) strain may be observed at zero fields if the domains do not switch to their original positions [34, 35]. As the contribution to the strain from movement of domain walls is strongly nonlinear and possess a hysteresis, this results in a non-linear $S-E$ curve, shown in Fig. 2.8. However, hysteresis free S-E behavior is desired for actuator applications [36].

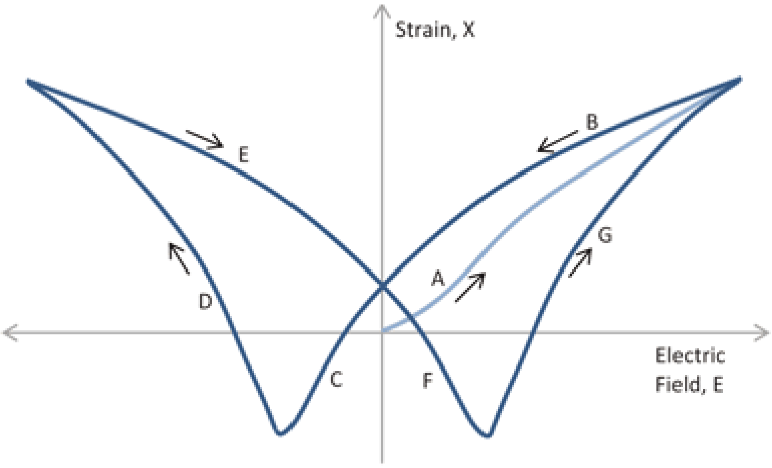

**Fig. 2.8:** Strain versus electric field behavior of a general ferroelectric material [37].

### 2.3.7.2 Poling

Inside a ferroelectric crystal, the regions with uniform polarization are called ferroelectric domains within which all the electric dipoles are aligned in the same direction. The domains in a crystal are separated by boundaries called domain walls. Adjacent domains can have their polarization vectors in antiparallel directions, at right angles to one another, etc. Neighbouring domains having polarization vectors at right angles and antiparallel directions are known as having $90^o$ or $180^o$ domain walls, respectively [24].

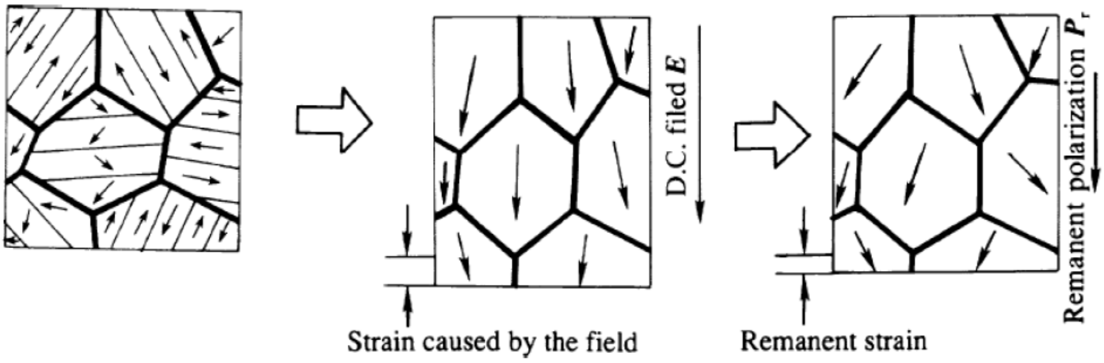

**Fig. 2.9:** Schematic illustration of the poling process [38].

A ferroelectric single crystal has multiple ferroelectric domains when it is grown. Poling is a process in which a single domain can be obtained by the motion of domain walls which is made possible by the application of a sufficiently high electric field. This is a very important process required for realizing the practical application of polycrystalline ferroelectric ceramics in various devices. Ferroelectric ceramics do not possess piezoelectric properties owing to the random orientations of the ferroelectric domains before poling. During poling, a DC electric field is applied on the ferroelectric sample, which forces the domains to be oriented in a particular direction. After poling i.e., even after the removal of the electric field, a remnant polarization and a remnant strain is maintained in the sample and because of which the sample exhibits piezoelectricity. A simple illustration of the poling process is shown in Fig. 2.9.

#### 2.3.7.3 Piezoelectric Coefficients

##### 2.3.7.3.1 Piezoelectric Charge Coefficient

As explained in the previous chapter, either direct or converse piezoelectric effects can be employed for evaluation of piezoelectric coefficients. Measurement of the piezoelectric coefficients using the direct piezoelectric effect is done by applying a normal load to a ferroelectric capacitor and then measuring the charge on the electrodes. To measure the piezoelectric coefficients using the converse piezoelectric effect, an electric field is applied and the strain in the ferroelectric material is measured. The equations for the direct and converse piezoelectric effects are given as:

$$\text{Direct effect: } D = dT \qquad (2.15)$$

$$\text{Converse effect: } S = dE \qquad (2.16)$$

where, '$d$' is the piezoelectric charge coefficient, '$D$' is the dielectric displacement, '$T$' is the mechanical stress, '$E$' is the electric field and '$S$' is the mechanical strain. Higher value of '$d$' is desirable for materials intended to be developed for applications which use motion or vibration, such as sonar or ultrasonic cleaner or transducers [24]. Since, piezoelectric coefficient is direction dependent i.e., it is a tensor quantity; the longitudinal piezoelectric coefficient ($d_{33}$) is the value of the piezoelectric coefficient that applies to the distortion measured in the same direction as that of the applied external electric field [39]. The strain induced in a piezoelectric material by an applied electric field depends on the value of $E$ and $d$, which decides the material's suitability for strain-dependent (actuator) applications [40].

#### 2.3.7.3.2 Electromechanical Coupling Coefficient

The electromechanical coupling factors, $k_{33}$, $k_{31}$, $k_p$, and $k_{15}$ describes the effectiveness with which a piezoelectric material converts electrical energy into mechanical energy, or converts mechanical energy into electrical energy. ‘k’ can be determined from the dimension of the sample. In the $k_{33}$, $k_{31}$, and $k_{15}$ electromechanical coupling coefficient notations, the first subscript denotes the direction along which the electrodes are connected; the second denotes the direction along which the mechanical energy is applied, or developed. In general, the electromechanical coupling factor can be expressed as [41]:

$$k^2 = \frac{Mechanical\ energy\ converted\ to\ electrial\ energy}{Input\ mechanical\ energy} \tag{2.17}$$

$$k^2 = \frac{Electrical\ energy\ converted\ to\ mechanial\ energy}{Input\ electrical\ energy} \tag{2.18}$$

In contrast to static DC conditions, the behavior of the piezoelectric materials is much more complex under dynamic DC conditions. Generally, it is characterized in terms of an equivalent electrical circuit, which exhibits both parallel and series resonance frequencies. The frequency of the minimum impedance ( $f_r$ ) and the frequency of the maximum impedance ( $f_a$ ) of a typical ferroelectric material are shown in Fig.2.10.

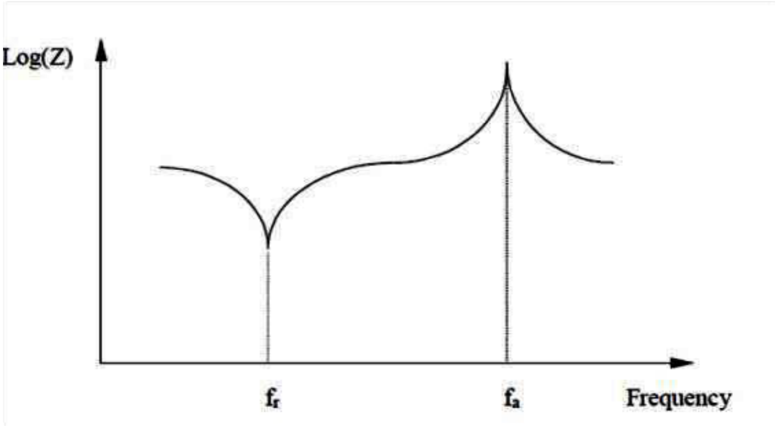

**Fig. 2.10:** A typical impedance vs. frequency curve of a ferroelectric material showing the resonance and anti-resonance frequencies [42].

These $f_r$ and $f_a$ frequencies are called as resonance and anti-resonance frequencies, respectively. The resonance frequency is the frequency at which the sample vibrates most readily and converts the input electrical energy into the mechanical energy most efficiently [43]. Fig.2.10 shows that initially with the increase of frequency, the impedance decreases and reaches a minimum value at $f_r$ and with the further increase in frequency the impedance increases and reaches a maximum value at $f_a$. The resonance frequency measurement of a material is strongly dependent upon its geometry. For a thin disc of piezoelectric ceramic, the planar mode coupling coefficient ($k_p$) expresses radial coupling which is the coupling between the electric field parallel to the direction in which the ceramic element is polarized and mechanical effects that produce radial vibrations. $k_p$ value measured from $f_r$ and $f_a$ values can be calculated by using the following relation, [44]

$$k_p^2 = 2.51\frac{(f_a - f_r)}{f_r} \qquad (2.19)$$

To assure the resonance behavior, sample geometry must be chosen carefully [43]. Geometries, suitable for measuring the different piezoelectric and elastic coefficients, are given in Table 2.1.

**Table 2.1:** Sample geometries for measurement of material properties.

| | 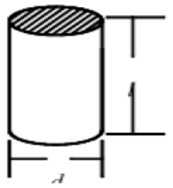 | 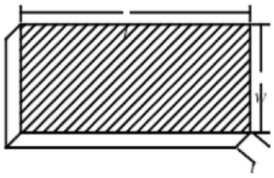 | 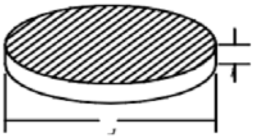 |
|---|---|---|---|
| Dimensional Requirement | Long, slender, length poled rod; $l > 3d$ | Thin flat plate, thickness poled; $l > 3.5t, w$ | Thin flat disc, thickness poled $d>10t$ |
| Properties Measured | $K_3^T, k_{33,}\ \tan\delta, s_{33}^D,$ $s_{33}^E, d_{33,} g_{33,} Q_M$ | $K_3^T, k_{31,}\ \tan\delta, s_{11}^D,$ $s_{11}^E, d_{31,} g_{31,} Q_M$ | $K_3^T, k_{p,}\ \tan\delta, Q_M$ |

## 2.3.8 Ferroelectric P-E Loop Study

The most important characteristic of a ferroelectric material is the polarization reversal (or switching) by an applied external electric field. Mainly, the domain wall switching in the ferroelectric materials leads to the development of polarization vs.

electric field ($P-E$) hysteresis loop. The hysteresis loop is the polarization responding to an applied voltage, *P(V)*. Its derivative with respect to voltage is expressed by,

$$\frac{\delta P}{\delta V} = \frac{\delta Q/\delta V}{Area} \qquad (2.20)$$

The domain switching in a ferroelectric material, results a ferroelectric hysteresis loop[30], shown in Fig. 2.11.At small values of the electric field, the polarization increases linearly with the increase of field amplitude. As the field is increased, the unfavourable direction of the polarization will start to switch in the direction of the field, rapidly increasing the measured charge density. An ideal hysteresis loop is symmetrical and in this case, $+E_C= -E_C$ and $+P_R= -P_R$, known as the coercive field and remnant polarization, respectively. The shapes of the P-E loop are affected by many factors such as the thickness of the sample, the presence of charged defects, mechanical stresses, preparation conditions, thermal treatment etc. The mechanism of polarization switching has been studied in detail for many bulk and thin-film ferroelectrics [39]. The polarization reversal takes place by the growth of existing antiparallel domains, by domain-wall motion, and by nucleation and growth of new antiparallel domains,  shown in Fig. 2.12 [45].

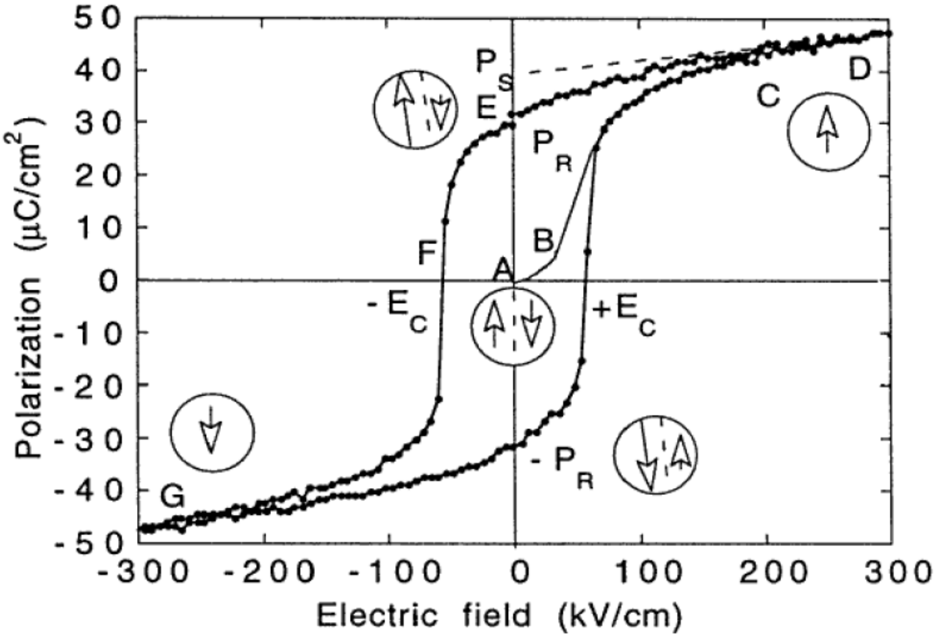

**Fig. 2.11:** Ferroelectric hysteresis ($P-E$) loop (Circles with arrows represent the polarization state of the material at the indicated fields) [46].

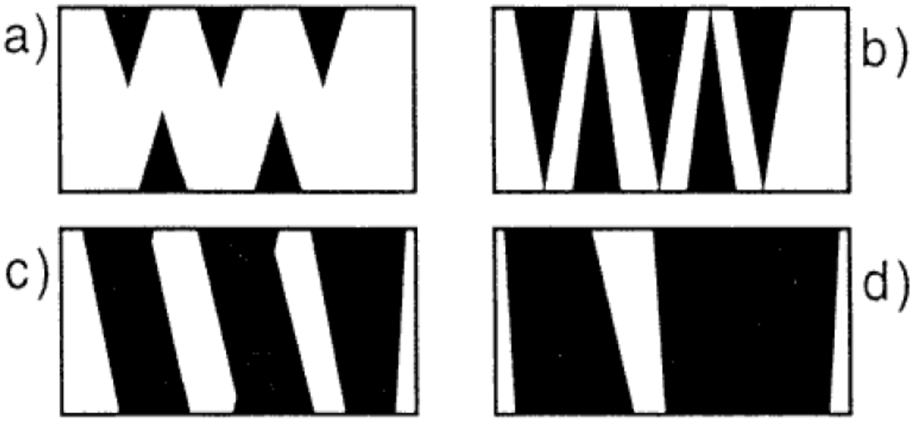

**Fig.2.12:**Probable sequence of polarization switching in ferroelectrics: (*a*) nucleation of oppositely oriented domains, (*b*) growth of oppositely oriented domains, (*c*) sidewise motion of domain walls and (*d*) coalescence of domains [45].

## 2.3.9 Polarization Fatigue Study

Polarization fatigue of ferroelectrics is the systematic suppression of switchable polarization after a repeated number of electrical pulses [47].The fatigue property in ferroelectric materials degrades their behavior and it is of particular concern for realizing their applications in memory devices. Although both bulk and thin-film materials are prone to ferroelectric fatigue, the mechanisms of this anomaly are still not well understood. However, extensive study on polarization fatigue has generated a large body of experimental data that led to many theoretical models of the fatigue phenomenon [47, 48]. Among several mechanisms proposed for the origin of polarization fatigue, the simplest and earliest one is the reduction of the effective area of the electrodes of the capacitors [49]. A decrease in the effective size of the capacitor can contribute to a decrease in the total switchable polarization due to failure of the electrode after a number of switching cycles. If this mechanism is the origin of the fatigue then the remnant polarization, switchable polarization and capacitor area are all reduced by the same factor. The second mechanism is the reduction of the effective electric field by the formation of a passive layer [50].

However, the domain wall pinning is regarded as the main conventional mechanism responsible for the fatigue in ferroelectric materials [51, 52]. In this pinning mechanism, mobile defects such as oxygen vacancies and electronic charge carriers get trapped at the domain walls. The domain walls get pinned and the domains surrounded by the pinned domain walls do not continue to switch. Fig. 2.13 is an illustration of the domain wall pinning mechanism. Warren *et al.* [53] proposed this mechanism by observing polarization fatigue in PZT thin films. According to their study, electronic charge carriers generated by optical and thermal treatments were trapped at domain boundaries, which led to a polarization discontinuity. Accumulation of electronic charge carriers makes the polarization reorientation difficult under an electric field.

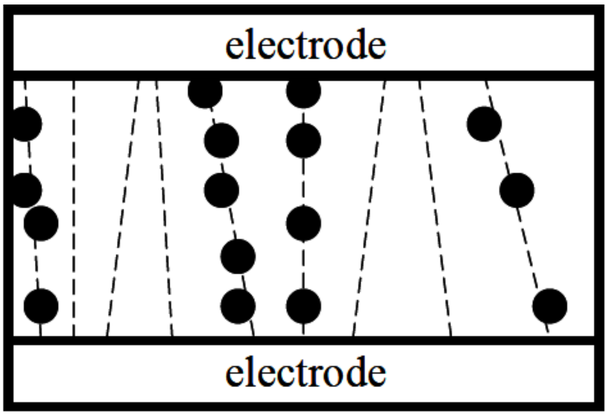

**Fig.2.13:** Schematic diagrams of fatigue mechanism domain wall pinning (dashed lines are domain walls and black circles are trapped defects) [54].

## References

[1] K. Keizer, E.H.J. Janssen, K.J. de Vries, A.J. Burggraaf, Influence of particle size and structure of $ZrO_2$ on microstructure development and dielectric constant of $PbZr_{0.5}Ti_{0.5}O_3$, Materials Research Bulletin, 8 (1973) 533-544.

[2] T. Yamamoto, Optimum Preparation Methods for Piezoelectric Ceramics and Their Evaluation, The American Ceramic Society Bulletin, 71 (1992) 978-985.

[3] G. Arlt, The influence of microstructure on the properties of ferroelectric ceramics, Ferroelectrics, 104 (1990) 217-227.

[4] A.J. Moulson , J.M. Herbert, Electroceramics: Materials, Properties, Applications, John Wiley & Sons, 2003.

[5] A.R. West, Solid State Chemistry and Its Applications, John Wiley & Sons 1987.

[6] J.K. A Beddow, Particle Characterization in Technology: Applications and microanalysis, CRC Press 1984.

[7] Y. Xu, Ferroelectric Materials and Their Applications, Elsevier Science 2013.

[8] J.D. Gilchrist, Extraction metallurgy, Pergamon, Oxford, Pergamon, 1989.

[9] M.L. Eggersdorfer, D. Kadau, H.J. Herrmann, S.E. Pratsinis, Multiparticle Sintering Dynamics: From Fractal-Like Aggregates to Compact Structures, Langmuir, 27 (2011) 6358-6367.

[10] M.N. Rahaman, Sintering of ceramics, CRC Press, Boca Raton (FL); London; New York, 2008.

[11] A. Gronotte, Development of new chemical processes to lead-free piezoelectric and ferroelectric materials, Dept. of Chemistry Simon Fraser University, 2009.

[12] J.A. Dean, Analytical Chemistry Handbook, McGraw-Hill Companies 1995.

[13] D.A. Skoog, F.J. Holler, T.A. Nieman, Principles of Instrumental Analysis, Saunders College Pub.1998.

[14] M.J. O'Neill, The Analysis of a Temperature-Controlled Scanning Calorimeter, Analytical Chemistry, 36 (1964) 1238-1245.

[15] M.F.C. Ladd, Structure Determination by X-Ray Crystallography, Springer US2012.

[16] A.R. West, Basic solid state chemistry, John Wiley & Sons, 1999.

[17]x-ray diffraction,http://www.veqter.co.uk/residual-stress-measurement/x-ray-diffraction1

[18] B.D. Cullity, Elements of X-Ray Diffraction, Addison-Wesley Publishing Company, Inc.1956.

[19] E. Suzuki, High-resolution scanning electron microscopy of immunogold-labelled cells by the use of thin plasma coating of osmium, Journal of Microscopy, 208 (2002)153-157.

[20] J. Goldstein, D.E. Newbury, P. Echlin, D.C. Joy, A.D. Romig, C.E. Lyman, C. Fiori, E. Lifshin, Scanning Electron Microscopy and X-Ray Microanalysis: A Text for Biologists, Materials Scientists, and Geologists, Springer, US, 2012.

[21] http://serc.carleton.edu/research_education/geochemsheets/electroninteractions.html

[22] C.E. Jeffree, N.D. Read, Ambient and Low-temperature Scanning Electron Microscopy, Electron microscopy of plant cells, Academic Press, London, 1991.

[23] G. Rangarajan, M.S. Vijaya, Materials Science, Tata McGraw-Hill 2014.

[24] B. Jaffe, W.R. Cook Jr., H. Jaffe, Piezoelectric Ceramics, Academic Press London and New York, 1971.

[25] S.N. Kumar, Synthesis and Characterization of $Sr_{0.53}Ba_{0.47}Nb_2O_6$ based Ferroelectric Composites for Pyroelectric Applications Department of Physics and Astronomy, National Institute of Technology, Rourkela, 2012.

[26] N. Izyumskaya, Y.I. Alivov, S.J. Cho, H. Morkoc, H. Lee, Y.S. Kang, Processing, Structure, Properties, and Applications of PZT Thin Films, Critical Reviews in Solid State and Materials Sciences, 32 (2007) 111-202.

[27] L. Pintilie, M. Alexe, Metal-ferroelectric-metal heterostructures with Schottky contacts. I. Influence of the ferroelectric properties, Journal of Applied Physics, 98 (2005) 124103.

[28] P. Zubko, D.J. Jung, J.F. Scott, Electrical characterization of $PbZr_{0.4}Ti_{0.6}O_3$ capacitors, Journal of Applied Physics, 100 (2006) 114113.

[29] R.H. Tredgold, Space charge conduction in solids, Elsevier Pub. Co.1966.

[30] S.M. Sze, Physics of Semiconductor Devices, John Wiley & Sons 1981.

[31] G.H. Haertling, Properties of Hot-Pressed Ferroelectric Alkali Niobate Ceramics, Journal of the American Ceramic Society, 50 (1967) 329-330.

[32] S.-T. Zhang, A.B. Kounga, W. Jo, C. Jamin, K. Seifert, T. Granzow, J. Rödel, D. Damjanovic, High-Strain Lead-free Antiferroelectric Electrostrictors, Advanced Materials, 21 (2009) 4716-4720.

[33] D. Damjanovic, Ferroelectric, dielectric and piezoelectric properties of ferroelectric thin films and ceramics, Reports on Progress in Physics, 61 (1998) 1267.

[34] K. Uchino, Electrostrictive actuators: materials and applications, Anglais, 65 (1986) 647-652.

[35] M.J. Zipparo, K.K. Shung, T.R. Shrout, Piezoceramics for high-frequency (20 to 100 MHz) single-element imaging transducers, Ultrasonics, Ferroelectrics, and Frequency Control, IEEE Transactions on, 44 (1997) 1038-1048.

[36] K. Furuta, K. Uchino, Advanced Ceramic Materials, 1(1986) 61.

[37] Piezo Engineering Tutorial, http://www.aerotech.com/product-catalog/piezo-nanopositioners/piezo-engineering-tutorial.aspx

[38] P. Palei, Structural and Electrical Properties of Conventional and Microwave Processed Lead-Free KNN Based Ceramics, Department of Physics and Astronomy, National Institute of Technology, Rourkela, 2012.

[39] M.E. Lines, A.M. Glass, Principles and Applications of Ferroelectrics and Related Materials, Clarendon Press, 1979.

[40] S.-E. Park, T.R. Shrout, Ultrahigh strain and piezoelectric behavior in relaxor based ferroelectric single crystals, Journal of Applied Physics, 82 (1997) 1804-1811.

[41] T. Ikeda, Fundamentals of Piezoelectricity, Oxford University Press1996.

[42] The Technical Ceramics business of Morgan Advanced Materials, http://www.morgantechnicalceramics.com/.

[43] Piezo theory, https://www.americanpiezo.com/knowledge-center/piezo-theory.html

[44] T.F. Hueter, D.P. Neuhaus, J. Kolb, An Experimental Study of Polarization Effects in Barium Titanate Ceramics, Journal of the Acoustical Society of America, 26 (1954) 696-703.

[45] Shur V, E. Rumyantsev, Arising and evolution of the domain structure in ferroics, Journal of Korean Physical Society, 32 (1998) S727-S732.

[46] Ferroelectrics, http://electrons.wikidot.com/ferroelectrics.

[47] A.K. Tagantsev, I. Stolichnov, E.L. Colla, N. Setter, Polarization fatigue in ferroelectric films: Basic experimental findings, phenomenological scenarios, and microscopic features, Journal of Applied Physics, 90 (2001) 1387-1402.

[48] P.J. Schorn, D. Brouhaus, U. Bottger, R. Waser, G. Beitel, N. Nagel, R. Bruchhaus, Fatigue effect in ferroelectric $PbZr_{1-x}Ti_xO_3$ thin films, Journal of Applied Physics, 99 (2006) 114104.

[49] D.J. Johnson, D.T. Amm, E. Griswold, K. Sreenivas, G. Yi, M. Sayer, Measuring Fatigue in PZT Thin Films, MRS Online Proceedings Library, 200 (1990) 289.

[50] A.K. Tagantsev, M. Landivar, E. Colla, N. Setter, Identification of passive layer in ferroelectric thin films from their switching parameters, Journal of Applied Physics, 78 (1995) 2623-2630.

[51] W. Li, A. Chen, X. Lu, J. Zhu, Y. Wang, Priority of domain wall pinning during the fatigue period in bismuth titanate ferroelectric thin films, Applied Physics Letters, 86 (2005) 192908.

[52] W.L. Warren, D. Dimos, B.A. Tuttle, G.E. Pike, R.W. Schwartz, P.J. Clews, D.C. McIntyre, Polarization suppression in $Pb(Zr,Ti)O_3$ thin films, Journal of Applied Physics, 77 (1995) 6695-6702.

[53] W.L. Warren, D. Dimos, B.A. Tuttle, R.D. Nasby, G.E. Pike, Electronic domain pinning in $Pb(Zr,Ti)O_3$ thin films and its role in fatigue, Applied Physics Letters, 65 (1994) 1018-1020.

[54] D.H. Do, Investigation of Ferroelectricity and Piezoelectricity in Ferroelectric Thin Film Capacitors using Synchrotron X-ray Micro Diffraction, Metallurgical Engineering, University of Wisconsin-Madison, 2006.

# Chapter 3

# Experimental Details

## 3.1 Introduction

This chapter presents the various steps involved in the synthesis of the selected $Na_{0.5}Bi_{0.5}TiO_3$ and $SrBi_2Ta_2O_9$ based systems as well as their ceramic-ceramic composite systems. Further, a brief detail of the different experiments performed on the studied samples, using various characterization techniques, is also discussed.

## 3.2 Synthesis of the Selected Ceramics

Solid state reaction route (SSRR) was employed for the synthesis of the selected ceramic samples. Detail of different ceramic samples, synthesized in this thesis work, is listed in Table 3.1.

**Table 3.1:** Synthesized materials.

| **Perovskite materials** | **BLSF materials** |
|---|---|
| $(1-x)Na_{0.5}Bi_{0.5}TiO_3-xBaTiO_3$/NBT-xBT<br>$(1-x)Na_{0.5}Bi_{0.5}TiO_3-xK_{0.5}Na_{0.5}NbO_3$/NBT-xKNN<br>(where x=0.05, 0.06, 0.07, 0.08) | $SrBi_2Ta_2O_9$/SBT,<br>$Sr_{0.8}Bi_{2.15}Ta_2O_9$/$SB_{ex}T$ and<br>$SrBi_2(Ta_{0.925}W_{0.075})_2O_9$/SBTW |
| **Perovskite-BLSF ceramic-ceramic composites** | |
| $(1-\phi)(0.93\ Na_{0.5}Bi_{0.5}TiO_3-0.07\ BaTiO_3$/ NBT-BT)-$\phi\ Sr_{0.8}Bi_{2.15}Ta_2O_9T$<br>$(1-\phi)(0.93\ Na_{0.5}Bi_{0.5}TiO_3-0.07\ K_{0.5}Na_{0.5}NbO_3$/ NBT-KNN)-$\phi\ Sr_{0.8}Bi_{2.15}Ta_2O_9$<br>(Where $\phi$= 2, 4, 8, 12, 16 wt. %) | |

In the present work, commercially available high purity (≥ 99%) powder precursors, as listed in Table. 3.2; were used as the starting raw materials for the synthesis of the selected materials.

**Table 3.2:** Precursors used in the synthesis of the selected materials.

| Chemical Name | Chemical Formula | Purity | Manufacturer |
|---|---|---|---|
| Bismuth oxide | $Bi_2O_3$ | 99.9% | Alfa Aesar |
| Sodium carbonate | $Na_2CO_3$ | 99.99% | Merck |
| Titanium oxide | $TiO_2$ | 99.9% | Merck |
| Barium carbonate | $BaCO_3$ | 99.9% | Merck |
| Potassium carbonate | $K_2CO_3$ | 99.9% | Loba Chemie |
| Niobium pentoxide | $Nb_2O_5$ | 99.9% | Merck |
| Strontium carbonate | $SrCO_3$ | 99.9% | Merck |
| Tantalum oxide | $Ta_2O_5$ | 99.9% | Alfa Aesar |
| Tungsten oxide | $WO_3$ | 99.9% | Merck |

**Table 3.3:** Details of the selected material processing steps.

| Ceramic Composition | | Precursors | Optimized Calcination Temp.($^oC$)/ 4 h | Optimized Sintering Temp.($^oC$)/ 4h | Sample Notation |
|---|---|---|---|---|---|
| **Perovskite** | $(1-x)Na_{0.5}Bi_{0.5}TiO_3-xBaTiO_3$ (x=0.05, 0.06, 0.07, 0.08) | $Bi_2O_3$, $Na_2CO_3$, $TiO_2$, $BaCO_3$ | 1000 | 1150 | NBT-xBT |
| | $(1-x)Na_{0.5}Bi_{0.5}TiO_3-x K_{0.5}Na_{0.5}NbO_3$ (x=0.05, 0.06, 0.07, 0.08) | $Bi_2O_3$,$Na_2CO$, $TiO_2$, $K_2CO_3$, $Nb_2O_5$ | 800 | 1100 | NBT-xKNN |
| **BLSF** | $SrBi_2Ta_2O_9$ | $SrCO_3$, $Bi_2O_3$, $Ta_2O_5$, | 1000 | 1150 | SBT |
| | $Sr_{0.8}Bi_{2.15}Ta_2O_9$ | | | 1200 | $SB_{ex}T$ |
| | $SrBi_2(Ta_{0.925}W_{0.075})_2O_9$ | $SrCO_3$,$Bi_2O_3$, $Ta_2O_5$,$WO_3$ | | 1150 | SBTW |
| **Perovskite-BLSF** | $(1-\phi)(0.93\ Na_{0.5}Bi_{0.5}TiO_3-0.07\ BaTiO_3)-\phi\ Sr_{0.8}Bi_{2.15}Ta_2O_9$ ($\phi$= 2, 4, 8, 12, 16 wt. %) | Calcined NBT-BT and $SB_{ex}T$ | ____ | 1150 | $(1-\phi)$(NBT-BT)-$\phi(SB_{ex}T)$ |
| | $(1-\phi)(0.93\ Na_{0.5}Bi_{0.5}TiO_3-0.07\ K_{0.5}Na_{0.5}NbO_3)-\phi\ Sr_{0.8}Bi_{2.15}Ta_2O_9$ ($\phi$= 2, 4, 8, 12, 16 wt. %) | Calcined NBT-KNN and $SB_{ex}T$ | ____ | 1150 | $(1-\phi)$(NBT-KNN)-$\phi(SB_{ex}T)$ |

The various steps involved in the processing of the selected ceramic samples by SSRR are already mentioned in the flow chart, given in the previous chapter (Fig.2.1). The raw materials with defined purity, given in Table 3.2, were used for the synthesis of the corresponding ceramic compositions, listed in Table 3.3. Stoichiometric weights of the starting precursor powders were taken into a jar and ball milled with acetone using zirconia balls as grinding media for 12 hours. DSC and TGA were carried out of the ball milled uncalcined powders in the temperature range of 30–1000°C with a constant heating rate of $10^oC$ per minute. The dried mixed powders were calcined at different temperatures (ascertained from TGA/DSC analysis) in normal atmosphere and the formation of single phase of the calcined powders of the NBT-xBT, NBT-xKNN, SBT, $SB_{ex}T$, SBTW ceramic samples were examined by X-ray diffractometer. The optimized calcined temperatures are listed in Table 3.3. Perovskite-BLSF ceramic-ceramic composites were prepared by taking calcined powders of the selected perovskites and BLSF ceramic powders. Polyvinyl alcohol (PVA) binder solution (3wt.%) was added into the calcined powders, which were compressed into pellets called green pellets of ~10 mm in diameter and ~1 mm in thickness, using a hydraulic press with a pressure ~ 70MPa. The green pellets were sintered in normal atmosphere at different temperatures (below their melting point) with a heating rate of 5°C/min. Optimized sintering temperatures are also listed in Table 3.3.

## 3.3 Characterization Techniques Used

This section presents the details about the different characterization instrument, used for the present study.

### 3.3.1 Thermal Analysis

For DSC analysis of the studied samples, temperature program is designed in such a way that the sample holder temperature varies linearly as a function of time. The reference sample should have a well-defined heat capacity over the range of temperatures to be scanned. DSC measures the difference in the amount of heat required to increase the temperature of the sample and reference, which is measured as a function of temperature. Both the sample and the reference are maintained at nearly same temperature throughout the experiment. Generally, the temperature program for a DSC analysis is designed such that the sample holder temperature increases linearly as a function of time. However, TGA is the measure of weight change of the specimen as a function of temperature. The specimen powder is placed on a refractory pan (mostly alpha alumina or platinum). The pan is suspended from a high precision balance. A thermocouple is in close proximity to the specimen but not in contact, so as not to interfere with the free float of the balance. The balances are electronically compensated so that the specimen pan does not move when the specimen gains or losses weight. In the present study, DSC/TGA experiments has been performed by taking ~10 mg of ball milled powder samples and heated at a constant heating rate of $10^{o}$C per minute by using Netzsch, STA 449C.

### 3.3.2 Structural Study

X-ray diffraction patterns of all the ceramic samples were studied for confirming about the single perovskite phase formation. XRD analysis was performed on Rigaku Ultima-IV using Cu $K_{\alpha}$ ($\lambda$=0.15405 nm) radiation. The diffraction data was taken in the $2\theta$ range from $20^{o}$ to $60^{o}$-$80^{o}$. Firstly, the Cu $K_{\alpha}$ radiation was stripped from the collected XRD data by using standard software “X’pert high score”. Then the crystal structure and the crystallographic parameters of the samples were determined from their respective diffraction peaks.

### 3.3.3 Density and Morphology Study

The experimental density of the sintered samples was measured using Archimedes method. In the present work, kerosene oil was used as the immersion medium. First, the dry weights of the sintered samples were measured. The sintered samples were then immersed in a glass beaker containing kerosene oil and kept in a desiccator connected with a suction pump for creating vacuum in it till the kerosene oil filled up the open pores of the ceramic samples completely, which is confirmed by observing the glass beaker to become bubbles free. Then the ceramic samples were suspended in kerosene oil with the help of a specially designed hanging pan to hold the ceramic samples inside kerosene oil and the suspended weights were measured. The soaked weights of the ceramic samples (whose pores are filled with kerosene oil) were also measured and the experimental density was calculated by the following formula;

$$\rho_{ex} = \left[ \frac{Dry\ weight}{Soaked\ weight - Suspended\ weight} \right] \times 0.81 (Density\ of\ \mathrm{kero}sene) \tag{3.1}$$

The SEM micrographs were taken using JEOL SEM- 6480LV and JEOL T-330. In order to avoid the potential build up during the measurement, the samples (non-conducting) were coated with platinum/gold using a sputter coater. Average grain size of the samples was measured using linear intercept method by using “ImageJ software”. Firstly, the scale was set by comparing the length scale from the SEM images. Secondly the diagonal lines were drawn on a maximum number of grains (to minimize the error) and the lengths were calculated. The average value of grains was calculated by dividing the total intercepted grain length by the number of grains.

### 3.3.4 Electroding of the Samples

The sintered pellets were polished and cleaned with acetone. Sufficient care was taken for keeping the faces of the pellets parallel. A thin layer of silver paste was applied on both sides of the samples and fired in a muffle furnace at 300°C for 15 min to ensure good adhesion. The sintered ceramic pellets now act as dielectric medium between the two parallel silver metallic plates and can be subjected to various electrical measurements.

### 3.3.5 Poling

The schematic diagram of the corona discharge poling method is shown in Fig.3.1. The unit consists of a bottom electrode (metallic plate) and sharp pointed corona needle (top electrode), made of brass of diameter ~ 2mm. A ring-shaped grid of ~12 mm diameter, made of thin copper wire, was kept between the tip of the corona needle and the base plate in such a way that the tip of the needle is ~1mm above the center of the grid.

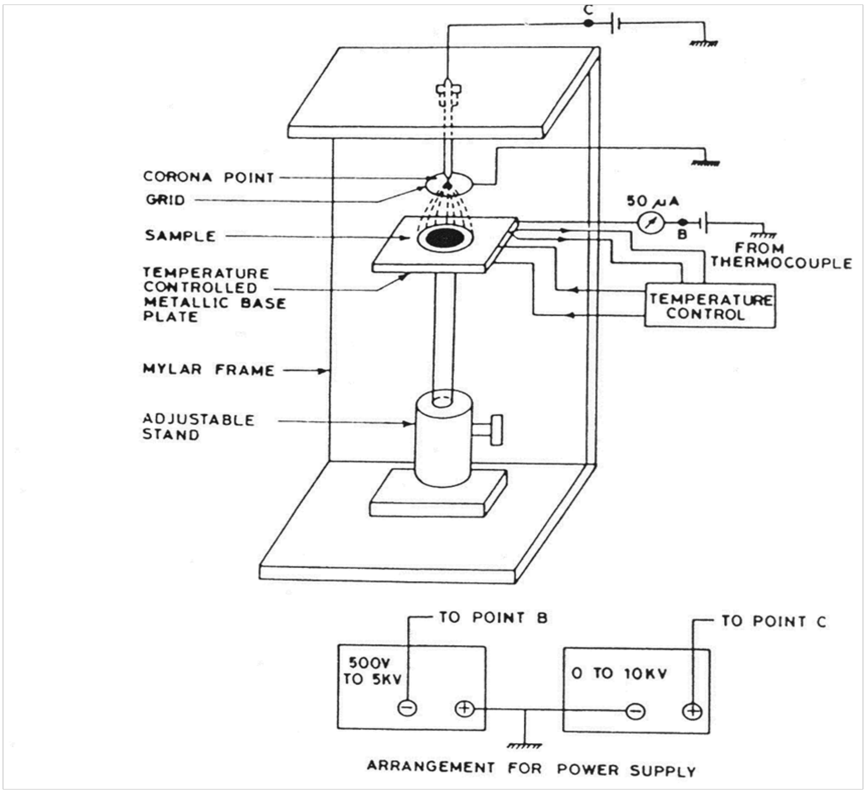

**Fig.3.1:** Schematic of the corona poling technique [1].

The samples were placed on the metallic base plate and a high voltage (5-6 kV) was applied between the corona point and the base plate. The chosen voltage was slightly higher than the voltage at which corona discharge starts. A bias voltage (1.5 kV) was applied between the grid and the metallic plate to accelerate the ions caused by breakdown of air. The samples were subjected to corona discharge for 30 minutes at RT and then the field was removed. This poling technique is better than the DC poling technique in terms of the safety of the samples. In corona poling of the samples, there is no need of putting the samples in silicon oil (which is usually done in DC poling of samples to avoid the breakdown through sideways), since there is no direct contact of the electrodes with the samples.

### 3.3.6 Dielectric Measurements

The dielectric measurements of the samples were carried out by using a computer interfaced HIOKI 3532-50 LCR Hi-Tester, shown in Fig. 3.2. The interfacing of the instrument was done by using "Lab VIEW software". Dielectric parameters, $\varepsilon_r$ and $\tan\delta$, were measured as a function of temperature at different frequencies (1kHz-1MHz). For temperature dependent dielectric measurements, the samples were heated with a heating rate of $2^{o}$C/min and the corresponding dielectric data were recorded at an interval of $1^{o}$C. $\varepsilon_r$ was calculated by using the following relation [2]:

$$\varepsilon_r = \frac{C \times t}{\varepsilon_o \times A} \qquad (3.2)$$

where, $C$ is the measured capacitance, $t$ is the thickness of the sample, $A$ is the surface area of the sample and $\varepsilon_o$ is the permittivity of the free space (~ $8.854 \times 10^{-12}$ F/m) [1].

**Fig. 3.2:** HIOKI-LCR meter (3532-50 HI-TESTER).

### 3.3.7 Polarization vs. Electric Field ($P-E$) Measurements

The RT ferroelectric hysteresis ($P-E$) loops of the studied ceramic samples were measured using Precision Premier II, a standard ferroelectric testing machine (Radiant Technology). The ferroelectric measurements were done based on the virtual ground measuring system, shown in Fig.3.3. The trans-impedance amplifier maintains the precision return terminal at a virtual ground potential in this configuration. All the charges, which flow through the sample as a result of the applied drive voltage, are collected by the integrator circuit and the voltage generated on the output of the integrator is then measured and translated into the test results that are displayed by the “Vision software”. The precision drive and return circuitry are matched with respect to speed and current sinking ability; therefore the precision testers can reject errors that might occur when the drive makes a transition faster than the trans-impedance amplifier. This enables the precision testers to accurately measure a large range of capacitance values over a wide range of speeds [3]. The unit image of the precision premier II is given in Fig. 3.4.

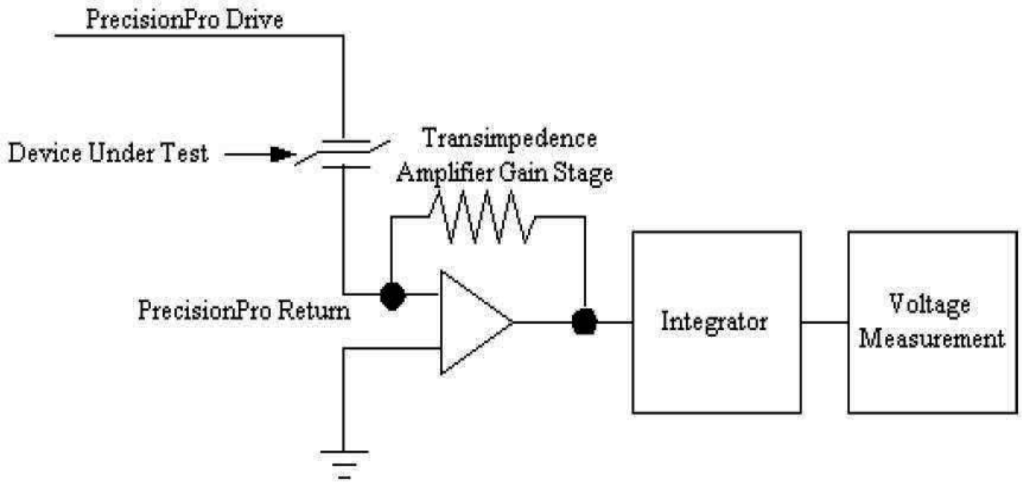

**Fig. 3.3:** Schematic of the virtual ground measuring system [3].

**Fig. 3.4:** Precision premier II unit.

### 3.3.8 Piezoelectric Constant ($d_{33}$) Measurements

The piezoelectric coefficient ($d_{33}$) of the studied samples was measured by a quasi-static method using a Piezometer (YE2730A $d_{33}$ Meter, APC International Ltd.). The piezoelectric coefficient, $d_{33}$, is defined by the following relation:

$$d_{33} = \left( \frac{D_s}{T_s} \right)_E \qquad (3.3)$$

Where, $D_s$ is the charge density (C/m$^2$) and $T_s$ is the mechanical stress (N/m$^2$) at constant electric field ($E$). Figure 3.5 shows a schematic diagram for the $d_{33}$ measurement using the Piezo-Meter. Equation 3.3 can be simplified as follows:

$$d_{33} = \left( \frac{D_s}{T_s} \right)_E = \frac{(Q/A)}{(F/A)} = \frac{Q}{F} = \frac{CV}{F} \qquad (3.4)$$

Where, $C$ is the shunt capacitance and $V$ is the potential difference across the shunt capacitor.

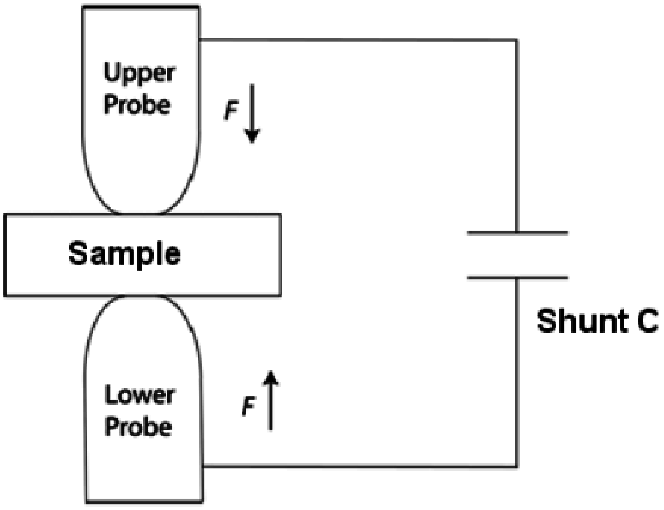

**Fig. 3.5:** Schematic diagram of the $d_{33}$ measurement process [4].

When a force (F) is applied on an area (A) of a poled sample by the upper and lower probes then due to the piezoelectric effect, a charge (Q) is produced. Hence, piezoelectric charge coefficient ($d_{33}$) measurement relates with the development of charge on the surface of the sample. The Piezo-Meter measures this potential difference, calculates the $d_{33}$ (in pC/N) of the sample and displays the value digitally.

### 3.3.9 Resonance and Anti-resonance Frequency Measurement

Resonance ( $f_r$ ) and anti-resonance ( $f_a$ ) frequencies, used to calculate the electromechanical coupling coefficients ( $k_p$ ), were measured by using HIOKI 3532-50 LCR HiTESTER. In the frequency vs. impedance graph, the point where impedance is minimum is called as resonance frequency and the point where impedance is maximum is called anti-resonance frequency. Relation between $k_p$, $f_r$ and $f_a$ values is given in chapter 2.

### 3.3.10 Strain vs. Electric Field Measurements

The strain vs. electric field (S-E) loops of the studied ceramic samples were measured by using the MTI-2100 Fotonic Sensor, associated with the Precision Premier II (Radiant Technology) unit. The schematic of the MTI-2100 Fotonic Sensor is shown in Fig. 3.6. The Fotonic Sensor unit consists of a dual-channel, fiber-optic measurement system that performs non-contact displacement and vibration measurements. The Fotonic Sensor utilizes the adjacent pairs of light-transmitting and receiving fibers which are bundled together. The displacement is based on the interaction between the field of illumination of the transmitting fibers and the field of view of the receiving fibers. The sample with electrode on both sides is connected into an external voltage source. The distance between the sample and the Fotonic probe is adjusted by a screw device. At contact or zero gaps, most of the light exiting the transmitting fibers is reflected directly back into the same fiber, providing a very little amount of light to the receiving fiber and produces a zero output signal. With an increase in the probe to the target distance [Fig. 3.6(b)], the amount of light being captured by the receiving fiber increases. This process continues until the entire face of the receiving fibers is illuminated with the reflected light. This point is called the “optical peak” and corresponds to maximum voltage output of the electrical signal. Further increase in distance would cause the diverging field of reflected light to exceed the field of view of the receiving fiber, thus causing a reversal in the output-versus-distance signal relationship. Therefore, “optical peak” point corresponds to maximum received signal at the receiving fiber. During the S-E measurements, firstly the distance between the sample and the Fotonic probe is reduced by screwing backwards to get away from the optical peak to the point that gives rise to minimum intensity of received light, secondly; distance between the sample and the Fotonic probe is adjusted to get the Fotonic meter value ~3.5 V, thirdly; the Fotonic sensor is calibrated and finally; the electrical signal is applied. Any displacement of the sample in response to the electric field would be compared with the optical peak and gives the relationship of displacement versus electric field(S-E) curve.

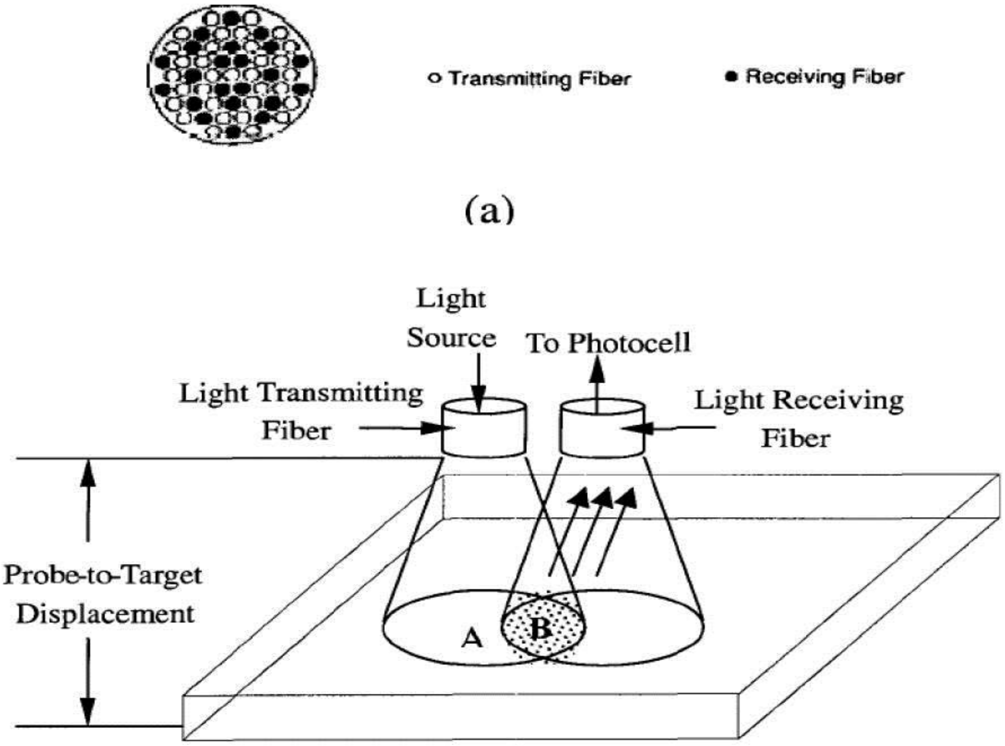

(a)

(b)

**Fig. 3.6:** A setup for the measurements of $S-E$ loop (a) fiber–optical probe tip configurations (b) displacement sensing mechanism of adjacent fiber optical elements.

### 3.3.11 Leakage Current Measurement

The leakage current measurement of the studied samples was carried out by using the Precision Premier II (Radiant Technology) ferroelectric tester with the help of "Vision" software. Ferroelectric materials are mainly used as capacitors under the application of an external voltage, which leads to unavoidable occurrence of leakage current through the samples. Measurement of this leakage current can be carried out by the Precision tester. The sample is subjected to a constant DC bias voltage. Before the measurement begins, a programmable delay or "Soak" period passes through the sample, which is intended to allow the passage of any polarization switching current or other currents, induced by the application of the voltage. After the delay period, a measurement period begins in which the current through the sample is regularly sampled and recorded. The leakage test stimulus and the measurement profile are shown in the Fig. 3.7.

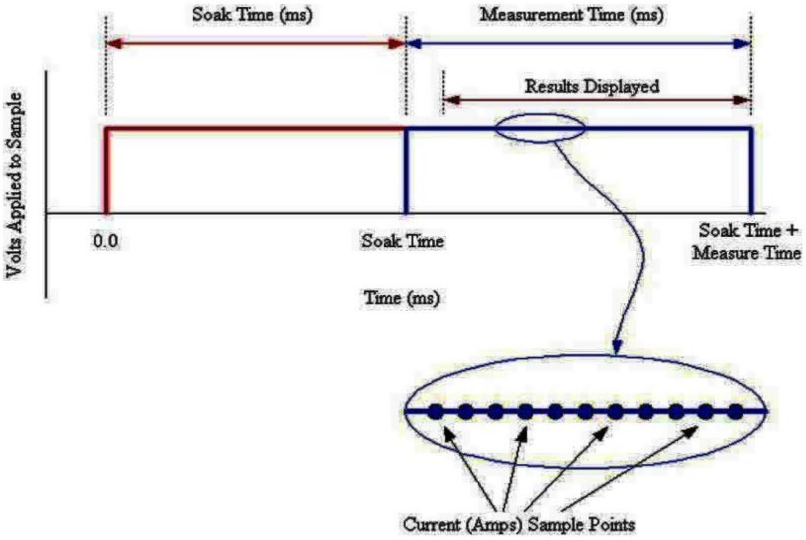

**Fig. 3.7:** Leakage test stimulus and measurement profile [3].

The current is sampled as frequently as possible during the time of leakage measurement. Sampling is restricted by the duration of the measurement and is adjusted to be the maximum number of possible points, given minimum and maximum per-point sample times. The current through the device under test is measured directly by the precision circuitry system. The other parameter, resistance (in Ohms), can be derived simply from the current measurement given by:

$$\mathrm{Re}\,sis\tan ce(\Omega) = DC\ Volts / Current(Amps) \qquad (3.5)$$

The main parameters specified by the user to configure the leakage measurement are the DC bias voltage, the soak time (ms) and the measurement time (ms).

### 3.3.12 Polarization Fatigue Measurement

The fatigue experiments were performed using the Radiant Precision Premier II (Radiant Technology) ferroelectric tester under long duration task using the “Vision” software. The measurement performs a complete fatigue characterization by first performing a pre-fatigue baseline PUND measurement; consisting of five pulses applied to the sample. Among the five pulses, the first pulse is a preset, switching the sample into a specific polarization state and is an unmeasured pulse. The second pulse is in the opposite direction of the Preset, switching the sample state. At the top of the pulse, the switched polarization value P* (μC/cm$^2$) is measured. After the pulse, the zero-Volt P*r (μC/cm$^2$) value is measured. The third pulse is in the same direction as the second. It measures unswitched polarization P^ (μC/cm$^2$). And, again at zero volts, P^r (μC/cm$^2$) is measured. The fourth and fifth pulses repeat the second and third pulses in the opposite voltage direction, giving -P* (μC/cm$^2$), -P*r (μC/cm$^2$), -P^ (μC/cm$^2$) and –P^r (μC/cm$^2$) parameters. Then a series of stress/measure cycles are performed in which an unmeasured waveform is applied for a period of time, followed by a PUND measurement. Each subsequent stress period adjusts its duration. Normally, the task is configured with longer stress periods at each stress/measure cycle, but this is entirely under user's control. Fig. 3.8 shows the fatigue measurement signal profile of the sample under test.

Elements of the experiment that are under user control include:

- Triangular waveform (most common choice).
- Maximum stress voltage.
- Stress waveform frequency.
- PUND measurement voltage.
- PUND measurement pulse width.
- Number of stress/measure cycles.
- Method of adjusting the stress period between cycles.

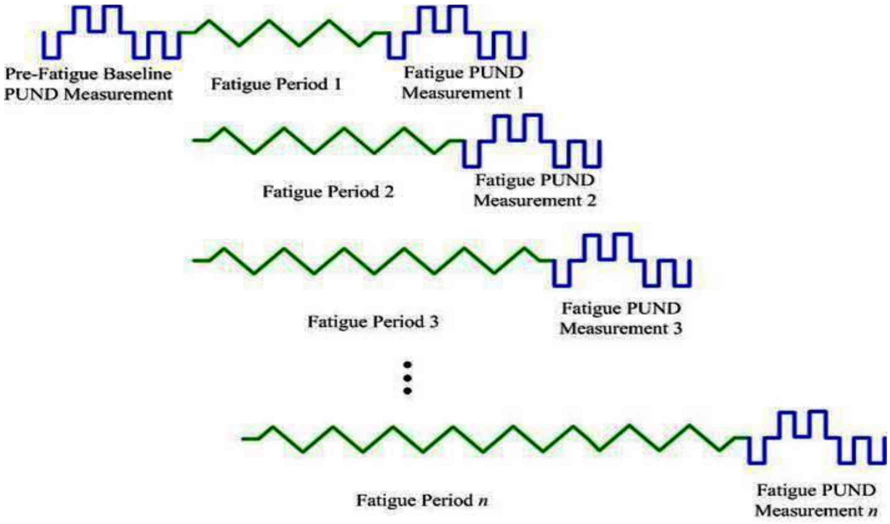

**Fig. 3.8:** Fatigue measurement signal profile [5].

## References

[1] K.C. Kao, Dielectric Phenomena in Solids, Elsevier Academic Press, London, 1990.

[2] E. Barsoukov, J. R. Macdonald, Impedance Spectroscopy: Theory, Experiment, and Applications (Wiley-Inter science, Hoboken, 2005).

[3] Radiant Technologies, Inc. 2835D Pan American Freeway NE Albuquerque, NM 87107.

[4] P. Palei, Structural and Electrical Properties of Conventional And Microwave Processed Lead-Free KNN Based Ceramics, Department of Physics and Astronomy, National Institute of Technology, Rourkela, 2012

[5] Precision Premier II standardized ferroelectric test system operation manual, Radiant Technologies Inc.

# Chapter 4

## *Dielectric, Piezoelectric, and Ferroelectric Properties of NBT-xBT and NBT-xKNN Ceramics near MPB*

### 4.1 Introduction

(1-x)$Na_{0.5}Bi_{0.5}TiO_3$-x$BaTiO_3$/NBT-xBT and (1-x)($Na_{0.5}Bi_{0.5}TiO_3$)-x$K_{0.5}Na_{0.5}NbO_3$ /NBT-xKNN (where x=0.05, 0.06, 0.07, 0.08) are the solid solutions of perovskite-structured NBT system with BT and KNN systems, respectively. In literature, it is reported that there exist an MPB in these systems within the above mentioned compositional ranges. For the NBT-xBT system, the MPB lies within the $0.06 \leq x \leq 0.08$ ranges [1] and for the NBT-xKNN system, the MPB lies for $x \approx 0.07$ [2]. Though, there are many reports on the NBT-xBT system and few reports on the NBT-xKNN system, yet the leakage current and polarization fatigue properties of these systems have not been studied in detail, which are detrimental for their use in many practical device applications. Therefore, in the present chapter along with structural, dielectric, piezoelectric and ferroelectric properties, the leakage current and the bipolar polarization fatigue behaviors of these systems are investigated and discussed in detail.

### 4.2 Thermal Analysis

Figs. 4.1(a) and (b) shows the DSC and TGA curves of the ball milled dried uncalcined powders of the NBT-xBT and NBT-xKNN systems with x=0.06 compositions, respectively. From the DSC and TGA curves, the solid-state reactions of both the NBT-BT and NBT-KNN powders show distinct mass losses, respectively. The initial mass loss ~ $100^{o}$C, is due to the evaporation of moisture and water content, present in both the powders. Decomposition of the carbonate groups of both the systems takes place in the 400-800°C temperature range. Among the carbonate groups, $Na_2CO_3$ is less stable, therefore it starts losing $CO_2$ at lower temperature (~400 °C) [3]. Therefore, weight loss, observed just above 400°C, can be associated with the decomposition of $Na_2CO_3$. The overall weight loss from the room temperature (RT) to ~980°C is ~13.42% and from RT to ~ 770°C, it is ~12.75% for the NBT-BT and NBT-KNN powders, respectively. For temperatures above 980°C and 770°C, there is no substantial weight loss, which suggest about the probable calcination temperatures of the NBT-BT and NBT-KNN powders, respectively.

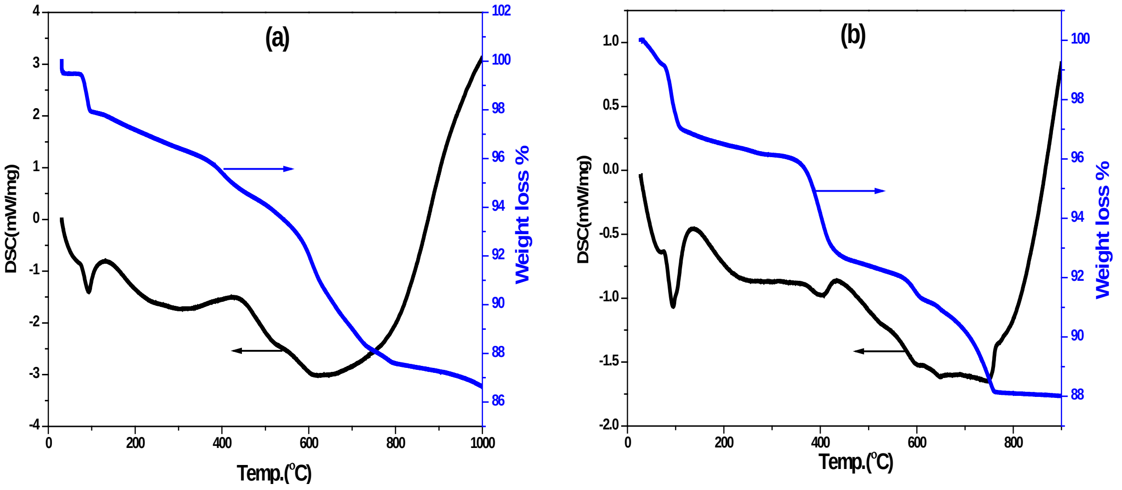

**Fig.4.1:** DSC and TGA curves of ball milled powders of x=0.06 compositions of (a) NBT-xBT, and (b) NBT-xKNN systems.

## 4.3 XRD Study

The X-ray diffraction (XRD) studies of the calcined NBT-xBT and NBT-xKNN (x=0.05, 0.06, 0.07, 0.08) ceramic powders are given in the following subsections.

### 4.3.1 XRD Study of the NBT-xBT Ceramics

The XRD patterns of the calcined NBT-xBT ceramic samples near MPB ($0.05 \leq x \leq 0.08$) are shown in Fig. 4.2. The XRD patterns reveal the single perovskite phase formation without any trace of secondary phase peaks, which confirm the complete solid solution formation of the BT system with the NBT system [4]. A close inspection of each diffraction peak shows that there is no splitting or broadening in the $2\theta$ between $40^o$ and $46^o$ range for all the compositions, which indicates that all these compositions have pseudo-cubic distortions [5]. Similar type of behavior is also reported by Rajeev *et al.* in the NBT-BT system [5]. The lattice parameters of rhombohedral NBT-xBT ($0.05 \leq x \leq 0.08$) ceramic samples are refined in hexagonal setting by using the standard computer program “POWD” [6]. The transformation expressions, used for rhombohedral (rh) (pseudo-cubic) to hexagonal (hex) symmetry, are taken from the earlier report on the NBT-BT system by Picht *et al.* [1]. The rhombohedral (pseudo-cubic) unit cell parameters of the NBT-xBT (0.05≤x≤0.08) ceramic samples are given in Table 4.1.

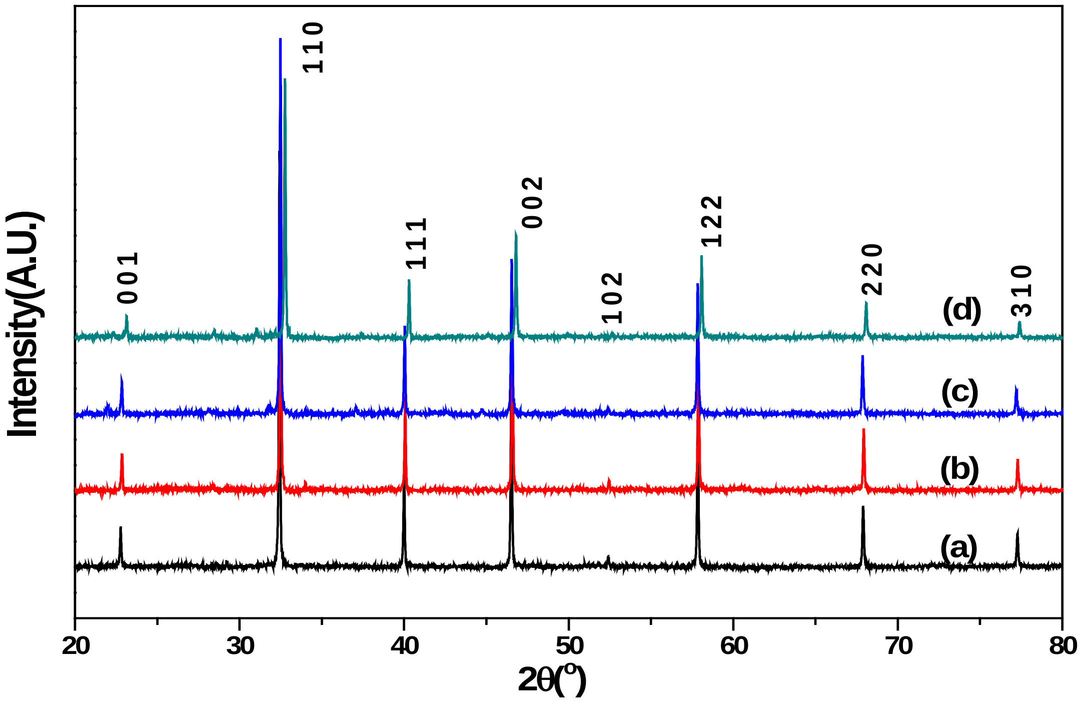

**Fig. 4.2:** XRD patterns of the calcined NBT-xBT ceramic samples with x = (a) 0.05, (b) 0.06, (c) 0.07, and (d) 0.08.

**Table 4.1:** Lattice parameters a, c (Å) and α (°) of NBT-xBT (x=0.05, 0.06, 0.07, 0.08) ceramics.

| **BT content** | $a_{hex}$ | $c_{hex}$ | $a_{rh}$ | $\alpha_{rh}$ |
|---|---|---|---|---|
| x = 0.05 | 5.5062(4) | 13.4615(2) | 3.8909(2) | 90.07(3) |
| x = 0.06 | 5.5105(8) | 13.4724(6) | 3.8940(1) | 90.07(5) |
| x = 0.07 | 5.5019(3) | 13.4173(5) | 3.8847(4) | 90.17(2) |
| x = 0.08 | 5.5143(6) | 13.4724(9) | 3.8823(4) | 90.09(6) |

As the XRD peaks showed pseudo-cubic distortions, it was difficult to observe the peak splitting remarkably. However, as shown in Fig. 4.3, the peak positions and intensities were analyzed with the software package “Peakfit” using a symmetric Gauss–Lorentz profile function. Deconvolution of XRD patterns of NBT-xBT (x=0.07) at 2θ ~ 46° is observed, which is indexed as $(200)_R$, $(200)_T$ and $(002)_T$ after deconvolution of the peak at the same position, corresponding to rhombohedral and tetragonal structures, respectively. Therefore, presence of double structures confirms the MPB nature of NBT-BT system. The tetragonal volume fraction was calculated using the formula:

$$V_{tr}(\%) = \frac{I_{tr(002)} + I_{tr(200)}}{I_{tr(002)} + I_{tr(200)} + I_{rh(200)}} \times 100\% \qquad (4.1)$$

Where, $I_{rh(2\,0\,0)}$ is the integral intensity of rhombohedral (2 0 0) reflection; $I_{tr(0\,0\,2)}$ and $I_{tr(2\,0\,0)}$ are the integral intensities of tetragonal (0 0 2) and (2 0 0) reflections, respectively. The rhombohedral volume fraction can be calculated as $V_{rh} = 1 - V_{tr}$ [1]. Using the above relations, volume fraction ratio of the rhombohedral and tetragonal phases of the MPB composition of NBT-xBT (x=0.07) was calculated to be 40:60.

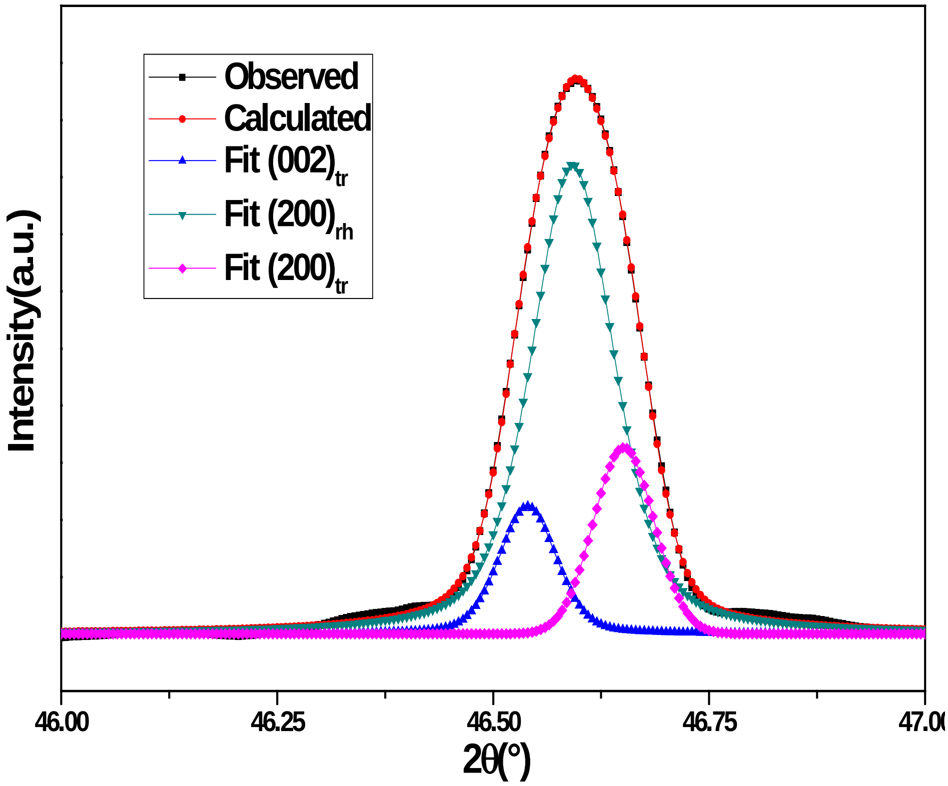

Fig. 4.3: XRD peak splitting at 2θ ~ 46° for NBT-xBT with x=0.07.

### 4.3.2 XRD Study of the NBT-xKNN Ceramics

Fig. 4.4 shows the XRD patterns of the calcined NBT-xKNN powder samples. Formation of single perovskite phase without any trace of secondary phase was confirmed in all the compositions of the NBT-xKNN systems. For knowing the crystal structure, the standard deviations (S.D. = $d_{obs}$- $d_{cal}$) was taken into account, which must be minimum (where, d is interplanar spacing). The best agreement between the observed (obs) and the calculated (cal) 'd' values, and the Bragg angles are found for the rhombohedral and the tetragonal structures in the x = 0.07 composition of the NBT-xKNN system. The presence of double structures confirms the MPB nature of this composition. Whereas, the rhombohedral structure is observed for both x=0.05 and 0.06 compositions and a single tetragonal structure is observed for the x=0.08 composition. The rhombohedral crystal structure of the NBT-xKNN ceramics are indexed in hexagonal setting by using the standard computer program "POWD" and the lattice parameters and the crystal structures are given in Table 4.2 [6]. The simulated XRD patterns of the NBT-xKNN ceramics exhibiting rhombohedral and tetragonal symmetry are also given as standard pattern in Fig. 4.5 [7].

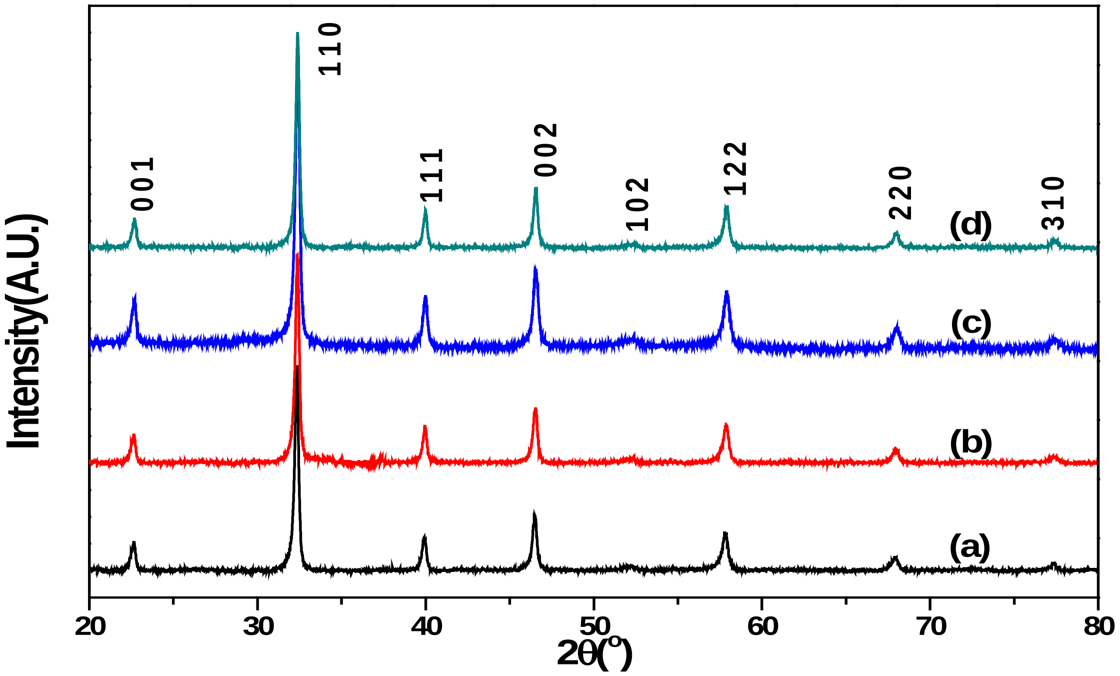

**Fig. 4.4:** XRD patterns of calcined NBT-xKNN ceramic samples with x = (a) 0.05, (b) 0.06, (c) 0.07, and (d) 0.08.

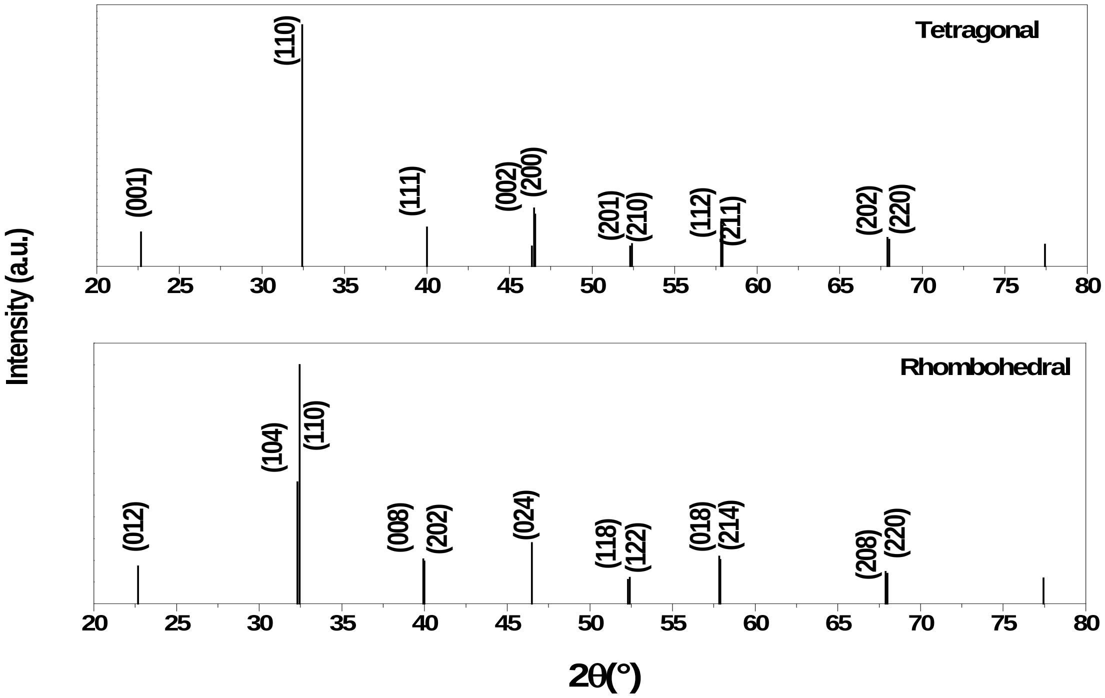

**Fig. 4.5:** The standard patterns of the rhombohedral and the tetragonal symmetries of NBT-xKNN samples [7].

**Table 4.2:** Lattice parameters of NBT-xKNN (x=0.05, 0.06, 0.07, 0.08) ceramics.

| **KNN content** | **Lattice parameters** | | **Crystal Structure** |
|---|---|---|---|
| | **a(Å)** | **c(Å)** | |
| x=0.05 | 5.5042(4) | 13.5511(2) | Rhombohedral |
| x=0.06 | 5.5058(2) | 13.5303(1) | Rhombohedral |
| x=0.07 | 5.5072(2) | 13.5271(9) | Rhombohedral |
| | 3.8952(1) | 3.9125(7) | Tetragonal |
| x=0.08 | 3.8987(2) | 3.9037(5) | Tetragonal |

To evaluate the tetragonal or rhombohedral phase contents for MPB composition of NBT-xKNN (x=0.05, 0.06, 0.07, 0.08) systems, the tetragonal (0 0 2) and (2 0 0) reflections (44.5–47.5° 2θ) were measured with a slow scan rate as shown in the Fig. 4.6 [1]. Using the relations (4.1), volume fraction ratio of the rhombohedral and tetragonal phases of the MPB composition NBT-xKNN (x=0.07) was calculated to be 32:68.

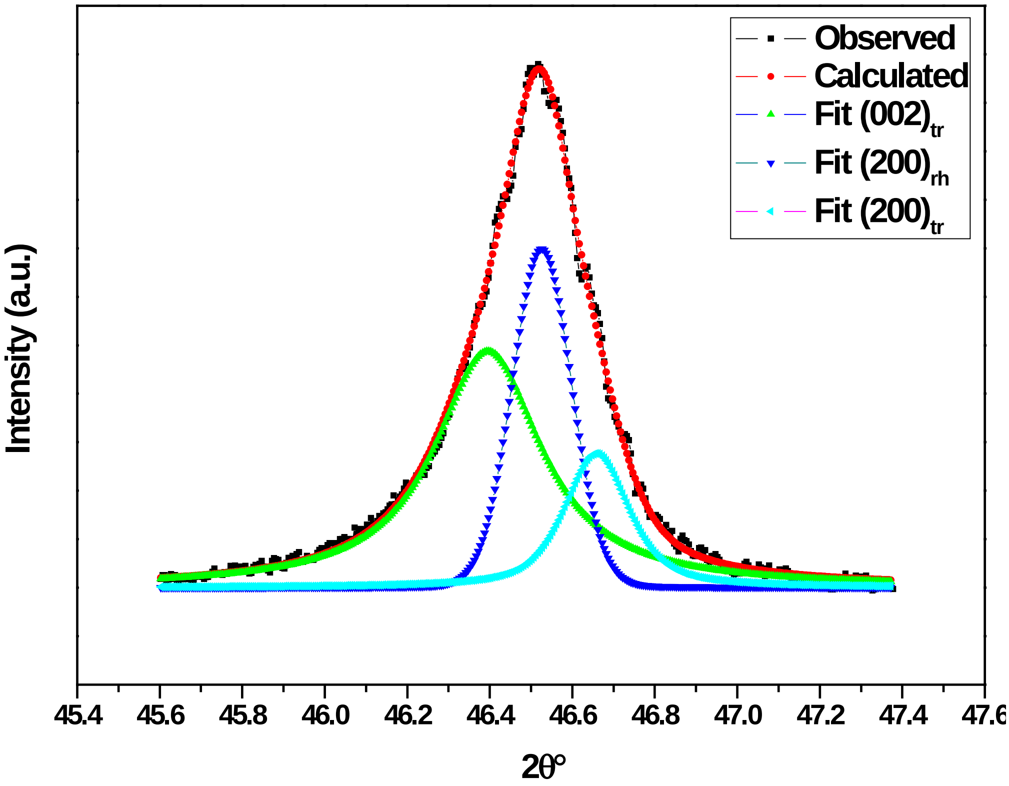

Fig. 4.6: XRD peak splitting at 2θ ~ 46° for NBT-xKNN with x=0.07.

## 4.4 Density and Morphological Study

### 4.4.1 Density and Morphological Study of the NBT-xBT Ceramics

Fig. 4.7 shows the SEM micrographs of all the sintered NBT–xBT (x =0.05, 0.06, 0.07, 0.08) ceramics. From the micrographs, densely packed and non-uniform distribution of the rectangular shaped grains of all the NBT–xBT ceramics can be observed. The slight inhibition of grain growth with the increase of BT addition into the NBT system is noticed with the initial increase of BT content. This may be related to the segregation of $Ba^{2+}$ ions near the crystal boundaries, which might have affected the migration of other ions and contributed against the growth of grains [8]. But, no remarkable change in grain size is observed with the variation of the BT content in the NBT–xBT system. Linear intercept method was used to find out the average grain size of all the NBT–xBT ceramics using “ImageJ” software. The average grain size of the MPB compositions of NBT–xBT system are given in Table 4.3.

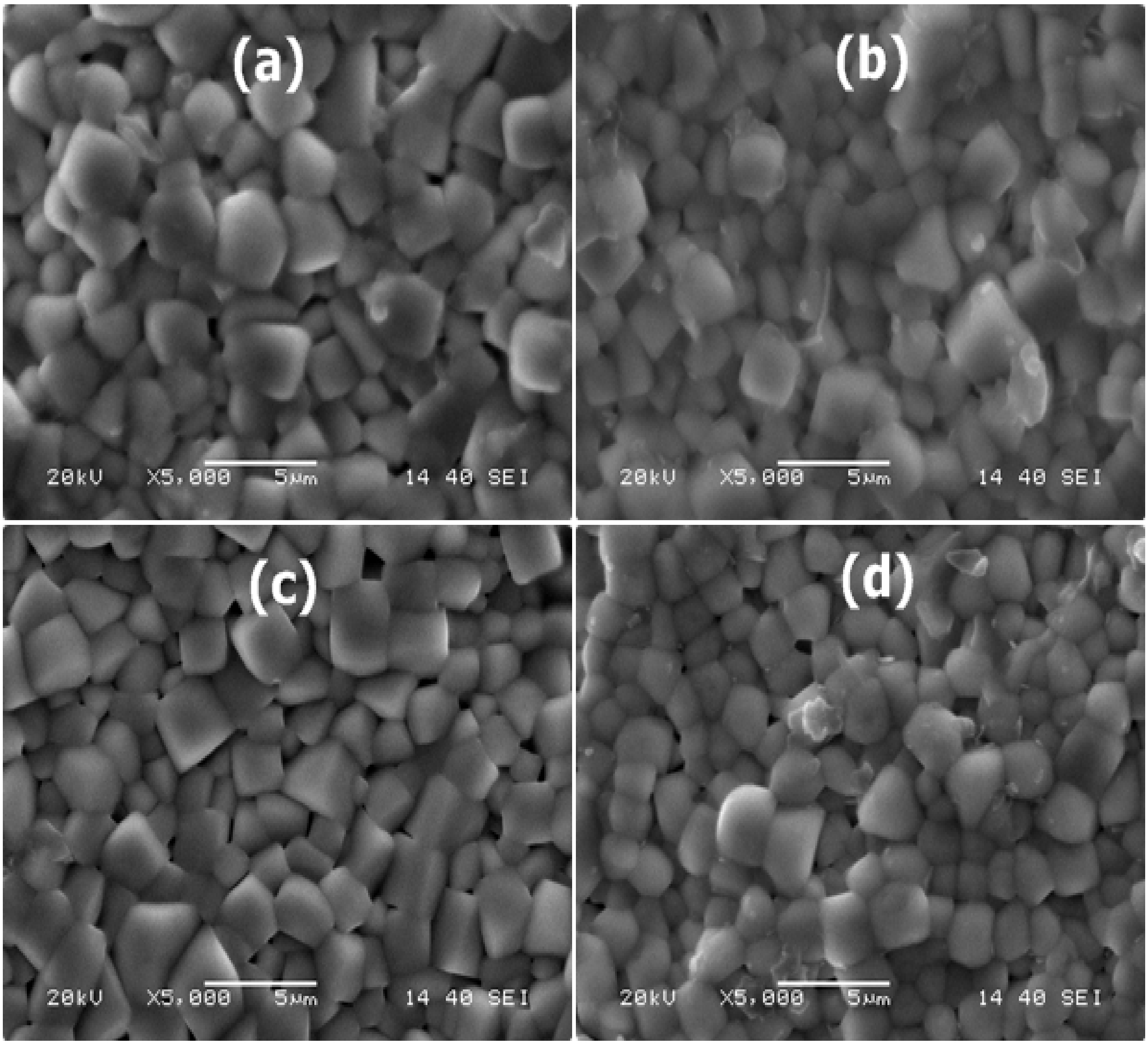

**Fig. 4.7:** SEM micrographs of NBT-xBT ceramics with x = (a) 0.05, (b) 0.06, (c) 0.07, and (d) 0.08.

Experimental density ($\rho_{ex}$) of all the NBT-xBT ceramic samples was calculated by using the Archimedes’ principle and its values are listed in Table 4.2. Highest $\rho_{ex}$, which is ~ 98.30% of the theoretical density ($\rho_{th}$), was obtained for the x=0.07 ceramic samples.

**Table 4.3:** Average grain size, and experimental density of NBT-xBT (x=0.05, 0.06, 0.07, 0.08) ceramics.

| BT content | Average grain size (μm) | Experimental density(g/cc) |
|---|---|---|
| x = 0.05 | 2.53 | 5.88 |
| x = 0.06 | 2.48 | 5.86 |
| x = 0.07 | 2.50 | 5.89 |
| x = 0.08 | 2.45 | 5.80 |

## 4.4.2 Density and Morphological Study of NBT-xKNN Ceramics

The SEM micrographs of the sintered NBT-xKNN (x=0.05, 0.06, 0.07, 0.08) ceramic samples are shown in Fig. 4.8. Closely packed, rectangular shaped and non-uniform arrangement of grains can be seen from the SEM micrographs. Since, non-uniform microstructure is a characteristic of KNN system [9], the non-uniformity of the NBT-xKNN grains can be attributed to the substitution of KNN in the NBT system. The average grain size was also calculated by linear intercept method using 'ImageJ' software and given in Table 4.4. The average grain size increases with the initial increase of KNN substitution in the NBT system and starts decreasing for the x=0.08 composition. This suggests that the excess substitution of KNN in the NBT-xKNN system acts as grain growth inhibitor [10]. The experimental density ($\rho_{ex}$) of the sintered NBT-xKNN ceramic samples is given in Table 4.4. The initial increase of grain size and $\rho_{ex}$ with the increase of KNN content in NBT-xKNN system may be due to the formation of liquid phase across the grain boundaries[11], which led to rearrangement of particles and providing more effective packing. Maximum grain size and $\rho_{ex}$ were observed for the x= 0.07 composition. The maximum grain size and $\rho_{ex}$ for the x=0.07 composition could be able to influence the enhancement of the electrical properties of this particular composition.

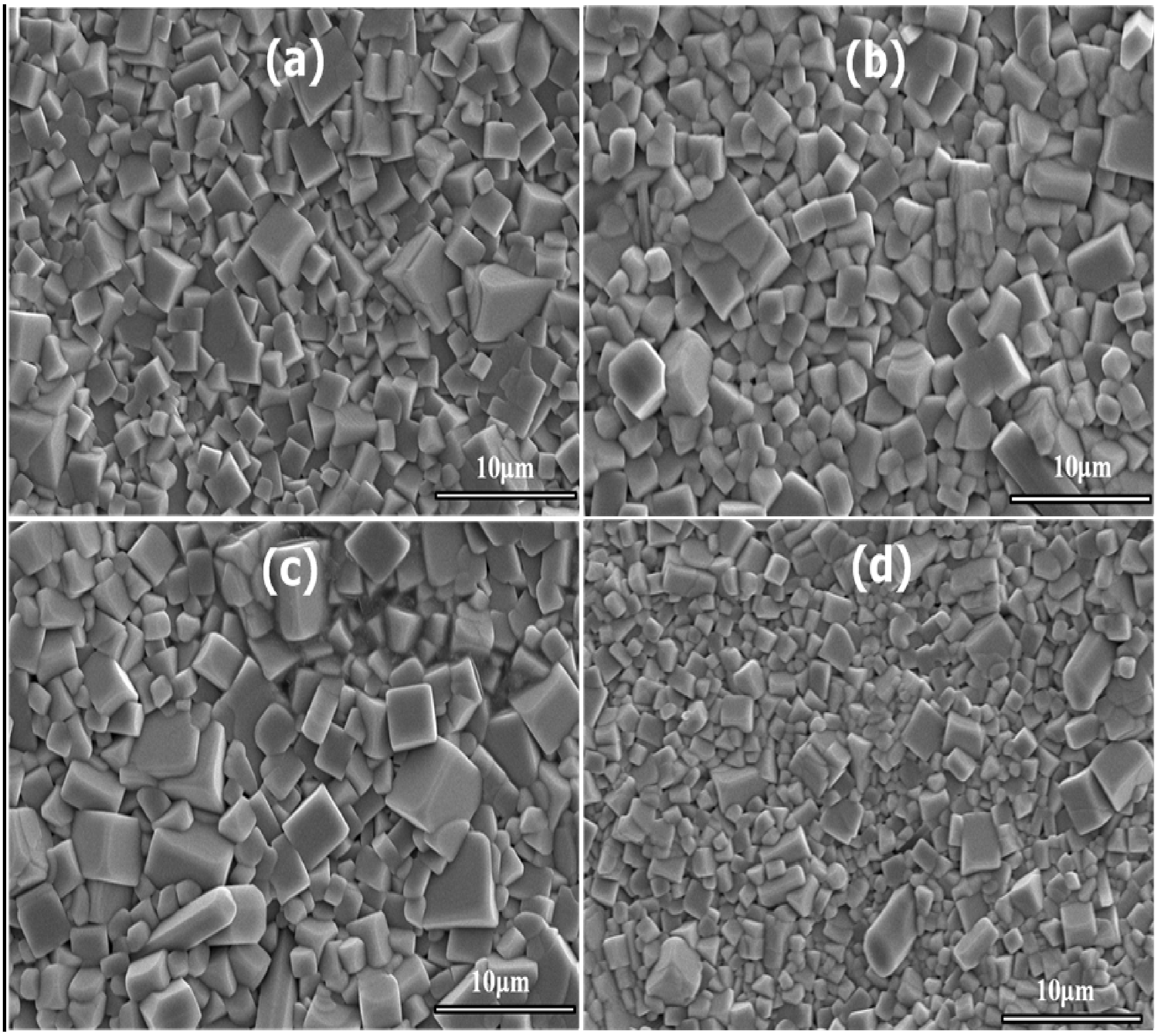

**Fig. 4.8:** SEM micrographs of NBT-xKNN ceramics with x = (a) 0.05, (b) 0.06, (c) 0.07, and (d) 0.08.

**Table 4.4:** Average grain size, and experimental density of NBT-xKNN (x=0.05, 0.06, 0.07, 0.08) ceramics.

| KNN content | Average grain size (μm) | Experimental density(g/cc) |
|---|---|---|
| x = 0.05 | 2.54 | 5.67 |
| x = 0.06 | 3.27 | 5.69 |
| x = 0.07 | 4.34 | 5.77 |
| x = 0.08 | 2.10 | 5.66 |

## 4.5 Dielectric Analysis

### 4.5.1 Temperature Dependent Dielectric Properties of NBT-xBT Ceramics

Fig. 4.9 (a-d) shows the temperature dependence of dielectric constant ($\varepsilon_r$) and dielectric loss (tanδ) at different frequencies of the NBT-xBT (x=0.05, 0.06, 0.07, 0.08) ceramic samples. Two major peaks are observed in all the NBT-xBT ceramic samples. The first peak in the 95-105°C temperature range corresponds to the depolarization temperature ($T_d$), where the ferroelectric (FE) phase undergoes to antiferroelectric (AFE) phase transition. The second peak ~ $T_m$ (where $\varepsilon_r$ reaches the maximum) corresponds to the transition from antiferroelectric to paraelectric state. $\varepsilon_r$ exhibits strong frequency dispersion below $T_d$ whereas above $T_d$ this dispersive nature is diminished. This indicates that there must be some dielectric relaxing mechanism present near the vicinity of RT [12]. Earlier, it is reported that in the pure $Na_{0.5}Bi_{0.5}TiO_3$ system, the phase region exhibiting P4bm symmetry with nano-domains embedded in the R3c matrix contributes towards the relaxor type nature [13]. Near $T_m$, at different frequencies no such appreciable dielectric peak shift is observed. But, these dielectric peaks near $T_m$ are relatively broad, suggesting the diffuse phase transition nature. This diffuse phase transition can be attributed to the random distribution of the $Na^+$, $Bi^{3+}$, and $Ba^{2+}$ ions at the A-site in the NBT-xBT system [14]. These behaviors also suggest that all the NBT-xBT ceramic systems exhibit relaxor nature. The dielectric properties of the NBT-xBT (x=0.05, 0.06, 0.07, 0.08) ceramics at 1 kHz frequency are given in Table 4.5. It can be observed that, among all the MPB compositions of the NBT-xBT system, x=0.07 shows the highest value of $\varepsilon_r$ at RT as well as at $T_m$, which hint towards its MPB nature. Moreover, x=0.07 composition exhibited lower $T_d$, which implies a reduction of the stability of ferroelectric domains at RT, since in the x=0.07 composition, there co-exists double structures (rhombohedral and tetragonal). This results in the decrease of the thermal stability of the long-range ferroelectric domains at RT in the double structure MPB composition [15, 16].

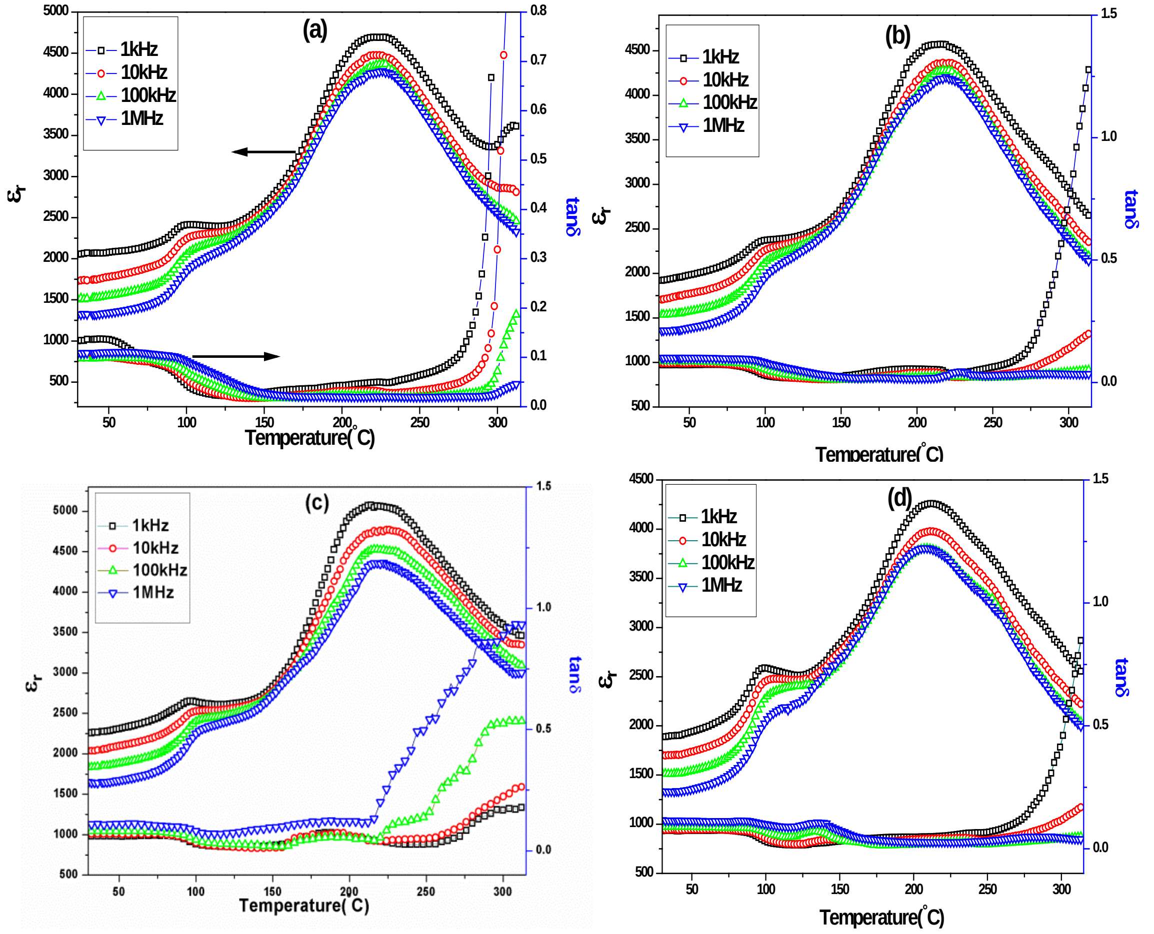

**Fig. 4.9:** Variation of $\varepsilon_r$ and tanδ with temperature at different frequencies of the NBT-xBT ceramics with x = (a) 0.05, (b) 0.06, (c) 0.07, and (d) 0.08.

**Table 4.5:** Dielectric properties (at 1 kHz frequency) of NBT-xBT (x=0.05, 0.06, 0.07, 0.08) ceramics.

| **BT content** | **$\varepsilon_r$ at RT** | **tanδ at RT** | **$T_d$ (°C)** | **$T_m$ (°C)** | **$\varepsilon_r$ at $T_m$** |
|---|---|---|---|---|---|
| x = 0.05 | 2023 | 0.09 | 102 | 226 | 4712 |
| x = 0.06 | 1946 | 0.05 | 101 | 219 | 4588 |
| x = 0.07 | 2275 | 0.04 | 99 | 219 | 5067 |
| x = 0.08 | 1898 | 0.08 | 100 | 215 | 4263 |

### 4.5.2 Temperature Dependent Dielectric Properties of NBT-xKNN Ceramics

Fig. 4.10 (a-d) shows the temperature dependence of $\varepsilon_r$ and tanδ at different frequencies of the NBT-xKNN (x=0.05, 0.06, 0.07, 0.08) ceramic samples. Two major dielectric anomalies are observed in all the samples, one below 150 °C and the other one ~ 250 °C. Similar type of dielectric patterns are also observed in the NBT-BT system, as studied by Jo *et al.* [17], where the commonly observed two dielectric anomalies are attributed to the thermal evolution of ferroelectric polar nanoregions (PNRs) of R3c (Rhombohedral) and P4bm (tetragonal) symmetries, which coexist throughout the temperature range, and reversibly transform into each other with the variation of temperature [17]. It is reported that around the MPB of the NBT-xKNN system, both the rhombohedral and tetragonal phases coexist simultaneously [2]. Broad dielectric peaks with slight frequency dependence of $\varepsilon_r$ and tanδ at $T_d$ and $T_m$ indicates the relaxor nature of all the NBT-xKNN ceramic samples [18]. The relaxor-like nature in this type of system is attributed to the coexistence of PNRs of different symmetries. Further, it is reported that an unpoled NBT sample exhibit relaxor nature at RT [19]. As the samples are unpoled, the first dielectric dispersion, observed below $T_d$ in the NBT-xKNN systems, suggest towards the relaxor contribution [18]. Whereas, the second dielectric anomaly can be attributed to the thermal evolution of the PNRs with the transformation of R3c to P4bm phase [17]. In addition, the increase of dielectric peak broadening with the increase of KNN content suggest the increase of disordered cation distribution at both the A- and B-sites in the NBT-xKNN system. The $\varepsilon_r$, $T_d$, $T_c$, and tanδ values at RT and at 1 kHz frequency of the MPB compositions of the NBT-xKNN system are given in Table 4.6. It is observed that $T_c$ decreases while the maximum $\varepsilon_r$ does not change significantly, with the increase of KNN content in the NBT-xKNN system up to x=0.07 composition. The highest $\varepsilon_r$ value at RT and at $T_c$ in the x=0.07 composition can be related to the presence of double structure and suggest its actual MPB nature. Since, the presence of double structure is the characteristic of an MPB composition, and it also increases the polarization, which ultimately improve the dielectric properties.

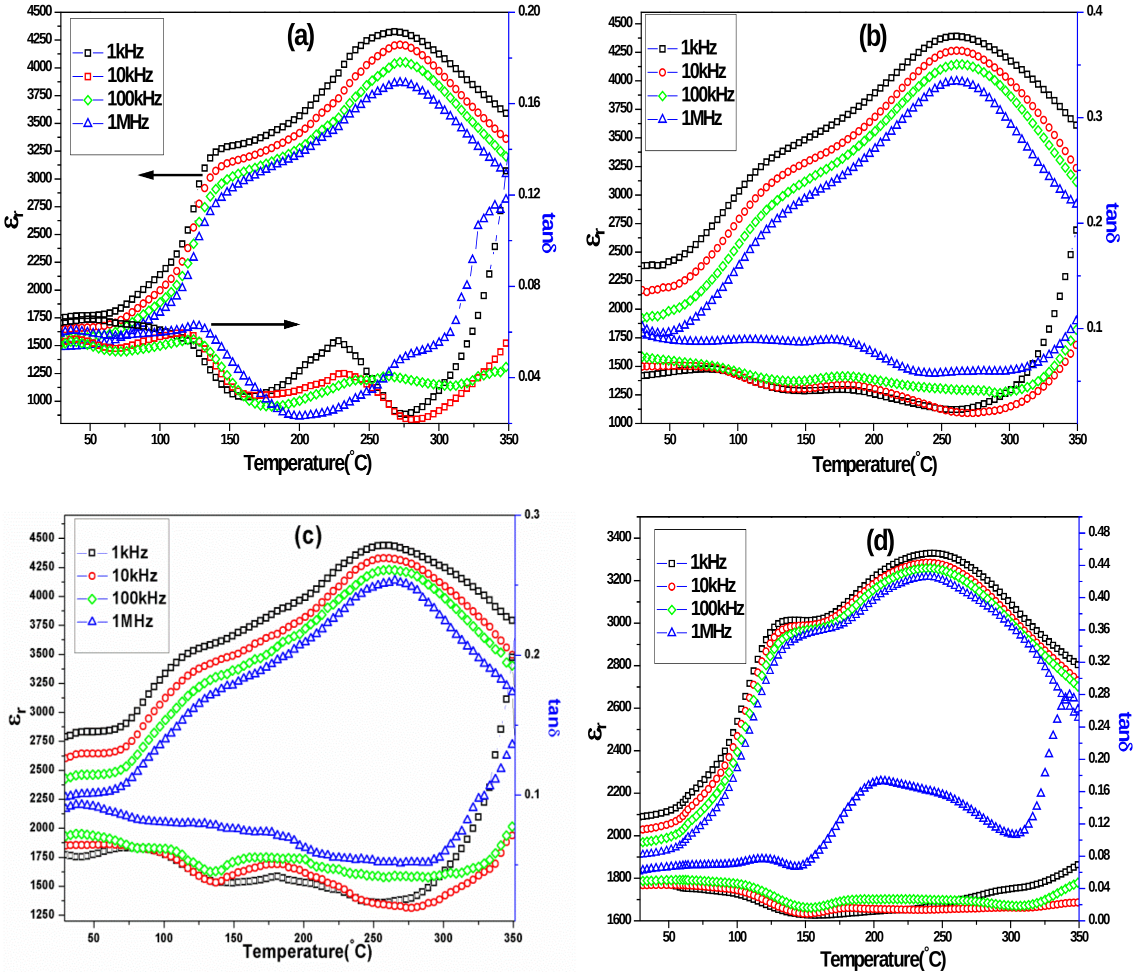

**Fig.4.10:** Variation of $\varepsilon_r$ and tanδ with temperature at different frequencies of NBT-xKNN ceramics with x = (a) 0.05, (b) 0.06, (c) 0.07, and (d) 0.08.

**Table 4.6:** Dielectric properties of NBT-xKNN (x=0.05, 0.06, 0.07, 0.08) ceramics at 1 kHz frequency.

| **KNN content** | **$\varepsilon_r$ at RT** | **tanδ at RT** | **$T_d$ (°C)** | **$T_m$ (°C)** | **$\varepsilon_r$ at $T_m$** |
|---|---|---|---|---|---|
| x = 0.05 | 1750 | 0.06 | 136 | 268 | 4324 |
| x = 0.06 | 2380 | 0.05 | 122 | 261 | 4389 |
| x = 0.07 | 2787 | 0.05 | 121 | 259 | 4438 |
| x = 0.08 | 2088 | 0.04 | 130 | 243 | 3328 |

# 4.6 Leakage Current Study

## 4.6.1 Leakage Current Properties of the NBT-xBT Ceramics

Fig. 4.11 shows the RT leakage current density vs. electric field (J-E) plots of the NBT-xBT ceramic samples up to ~ 40kV/cm. A slight asymmetry in the J-E plots suggest towards the electrode dependent nature of the NBT-xBT ceramic samples [20]. The leakage current characteristics at lower electric fields suggest that the conduction mechanism in all the NBT-xBT ceramic samples can be attributed to be of Ohmic type, whereas at higher fields, the conduction mechanism can be associated with the space charge limited conduction [21-23]. The RT leakage current density values of all the NBT-xBT ceramic samples at ~ 40kV/cm are given in Table 4.7. Among all the NBT-xBT ceramic samples, x=0.07 composition shows the lowest leakage current density (~5.72x10$^{-7}$ A/cm$^2$), which hints towards its better suitability in ferroelectric device applications compared to the other studied compositions. The current density are observed to be between 10$^{-7}$ - 10$^{-6}$ A/cm$^2$ for all the NBT-xBT ceramic samples. A remarkable hump at electric field >30kV/cm in the J-E plot can be related with the ferroelectric switching behavior, i.e. coercive field of the studied ceramic samples [24].

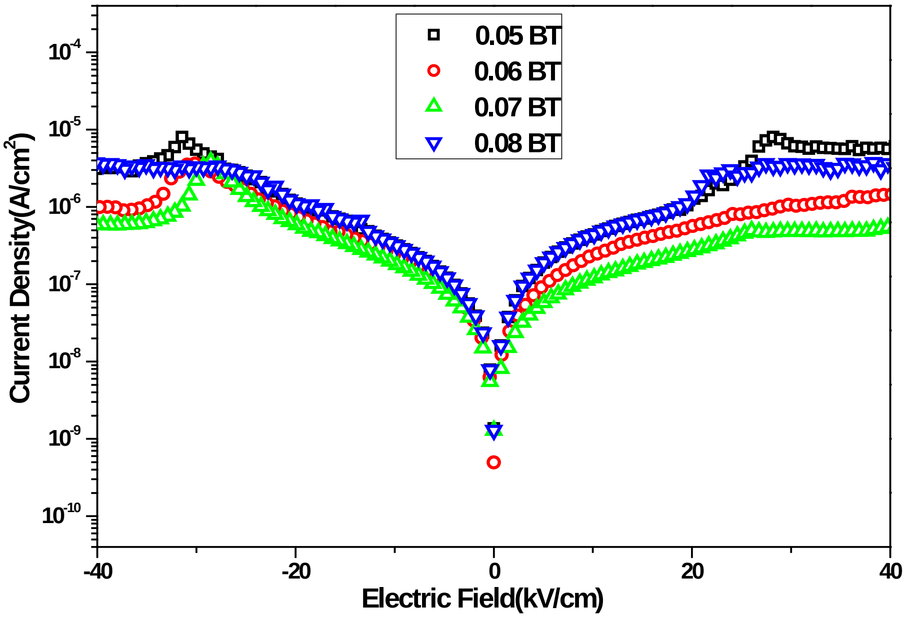

**Fig. 4.11:** Room temperature leakage current density vs. electric field plots of the NBT-xBT (0.05≤x≤0.08) ceramic samples.

**Table 4.7:** Leakage properties of NBT-xBT (x=0.05, 0.06, 0.07, 0.08) ceramics at the electric field of 40kV/cm.

| **BT content** | x =0.05 | x =0.06 | x =0.07 | x =0.08 |
|---|---|---|---|---|
| **Current density(A/cm$^2$)** | 3.14x10$^{-6}$ | 1.03x10$^{-6}$ | 5.72x10$^{-7}$ | 3.23x10$^{-6}$ |

### 4.6.2 Leakage Current Properties of the NBT-xKNN Ceramics

Fig. 4.12 shows the leakage current vs. applied electric field behavior of the NBT-xKNN ceramic samples. The insulating characteristics of a dielectric ceramic can be determined by the value of its leakage current. The leakage current density of all the NBT-xKNN ceramic samples gradually increases with the increase of applied electric field up to ~10kV/cm. The conduction mechanism at lower fields may be attributed to the Ohmic type conduction. With the further increase of the electric field, the conduction mechanism can be related to the space charge limited conduction [21-23]. Here also, among all the NBT-xKNN ceramic samples, x=0.07 composition shows the lowest leakage current density of ~$1.04\times10^{-6}$ A/cm$^2$ at ~ 40kV/cm. In this case, the observed least leakage current density can be attributed to the maximum grain size of the x=0.07 composition samples. Since, larger grains contribute towards interfacial areas between the grains is small and these interfaces provide a leakage path for charge carriers, therefore larger the grain size, least is the leakage current [25]. However, unlike NBT-BT samples, absence of any hump in J-E characteristics suggests some kind of role of non-attainment of polarization saturation within the applied electric field range in NBT-xKNN samples. The values of leakage current density of all the NBT-xKNN ceramic samples at 40kV/cm electric field are given in Table 4.8.

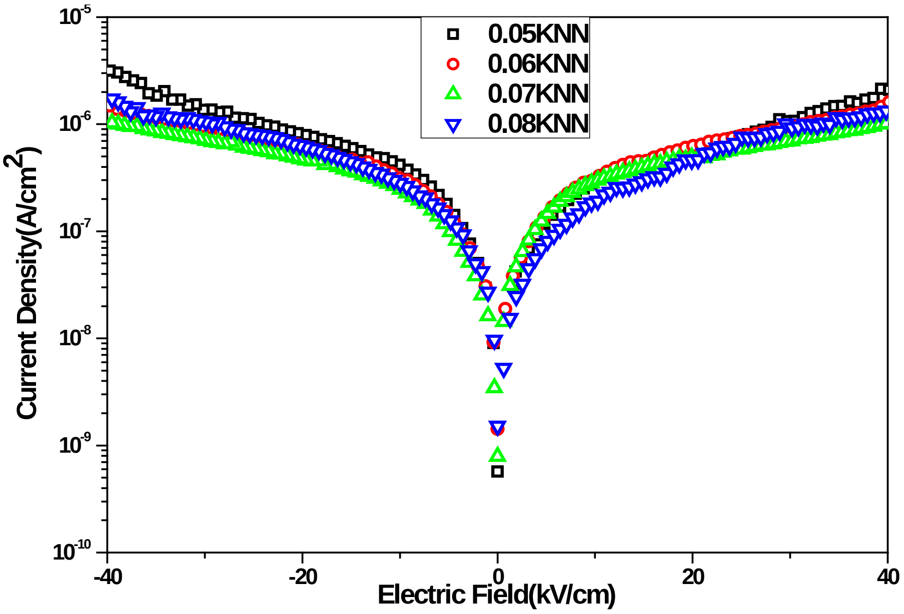

**Fig. 4.12:** Room temperature leakage current density vs. electric field plots of NBT-xKNN ($0.05\leq x\leq0.08$) ceramics.

**Table 4.8:** Leakage properties of NBT-xKNN (x=0.05, 0.06, 0.07, 0.08) ceramics at the electric field of 40kV/cm.

| **KNN content** | x =0.05 | x =0.06 | x =0.07 | x =0.08 |
|---|---|---|---|---|
| **Current density(A/cm$^2$)** | $3.37x10^{-6}$ | $1.46x10^{-6}$ | $1.04x10^{-6}$ | $1.89x10^{-6}$ |

# 4.7 Piezoelectric Study

## 4.7.1 Piezoelectric Studies of NBT-xBT Ceramics

### 4.7.1.1 Strain vs. Electric Field Study

Fig. 4.13 (a-d) shows the RT-induced strain% vs. external electric field (S-E) curves of all the NBT-xBT(x=0.05, 0.06, 0.07, 0.08) compositions. From the S-E plots, it is observed that in all the NBT-xBT ceramic samples, initially the strain% increases with the increase in applied external electric field, which is due to the alignment of the domains along the field direction. At higher electric fields, the alignments of domains get saturated, which results in the maximum induced strain%. A slight asymmetry is observed in the (S-E) plots of the NBT-xBT system near MPB, which may be due to the internal field induced by the presence of certain defects [26]. In the present case, a maximum strain of ~0.45% is obtained in the x=0.07 composition samples, which suggests the dominance of the movement and switching of the non-180° domain walls [27]. This also indicates that small displacements of all types of domain walls can affect the polarization of the material. It is a known fact, that in addition to the pure piezoelectric response of the material within each domain, the movement and switching of non-180° walls will involve a significant change in the dimensions of the sample. Furthermore, the development of typical butterfly-shaped loops and the existence of remnant strain in the NBT-xBT ceramics indicate their piezoelectric nature [28]. The maximum induced strain% of the studied MPB compositions of the NBT-xBT system are given in Table 4.9.

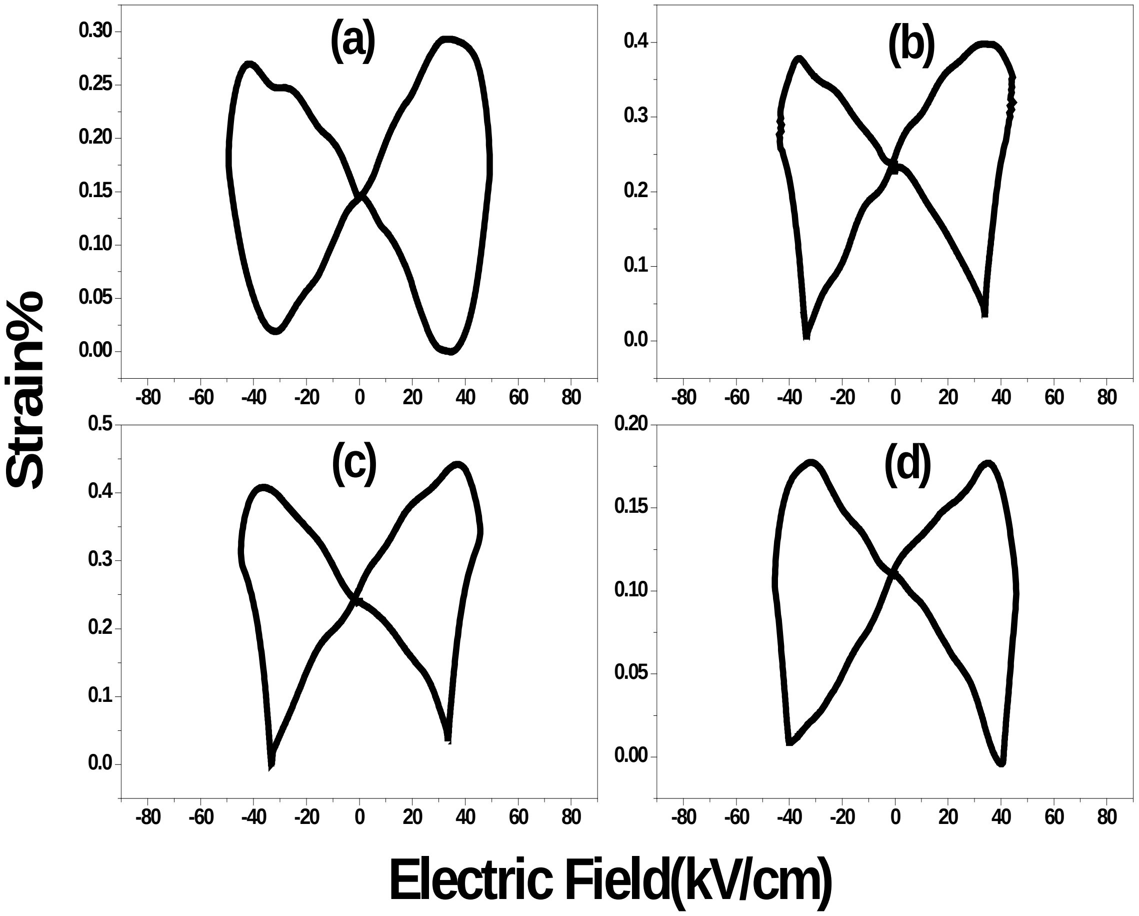

**Fig. 4.13:** Variation of induced strain% vs. bipolar electric field of the NBT-xBT ceramics with x = (a) 0.05, (b) 0.06, (c) 0.07, and (d) 0.08.

### 4.7.1.2 Piezoelectric Coefficients ($d_{33}$ and $k_p$) Study

Fig. 4.14 shows the RT variation of the piezoelectric coefficient ($d_{33}$) and the electromechanical coupling coefficient ($k_p$) with the variation of BT content in the NBT-xBT system. Electromechanical coupling coefficient, $k_p$, is calculated by using relation 4.2 [29]. The resonance ($f_r$) and anti-resonance ($f_a$) frequencies, used in the eq. 4.2 are obtained from frequency vs. impedance (Z) plots. The frequency vs. impedance (Z), and phase angle plots of the x=0.07 composition is shown in Fig. 4.15.

$$k_p = \left[ 2.51 \times (\frac{f_a - f_r}{f_r}) \right]^{\frac{1}{2}} \qquad (4.2)$$

The values of $d_{33}$ and $k_p$ coefficients are given in Table 4.9. The highest value of $d_{33}$ and $k_p$ coefficients are obtained in the x=0.07 composition samples. The highest value of the $d_{33}$ coefficient in the x=0.07 composition again suggest its actual MPB nature. Since, there exists a large number of poling directions in a MPB composition, which result in the better piezoelectric and electromechanical properties.

The values of $k_p$ and $d_{33}$ is not in linear variation (as shown in fig 4.14), i.e. the values are higher for x=0.05 rather than for x=0.06 composition. Linear trend is not followed as the observed results suggest that 0.05 composition is also within the MPB region. Since within the MPB region, electrical properties varies as per the % of different constituent phases present in the selected compositional range. This also suggests the need of further study of effect of different constituent phases on electrical properties of these MPBs compositions.

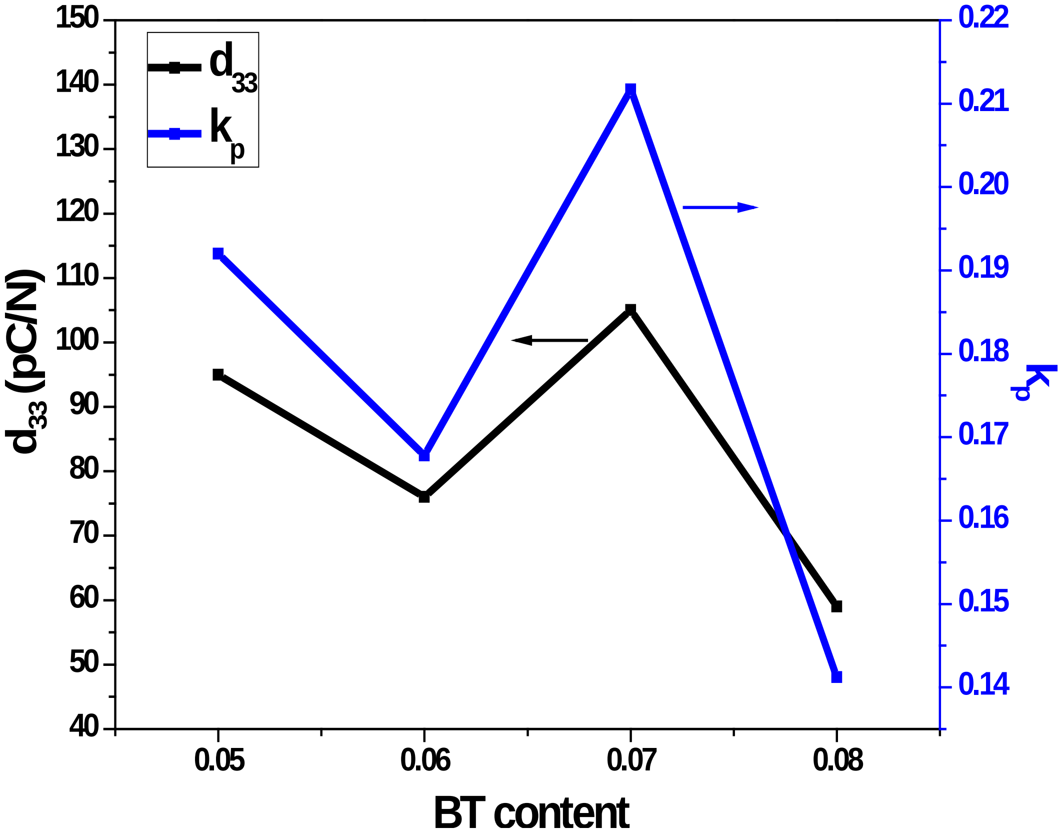

**Fig. 4.14:** Variation of piezoelectric ($d_{33}$) and electromechanical coupling ($k_p$) coefficients with BT content in the NBT-xBT system.

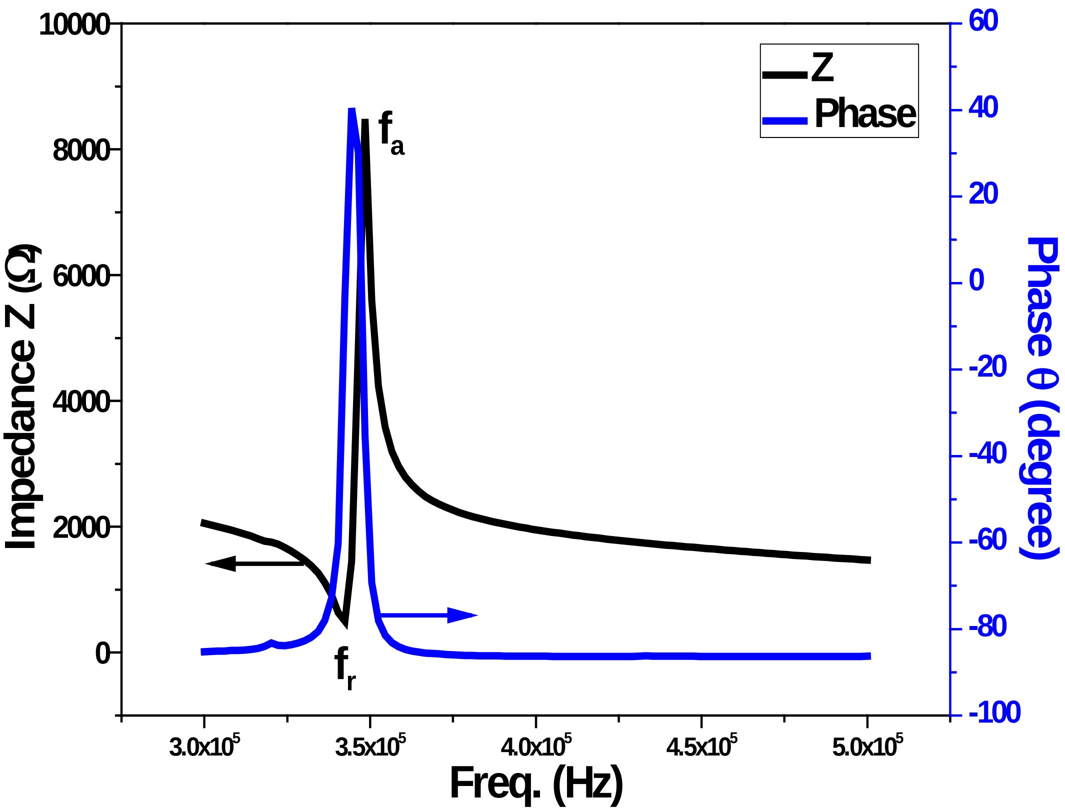

**Fig. 4.15:** Impedance (Z) and phase angle (θ) variations with frequency of the x=0.07 poled samples of the NBT-xBT system.

**Table 4.9:** Piezoelectric parameters of NBT-xBT (x=0.05, 0.06, 0.07, 0.08) ceramics.

| BT content | $k_p$ | $d_{33}$ (pC/N) | Strain% |
|---|---|---|---|
| x = 0.05 | 0.19 | 95 | 0.27 |
| x = 0.06 | 0.16 | 76 | 0.38 |
| x = 0.07 | 0.21 | 105 | 0.45 |
| x = 0.08 | 0.14 | 59 | 0.18 |

## 4.7.2 Piezoelectric Study of the NBT-xKNN Ceramics

### 4.7.2.1 Strain vs. Electric Field Study

Fig. 4.16 shows RT the S-E plots of the NBT-xKNN (x=0.05, 0.06, 0.07, 0.08) ceramic samples. Though, the remnant strain value of all the NBT-xKNN ceramic samples is observed to be smaller, compared to the NBT-xBT systems, but the development of typical butterfly-shaped S-E loops confirm their piezoelectric nature. This S-E plots also shows the characteristic of a ferroelectric ceramic sample [30]. The maximum induced strain% of all the NBT-xKNN ceramic samples is given in Table 4.10. Development of maximum strain% ~ 0.36 is observed in the x=0.07 composition samples. This suggests that, at x=0.07 composition, the movement and switching of the non-180° domain walls is dominant [27]. The maximum strain% in the x=0.07 composition further suggest the actual MPB nature of this composition [31].

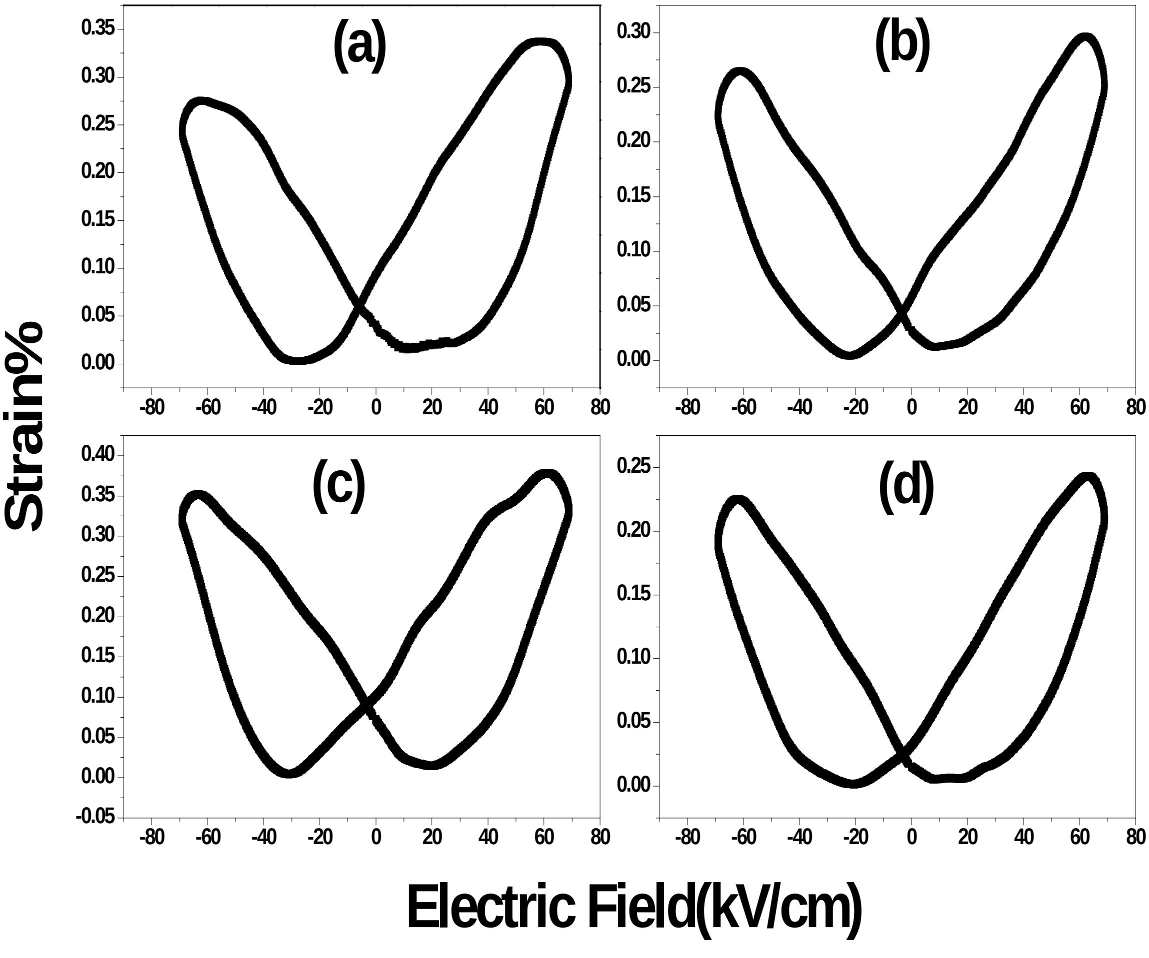

**Fig. 4.16:** Variation of induced strain% vs. bipolar electric field of the NBT-xKNN ceramics with x = (a) 0.05, (b) 0.06, (c) 0.07, and (d) 0.08.

### 4.7.2.2 Piezoelectric Coefficients ($d_{33}$ and $k_p$) Study

Fig. 4.17 shows the RT variation of the piezoelectric coefficient ($d_{33}$), and the electromechanical coupling coefficient ($k_p$) with the variation of KNN content in the NBT-xKNN system. The electromechanical coupling coefficient ($k_p$) was calculated by using eq. 4.1 [29]. Similar to NBT-xBT systems, the $f_r$ and $f_a$ frequencies, used in the eq. 4.2, are obtained from frequency vs. impedance (Z) plots. The frequency vs. impedance (Z), and phase angle plots of the x=0.07 composition is shown in Fig. 4.18. $d_{33}$ and $k_p$ values are summarized in Table 4.10. Highest value of $d_{33}$ and $k_p$ are observed in x=0.07 composition samples, which suggest its actual MPB nature. This is because the MPB composition of a ferroelectric system has relatively high piezoelectric and electromechanical activities, which is attributed to an increase in the number of possible spontaneous polarization directions due to the coexistence of mixed structures [31]. Since, the presence of double structure in the x=0.07 composition samples can increase the number of polarization directions, which can ultimately increase the piezoelectric properties.

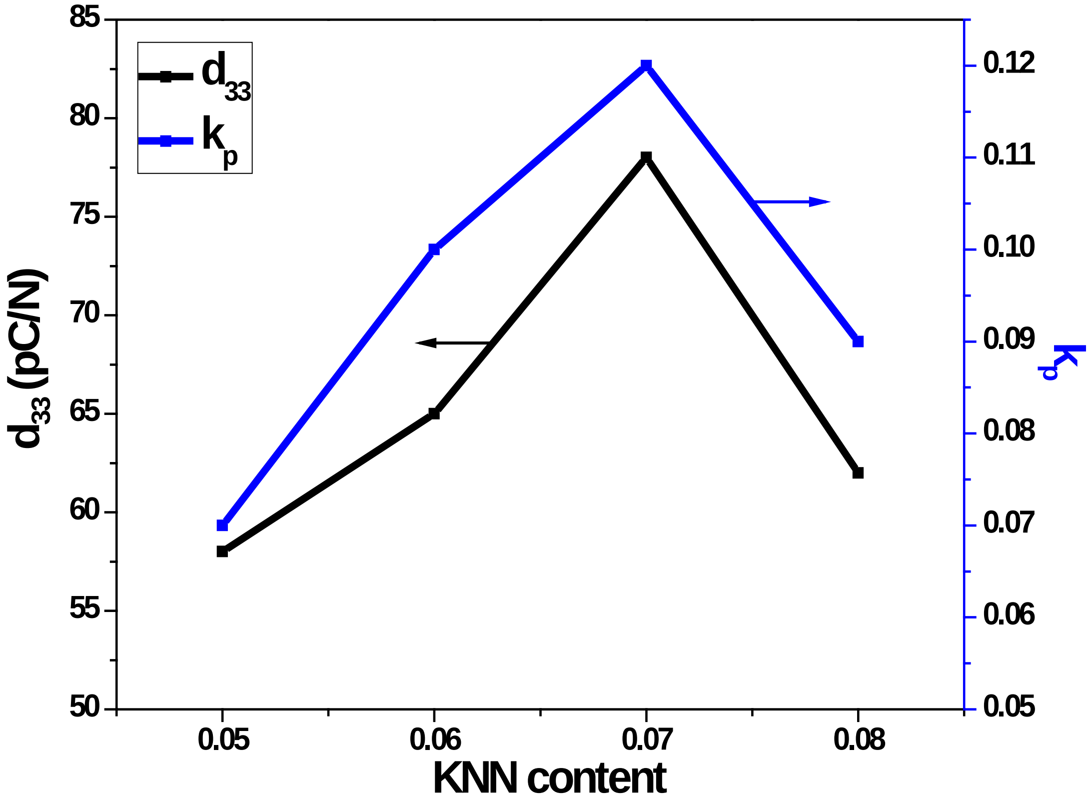

**Fig. 4.17:** Variation of piezoelectric ($d_{33}$) and electromechanical ($k_p$) coupling coefficients with the variation of KNN content in the NBT-xKNN system.

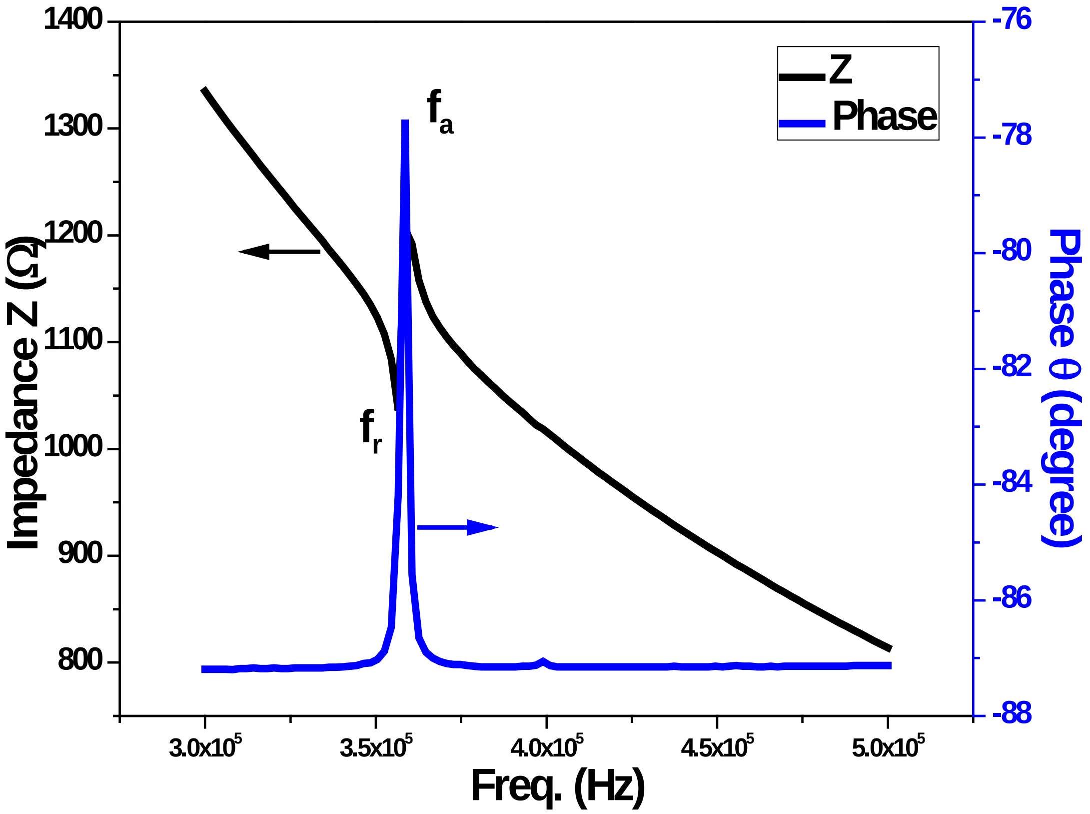

**Fig. 4.18:** Impedance (Z) and phase angle (θ) variations with frequency of the poled x=0.07 samples of NBT-xKNN system.

**Table 4.10:** Piezoelectric parameters of NBT-xKNN (x=0.05, 0.06, 0.07, 0.08) ceramics.

| **KNN content** | **$k_p$** | **$d_{33}$ (pC/N)** | **Strain%** |
|---|---|---|---|
| x = 0.05 | 0.07 | 58 | 0.30 |
| x = 0.06 | 0.10 | 65 | 0.28 |
| x = 0.07 | 0.12 | 78 | 0.36 |
| x = 0.08 | 0.09 | 62 | 0.23 |

## 4.8 Ferroelectric Study

### 4.8.1 Ferroelectric Study of NBT-xBT Ceramics

Fig. 4.19 shows the RT polarization vs. electric field (P-E) hysteresis loops of the NBT-xBT (x=0.05, 0.06, 0.07, 0.08) ceramic samples. Remnant polarization ($P_r$) and coercive field ($E_c$) values of all the NBT-xBT ceramic samples are given in Table 4.11. The development of well saturated P-E hysteresis loops confirms the ferroelectric nature of all the NBT-xBT ceramic samples. However, maximum value of $P_r$ ~ 31.71 μC/cm$^2$ with $E_c$ ~ 40 kV/cm were obtained in the x=0.07 ceramic samples, which suggest the actual MPB nature of this composition. The low value of $E_c$ in the x=0.07 ceramic samples compared to x= 0.05 and 0.06 compositions supports the observed enhanced piezoelectric properties of this composition. Since, with lower $E_c$ value, the domain movement can take place easily, which results in better piezoelectric properties. With the further increase of BT content i.e. for x= 0.08 in the NBT-xBT system, a considerably low $P_r$ value is observed, which can be attributed to the introduction of greater lattice distortion into the NBT system [32].

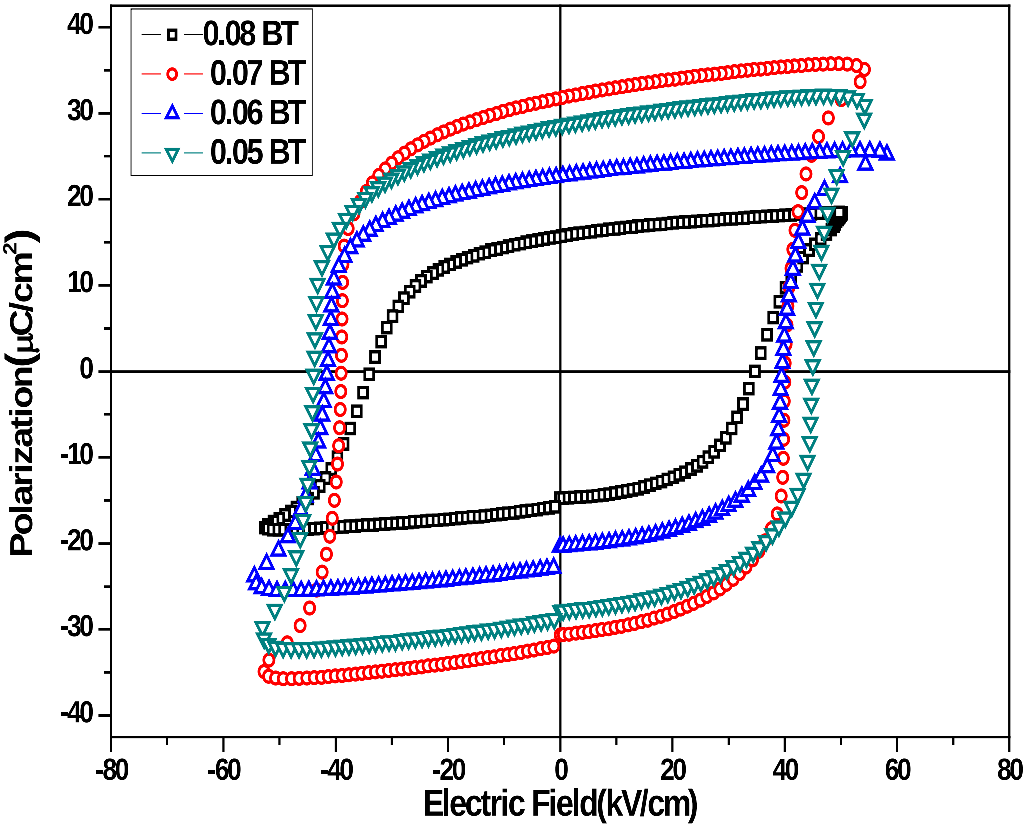

**Fig. 4.19:** P-E hysteresis loops of NBT-xBT (x=0.05, 0.06, 0.07, 0.08) ceramics.

**Table 4.11:** Ferroelectric parameters of NBT-xBT (x=0.05, 0.06, 0.07, 0.08) ceramics.

| **BT content** | x = 0.05 | x = 0.06 | x = 0.07 | x = 0.08 |
|---|---|---|---|---|
| **$P_r$ (μC/cm$^2$)** | 28.73 | 23.50 | 31.71 | 15.66 |
| **$E_c$(kV/cm)** | 45.33 | 42.62 | 40.00 | 34.65 |

### 4.8.2 Ferroelectric Study of NBT-xKNN Ceramics

Fig. 4.20 shows the polarization vs. electric field (P-E) hysteresis loops of the NBT-xKNN ceramic samples. Well saturated (P-E) hysteresis loops of all the NBT- xKNN ceramic samples are developed. The fine saturation, which relate with the insulating property of a sample, might have been prevented by the increase of leakage current at higher applied external electric field [33]. Maximum remnant polarization ($P_r$) ~ 20.61 μC/cm$^2$ and small coercive field ($E_c$) ~ 19.90 kV/cm were obtained for the x = 0.07 composition. The maximum $P_r$ value of the x=0.07 composition can be associated with the increase in domain wall motion. The highest grain size in this composition can be related with the easy switching of the domains and hence maximum $P_r$ among the studied NBT-xKNN ceramic samples [34, 35]. Further, the highest value of $P_r$ in this composition suggests the its actual MPB nature [36]. As, the existence of mixed structures in the x=0.07 composition increases the number of polarizations directions (14, 6 for tetragonal structure and 8 for rhombohedral structure) and hence highest value of $P_r$ among the studied NBT-xKNN ceramic samples [37]. The $P_r$ and $E_c$ values of all the NBT-xKNN ceramic samples are given in Table 4.12.

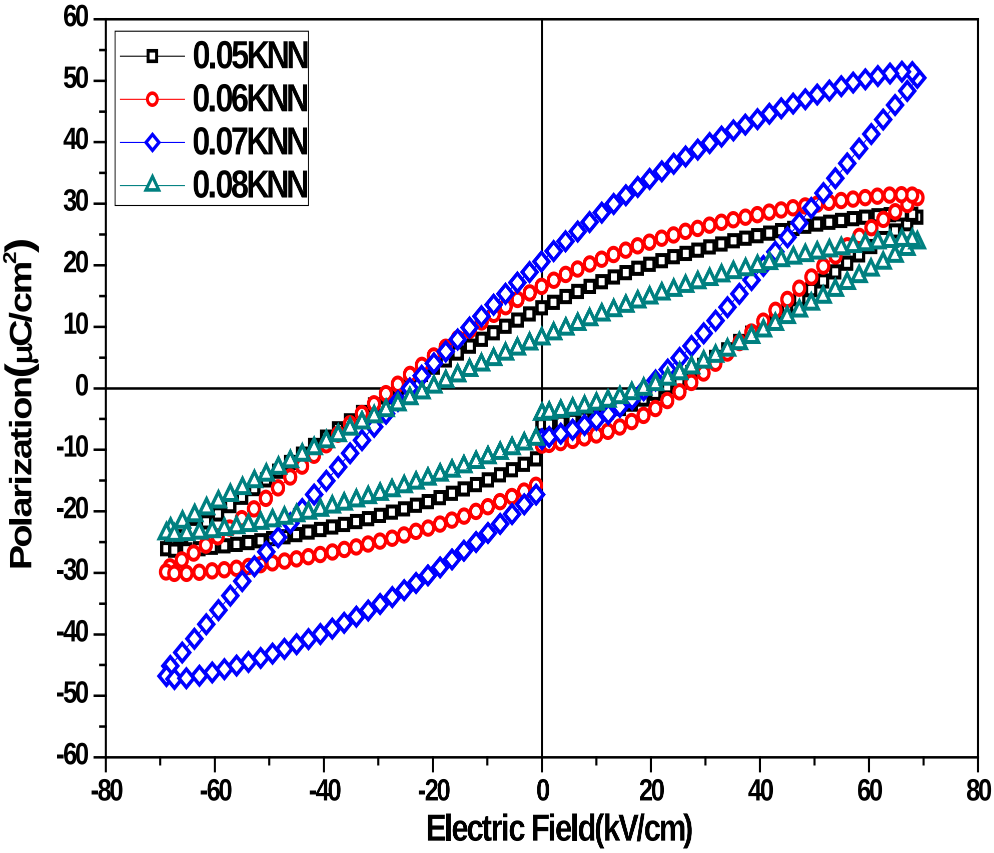

**Fig. 4.20:** P-E hysteresis loops of NBT-xKNN(x=0.05, 0.06, 0.07, 0.08) ceramics.

**Table 4.12:** Ferroelectric parameters of NBT-xKNN (x=0.05, 0.06, 0.07, 0.08) ceramics.

| **KNN content** | x = 0.05 | x = 0.06 | x = 0.07 | x = 0.08 |
|---|---|---|---|---|
| **$P_r$ (μC/cm$^2$)** | 12.93 | 16.26 | 20.61 | 7.95 |
| **$E_c$(kV/cm)** | 24.19 | 25.64 | 19.90 | 19.00 |

# 4.9 Polarization Fatigue Study

## 4.9.1 Polarization Fatigue Study of NBT-xBT Ceramics

Fig. 4.21 shows the normalized polarization vs. number of cycles (up to $10^9$) of the applied external electric field, measured at $10^5$Hz frequency of the NBT-xBT ceramic samples. Polarization fatigue in ferroelectric materials is the systematic suppression of the spontaneous polarization under bipolar or unipolar electrical cycling [38, 39]. In the present study, the bipolar fatigue study is undertaken because in many ferroelectric random access memory (FeRAM) and non-volatile memory devices, each cell is controlled by bipolar pulses [40]. Here, P* and -P* (μC/cm$^2$) denotes the switched polarization value in positive and negative applied electric field cycles. In this case, the switched polarizations were observed at the cycle numbers of 1, 300000, $1.5 \times 10^6$, $1.17 \times 10^7$, $1.11 \times 10^8$, and $1.23 \times 10^9$, respectively. All the NBT-xBT ceramics follow the same trends of normalized polarization vs. no. of cycles of the applied external electric field and there is a substantial decrease in the polarization value after $10^7$ cycles of all the ceramics, which indicates the degradation of their ferroelectric properties. The relative polarization fatigue% (after $10^9$ cycles) of all the NBT-xBT ceramic samples is given in Table 4.13. Generally, in a ferroelectric material, different factors are responsible for such type of polarization degradation. Pinning of the domain walls by the defects with charges (such as oxygen vacancies, electronic or ionic charges etc.), segregated in the wall region [41-43], may be considered as the mechanism responsible for the fatigue behavior in the NBT-xBT ceramics. In the present study, the pinning of the domain walls can be associated mainly with the oxygen vacancies, because the oxygen vacancy formation is most common in the perovskite ceramics during sintering at high temperatures [44].

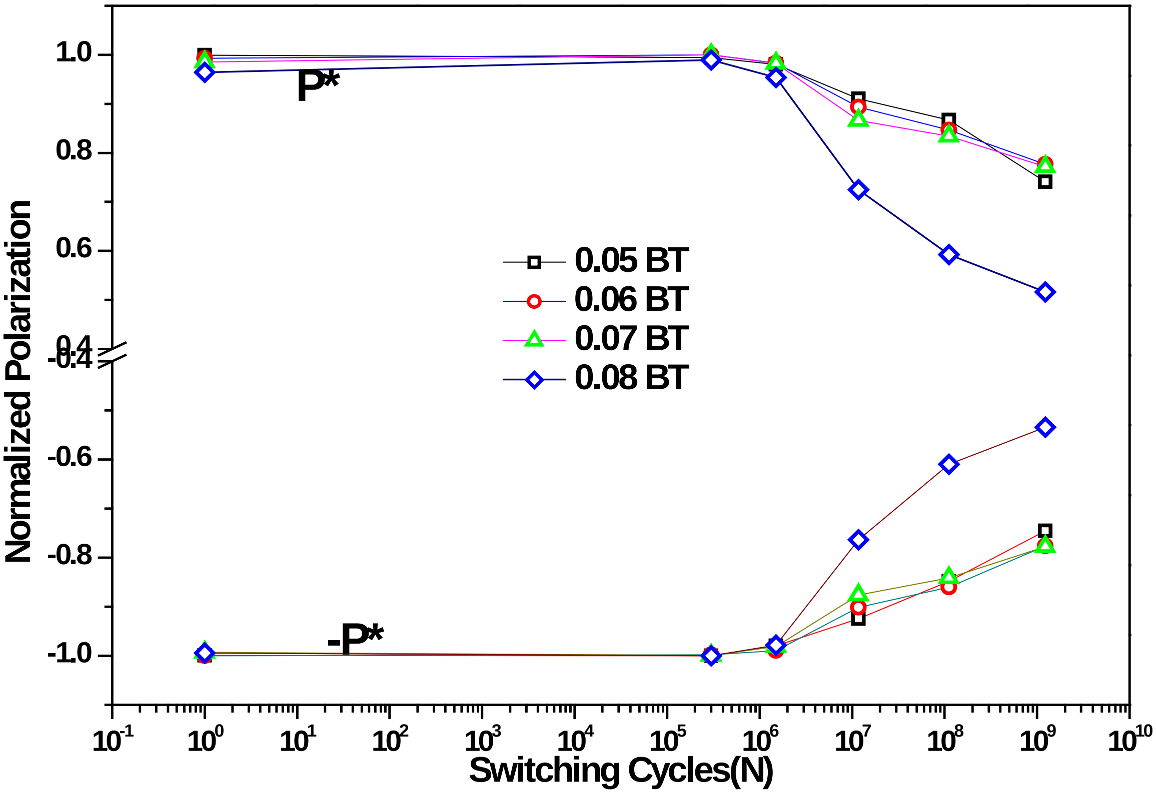

**Fig. 4.21:** Normalized polarization vs. number of cycles plots of NBT-xBT (x=0.05, 0.06, 0.07, 0.08) ceramics.

**Table 4.13:** Relative polarization fatigue % (after $10^9$ cycle) of NBT-xBT (x=0.05, 0.06, 0.07, 0.08) ceramics.

| **BT content** | x = 0.05 | x = 0.06 | x = 0.07 | x = 0.08 |
|---|---|---|---|---|
| **Relative polarization fatigue% ($10^9$ cycle)** | 25.66 | 22.37 | 22.54 | 47.48 |

Fig. 4.22 (a-d) shows the P-E hysteresis loops before and after $10^7$ cycles of the applied external electric field to confirm the fatigue behavior of all the NBT-xBT ceramics. Decrease of remnant polarization confirmed the fatigue behavior in these ceramics. The NBT-xBT ceramics corresponding to x=0.08, show the greatest degree of polarization degradation. Generally, the fatigue mechanism and polarization in ferroelectric materials are related to the defect agglomeration and deformation of grains [45, 46]. Therefore, relatively non-uniform and agglomerated grains in the x=0.08 NBT-xBT ceramics can account the greatest degree of polarization degradation among the

studied MPB compositions of NBT-xBT system. Except the NBT-xBT ceramics, corresponding to x=0.05, all the ceramics show an increase in the coercive field after loading cycles. The geometrically less constrained grains in the NBT-xBT ceramics corresponding to x=0.05 can explain the retention of same coercive field after loading cycles [46].

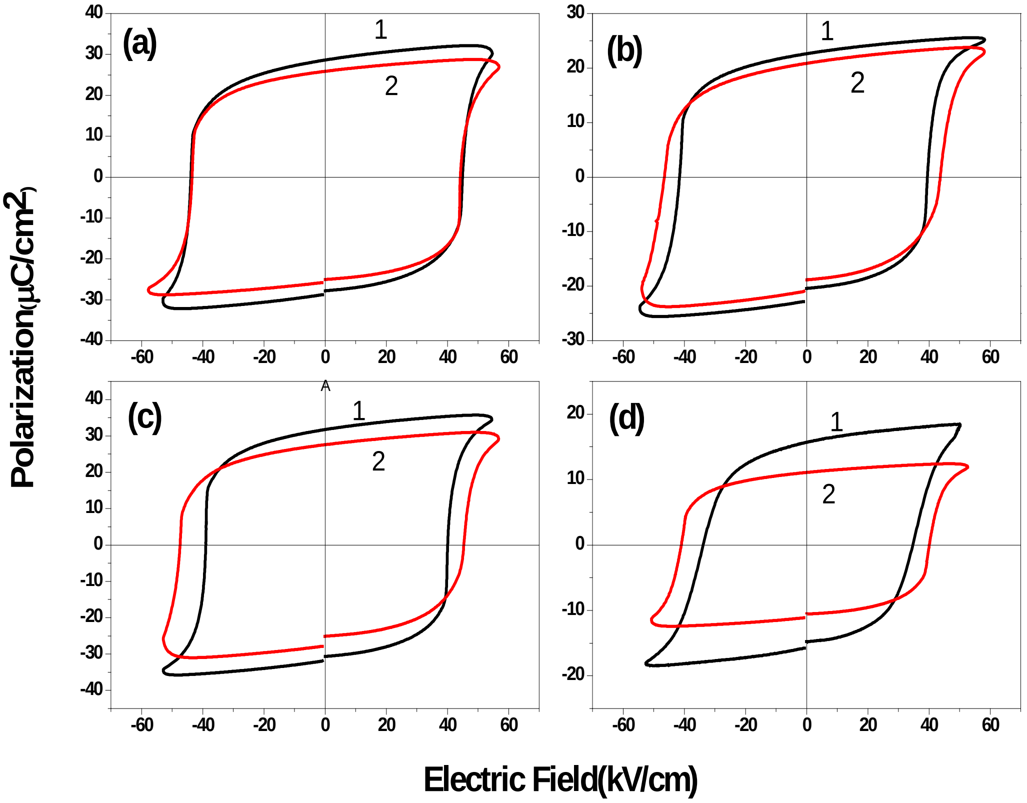

**Fig 4.22:** P-E hysteresis loops before (1) and after (2) $10^7$ cycles of the NBT-xBT (x=0.05, 0.06, 0.07, 0.08) ceramics.

## 4.9.2 Polarization Fatigue Study of NBT-xKNN Ceramics

Room temperature normalized polarization vs. number of cycle's plots at $10^5$Hz bipolar triangular pulses of the NBT-xKNN ceramic samples are shown in Fig. 4.23. There are various factors such as the formation of space charges, and point defects, which are responsible for such type of polarization loss. Space charge polarization is a common factor observed over most of the perovskite ceramics [47]. It is reported that formation of the domain is a fast process resulting in a domain pattern with extended space charge region near domain walls and is related with semiconductor properties. Within these space charge regions, a significant depolarization field is still present which could drive the much slower ionic charge carriers like oxygen vacancies thus providing fatigue according to the space charge mechanism [21]. Correlating with the fatigue mechanisms, it is observed that all the NBT-xKNN ceramic samples start showing the degradation of the polarization after 1.5x $10^6$ switching cycles. The relative polarization fatigue % (after $10^9$ cycles) of all the NBT-xKNN ceramic samples is given in Table 4.14.

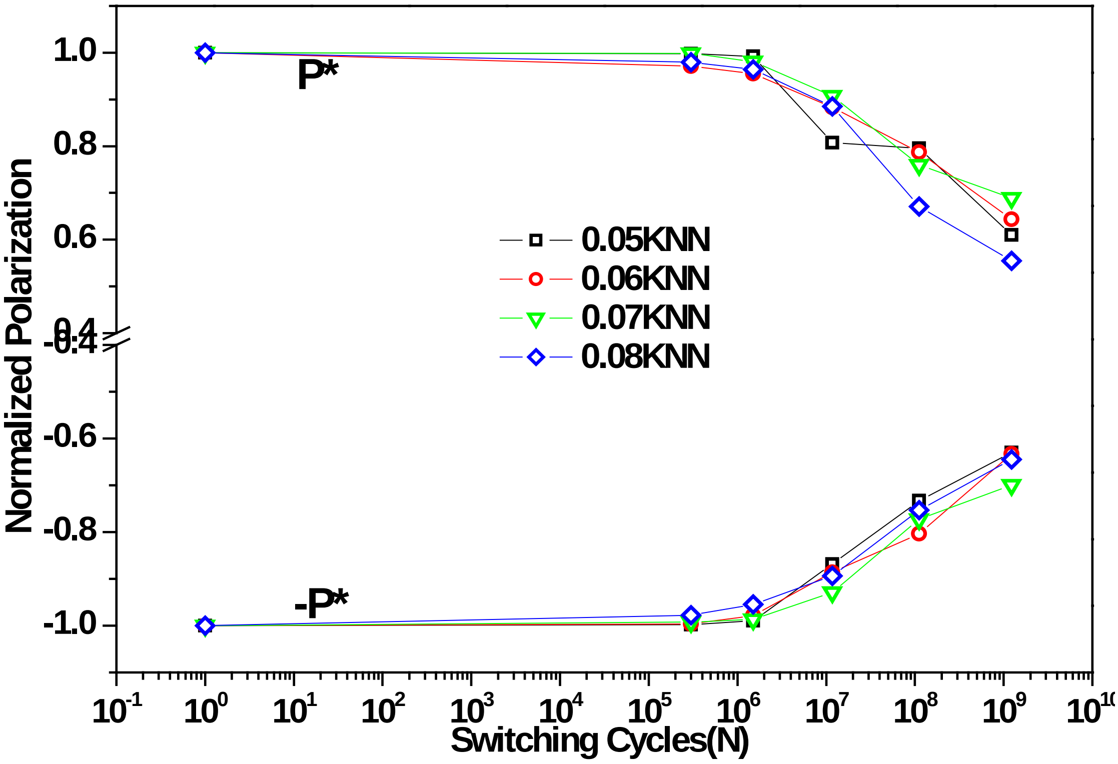

**Fig. 4.23:** Normalized polarization vs. number of cycles plots of NBT-xKNN (x=0.05, 0.06, 0.07, 0.08) ceramics.

**Table 4.14:** Relative polarization fatigue % (after $10^9$ cycle) of NBT-xKNN (x=0.05, 0.06, 0.07, 0.08) ceramics.

| **KNN content** | x = 0.05 | x = 0.06 | x = 0.07 | x = 0.08 |
|---|---|---|---|---|
| **Relative polarization fatigue %($10^9$ cycle)** | 38.01 | 36.20 | 30.57 | 67.69 |

Similar to NBT-xBT systems, P-E hysteresis loops of the NBT-xKNN ceramics, before electric fatigue, and after $10^7$ polarization switching cycles are compared and shown in Fig. 4.24(a-d). As can be seen from the P-E plots, there is a significant degradation of the saturation polarization. Furthermore, degradation in $P_r$ value is observed for all the samples and interestingly, the value of $E_c$ behaves exactly opposite i.e. increases negligibly for x=0.05, whereas for all other samples they are almost same compared to the loops before fatiguing. It has been suggested that the degradation of $P_r$ value after $10^7$ cycles can be due to the domain wall pinning at charged defects, which is the dominant degradation mechanism in perovskite ceramics [48]. The interaction of charged defects such as oxygen vacancies and charged domain walls can lead to local agglomeration of defects and the eventual stabilization of domains. Whereas, the formation and growth of microcracks in the near-electrode region can be associated with the increase in the $E_c$ value of the x=0.05 ceramics [49]. These cracks result from the high internal stress under bipolar cycling in a ferroelectric ceramic [50].

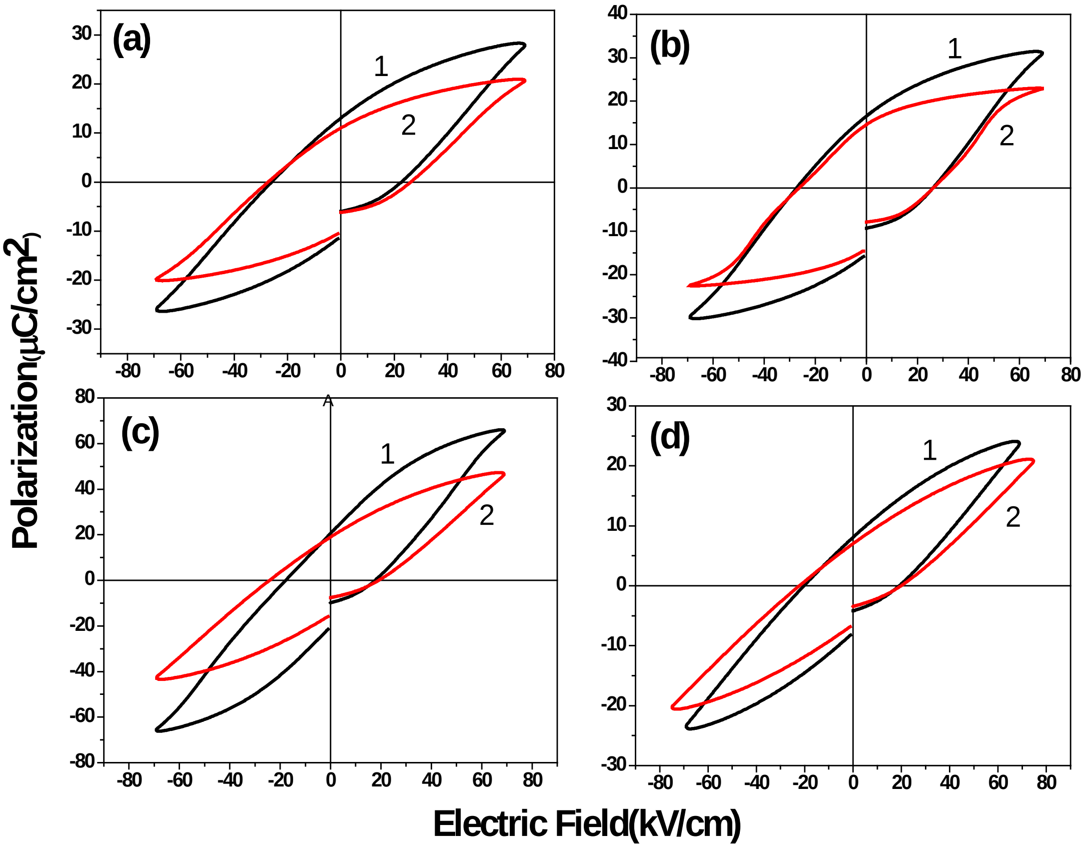

**Fig. 4.24:** P-E hysteresis loops before (1) and after (2) $10^7$ cycles of the NBT-xKNN ceramics with x = (a) 0.05, (b) 0.06 (c) 0.07 (d), and 0.08.

## References

[1] G. Picht, J. Töpfer, E. Hennig, Structural properties of $(Bi_{0.5}Na_{0.5})_{1-x}Ba_xTiO_3$ lead-free piezoelectric ceramics, Journal of the European Ceramic Society, 30 (2010) 3445-3453.

[2] A.B. Kounga, S.-T. Zhang, W. Jo, T. Granzow, J. Roedel, Morphotropic phase boundary in (1-x)$Bi_{0.5}Na_{0.5}TiO_3$-x$K_{0.5}Na_{0.5}NbO_3$ lead-free piezoceramics.

[3] P. Patnaik, Handbook of inorganic chemicals (McGraw-Hill, New York, 2002)

[4] C. Xu, D. Lin, K.W. Kwok, Structure, electrical properties and depolarization temperature of $(Bi_{0.5}Na_{0.5})TiO_3$–$BaTiO_3$ lead-free piezoelectric ceramics, Solid State Sciences, 10 (2008) 934-940.

[5] R. Ranjan, A. Dwivedi, Structure and dielectric properties of $(Na_{0.50}Bi_{0.50})_{1-x}Ba_xTiO_3$: $0 \leq x \leq 0.10$, Solid State Communications, 135 (2005) 394-399.

[6] E. Wu, POWD, an interactive program for powder diffraction data interpretation and indexing, Journal of Applied Crystallography, 22 (1989) 506-510.

[7] W.-C. Lee, C.-Y. Huang, L.-K. Tsao, Y.-C. Wu, Crystal Structure, dielectric and ferroelectric properties of $(Bi_{0.5}Na_{0.5})TiO_3$–$(Ba,Sr)TiO_3$ lead-free piezoelectric ceramics, Journal of Alloys and Compounds, 492 (2010) 307-312.

[8] M.N. Rahaman, Sintering of ceramics, CRC Press, Boca Raton, London; New York, (2008).

[9] B. Malic, J. Bernard, J. Holc, D. Jenko, M. Kosec, Alkaline-earth doping in (K,Na)NbO3 based piezoceramics, Journal of the European Ceramic Society, 25 (2005) 2707-2711.

[10] P. Laoratanakul, R. Yimnirun, S. Wongsaenmai, Phase formation and dielectric properties of bismuth sodium titanate–potassium sodium niobate ceramics, Current Applied Physics, 11 (2011) S161-S166.

[11] M. Masato, Y. Toshiaki, K. Koichi, H. Shin-ichi, Sinterability and Piezoelectric Properties of $(K,Na)NbO_3$ Ceramics with Novel Sintering Aid, Japanese Journal of Applied Physics, 43 (2004) 7159.

[12] L.A. Schmitt, J. Kling, M. Hinterstein, M. Hoelzel, W. Jo, H.J. Kleebe, H. Fuess, Structural investigations on lead-free $Bi_{1/2}Na_{1/2}TiO_3$-based piezoceramics, J Mater Sci, 46 (2011) 4368-4376.

[13] C. Ma, X. Tan, Dul, apos, E. kin, M. Roth, Domain structure-dielectric property relationship in lead-free (1−x)$(Bi_{1/2}Na_{1/2})TiO_3$-x$BaTiO_3$ ceramics, Journal of Applied Physics, 108 (2010) 104105.

[14] A.A. Bokov, Z.G. Ye, Recent progress in relaxor ferroelectrics with perovskite structure, J Mater Sci, 41 (2006) 31-52.

[15] X. Dai, A. DiGiovanni, D. Viehland, Dielectric properties of tetragonal lanthanum modified lead zirconate titanate ceramics, Journal of Applied Physics, 74 (1993) 3399-3405.

[16] Y. Man-Soon, M.J. Hyun, K. Sunuk, Spontaneous Micro-Macro Ferroelectric Domain Switching in $PbZrO_3$-doped $Pb(Ni_{1/3}Nb_{2/3})O_3$-$PbTiO_3$ System, Japanese Journal of Applied Physics, 34 (1995) 1916.

[17] W. Jo, S. Schaab, E. Sapper, L.A. Schmitt, H.-J. Kleebe, A.J. Bell, J. Rödel, On the phase identity and its thermal evolution of lead-free $(Bi_{1/2}Na_{1/2})TiO_3$-6 mol% $BaTiO_3$, Journal of Applied Physics, 110 (2011) 074106.

[18] K. Wang, A. Hussain, W. Jo, J. Rödel, Temperature-Dependent Properties of $(Bi_{1/2}Na_{1/2})TiO_3$–$(Bi_{1/2}K_{1/2})TiO_3$–$SrTiO_3$ Lead-Free Piezoceramics, Journal of the American Ceramic Society, 95 (2012) 2241-2247.

[19] K. Sakata, Y. Masuda, Ferroelectric and antiferroelectric properties of $(Na_{0.5}Bi_{0.5})$TiO3-$SrTiO_3$ solid solution ceramics, Ferroelectrics, 7 (1974) 347-349.

[20] A.R. Chaudhuri, A. Laha, S. Krupanidhi, Enhanced ferroelectric properties of vanadium doped bismuth titanate (BTV) thin films grown by pulsed laser ablation technique, Solid state communications, 133 (2005) 611-614.

[21] Y.A. Genenko, J. Glaum, M.J. Hoffmann, K. Albe, Mechanisms of aging and fatigue in ferroelectrics, Materials Science and Engineering: B, 192 (2015) 52-82.

[22] A.Z. Simões, M.A. Ramírez, E. Longo, J.A. Varela, Leakage current behavior of $Bi_{3.25}La_{0.75}Ti_3O_{12}$ ferroelectric thin films deposited on different bottom electrodes, Materials Chemistry and Physics, 107 (2008) 72-76.
[23] S.-T. Chang, J.Y.-m. Lee, Electrical conduction mechanism in high-dielectric-constant $(Ba_{0.5}Sr_{0.5})TiO_3$ thin films, Applied Physics Letters, 80 (2002) 655-657.
[24] A. Mukherjee, P. Victor, J. Parui, S. Krupanidhi, Leakage current behavior in pulsed laser deposited Ba $(Zr_{0.05}Ti_{0.95})O_3$ thin films, Journal of applied physics, 101 (2007) 034106.
[25] K.D. Matthews, X. Chen, D. Hao, W.J. Schaff, L.F. Eastman, GaN photovoltaic leakage current and correlation to grain size, Journal of Applied Physics, 108 (2010) 073105.
[26] X.J. Zheng, J.Y. Liu, J.F. Peng, X. Liu, Y.Q. Gong, K.S. Zhou, D.H. Huang, Effect of potassium content on electrostrictive properties of $Na_{0.5}Bi_{0.5}TiO_3$-based relaxor ferroelectric thin films with morphotropic phase boundary, Thin Solid Films, 548 (2013) 118-124.
[27] D. Fu, M. Endo, H. Taniguchi, T. Taniyama, S.-y. Koshihara, M. Itoh, Piezoelectric properties of lithium modified silver niobate perovskite single crystals, Applied Physics Letters, 92 (2008) 172905.
[28] B. Jaffe, W. R. Cook Jr.,H. Jaffe, Piezoelectric Ceramics, Academic Press London and New York, 1971.
[29] J.-N.L. J.-H. Oh, S.-s. Lee, K.-J. Lim, Relativity of Electric Field to Resonance Characteristics and Piezoelectric Constants of Modified PZT Ceramics, TEEM, 10 (2009).
[30] S.-T. Zhang, F. Yan, B. Yang, W. Cao, Phase diagram and electrostrictive properties of $Bi_{0.5}Na_{0.5}TiO_3$–$BaTiO_3$–$K_{0.5}Na_{0.5}NbO_3$ ceramics, Applied Physics Letters, 97 (2010) 122901.
[31] W. Liu, X. Ren, Large Piezoelectric Effect in Pb-Free Ceramics, Physical Review Letters, 103 (2009) 257602.
[32] Q. Zhang, X. Zhao, R. Sun, H. Luo, Crystal growth and electric properties of lead-free NBT-BT at compositions near the morphotropic phase boundary, Physica status solidi (a), 208 (2011) 1012-1020.
[33] N. Scarisoreanu, F. Craciun, V. Ion, S.Birjega, M. Dinescu, Structural and electrical characterization of lead-free ferroelectric $Na_{1/2}Bi_{1/2}TiO_3$–$BaTiO_3$ thin films obtained by PLD and RF-PLD, Applied Surface Science, 254 (2007) 1292-1297.
[34] F. Xu, S. Trolier-McKinstry, W. Ren, B. Xu, Z.-L. Xie, K.J. Hemker, Domain wall motion and its contribution to the dielectric and piezoelectric properties of lead zirconate titanate films, Journal of Applied Physics, 89 (2001) 1336-1348.
[35] S. Swain, P. Kumar, Dielectric, ferroelectric and bipolar electric field induced strain properties of MPB composition of NBT-xKNN system, Journal of Electroceramics, 32 (2014) 102-107.
[36] H. Fan, H.-E. Kim, Perovskite stabilization and electromechanical properties of polycrystalline lead zinc niobate–lead zirconate titanate, Journal of Applied Physics, 91 (2002) 317-322.
[37] A. Safari, R. K. Panda, V. F. Janas, Department of Ceramic science and Engineering, Rutgers University, Piscataway NJ 08855, USA.
[38] X.J. Lou, Polarization fatigue in ferroelectric thin films and related materials, Journal of Applied Physics, 105 (2009) 024101.
[39] J. F. Scott, Ferroelectric Memories, Springer-Verlag Berlin Heidelberg New York, 2000.
[40] X.J. Lou, J. Wang, Bipolar and unipolar electrical fatigue in ferroelectric lead zirconate titanate thin films: An experimental comparison study, Journal of Applied Physics, 108 (2010) 034104.
[41] C.-C. Chou, C.-S. Hou, T.-H. Yeh, Domain pinning behavior of ferroelectric $Pb_{1-x}Sr_xTiO_3$ ceramics, Journal of the European Ceramic Society, 25 (2005) 2505-2508.
[42] C. Verdier, D.C. Lupascu, J. Rödel, Stability of defects in lead–zirconate–titanate after unipolar fatigue, Applied Physics Letters, 81 (2002) 2596-2598.
[43] D. Lupascu, Fatigue of Ferroelectric Ceramics and Related Issues, Springer Berlin Heidelberg, 2004.

[44] W.L. Warren, K. Vanheusden, D. Dimos, G.E. Pike, B.A. Tuttle, Oxygen Vacancy Motion in Perovskite Oxides, Journal of the American Ceramic Society, 79 (1996) 536-538.
[45] E.A. Patterson, D.P. Cann, Bipolar piezoelectric fatigue of $Bi(Zn_{0.5}Ti_{0.5})O_3$-$(Bi_{0.5}K_{0.5})TiO_3$-$(Bi_{0.5}Na_{0.5})TiO_3$ Pb-free ceramics, Applied Physics Letters, 101 (2012) 042905.
[46] D. Dragan, Ferroelectric, dielectric and piezoelectric properties of ferroelectric thin films and ceramics, Reports on Progress in Physics, 61 (1998) 1267.
[47] O. Bidault, P. Goux, M. Kchikech, M. Belkaoumi, M. Maglione, Space-charge relaxation in perovskites, Physical Review B, 49 (1994) 7868-7873.
[48] Z. Luo, J. Glaum, T. Granzow, W. Jo, R. Dittmer, M. Hoffman, J. Rödel, Bipolar and Unipolar Fatigue of Ferroelectric BNT-Based Lead-Free Piezoceramics, Journal of the American Ceramic Society, 94 (2011) 529-535.
[49] J. Nuffer, D.C. Lupascu, A. Glazounov, H.-J. Kleebe, J. Rödel, Microstructural modifications of ferroelectric lead zirconate titanate ceramics due to bipolar electric fatigue, Journal of the European Ceramic Society, 22 (2002) 2133-2142.
[50] Z. Luo, T. Granzow, J. Glaum, W. Jo, J. Rödel, M. Hoffman, Effect of Ferroelectric Long-Range Order on the Unipolar and Bipolar Electric Fatigue in $Bi_{1/2}Na_{1/2}TiO_3$-Based Lead-Free Piezoceramics, Journal of the American Ceramic Society, 94 (2011) 3927-3933.

# Chapter 5

## *Dielectric, Piezoelectric and Ferroelectric Properties of the 2-Layered $SrBi_2Ta_2O_9$ based Ceramics*

### 5.1 Introduction

Bismuth layered perovskite materials are useful for memory-based applications because of their low leakage current, fatigue endurance, and good electrical characteristics [1-3]. Among the 2-layer layered perovskites, commonly called Aurivillius phases, $SrBi_2Nb_2O_9$, $SrBi_2Ta_2O_9$/SBT, $Bi_4Ti_3O_{12}$ and $SrBi_4Ti_4O_{15}$ are the well-known materials. Among these different materials, the electrical properties of the SBT system are known to be sensitive to composition variation, especially to the content of $Bi^{3+}$ or any other substitutions [4, 5]. In literature, the non-stoichiometric SBT and donor doped SBT systems were reported to show better dielectric and ferroelectric properties [6,7]. Therefore, among 2-layer layered perovskites, in the present work, $SrBi_2Ta_2O_9$/SBT, $Sr_{0.8}Bi_{2.15}Ta_2O_9$/$SB_{ex}T$ and $SrBi_2(Ta_{0.925}W_{0.075})_2O_9$/SBTW systems were selected and synthesized by solid state reaction route. The detail experimental procedure of their synthesis is explained in chapter 3. The dielectric, ferroelectric, leakage current, polarization fatigue, and the piezoelectric properties of these ceramic samples are investigated, compared and discussed in detail in this chapter.

### 5.2 Thermal Analysis

Fig 5.1 shows the DSC and TGA curves of ball milled and dried uncalcined precursor powder of SBT system. From RT to 1000$^oC$, the overall weight loss is ~ 10%. The observed weight loss around ~ 400$^oC$ can be associated with the evaporation of $CO_2$ and $O_2$ gases, resulting from the decomposition of strontium carbonate, bismuth oxide, and tantalum dioxide. The exothermic peak ~1000ºC in DSC plot with no substantial weight loss in TGA plot can be attributed to the phase formation of SBT system. As per this study, all the SBT based ceramics were calcined within the temperature range of 900-1100ºC.

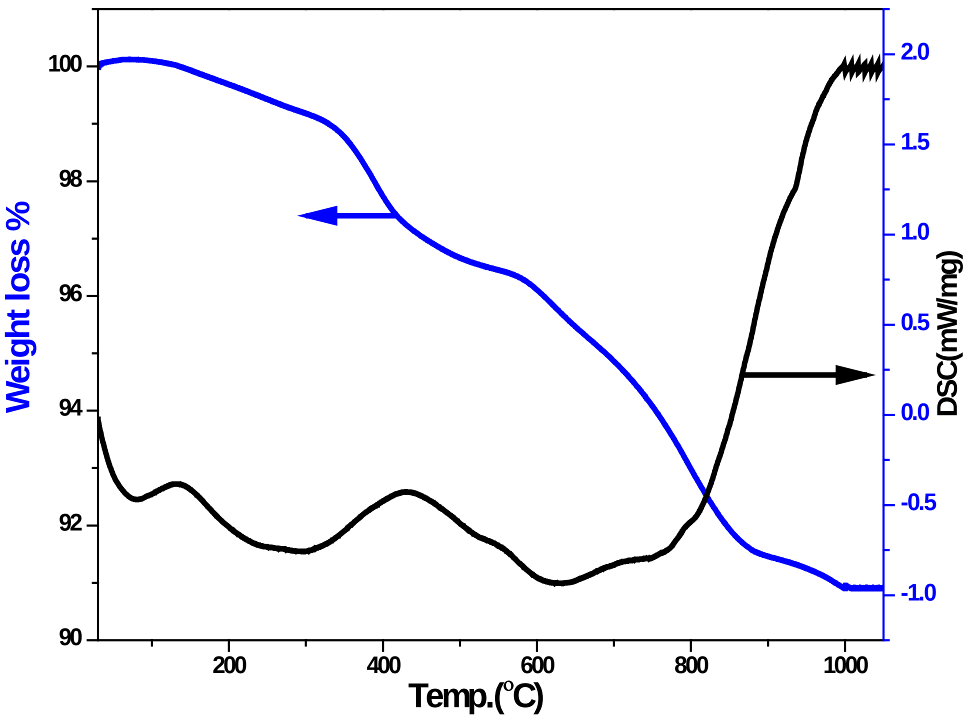

**Fig 5.1:** DSC and TGA curves of the ball milled uncalcined SBT powder.

## 5.3 XRD Analysis

The XRD patterns of the calcined powders of the SBT, $SB_{ex}T$ and SBTW ceramics are shown in Fig 5.2. Single layered perovskite phase is formed in all the SBT based samples, calcined at 1000°C. In XRD pattern of SBTW sample, very low intensity peaks at ~ $33^o$, $36^o$, $45^o$, $51^o$, and $52^o$ were observed. Those peaks are belongs to the segregated phase of W, which suggest about the solubility limit of $W^{6+}$ in the SBT system. Using diffraction angles (2θ) and intensity of the diffracted peaks, indexing of the XRD patterns was carried out using a computer program package 'POWD'[8]. For a probable crystal structure, the standard deviations, S.D. = ($d_{obs}$-$d_{cal}$) was considered to be minimum, The best agreement between the observed (obs) and the calculated (cal) interplanar spacing (d) was found, and the diffraction patterns of all the SBT based samples are assigned to the BLSFs (m=2) single phase with orthorhombic symmetry (space group $A2_1am$). There is a slight shift of XRD diffraction peak position towards the higher diffraction angle side of the SBTW ceramic samples. This can be associated with the decrease in lattice parameters of the SBTW ceramic samples, resulting from the substitution of smaller ionic radii $W^{6+}$ (0.60 Å) ions in place of $Ta^{5+}$ (0.64 Å) ions in the SBT system [9]. The lattice parameters of the SBT, $SB_{ex}T$ and SBTW ceramics are given in Table 5.1. There is also a slight reduction in the lattice parameters of the $SB_{ex}T$

ceramic samples, which can again be associated with the substitution of smaller ionic radii $Bi^{3+}$ (0.96 Å) ions in place of larger $Sr^{2+}$ (1.44 Å) ions site.

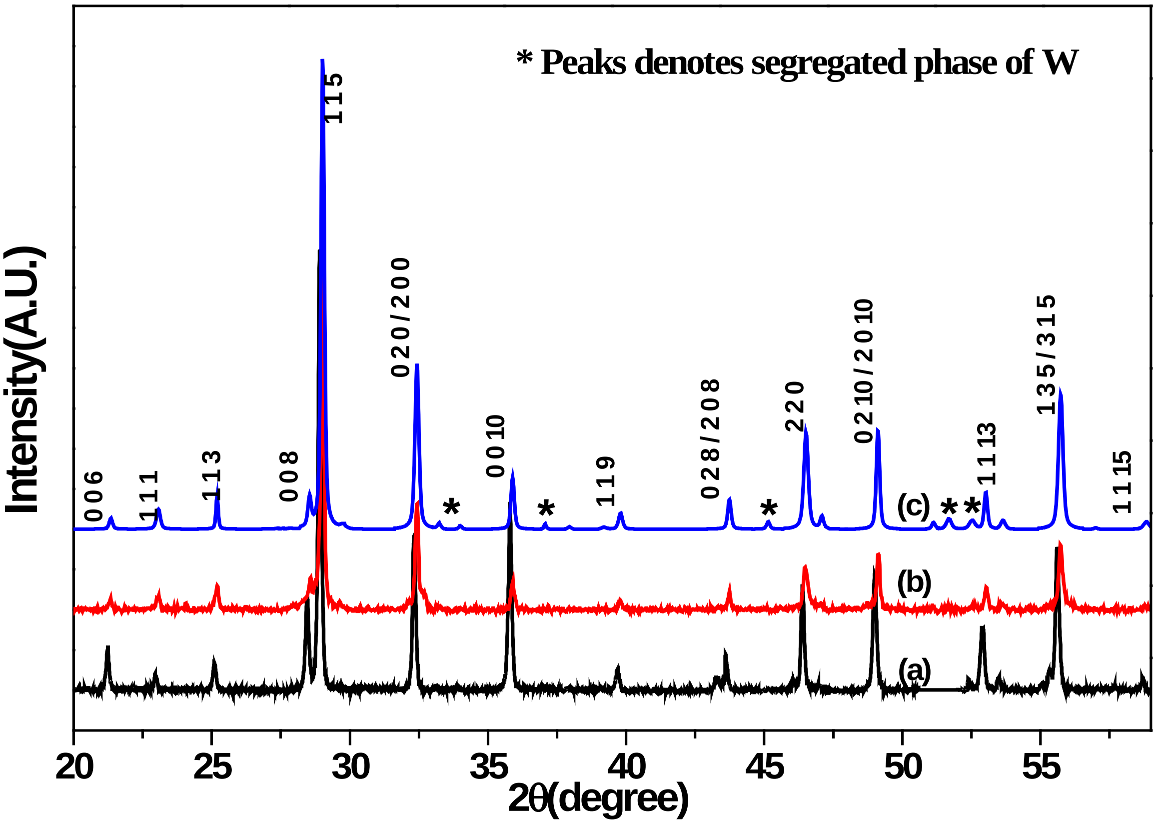

**Fig. 5.2:** XRD patterns of (a) SBT, (b) $SB_{ex}T$ and (c) SBTW samples calcined at 1000°C for 4hrs.

**Table 5.1**: Lattice parameters of SBT, $SB_{ex}T$ and SBTW ceramic samples.

| **Sample** | **lattice parameters** | | |
|---|---|---|---|
| | **a (Å)** | **b (Å)** | **c (Å)** |
| **SBT** | 5.8429(3) | 5.2126(1) | 25.2296(1) |
| **$SB_{ex}T$** | 5.8027(2) | 5.2025(1) | 25.2114(1) |
| **SBWT** | 5.8279(3) | 5.2121(3) | 25.2179(1) |

## 5.4 Microstructure and Density Study

Fig. 5.3 shows the variation of experimental density with sintering temperature of the (a) SBT, (b) $SB_{ex}T$ and (c) SBTW ceramic samples. The theoretical density of the pure SBT ceramic samples is ~8.93 g/cc [6]. For all the SBT based ceramic samples, the experimental density increases up to a particular sintering temperature and then starts decreasing. The decrease of experimental density at higher sintering temperature can be attributed to the volatilization of bismuth oxide in all the SBT based ceramic samples [10]. 1150°C, 1200°C and 1150°C are the optimized sintering temperatures of the SBT, $SB_{ex}T$ and SBTW ceramic samples, respectively. The relative density of the SBT, $SB_{ex}T$ and SBTW ceramic samples at optimized sintering temperatures was found to be ~95, 98 and 95%, respectively. Optimization of highest sintering temperature and detection of highest relative density of $SB_{ex}T$ ceramic samples suggest that excess bismuth content enhances the sintering temperature, which ultimately enhances the densification process.

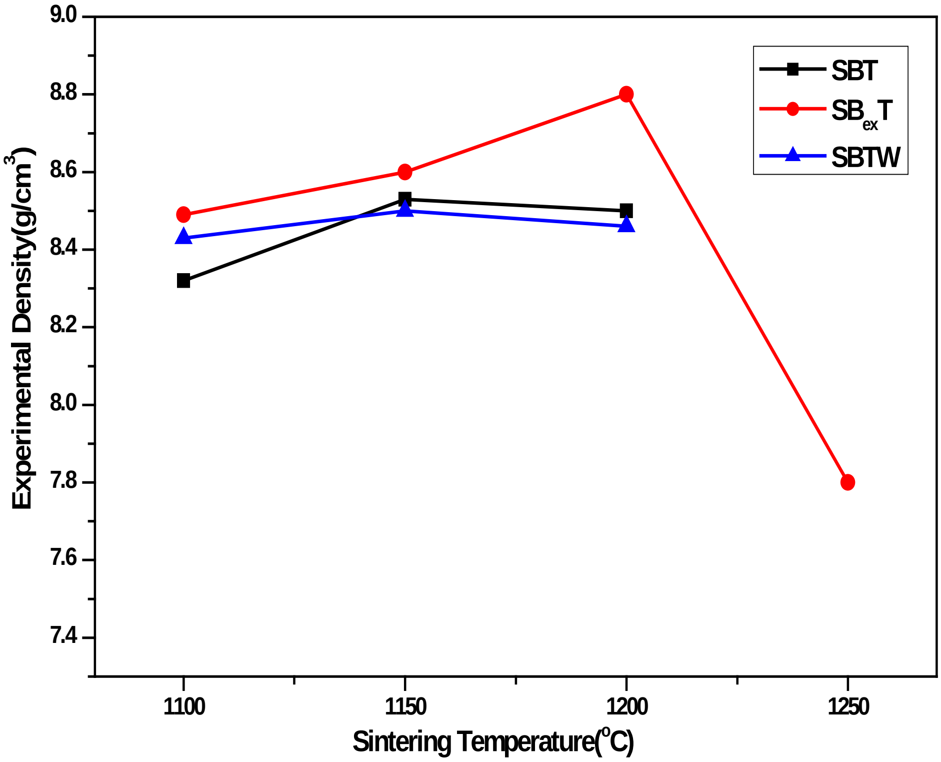

**Fig. 5.3:** Variation of experimental density with sintering temperature of the SBT, $SB_{ex}T$, and SBTW ceramics.

Fig. 5.4 shows the micrographs of the SBT based ceramic samples, sintered at different temperatures. A systematic study of the micrographs reveals that the pure SBT ceramic samples, sintered at 1100°C (Fig. 5.4(a)), show the round shaped grains, which changes to square shapes grains with increased average grain size at 1150°C (Fig. 5.4(b)) sintering temperature. However, densely packed microstructures of the $SB_{ex}T$ ceramic samples are observed at different sintering temperatures. At different sintering temperatures, randomly oriented plate-like grains are observed in the $SB_{ex}T$ ceramic samples. The average grain size of the $SB_{ex}T$ ceramic samples increases with the increase of sintering temperature, visible in Fig 5.4 (d)-(g). Among SBT, $SB_{ex}T$, and SBTW sintered ceramics, the maximum average grain size is observed in the $SB_{ex}T$ ceramic samples, sintered at 1200$^{o}$C. Fig 5.4(h)-(j) shows the highly non-uniform distribution of grains of SBTW ceramic samples, sintered at 1100$^{o}$C. This non-uniformity of grains of SBTW ceramic samples decreases at 1150$^{o}$C, optimized sintering temperature. The experimental density and microstructure of all the SBT based ceramics can be co-related to the volatility of the bismuth at higher sintering temperatures [10]. The average grain size and the experimental density of all the SBT based ferroelectric ceramics, sintered at different optimized temperatures are listed in Table 5.2.

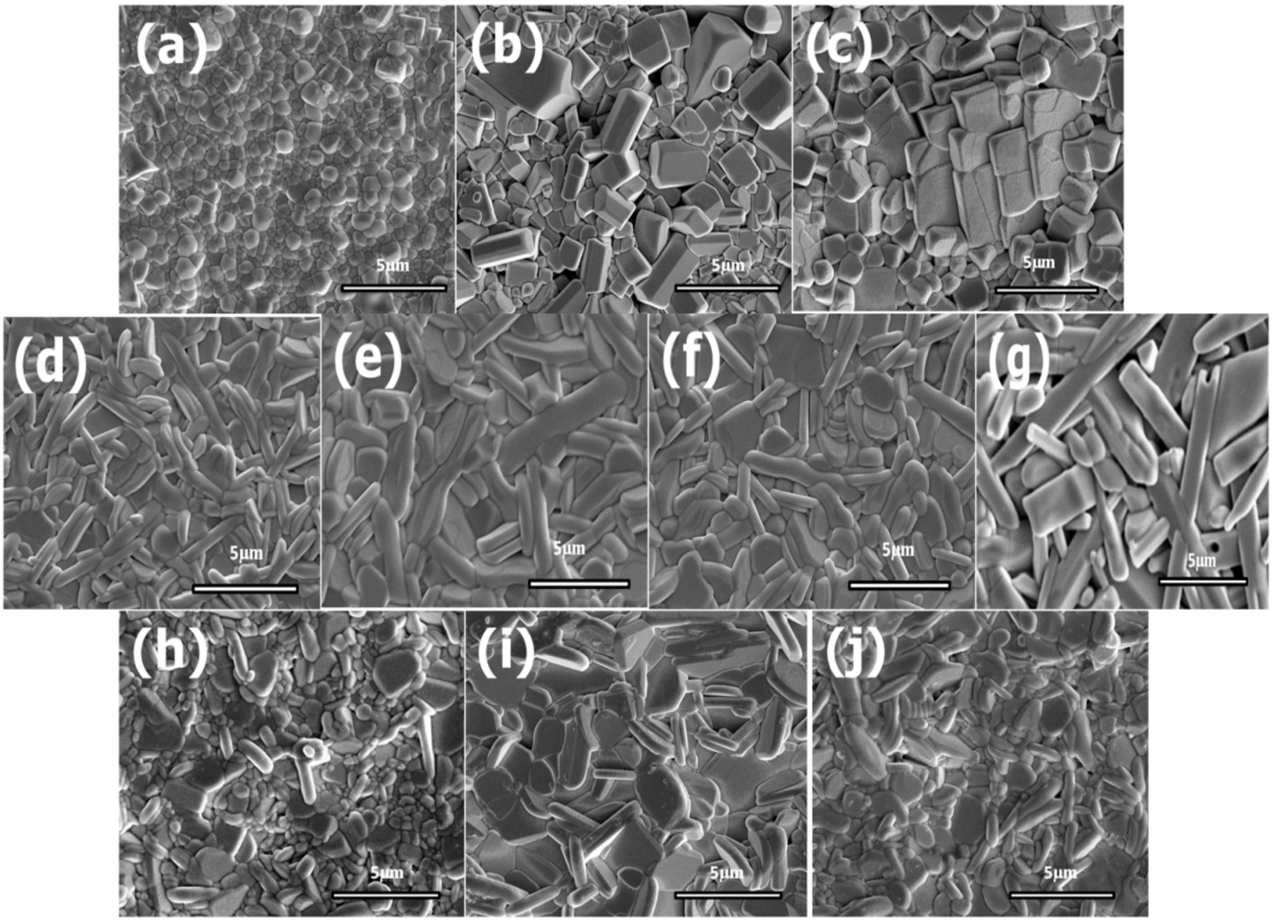

**Fig. 5.4:** SEM micrographs **(a-c)** of the SBT ceramic samples sintered at 1100, 1150 and 1200$^{o}$C, **(d-g)** of the $SB_{ex}T$ ceramic samples sintered at 1100, 1150, 1200 and 1250$^{o}$C, and **(h-j)** of the SBTW ceramic samples sintered at 1100, 1150 and 1200$^{o}$C temperatures.

**Table 5.2:** Average grain size and experimental density of SBT, $SB_{ex}T$, and SBTW ceramic samples.

| Sample | Sintering temperature($^oC$) | Average grain size (µm) | Experimental density(g/cc) |
|---|---|---|---|
| SBT | 1100 | 1.09 | 8.32 |
|  | 1150 | 2.52 | 8.53 |
|  | 1200 | 2.11 | 8.51 |
| $SB_{ex}T$ | 1100 | 1.46 | 8.49 |
|  | 1150 | 2.04 | 8.62 |
|  | 1200 | 3.65 | 8.87 |
|  | 1250 | 4.62 | 7.84 |
| SBTW | 1100 | 1.63 | 8.43 |
|  | 1150 | 2.84 | 8.52 |
|  | 1200 | 2.43 | 8.46 |

## 5.5 Dielectric Study

Fig 5.5(a-c) shows the variation of $\varepsilon_r$ (at different frequencies) vs. temperature of the SBT, $SB_{ex}T$ and SBTW ceramics, sintered at 1150$^o$C, 1200$^o$C and 1150$^o$C, respectively. These dielectric plots show the composition and doping effects on the dielectric properties of the SBT based ceramics. The dielectric constant of a ferroelectric material depends upon the composition, grain size, secondary phases, etc. [11]. From these dielectric plots, three important dielectric observations have been inferred. For the $SB_{ex}T$ and SBTW ceramics, there is (i) sharp ferroelectric-paraelectric transition at the Curie temperature ($T_c$), (ii) enhancement of the value of dielectric constant, and (iii) peak shifting towards higher temperature side compared to the pure SBT ceramic samples. Both the Bi-excess and $W^{6+}$-substituted samples exhibited sharp transition at their respective $T_c$. Whereas, in the pure SBT ceramic samples, a diffused phase transition behaviour is observed, which agrees with the earlier reports [12]. This suggests that there exist various regions in the pure SBT ceramic samples with various $T_c$ values [13], which can be attributed to the defects and poor microstructure. The low-frequency dispersion at high temperatures is also observed in the pure SBT ceramic samples, which may be associated with the defects in the samples such as oxygen vacancies, $V_o^{\bullet\bullet}$, created from the volatilization of $Bi_2O_3$ at high sintering temperatures [14-16]. Moreover, the diffuse phase transition nature near $T_c$ in the pure SBT system can be discussed on the basis of the cation disorder in the Sr-based bismuth layer-structured compounds. There is cation redistribution at A-sites in the perovskite lattice and at the bismuth sites in the $(Bi_2O_2)^{2+}$

layers in the $SrBi_2Ta_2O_9$ system [17]. The sharp transition of the $SB_{ex}T$ and SBTW ceramic samples suggests that the respective lattices maintain electrical neutrality [18, 19]. Unlike in the pure SBT system, the addition of excess bismuth in the $SB_{ex}T$ system and by the donor doping in the SBTW system, the oxygen vacancies, created at high sintering temperature, get compensated. Enhancement of $T_c$ value of the $SB_{ex}T$ ceramic samples can be associated with the creation of cation vacancies at the Sr site [18, 19]. The substitution of Bi at the Sr sites in the $SB_{ex}T$ ceramic samples can enhance the structural distortion of the $TaO_6$ octahedra, which ultimately lead to the higher $T_c$ value [19]. In the SBTW ceramic samples, the introduction of cation vacancies at the A-site possibly lead to an enhancement of ferroelectric structural distortion, which eventually increases the $T_c$ value [18, 20]. The introduction of cation vacancies can make the domain motion easier and lead to the increase of $\varepsilon_r$ value of both the $SB_{ex}T$ and SBTW systems compared to the pure SBT system [18, 20].

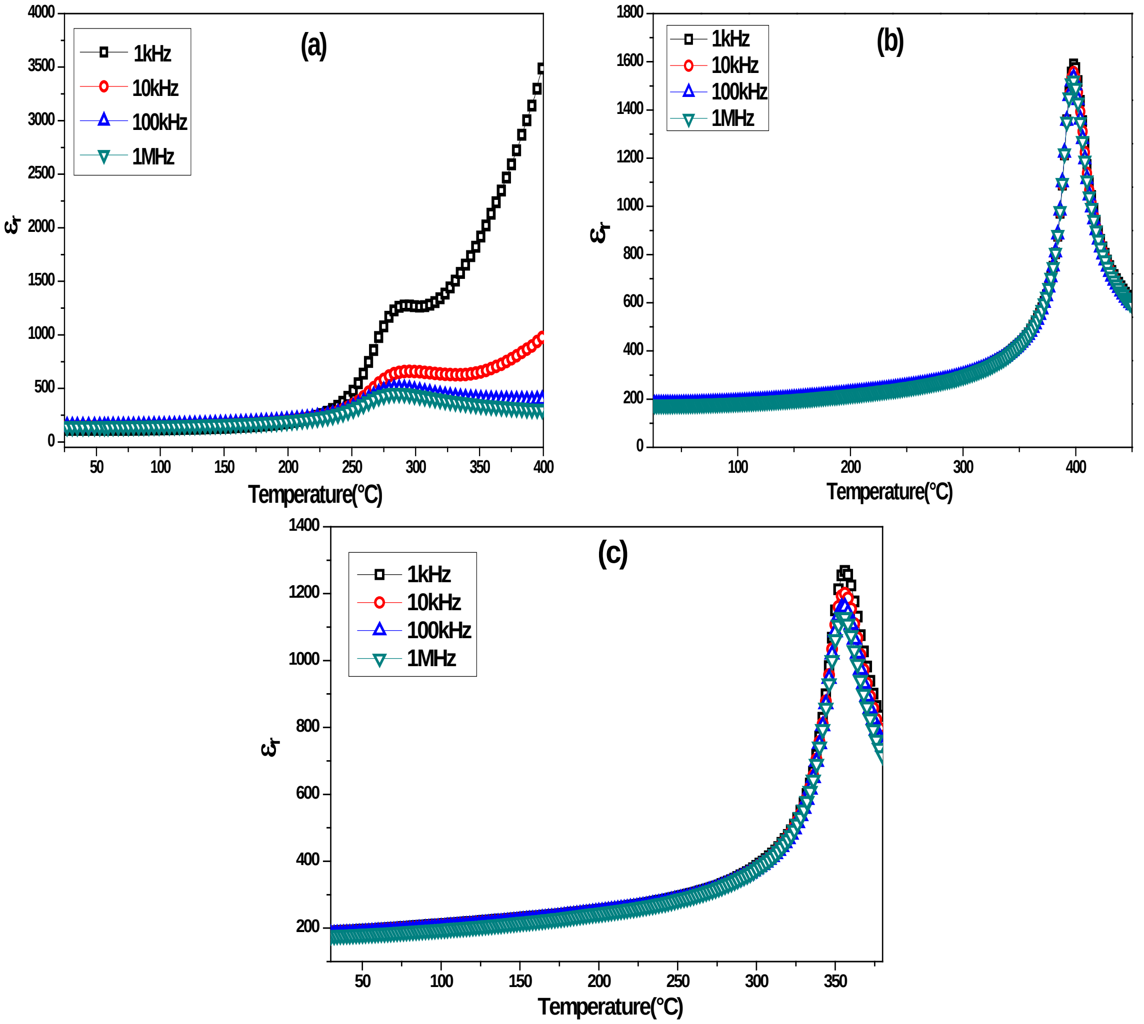

**Fig. 5.5:** Temperature dependence of $\varepsilon_r$ at different frequencies of (a) SBT, (b) $SB_{ex}T$ and (c) SBTW ceramics.

Temperature dependence of tanδ of all the SBT-based ceramic samples at different frequencies is shown in Fig 5.6(a-c). The temperature dependence of tanδ follows the similar variation as that of $\varepsilon_r$ vs. temperature plots of respective SBT based systems. There is a marginal decrease in the tanδ value compared to that of the pure SBT ceramic samples, which may be due to the reduction of oxygen vacancies during the processing of the $SB_{ex}T$ and SBTW ceramic samples [19]. The RT dielectric properties at 1 kHz frequency of all the SBT based ceramic samples are summarized in Table 5.3.

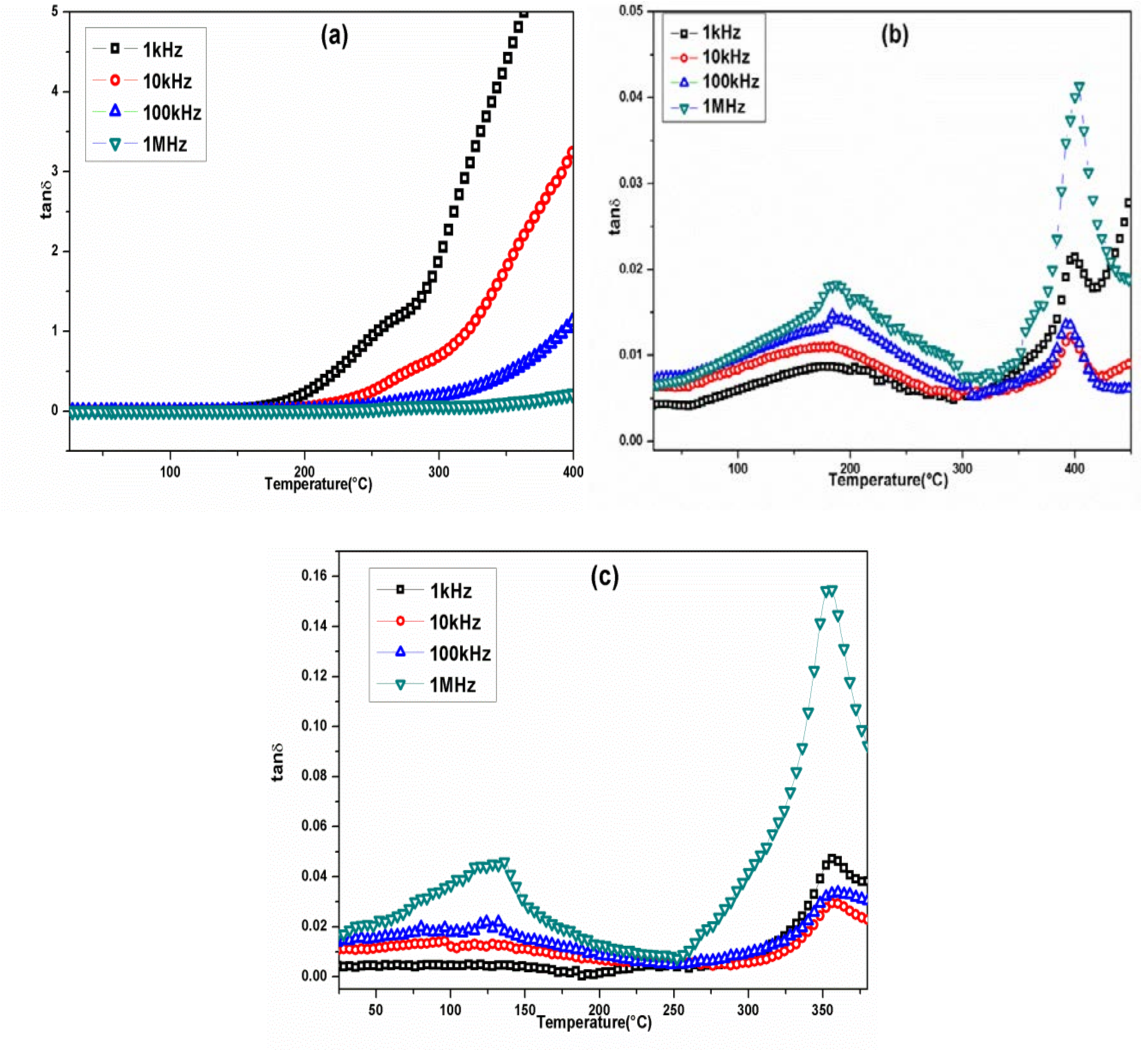

**Fig. 5.6:** Temperature dependence of tanδ at different frequencies of (a) SBT, (b) $SB_{ex}T$, and (c) SBTW ceramics.

**Table 5.3:** Dielectric properties (at 1 kHz frequency) Dielectric properties of SBT, $SB_{ex}T$, and SBTW ceramics.

| **Sample** | **$\varepsilon_r$ at RT** | **tanδ at RT** | **$T_c$ ( °C)** | **$\varepsilon_r$ at $T_c$** |
|---|---|---|---|---|
| SBT | 147 | 0.05 | 290 | 1260 |
| $SB_{ex}T$ | 182 | 0.04 | 398 | 1590 |
| SBTW | 187 | 0.04 | 356 | 1270 |

## 5.6 Leakage Current Analysis

Fig 5.7 shows the RT variation of leakage current density as a function of applied electric field of the SBT based ceramic samples. The observed RT leakage current density values of the SBT based ceramic samples are given in Table 5.4**.** The leakage current density of the $SB_{ex}T$ and SBTW ceramic samples decreased compared to the pure SBT ceramic samples, which suggest that there might be a relation between the electrical properties and the orientation of the grains. As reported earlier [21], because the $Bi_2O_2$ layers act as insulating layer, the resistivity along the c-axis is two to three orders of magnitude higher than that along the a–b plane in the Bi-layer systems. With excess $Bi^{3+}$ or with the $W^{6+}$-substitution in the SBT system, the c-axis orientation may start dominating, which increases the insulating nature of these samples and lead to the decrease in the leakage current density [22]. Both excess $Bi^{3+}$ and $W^{6+}$-substitution in the SBT system can act as donor impurities, which might have compensated the oxygen vacancy-related charge carriers and hence there is a decrease in the values of the leakage current of the $SB_{ex}T$ and SBTW ceramic samples compared to the pure SBT system [23]. As evident from the plots, the observed leakage current characteristics are almost symmetric in nature, which confirms the electrode independent nature of the samples [22]. In all the SBT based ceramics, at lower voltages, the leakage current can be attributed to the Ohmic-type conduction process and at high voltages the leakage current can be attributed to the space charge limited conduction process [24, 25]. However, a noticeable crest around +/- 20kV/cm can be related to the coercive fields ($E_c$) of the studied SBT based ceramic samples [26].

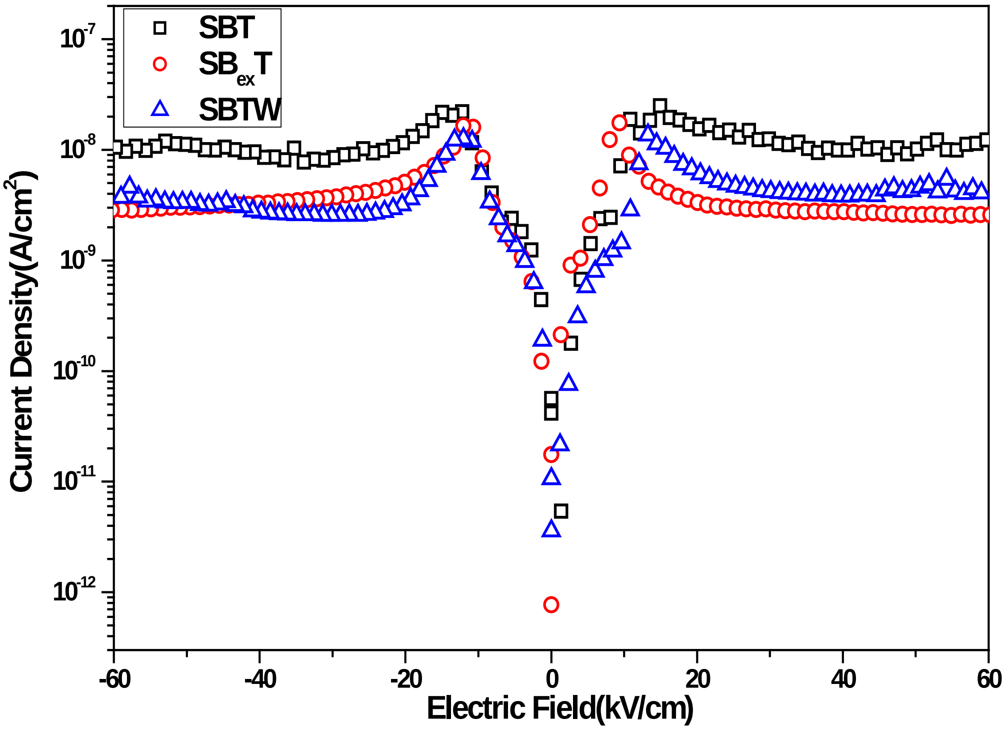

**Fig. 5.7:** Room temperature leakage current density vs. electric field plots of SBT, SB$_{ex}$T, and SBTW ferroelectric ceramics.

**Table 5.4:** RT leakage current properties of SBT, SB$_{ex}$T and SBTW ceramics at 60kV/cm.

| **Sample** | SBT | SB$_{ex}$T | SBTW |
|---|---|---|---|
| **Current density(A/cm$^2$)** | $1.09 \times 10^{-8}$ | $3.14 \times 10^{-9}$ | $3.81 \times 10^{-9}$ |

## 5.7 Piezoelectric Study

The S-E loops of the SBT based ceramic samples are shown in Fig. 5.8. It can be seen that the S-E loop is not well formed for the pure SBT ceramics whereas the typical butterfly shaped loops are observed for the SB$_{ex}$T and SBTW ceramic samples. The enhancement of the piezoelectric and ferroelectric properties can be attributed to the incorporation of higher valent ions accompanied by cation vacancies at the A-site of the SB$_{ex}$T and SBTW ceramic samples [27, 28]. The maximum strain % ~ 0.011 is observed in the SB$_{ex}$T ceramic samples. In order to find the piezoelectric coefficient ($d_{33}$) and electromechanical coupling factor ($k_p$), the SBT based ceramics were poled by Corona discharge technique. Among the SBT based ceramics, the maximum value of $k_p$ ~ 0.09 and $d_{33}$ ~ 24pC/N are observed in the SB$_{ex}$T ceramic samples, which can be attributed to its maximum grain size. Since, higher grain size enhances the domain wall mobility, which can result in better piezoelectric properties [27]. The values of strain%, $k_p$ and $d_{33}$ of all the studied SBT based ceramic samples are given in Table 5.5.

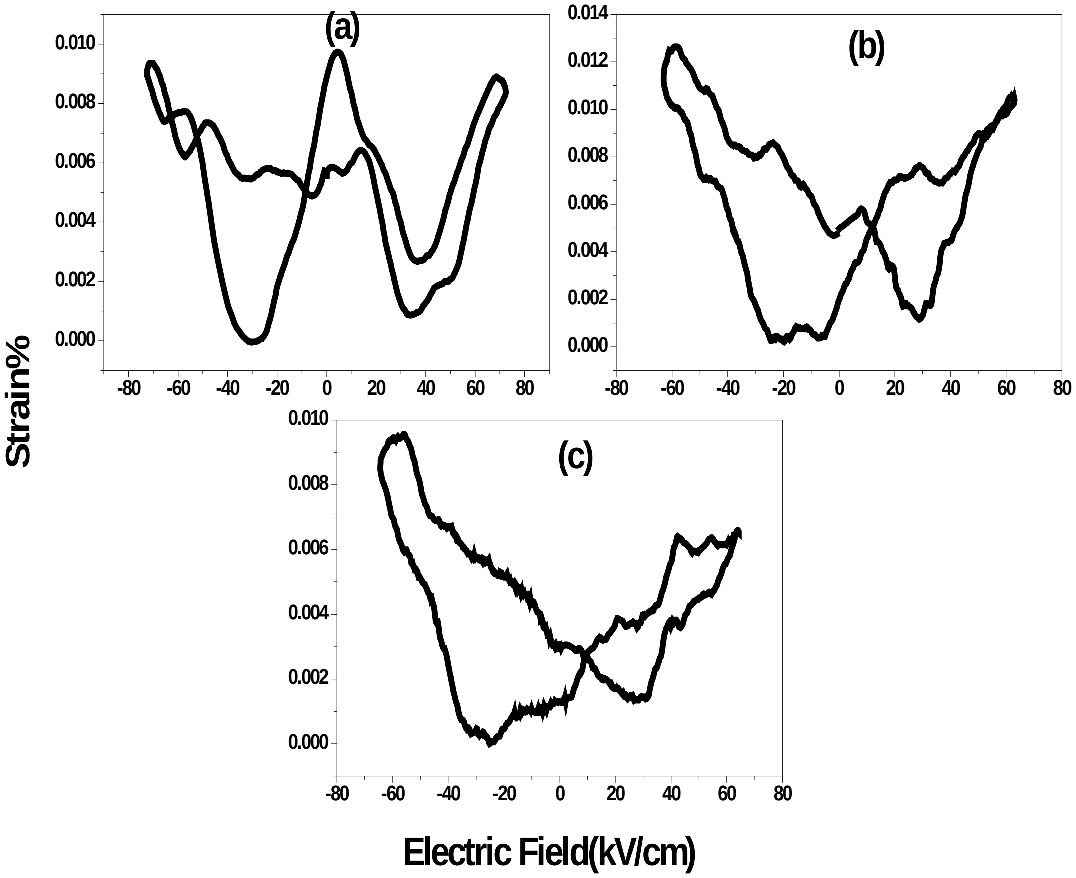

**Fig. 5.8:** S-E loops of (a) SBT, (b) $SB_{ex}T$ and (c) SBTW ferroelectric ceramics.

**Table 5.5:** Piezoelectric properties of SBT, $SB_{ex}T$ and SBTW ceramics.

| **Sample** | $k_p$ | $d_{33}$ **(pC/N)** | **Maximum strain%** |
|---|---|---|---|
| SBT | 0.06 | 16 | 0.008 |
| $SB_{ex}T$ | 0.09 | 24 | 0.011 |
| SBTW | 0.08 | 20 | 0.007 |

## 5.8 Ferroelectric Study

Fig. 5.9 shows the well-saturated P-E hysteresis loops of all the SBT based ceramic samples. Highest remnant polarization ($P_r$) ~ 8.07μC/cm$^2$ was observed in the SB$_{ex}$T ceramic samples. The enhanced polarization in the SB$_{ex}$T ceramic samples can be explained on the basis of larger distortion of its $TaO_6$ octahedra. As reported earlier, bismuth layer based $Sr^{2+}$-deficient and-$Bi^{3+}$-excess thin films show larger $P_r$ than that of the corresponding stoichiometric thin films [29, 30]. From the crystal structure study of the SBT system, the $TaO_2$ plane in the $TaO_6$ octahedra is reported as the densest plane, which can cause tensile stress in the $Bi_2O_2$ layers and compressive stress in the perovskite-like unit cells [31]. In the present case, the substitution of smaller $Bi^{3+}$ ions at the $Sr^{2+}$ ions site can cause compressive stress in the perovskite-like unit cell in the SB$_{ex}$T ceramic samples. This can result in the increased mismatch between the perovskite-like unit cells and the $Bi_2O_2$ layers in the SB$_{ex}$T samples, which will lead to larger distortion of the $TaO_6$ octahedra and hence enhanced ferroelectric properties [31]. The higher value of $P_r$ of the SBTW ceramic samples compared to the pure SBT samples can related to the formation of cation vacancies [32]. The substitution of $W^{6+}$ ions at the $Ta^{5+}$ ions site can suppress the concentration of the oxygen vacancies in the SBTW system. Further, the lowering of the number of oxygen vacancies in the SBTW system can reduce the domain walls pinning effect and enhanced $P_r$ and reduced $E_c$ values [32]. $P_r$ and $E_c$ values of the SBT, SB$_{ex}$T, and SBTW ceramics are given in Table 5.5.

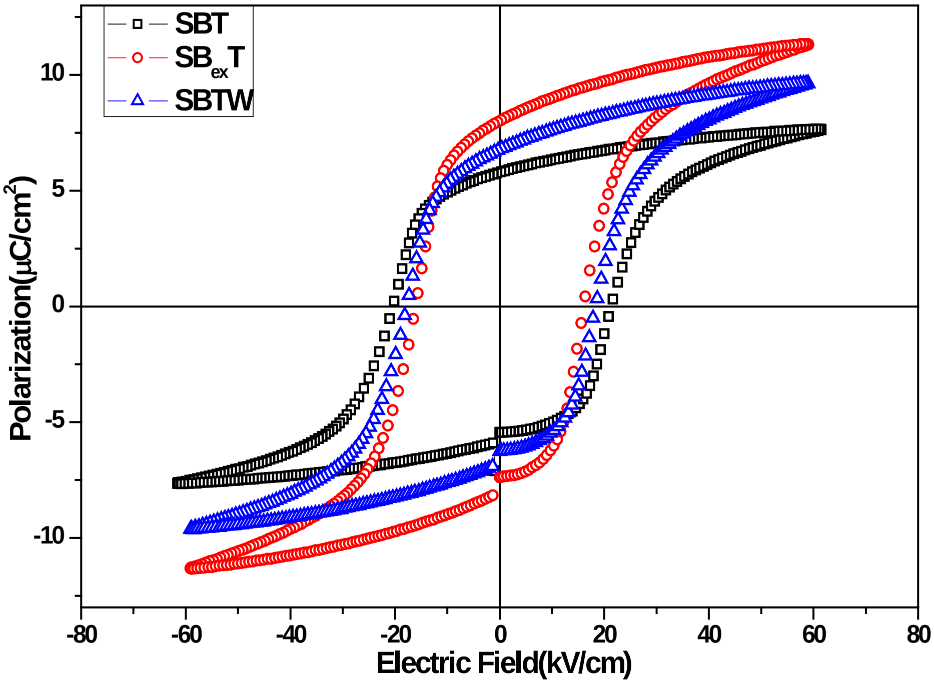

**Fig. 5.9:** P-E hysteresis loops of SBT, SB$_{ex}$T, and SBTW ferroelectric ceramics.

**Table 5.6:** Ferroelectric properties of SBT, $SB_{ex}T$ and SBTW ceramics.

| **Sample** | **$P_r$ (μC/cm$^2$)** | **$E_c$ (kV/cm)** |
|---|---|---|
| SBT | 5.89 | 20.70 |
| $SB_{ex}T$ | 8.07 | 15.18 |
| SBTW | 6.90 | 17.24 |

## 5.9 Polarization Fatigue Studies

Fig. 5.10 shows the normalized polarization vs. number of cycles (up to $10^9$) of the (a) SBT, (b) $SB_{ex}T$ and (c) SBTW ferroelectric ceramics with the applied external electric field measured at $10^5$Hz frequency. Under the present bipolar fatigue study, P* and -P* (μC/cm$^2$) are the switched polarization value in the positive and negative applied electric field cycles [33]. The switched polarizations are observed after 1, 300000, $1.5x10^6$, $1.17x10^7$, 1.11 $x10^8$, and $1.23x10^9$ electric field cycle numbers. All the SBT based ceramics follow the same trend of polarization variation without any substantial polarization decrease, which indicate that there is no/marginal degradation of the ferroelectric properties. Polarization fatigue% values after $10^9$ electric field cycles of the SBT, $SB_{ex}T$, and SBTW ceramics are given in Table 5.7. This measurement confirms that the SBT based materials are more or less inherently fatigue-free in nature. The fatigue-free behavior of the SBT based materials can be attributed to the charge compensation of the oxygen vacancies, created at high processing temperatures, by the self-regulated $(Bi_2O_2)^{2+}$ layers in the SBT based systems [2]. However, the self-regulating $(Bi_2O_2)^{2+}$ layers effect is not enough to explain the fatigue-free nature, since many BLSF's does not show fatigue-free behavior even if there is a presence of $(Bi_2O_2)^{2+}$ layers [34]. Fatigue-free nature of the studied ceramics is possible due to the oxygen stability by the combination of double perovskite layers and $(Bi_2O_2)^{2+}$ layers [34].

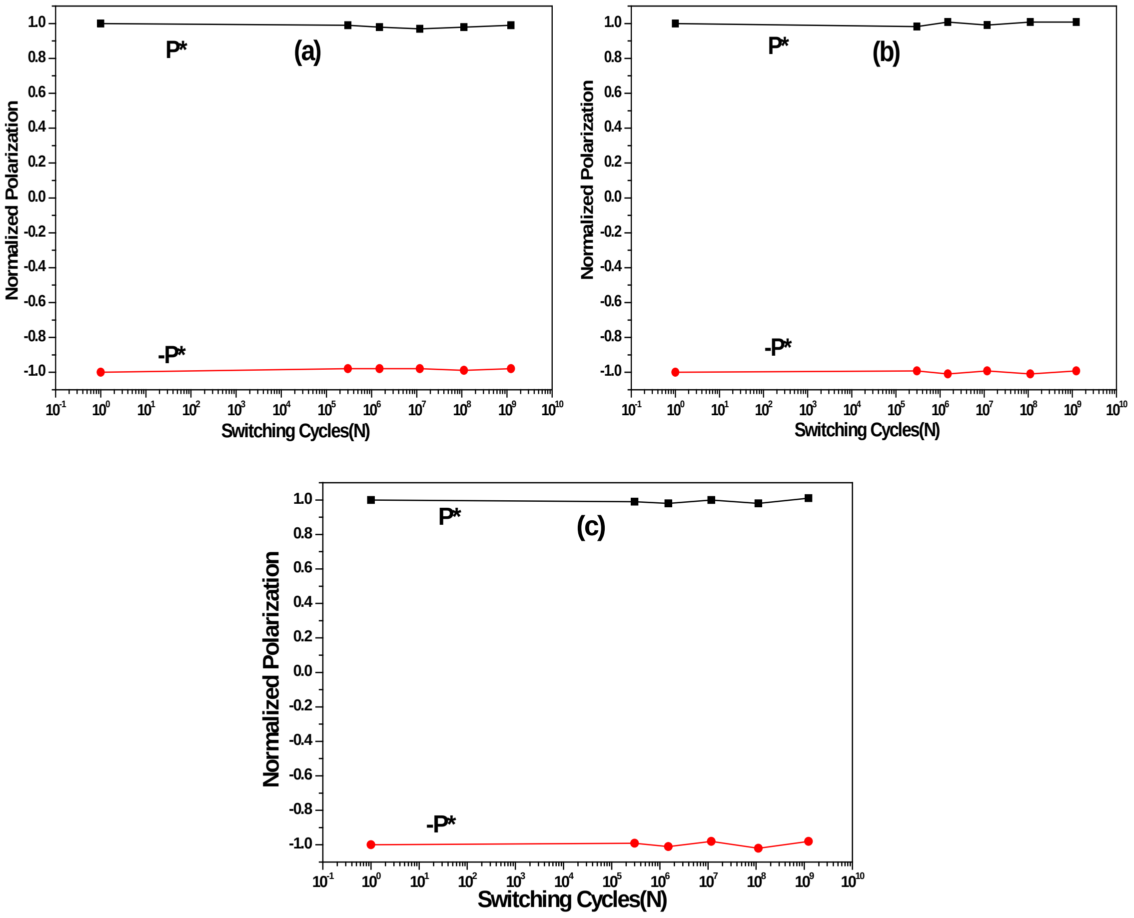

**Fig. 5.10:** Normalized polarization vs. number of cycles plots of (a) SBT, (b) SB$_{ex}$T and (c) SBTW ferroelectric ceramics.

**Table 5.7:** Polarization fatigue properties of SBT, SB$_{ex}$T and SBTW ceramics.

| **Sample** | SBT | SB$_{ex}$T | SBTW |
|---|---|---|---|
| **Relative polarization fatigue % (10$^9$ cycle)** | 1.56 | 0.86 | 1.46 |

## References

[1] J.F. Scott, C.A. Paz De Araujo, Ferroelectric memories, Science (New York, N.Y.), 246 (1989) 1400-1405.

[2] C.A.P. de Araujo, J.D. Cuchiaro, L.D. McMillan, M.C. Scott, J.F. Scott, Fatigue-free ferroelectric capacitors with platinum electrodes, Nature, 374 (1995) 627-629.

[3] S.B. Desu, D.P. Vijay, Novel fatigue-free layered structure ferroelectric thin films, Materials Science and Engineering: B, 32 (1995) 75-81.

[4] H. Bachhofer, F. Hintermaier, M. Hauf, O. Spindler, T. Haneder, C. Dehm, H. von Philipsborn, R. Waser, Effect of Film Composition on Low-Temperature Processing of SBT Deposited by MOCVD, MRS Online Proceedings Library, 596 (1999) null-null.

[5] J. Ricote, M.L. Calzada, A. González, C. Ocal, Microstructural Studies on the Low-Temperature Crystallization Process of Strontium Bismuth Tantalate Thin Films, Journal of the American Ceramic Society, 87 (2004) 138-143.

[6] R. Aoyagi, H. Takeda, S. Okamura, T. Shiosaki, Ferroelectric and piezoelectric properties of bismuth layered-structure ferroelectric (Sr,Na,Bi)$Bi_2Ta_2O_9$ ceramics, Materials Science and Engineering: B, 116 (2005) 156-160.

[7] I. Coondoo, N. Panwar, A.K. Jha, Effect of sintering temperature on the structural, dielectric and ferroelectric properties of tungsten substituted SBT ceramics, Physica B: Condensed Matter, 406 (2011) 374-381.

[8] E. Wu, POWD, an interactive program for powder diffraction data interpretation and indexing, Journal of Applied Crystallography, 22 (1989) 506-510.

[9] R.D. Shannon, C.T. Prewitt, Effective ionic radii in oxides and fluorides, Acta Crystallographica Section B, 25 (1969) 925-946.

[10] A. Simões, G. da Costa, M. Ramirez, J.A. Varela, E. Longo, Effect of the excess of bismuth on the morphology and properties of the $BaBi_2Ta_2O_9$ ceramics, Materials Letters, 59 (2005) 656-661.

[11] R.R. Das, P. Bhattacharya, W. Pérez, R.S. Katiyar, Effect of Ca on structural and ferroelectric properties of $SrBi_2Ta_2O_9$ and $SrBi_2Nb_2O_9$ thin films, Ceramics International, 30 (2004) 1175-1179.

[12] I. Coondoo, A.K. Jha, S.K. Agarwal, Enhancement of dielectric characteristics in donor doped Aurivillius $SrBi_2Ta_2O_9$ ferroelectric ceramics, Journal of the European Ceramic Society, 27 (2007) 253-260.

[13] K. Takemura, T. Noguchi, T. Hase, Y. Miyasaka, Dielectric anomaly in strontium bismuth tantalate thin films, Applied Physics Letters, 73 (1998) 1649-1651.

[14] B.H. Park, S.J. Hyun, S.D. Bu, T.W. Noh, J. Lee, H.-D. Kim, T.H. Kim, W. Jo, Differences in nature of defects between $SrBi_2Ta_2O_9$ and $Bi_4Ti_3O_{12}$, Applied Physics Letters, 74 (1999) 1907-1909.

[15] T. Friessnegg, S. Aggarwal, R. Ramesh, B. Nielsen, E.H. Poindexter, D.J. Keeble, Vacancy formation in (Pb,La)(Zr,Ti)$O_3$ capacitors with oxygen deficiency and the effect on voltage offset, Applied Physics Letters, 77 (2000) 127-129.

[16] C. Ang, Z. Yu, L.E. Cross, Oxygen-vacancy-related low-frequency dielectric relaxation and electrical conduction in Bi:$SrTiO_3$, Physical Review B, 62 (2000) 228-236.

[17] S. M. Blake, M.J. Falconer, M. McCreedy, P. Lightfoot, Cation disorder in ferroelectric Aurivillius phases of the type $Bi_2ANb_2O_9$(A=Ba, Sr, Ca), Journal of Materials Chemistry, 7 (1997) 1609-1613.

[18] Y. Wu, S.J. Limmer, T.P. Chou, C. Nguyen, G. Cao, Influence of tungsten doping on dielectric properties of strontium bismuth niobate ferroelectric ceramics, Journal of Materials Science Letters, 21 (2002) 947-949.

[19] Y. Wu, C. Nguyen, S. Seraji, M.J. Forbess, S.J. Limmer, T. Chou, G. Cao, Processing and Properties of Strontium Bismuth Vanadate Niobate Ferroelectric Ceramics, Journal of the American Ceramic Society, 84 (2001) 2882-2888.

[20] T. Sadayuki, T. Masao, Effects of Impurities on the Mechanical Quality Factor of Lead Zirconate Titanate Ceramics, Japanese Journal of Applied Physics, 11 (1972) 31.

[21] S.K. Kim, M. Miyayama, H. Yanagida, Electrical anisotropy and a plausible explanation for dielectric anomaly of $Bi_4Ti_3O_{12}$ single crystal, Materials Research Bulletin, 31 (1996) 121-131.

[22] A.R. Chaudhuri, A. Laha, S.B. Krupanidhi, Enhanced ferroelectric properties of vanadium doped bismuth titanate (BTV) thin films grown by pulsed laser ablation technique, Solid State Communications, 133 (2005) 611-614.

[23] Y.-M. Kan, G.-J. Zhang, P.-L. Wang, Y.-B. Cheng, Preparation and properties of neodymium-modified bismuth titanate ceramics, Journal of the European Ceramic Society, 28 (2008) 1641-1647.

[24] S.-T. Chang, J.Y.-m. Lee, Electrical conduction mechanism in high-dielectric-constant $(Ba_{0.5}Sr_{0.5})TiO_3$ thin films, Applied Physics Letters, 80 (2002) 655-657.

[25] A. Mukherjee, P. Victor, J. Parui, S. Krupanidhi, Leakage current behavior in pulsed laser deposited Ba $(Zr_{0.05}Ti_{0.95})O_3$ thin films, Journal of applied physics, 101 (2007) 034106.

[26] N. Tsutsumi, T. Kitano, K. Kinashi, W. Sakai, Ferroelectric Switching of Vinylidene and Trifluoroethylene Copolymer Thin Films on Au Electrodes Modified with Self-Assembled Monolayers, Materials, 7 (2014) 6367.

[27] H.T. Martirena, J.C. Burfoot, Grain-size effects on properties of some ferroelectric ceramics, Journal of Physics C: Solid State Physics, 7 (1974) 3182.

[28] C. Fujioka, R. Aoyagi, H. Takeda, S. Okamura, T. Shiosaki, Effect of non-stoichiometry on ferroelectricity and piezoelectricity in strontium bismuth tantalate ceramics, Journal of the European Ceramic Society, 25 (2005) 2723-2726.

[29] A. Tsutomu, S. Nobuyuki, Y. Tadashi, O. Katsumi, Preparation of Bi-Based Ferroelectric Thin Films by Sol-Gel Method, Japanese Journal of Applied Physics, 34 (1995) 5096.

[30] N. Takehiro, H. Takashi, M. Yoichi, Analysis of the Dependence of Ferroelectric Properties of Strontium Bismuth Tantalate (SBT) Thin Films on the Composition and Process Temperature, Japanese Journal of Applied Physics, 35 (1996) 4900.

[31] Y. Shimakawa, Y. Kubo, Y. Nakagawa, T. Kamiyama, H. Asano, F. Izumi, Crystal structures and ferroelectric properties of $SrBi_2Ta_2O_9$ and $Sr_{0.8}Bi_{2.2}Ta_2O_9$, Applied Physics Letters, 74 (1999) 1904-1906.

[32] I. Coondoo, N. Panwar, Enhanced Dielectric and Ferroelectric Properties of Donor ($W^{6+}$, $Eu^{3+}$) Substituted SBT Ferroelectric Ceramics, the book "Ferroelectrics" ISBN 978-953-307-439-9, InTech, (2010) pp-241-242.

[33] X.J. Lou, J. Wang, Bipolar and unipolar electrical fatigue in ferroelectric lead zirconate titanate thin films: An experimental comparison study, Journal of Applied Physics, 108 (2010) 034104.

[34] B. Park, B. Kang, S. Bu, T. Noh, J. Lee, H. Kim, T. Kim, Origins for fatigue-free properties of Bi-layered perovskite materials, Journal-Korean physical society, 35 (1999) s1306-s1309.

# Chapter 6

## *Dielectric, Piezoelectric and Ferroelectric Properties of $SB_{ex}T$ modified NBT-xBT and NBT-xKNN (x=0.07) Ceramics*

## 6.1 Introduction

In the NBT-xBT and NBT-xKNN systems, the respective MPB existed at x=0.07 composition (reported in chapter 4). On the other hand, $SB_{ex}T$ system showed overall improved electrical, ferroelectric, and polarization fatigue along with lower leakage current properties (reported in chapter 5). Compared to the $SB_{ex}T$ system, the leakage current density is higher and polarization fatigue behavior is poor of the MPB compositions of the NBT-xBT and NBT-xKNN systems, respectively. Modification of the MPB compositions of the NBT-xBT and NBT-xKNN systems with $SB_{ex}T$ system can combine the excellent ferroelectric properties of the perovskite phase with the anti-polarization fatigue and low leakage properties. In this chapter, a systematic study of the dielectric, leakage current density, ferroelectric, piezoelectric and polarization fatigue properties of the synthesized $(1-\phi)(0.93Na_{0.5}Bi_{0.5}TiO_3-0.07BaTiO_3/NBT-BT)-\phi Sr_{0.8}Bi_{2.15}Ta_2O_9$ and $(1-\phi)(0.93Na_{0.5}Bi_{0.5}TiO_3-0.07K_{0.5}Na_{0.5}NbO_3/NBT-KNN)-\phi Sr_{0.8}Bi_{2.15}Ta_2O_9$ ($\phi$= 2, 4, 8, 12, 16 wt. %) ceramics is presented.

## 6.2 XRD Study

In the following subsections, the XRD study of the sintered $(1-\phi)(NBT-BT)-\phi SB_{ex}T$ and $(1-\phi)(NBT-KNN)-\phi SB_{ex}T$ ($\phi$= 0, 2, 4, 8, 12, 16 wt. %) ceramics are given.

### 6.2.1 XRD Study of the $(1-\phi)(NBT-BT)-\phi SB_{ex}T$ Ceramics

XRD pattern of the MPB composition (for $\phi$= 0) of the NBT-xBT system shows the single perovskite phase with pseudo-cubic distortion (explained in chapter 4 and shown in Fig. 6.1(a)), whereas, Fig. 6.1(b) shows the development of single phase layered perovskite with orthorhombic crystal structure of the $SB_{ex}T$ system. Fig. 6.1 (c) shows the XRD patterns of the sintered $(1-\phi)$ $(NBT-BT)-\phi SB_{ex}T$ for $\phi$= 2, 4, 8, 12, 16 wt. % ceramic samples. Fig. 6.1 (c) confirms the presence of both the $SB_{ex}T$ and the NBT-BT ceramic phases and the XRD peaks intensity of the $SB_{ex}T$ phase increases with the increase of its wt.% in the (1-ϕ)(NBT-BT)-ϕ$SB_{ex}T$ system. The XRD peaks of the NBT-BT and $SB_{ex}T$ phases are marked with 'Δ' and '#' symbols. Later, the existence of both $SB_{ex}T$ and NBT-BT phases in the (1-ϕ)(NBT-BT)-ϕ$SB_{ex}T$ ceramics is also confirmed from the SEM micrograph study. With the increase of $SB_{ex}T$ content in the (1-ϕ)(NBT-BT)-ϕ$SB_{ex}T$ system, some unwanted secondary phase XRD peaks (marked as *) starts appearing. This suggests the possible reaction between the NBT-BT and $SB_{ex}T$ phases at high sintering temperature [1].

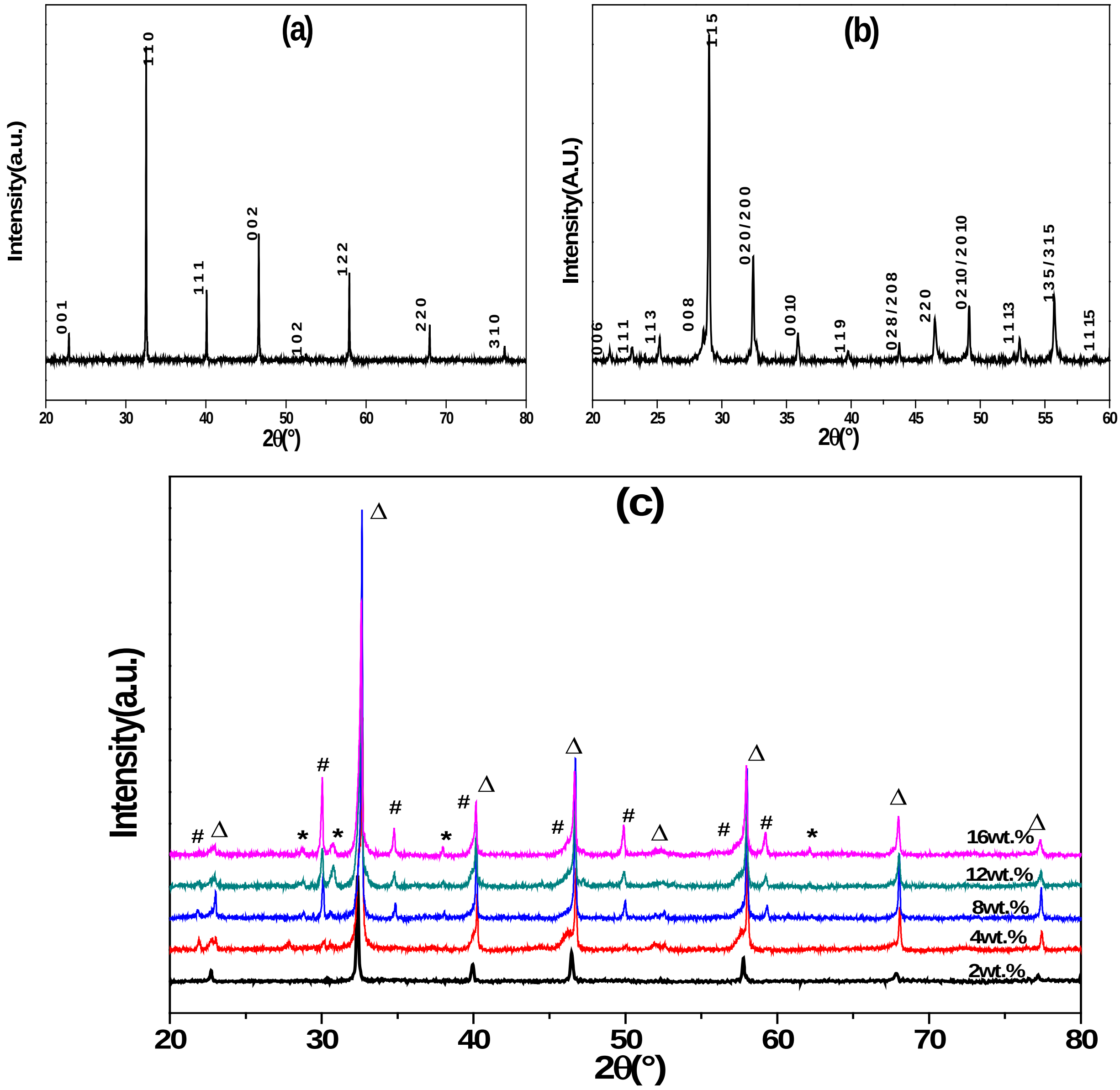

**Fig. 6.1:** X-ray diffraction patterns of (a) MPB composition of NBT-BT, (b) $SB_{ex}T$ and (c) (1-ϕ) (NBT-BT)-ϕ $SB_{ex}T$ (ϕ= 2, 4, 8, 12, 16 wt. %) ceramics.

### 6.2.2 XRD Study of the (1-$\phi$)(NBT-KNN)-$\phi$SB$_{ex}$T Ceramics

Fig. 6.2 shows the RT X-ray diffraction (XRD) patterns of the sintered (1-$\phi$)(NBT-KNN)-$\phi$SB$_{ex}$T ($\phi$= 0, 2, 4, 8, 12, 16 wt. %) ceramics, whereas the inset figure is for $\phi$= 0 wt. %. These XRD patterns show the presence of both the NBT-KNN and the SB$_{ex}$T phases. The existence of the NBT-KNN (marked as Δ) and SB$_{ex}$T (marked as #) phases in the XRD pattern separately suggest the possibilities of affecting each other properties. Moreover, some impurity peaks (marked as *) are also detected in the XRD patterns of the (1-$\phi$)(NBT-KNN)-$\phi$SB$_{ex}$T ceramics, which corresponds to the pyrochlore/intermediate phases [1]. Later, the existence of both SB$_{ex}$T and NBT-KNN phases in the (1-$\phi$)(NBT-KNN)-$\phi$SB$_{ex}$T ceramics is also confirmed from the SEM micrograph study. Development of unwanted XRD peaks (other than the SB$_{ex}$T and the NBT-KNN phases) suggest the possible reaction between the NBT-KNN and SB$_{ex}$T systems during sintering stage [2,3].

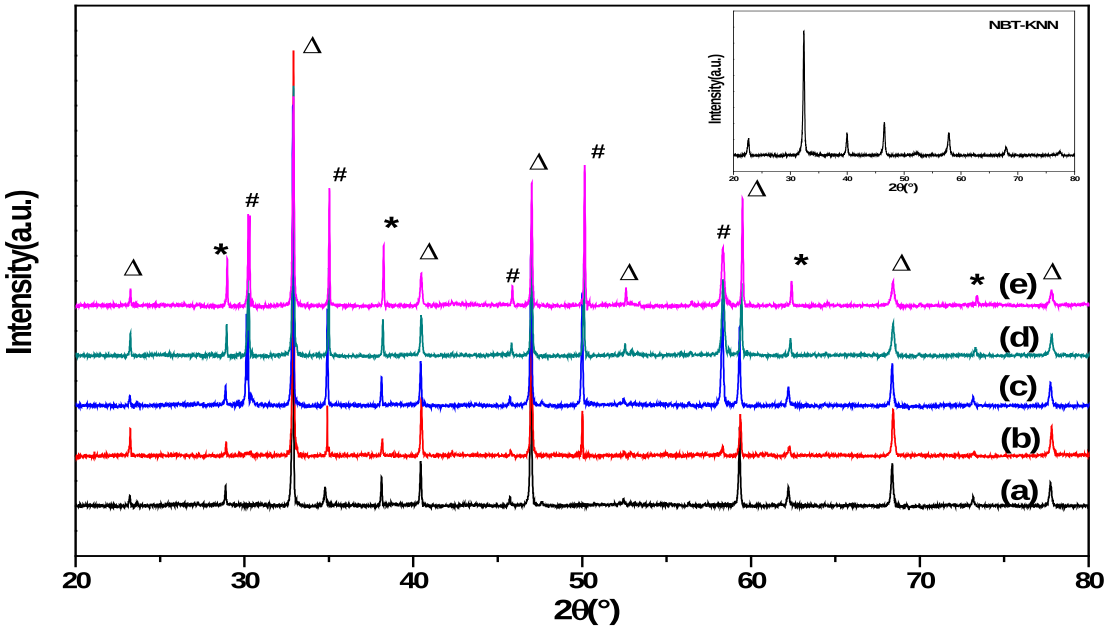

**Fig. 6.2:** X-ray diffraction patterns of (1-$\phi$)(NBT-KNN)-$\phi$SB$_{ex}$T ceramics with $\phi$ (in wt. %) = (a) 2, (b) 4, (c) 8, (d) 12, and (e) 16. **Inset:** XRD pattern of NBT-xKNN (with x=0.07).

## 6.3 Density and Morphological Study

### 6.3.1 Density and Morphological Study of the (1-$\phi$)(NBT-BT)-$\phi$SB$_{ex}$T Ceramics

Fig. 6.3 (a-f) shows the SEM images of the (1-$\phi$)(NBT-BT)-$\phi$ SB$_{ex}$T ($\phi$= 0, 2, 4, 8, 12, 16 wt. %) ceramic samples. The incorporation of SB$_{ex}$T phase beyond $\phi \geq 8$ wt. %

influences the microstructure of the NBT-BT ceramic samples. Up to $\phi$ =4 wt. %, the grain shapes are of typical NBT-BT ceramics type. However, long, randomly oriented and platelike grains starts developing with the increase of $SB_{ex}T$ content beyond $\phi$ = 4 wt.% in the (1-$\phi$) (NBT-BT)-$\phi$ $SB_{ex}T$ ceramic samples. In addition, with the increase of $SB_{ex}T$ content, the non-uniformity of ractangular grains increases and the average grain size decreases. This decrease of average grain size with the increase of $SB_{ex}T$ content suggest that $SB_{ex}T$ acts as grain growth inhibitor in the (1-$\phi$)(NBT-BT)-$\phi$ $SB_{ex}T$ ceramic samples. The decrease of average grain size with the increase of $SB_{ex}T$ content can also be associated with the appearance of secondary phases in the (1-$\phi$)(NBT-BT)-$\phi$ $SB_{ex}T$ ceramic samples [2]. The avaerage grain size of the NBT-BT-type rectangular grains and the $SB_{ex}T$-type platelike grains of the (1-$\phi$)(NBT-BT)-$\phi SB_{ex}T$ ceramics are given in Table 6.1. The experimental density ($\rho_{ex}$) of all the sintered (1-$\phi$)(NBT-BT)-$\phi$ $SB_{ex}T$ ceramic samples is also given in Table 6.3. $\rho_{ex}$ increases with the increase of $SB_{ex}T$ content and becomes maximum for $\phi$=12 wt.%. This enhancement of density can be linked to the introduction of a denser layered perovskite $SB_{ex}T$ phase in the (1-$\phi$)(NBT-BT)-$\phi SB_{ex}T$ ceramic samples [4].

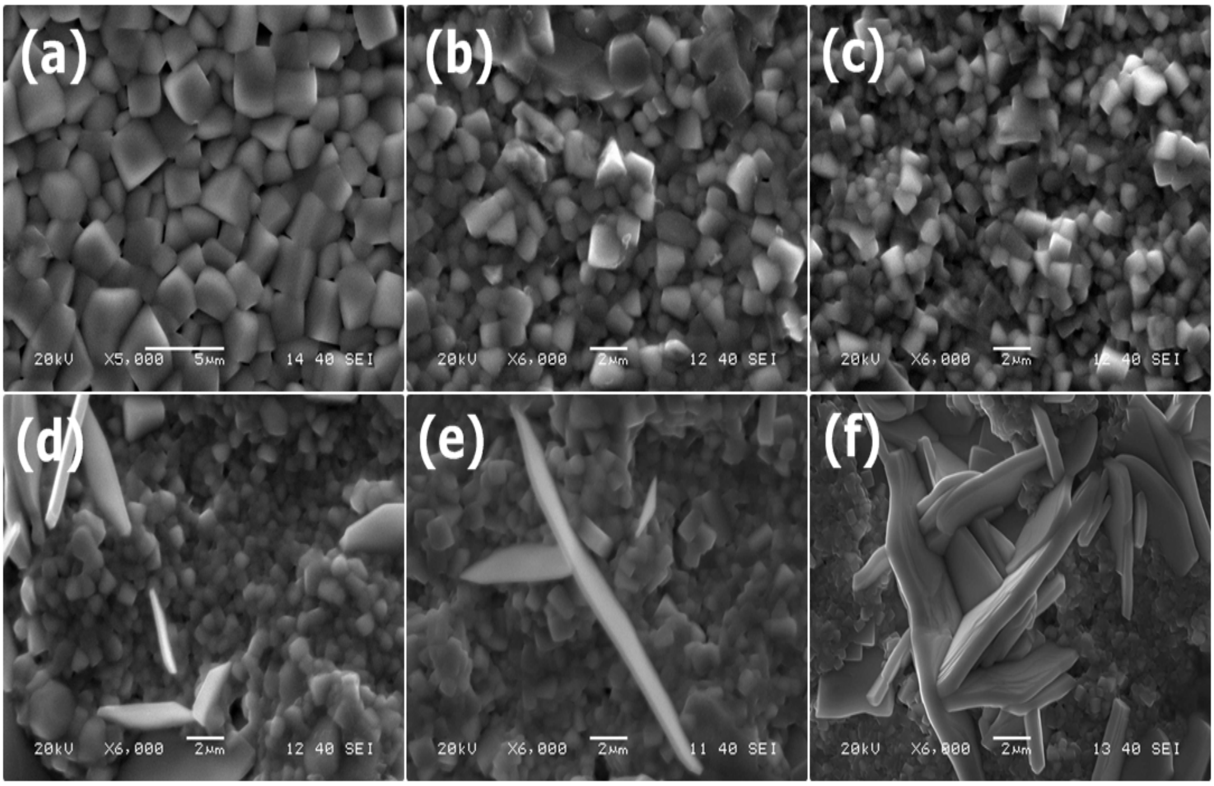

**Fig. 6.3:** SEM micrographs of (1-$\phi$) (NBT-BT)-$\phi$ $SB_{ex}T$ with $\phi$ (in wt.%) = (a) 0, (b) 2, (c) 4, (d) 8, (e) 12 and (f) 16.

**Table 6.1:** Average grain size, and experimental density of (1-$\phi$) (NBT-BT)-$\phi$ $SB_{ex}T$ ($\phi$= 0, 2, 4, 8, 12, 16 wt. %) ceramics.

| **(1-$\phi$) (NBT-BT)-$\phi$ $SB_{ex}T$** | $\phi$ = 0 wt. % | $\phi$ = 2 wt. % | $\phi$ = 4 wt. % | $\phi$ = 8 wt. % | $\phi$ = 12 wt. % | $\phi$ = 16 wt. % |
|---|---|---|---|---|---|---|
| **Average grain size (µm)** | 2.50 | 1.94 | 1.68 | 1.22<br>l*=4.24 | 1.65<br>l* =15.3 | 1.16<br>l*=11.21 |
| **Experimental density(g/cc)** | 5.89 | 5.92 | 5.95 | 5.96 | 6.09 | 5.62 |

Where, l*=length of plate like grains

### 6.3.2 Density and Morphological Study of (1-$\phi$)(NBT-KNN)-$\phi SB_{ex}T$ Ceramics

Fig. 6.4 (a-f) shows the SEM images of the (1-$\phi$) (NBT-KNN)-$\phi$ $SB_{ex}T$ ($\phi$= 0, 2, 4, 8, 12, 16 wt. %) ceramic samples. Non-uniform arrangement of rectangular grains can be seen from the SEM micrographs of the NBT-KNN samples. However, long, randomly oriented and platelike grains starts emerging for $\phi \geq 8$ wt.% samples in the(1-$\phi$) (NBT-KNN)-$\phi SB_{ex}T$ system, which is similar to the $SB_{ex}T$ modified NBT-BT systems. The average grain size of the (1-$\phi$)(NBT-KNN)-$\phi SB_{ex}T$ ceramics is calculated by the linear intercept method and given in Table 6.2. There is a small decrease of the average grain size of the rectangular shaped grains with the increase of $SB_{ex}T$ content in the (1-$\phi$)(NBT-KNN)-$\phi SB_{ex}T$ ceramics. The experimental density ($\rho_{ex}$) of the sintered (1-$\phi$)(NBT-KNN)-$\phi SB_{ex}T$ ceramics was measured by Archimedes principle. The values of $\rho_{ex}$ of the (1-$\phi$)(NBT-KNN)-$\phi SB_{ex}T$ ceramics are given in Table 6.2. $\rho_{ex}$ increases with the increase of $SB_{ex}T$ content in the (1-$\phi$)(NBT-KNN)-$\phi$ $SB_{ex}T$ system, which is again obvious because the $SB_{ex}T$ system is a denser layered perovskite than the NBT-KNN system [4].

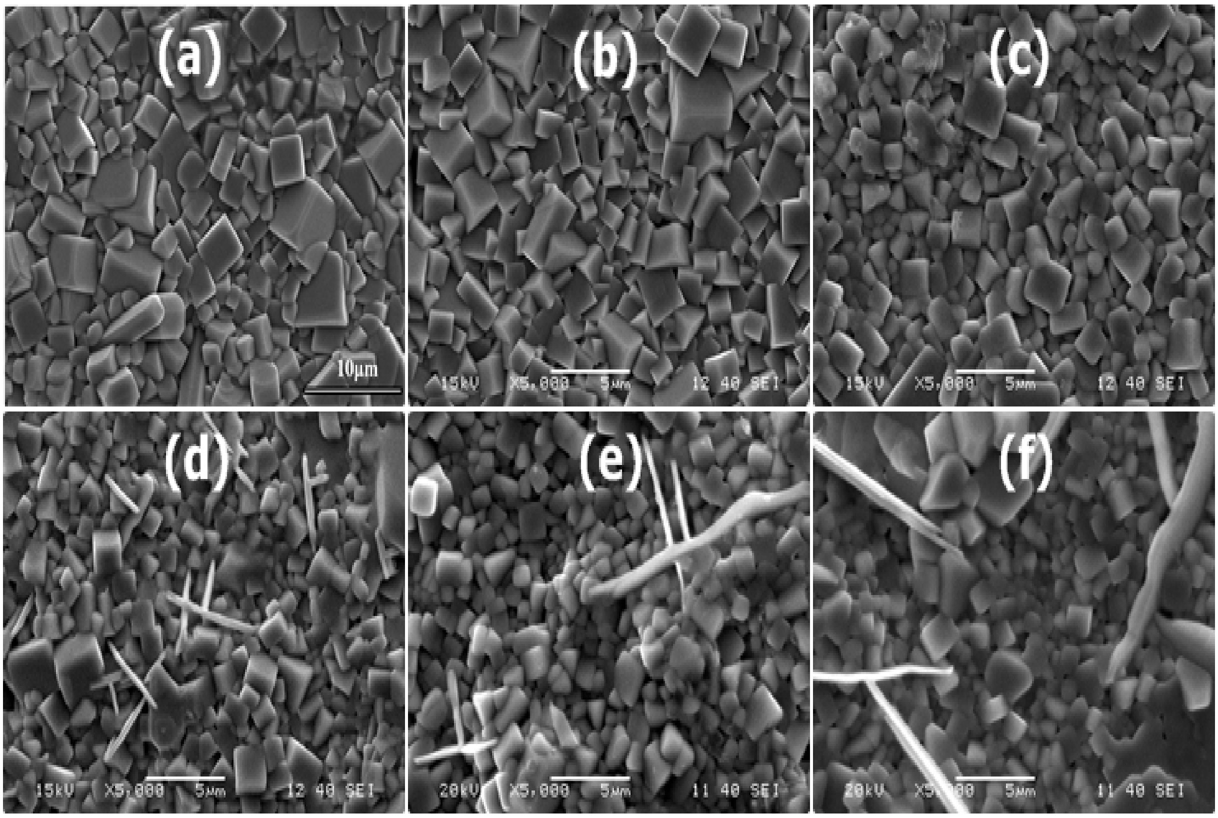

**Fig. 6.4:** SEM micrographs of (1-ϕ) (NBT-KNN)-ϕ $SB_{ex}T$ ceramics with ϕ (in wt.%) = (a) 0, (b) 2, (c) 4, (d) 8, (e) 12 and (f) 16.

**Table 6.2:** Average grain size, and experimental density of (1-ϕ) (NBT-KNN)-ϕ $SB_{ex}T$ (ϕ= 0, 2, 4, 8, 12, 16 wt. %) ceramics.

| **(1-ϕ)(NBT-KNN)-ϕ$SB_{ex}T$** | ϕ = 0 wt. % | ϕ = 2 wt. % | ϕ = 4 wt. % | ϕ = 8 wt. % | ϕ = 12 wt. % | ϕ = 16 wt. % |
|---|---|---|---|---|---|---|
| **Average grain size (μm)** | 4.34 | 1.53 | 1.31 | 1.27<br>l*=3.54 | 1.25<br>l*=6.28 | 1.26<br>l*=9.62 |
| **Experimental density($g/cm^3$)** | 5.77 | 5.80 | 5.84 | 5.85 | 5.94 | 6.01 |

Where, l*=length of plate-like grains

## 6.4 Dielectric Study

### 6.4.1 Temperature Dependent Dielectric Properties of (1-ϕ)(NBT-BT)-ϕ$SB_{ex}$T Ceramics

Fig. 6.5 (a-f) show the temperature dependence of $\varepsilon_r$ and tanδ at different frequencies of the (1-ϕ)(NBT-BT)-ϕ$SB_{ex}$T (ϕ = 0, 2, 4, 8, 12, 16 wt. %) ceramic samples. It is observed that $\varepsilon_r$ decreases gradually with the increase of $SB_{ex}$T content, which may be due to the increase of multiple cationic arrangements in the (1-ϕ)(NBT-BT)-ϕ$SB_{ex}$T ceramic samples [5]. Two major peaks (~$T_d$ and $T_m$) appear in the $\varepsilon_r$ vs. temperature plots of all the ceramics except for ϕ=16 wt. %. Strong frequency dispersion is observed near $T_d$, whereas diffuse phase transition is observed near $T_m$ [6]. Near $T_m$, the broadening of $\varepsilon_r$ vs. temperature peak with the increase in $SB_{ex}$T content suggests the increase of cationic disorder [5]. Clear demarcation of $T_d$ and $T_m$ is visible up to ϕ= 12 wt. %, which starts diminishing for ϕ= 16 wt.%. For ϕ= 16 wt.%, the sharp increase of $\varepsilon_r$ at higher temperatures may be related to the space charge polarization, which results from the increase in conductivity of the ceramic samples [7, 8]. This can also be related to the oxygen vacancies and defects, created in the material during high-temperature processing conditions. Formation of oxygen vacancies during high temperature sintering is a common result in all type of oxide based perovskite materials. However, amount of oxygen loss and their effect on the conduction process in different materials is different. These are expressed as Kröger-Vink notation as follows:

$$O_O^X \rightarrow \frac{1}{2}O_2 + V_O^{\bullet} + e' \qquad (6.1)$$

$$O_O^X \rightarrow \frac{1}{2}O_2 + V_O^{\bullet\bullet} + 2e' \qquad (6.2)$$

Where, $V_o^{\bullet}$ and $V_o^{\bullet\bullet}$ are singly and doubly ionized oxygen vacancies, respectively.

Dielectric properties of the (1-ϕ) (NBT-BT)-ϕ$SB_{ex}$T (ϕ= 0, 2, 4, 8, 12, 16 wt. %) ceramics at 1 kHz frequency are given in Table 6.3.

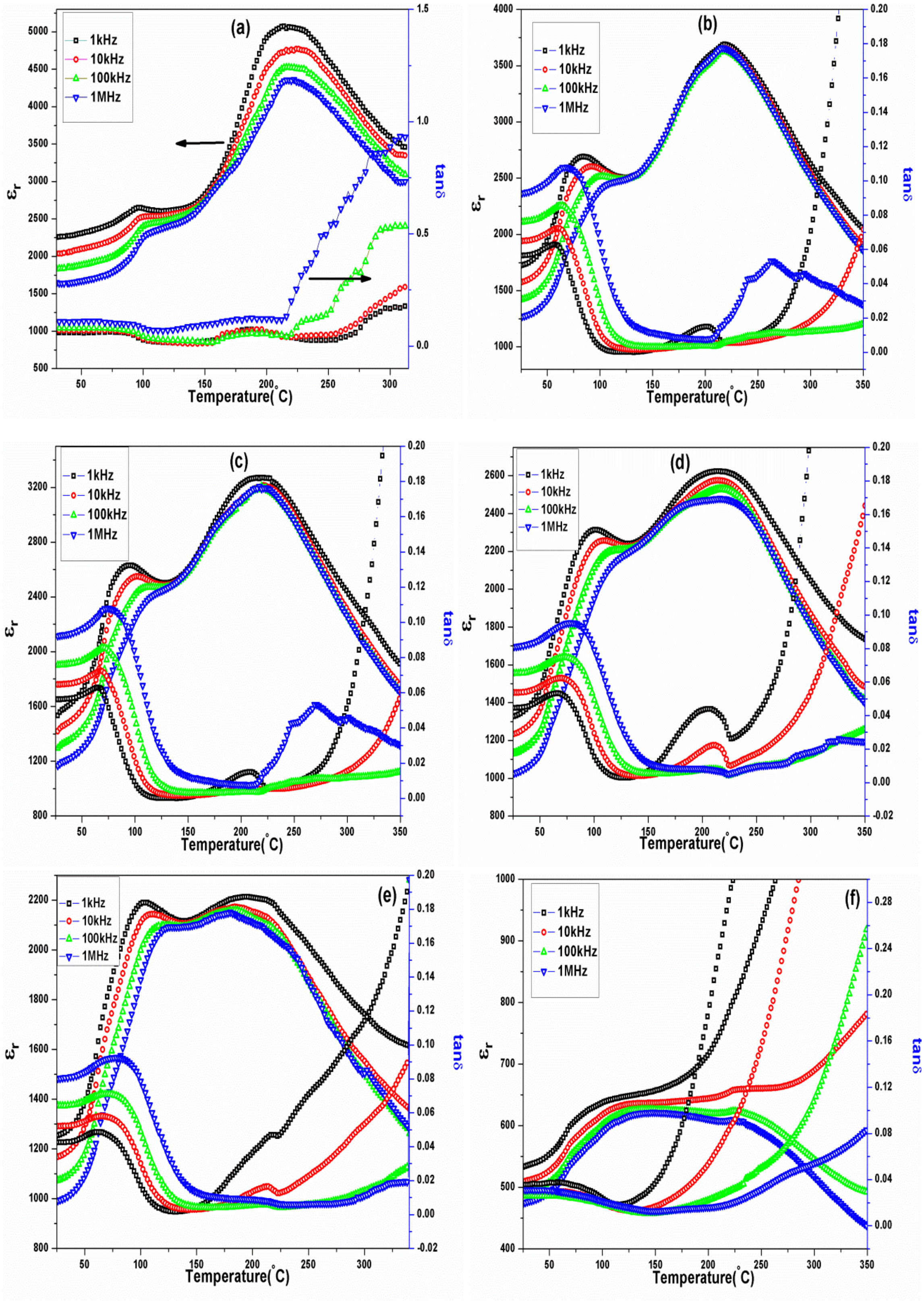

**Fig. 6.5:** Variation of εr and tanδ with temperature at different frequencies of (1-ϕ)(NBT-BT)-ϕ$SB_{ex}T$ ceramics with ϕ (in wt.%) = (a) 0, (b) 2, (c) 4, (d) 8, (e) 12 and (f) 16.

**Table 6.3:** Dielectric values (at 1 kHz frequency) of (1-ϕ) (NBT-BT)-ϕ $SB_{ex}T$ ceramic samples.

| **(1-ϕ) (NBT-BT)-ϕ $SB_{ex}T$** | **$\varepsilon_r$ at RT** | **tanδ at RT** | **$T_d$ (°C)** | **$T_m$ (°C)** | **$\varepsilon_r$ at $T_m$** |
|---|---|---|---|---|---|
| ϕ = 0 wt.% | 2275 | 0.04 | 99 | 219 | 5067 |
| ϕ = 2 wt.% | 1725 | 0.05 | 81 | 216 | 3687 |
| ϕ = 4 wt.% | 1534 | 0.05 | 88 | 214 | 3272 |
| ϕ = 8 wt.% | 1326 | 0.04 | 96 | 214 | 2624 |
| ϕ = 12 wt.% | 1253 | 0.04 | 99 | 201 | 2209 |
| ϕ =16 wt.% | 532 | 0.03 | - | - | - |

## 6.4.2 Temperature Dependent Dielectric Properties of (1-ϕ)(NBT-KNN)-ϕ$SB_{ex}T$ Ceramics

Fig. 6.6 (a-f) shows the temperature dependence of $\varepsilon_r$ and tanδ at different frequencies of the (1-ϕ) (NBT-KNN)-ϕ$SB_{ex}T$ (ϕ=0, 2, 4, 8, 12, 16 wt. %) ceramics. Two significant peaks (near $T_d$ and $T_m$) appear in the temperature dependence of $\varepsilon_r$ plots of the (1-ϕ) (NBT-KNN)-ϕ$SB_{ex}T$ ceramics. At RT, the variation of $\varepsilon_r$ vs. T plots exhibit frequency dispersion, whereas above $T_d$ this dispersion nature is reduced, which suggest the existence of relaxing phenomena close to RT, which is absent at higher temperatures [6]. However, near $T_m$, $\varepsilon_r$ vs. T peaks are comparatively broad, indicating the diffuse phase transition (DPT) nature of the samples. It is observed that $\varepsilon_r$ increases with the increase in temperature up to $T_m$ and starts decreasing slowly with the increase of temperature above $T_m$. Also, $T_m$ decreases with the increase of $SB_{ex}T$ content in the (1-ϕ) (NBT-KNN)-ϕ$SB_{ex}T$ ceramics. The decrease of $T_m$ with the increase of $SB_{ex}T$ content can be related to the internal stress in the (1-ϕ) (NBT-KNN)-ϕ$SB_{ex}T$ ceramics [9]. This behavior suggests that there might have decrease in internal stress, which gives rise to decrease in $T_m$. However, $T_d$ shows a marginal shift without any systematic trend with the variation of $SB_{ex}T$ content in the (1-ϕ) (NBT-KNN)-ϕ$SB_{ex}T$ ceramics. Furthermore, there is no clear distinction between $T_d$ and $T_m$ for ϕ=16 wt.% ceramic samples.The value of $\varepsilon_r$ at RT as well as at $T_m$ decreases with the increase of $SB_{ex}T$ content, which suggest the increase of multiple cationic arrangements in the (1-ϕ)(NBT-KNN)-ϕSB$_{ex}$T ceramics [5]. RT value of tanδ at 1 kHz frequency drastically decreases for ϕ = 16 wt. % ceramic samples, which suggest the usefulness of this system for capacitor applications. Dielectric properties at 1 kHz frequency of the (1-ϕ) (NBT-KNN)-ϕSB$_{ex}$T (ϕ= 0, 2, 4, 8, 12, 16 wt. %) ceramics are given in Table 6.4.

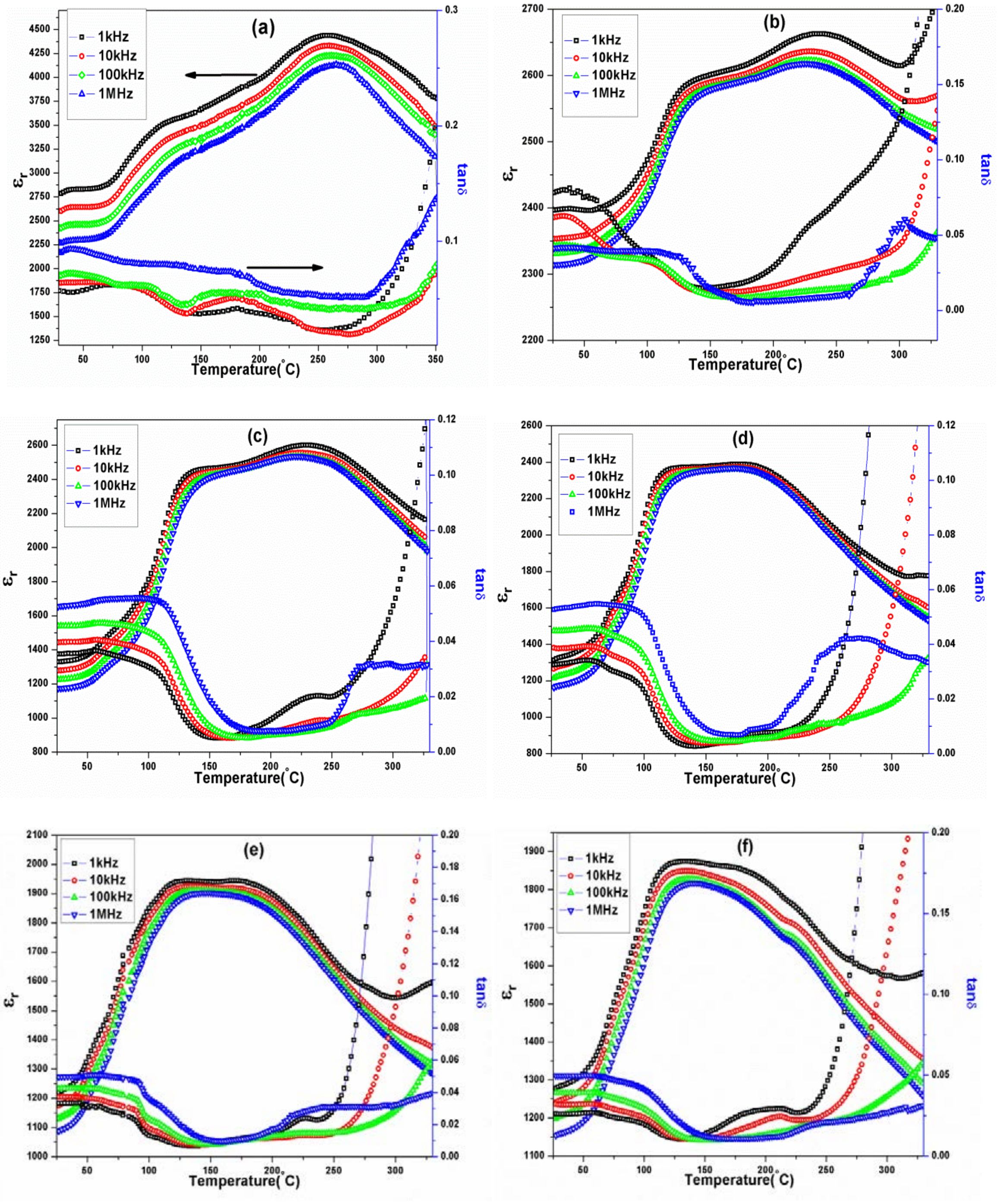

**Fig. 6.6:** Variation of ε$_r$ and tanδ with temperature at different frequencies of (1-ϕ) (NBT-KNN)-ϕ SB$_{ex}$T ceramics with ϕ (in wt.%) = (a) 0, (b) 2, (c) 4, (d) 8, (e) 12 and (f) 16.

**Table 6.4:** Dielectric values (at 1 kHz frequency) of (1-$\phi$) (NBT-KNN)-$\phi$ SB$_{ex}$T ceramic samples.

| **(1-$\phi$) (NBT-KNN)-$\phi$ SB$_{ex}$T** | **$\varepsilon_r$ at RT** | **tanδ at RT** | **$T_d$ (°C)** | **$T_m$ (°C)** | **$\varepsilon_r$ at $T_m$** |
|---|---|---|---|---|---|
| $\phi$ = 0 wt.% | 2787 | 0.05 | 121 | 259 | 4438 |
| $\phi$ = 2 wt.% | 2396 | 0.07 | 128 | 231 | 2663 |
| $\phi$ = 4 wt.% | 1329 | 0.03 | 128 | 228 | 2606 |
| $\phi$ = 8 wt.% | 1313 | 0.03 | 115 | 197 | 2398 |
| $\phi$ = 12 wt.% | 1220 | 0.03 | 115 | 186 | 1946 |
| $\phi$ =16 wt.% | 1278 | 0.02 | 124 | - | - |

## 6.5 Leakage Current Study

### 6.5.1 Leakage Current Properties of (1-$\phi$)(NBT-BT)-$\phi$SB$_{ex}$T Ceramics

The room temperature (RT) leakage current density vs. electric field (J–E) characteristics of the (1-$\phi$)(NBT-BT)-$\phi$SB$_{ex}$T ($\phi$= 0, 2, 4, 8, 12, 16 wt. %) ceramic samples are shown in Fig. 6.7. The values of leakage current density of all the (1-$\phi$) (NBT-BT)-$\phi$ SB$_{ex}$T ceramic samples are observed to be between ~$10^{-7}$ to $10^{-8}$A/cm$^2$ at the maximum applied electric field of 40kV/cm. Leakage current density values of the SB$_{ex}$T modified systems are lower than the pure NBT-BT ceramic sample. In contrast, as shown in Fig. 6.7, even at low electric fields, the NBT-BT ceramic samples exhibits high leakage current density. Bi vacancies ($V_{Bi}'''$) accompanied by oxygen vacancies ($V_o^{\bullet\bullet}$) in the NBT-BT system can be related to its high leakage current behavior [10, 11]. The decrease of leakage current density with the incorporation of SB$_{ex}$T ceramics can be related to the decrease in space charge density [12]. The leakage current conduction mechanism of the (1-$\phi$)(NBT-BT)-$\phi$SB$_{ex}$T ceramic samples can be explained in terms of ohmic behavior at low electric fields and space charge limited conduction (SCLC) behavior at high electric fields [13]. In addition, a distinct hump at ~30kV/cm electric field in the J-E plot of the

NBT-BT ceramic samples relates with the coercive field for the particular composition [14]. Moreover, asymmetric nature of the J-E plot of the NBT-BT ceramic samples suggests the electrode dependent behavior [15]. The values of leakage current density at an electric field of 40kV/cm are given in Table 6.5. The leakage current density value decreases up to ϕ= 12wt. %. This decrease of leakage current density with the modification of $SB_{ex}T$ ceramics can be associated with the introduction of lattice defects, which block the electron movement and results in less electrical conductivity [16]. However for ϕ =16 wt.%, the leakage current density value starts increasing which may be related to the dominance of space charge effect and presence of secondary phases in the systems.

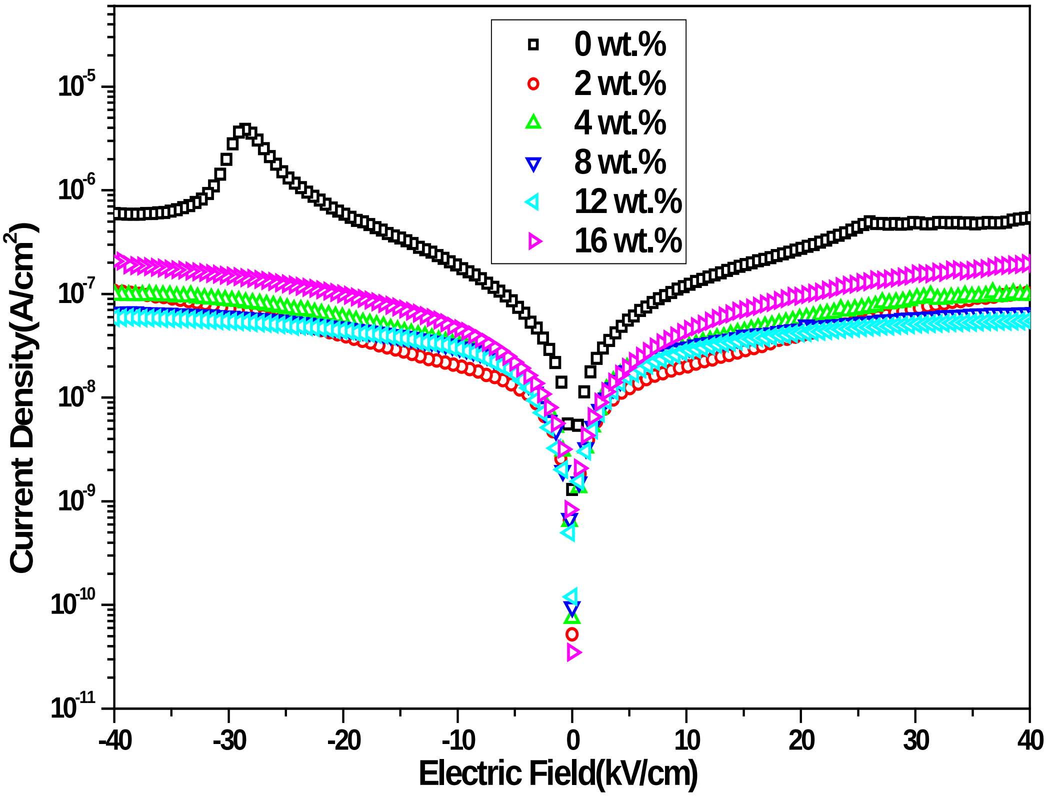

**Fig. 6.7** Room temperature leakage current density vs. electric field plots of (1-ϕ) (NBT-BT)-$\phi SB_{ex}T$ (ϕ=0, 2, 4, 8, 12, 16 wt. %) ceramics.

**Table 6.5:** Leakage current density of (1-ϕ) (NBT-BT)-ϕ $SB_{ex}T$ (ϕ= 0, 2, 4, 8, 12, 16 wt. %) ceramics at 40kV/cm.

| **(1-ϕ) (NBT-BT)-ϕ $SB_{ex}T$** | ϕ = 0 wt. % | ϕ = 2 wt. % | ϕ = 4 wt. % | ϕ = 8 wt. % | ϕ = 12 wt. % | ϕ = 16 wt. % |
|---|---|---|---|---|---|---|
| **Current Density(A/cm$^2$)** | $5.72\text{x}10^{-7}$ | $1.24\text{x}10^{-7}$ | $9.60\text{x}10^{-8}$ | $7.14\text{x}10^{-8}$ | $5.72\text{x}10^{-8}$ | $2.35\text{x}10^{-7}$ |

## 6.5.2 Leakage Current Properties of (1-ϕ)(NBT-KNN)-ϕ$SB_{ex}T$ Ceramics

Fig. 6.8 shows nearly symmetrical J–E characteristics of (1-ϕ) (NBT-KNN)-ϕ$SB_{ex}T$ (ϕ=0, 2, 4, 8, 12, 16 wt %) ferroelectric ceramics at both positive and negative biased voltages. The bulk-limited current plays a critical role in the conduction mechanism of the (1-ϕ)(NBT-KNN)-ϕ$SB_{ex}T$ ceramics [17]. Again, the symmetric nature of the J–E plots suggests the electrode independent nature of all the (1-ϕ) (NBT-KNN)-ϕ$SB_{ex}T$ ceramic samples [15]. The value of the leakage current density of all the (1-ϕ) (NBT-KNN)-ϕ$SB_{ex}T$ ceramics at an electric field of 40kV/cm are given in Table 6.6. The value of the leakage current is two order less compared to the parent NBT-KNN ceramic samples. The decrease of leakage current value with the increase of $SB_{ex}T$ content in the (1-ϕ)(NBT-KNN)-ϕ$SB_{ex}T$ system can be accounted in terms of the moderate leakage behavior of $SB_{ex}T$ [18]. Whereas, the small leakage current of $SB_{ex}T$ system can be explained with its layer structure nature [19]. The conduction mechanism in any ceramic is of bulk and/or interface limited type [20]. In this case, the RT leakage current behavior at low voltage is of Ohmic conduction type and at high voltage is of SCLC type [21].

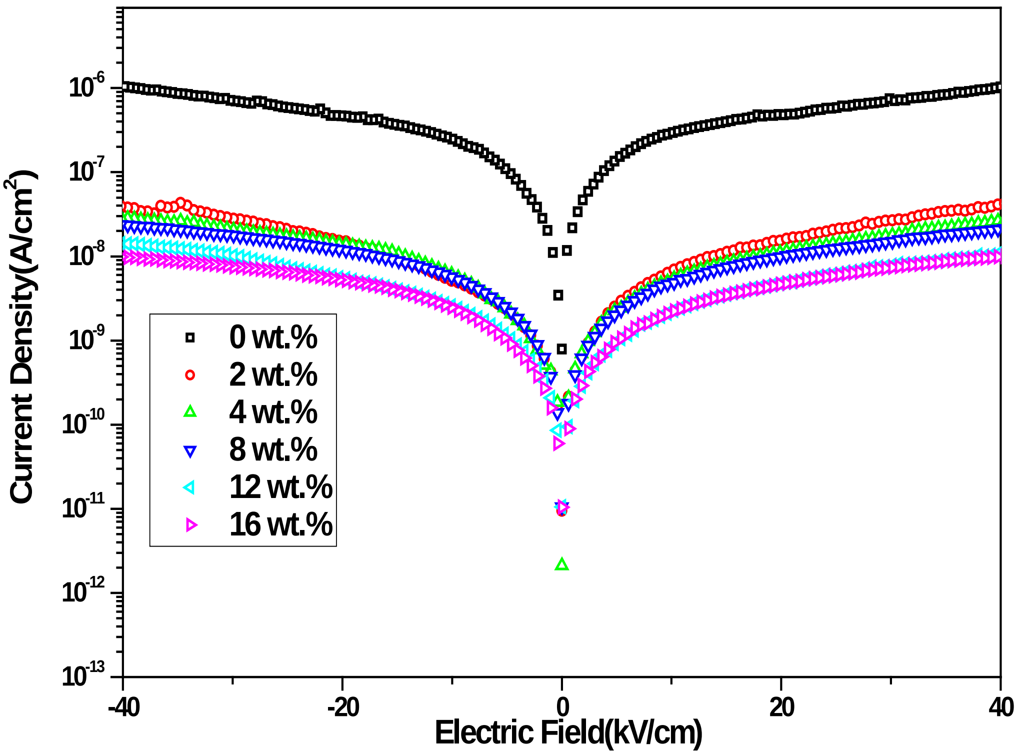

**Fig. 6.8:** Room temperature leakage current density vs. electric field plots of (1-ϕ) (NBT-KNN)-ϕ SB$_{ex}$T (ϕ= 0, 2, 4, 8, 12, 16 wt. %) ceramics.

**Table 6.6:** Leakage current density of (1-ϕ) (NBT-KNN)-ϕ SB$_{ex}$T (ϕ= 0, 2, 4, 8, 12, 16 wt. %) ceramics at 40kV/cm.

| **(1-ϕ) (NBT-KNN)-ϕ SB$_{ex}$T** | ϕ = 0 wt. % | ϕ = 2 wt. % | ϕ = 4 wt. % | ϕ = 8 wt. % | ϕ = 12 wt. % | ϕ = 16 wt. % |
|---|---|---|---|---|---|---|
| **Current Density (A/cm$^2$)** | 1.04x10$^{-6}$ | 3.36x10$^{-8}$ | 3.85x10$^{-8}$ | 2.92x10$^{-8}$ | 1.72x10$^{-8}$ | 1.23x10$^{-8}$ |

## 6.6 Piezoelectric Study

### 6.6.1 Piezoelectric Study of (1-ϕ) (NBT-BT)-ϕSB$_{ex}$T Ceramics

Fig. 6.9 shows the RT-induced strain% vs. external electric field (S-E) plots of the (1-ϕ) (NBT-BT)-ϕ SB$_{ex}$T (with ϕ= 0, 2, 4, 8, 12, 16 wt. %) ceramic samples. The typical butterfly shape S-E loop with a maximum strain of ~0.45% of the NBT-BT ceramic samples confirmed its piezoelectric nature. While for the SB$_{ex}$T modified systems, the shape of the S-E loops changes to a typical relaxor ferroelectric type, which may be due to the dependence of $T_d$ on frequency, confirmed in the dielectric spectrum [22]. The significant reduction of the induced strain%, accompanied by the deviation from the butterfly shaped S–E loops reveals that the ferroelectric and non-polar phases coexist in the (1-ϕ) (NBT-BT)-ϕ$SB_{ex}T$ (with ϕ= 2, 4, 8, 12, 16 wt. %) ceramic samples. Moreover, this suggests that an easy transition between the ferroelectric and non-polar phases can occur under an applied external electric field [23]. The S-E loop of the ceramics for ϕ=16 wt. % composition is highly disrupted and the value of induced strain% gets drastically lowered. This can be attributed to the low piezoelectric property $SB_{ex}T$ and presence of secondary phase in the (1-ϕ)(NBT-BT)-ϕ$SB_{ex}T$ ceramic composites for ϕ=16 wt. %. The $d_{33}$ and $k_p$ values of all the poled (1-ϕ) (NBT-BT)-ϕ$SB_{ex}T$ ceramics are also measured. The $d_{33}$ and $k_p$ values are found to decrease with increase in $SB_{ex}T$ incorporation and get completely disappear after ϕ = 12 wt. % and 8 wt. %, respectively. Maximum induced strain %, $d_{33}$ and $k_p$ of all the (1-ϕ) (NBT-BT)-ϕ$SB_{ex}T$ ceramic samples are given in Table 6.7.

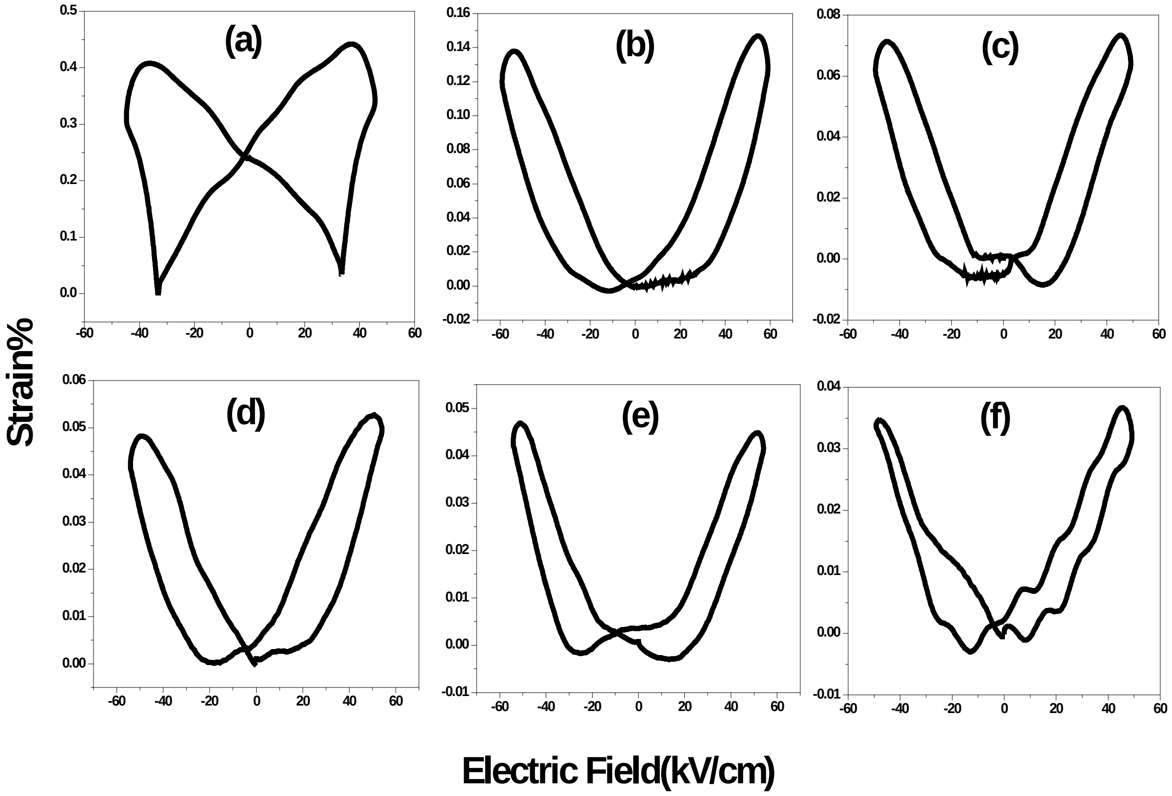

**Fig. 6.9** Bipolar field-induced strains of (1-ϕ) (NBT-BT)-ϕ $SB_{ex}T$ ceramics with ϕ (in wt. %) = (a) 0, (b) 2, (c) 4, (d) 8, (e) 12 and (f) 16.

**Table 6.7:** Piezoelectric parameters of (1-$\phi$) (NBT-BT)-$\phi$ $SB_{ex}T$ ($\phi$= 0, 2, 4, 8, 12, 16 wt. %) ceramics.

| **(1-$\phi$) (NBT-BT)-$\phi$ $SB_{ex}T$** | $\phi$ = 0 wt. % | $\phi$ = 2 wt. % | $\phi$ = 4 wt. % | $\phi$ = 8 wt. % | $\phi$ = 12 wt. % | $\phi$ =16 wt. % |
|---|---|---|---|---|---|---|
| **$k_p$** | 0.21 | 18.24 | 13.31 | 8.11 | - | - |
| **$d_{33}$ (pC/N)** | 105 | 85 | 43 | 25 | 14 | - |
| **Strain%** | 0.45 | 0.14 | 0.07 | 0.05 | 0.04 | 0.03 |

### 6.6.2 Piezoelectric Study of (1-$\phi$) (NBT-KNN)-$\phi SB_{ex}T$ Ceramics

Fig. 6.10 shows the development of S-E loops of the (1-$\phi$)(NBT-KNN)-$\phi SB_{ex}T$ (with $\phi$= 0, 2, 4, 8, 12, 16 wt. %) ceramics, which suggests the movement and switching of the non-180° domain walls [24]. Butterfly shaped S-E loops are observed in all the (1-$\phi$)(NBT-KNN)-$\phi SB_{ex}T$ ceramic samples. Unlike $SB_{ex}T$ modified NBT-BT systems, the butterfly shape of the S-E loops of the (1-$\phi$)(NBT-KNN)-$\phi SB_{ex}T$ ceramics is retained. However, with the increase of $SB_{ex}T$ content, the asymmetry of the S-E loops increases, which can be attributed to the increase of defects/secondary phase in the (1-$\phi$)(NBT-KNN)-$\phi SB_{ex}T$ ceramics [25]. Maximum induced strain% values of all the studied ceramic samples are given in Table 6.8. The maximum strain% value gradually decreases with the increase of $SB_{ex}T$ content in the (1-$\phi$)(NBT-KNN)-$\phi SB_{ex}T$ ceramics. The $d_{33}$ and $k_p$ values of all the (1-$\phi$)(NBT-KNN)-$\phi SB_{ex}T$ ceramics are given in the Table 6.8. Like the decrease of maximum strain% values, the $d_{33}$ and $k_p$ values are also decreasing with the increase of $SB_{ex}T$ content in the (1-$\phi$)(NBT-KNN)-$\phi SB_{ex}T$ ceramics. Moreover, no significant value of $k_p$ and $d_{33}$ of the (1-$\phi$)(NBT-KNN)-$\phi SB_{ex}T$ ceramics are observed for $\phi$ = 4 wt.% and 8 wt.% ceramics, respectively.

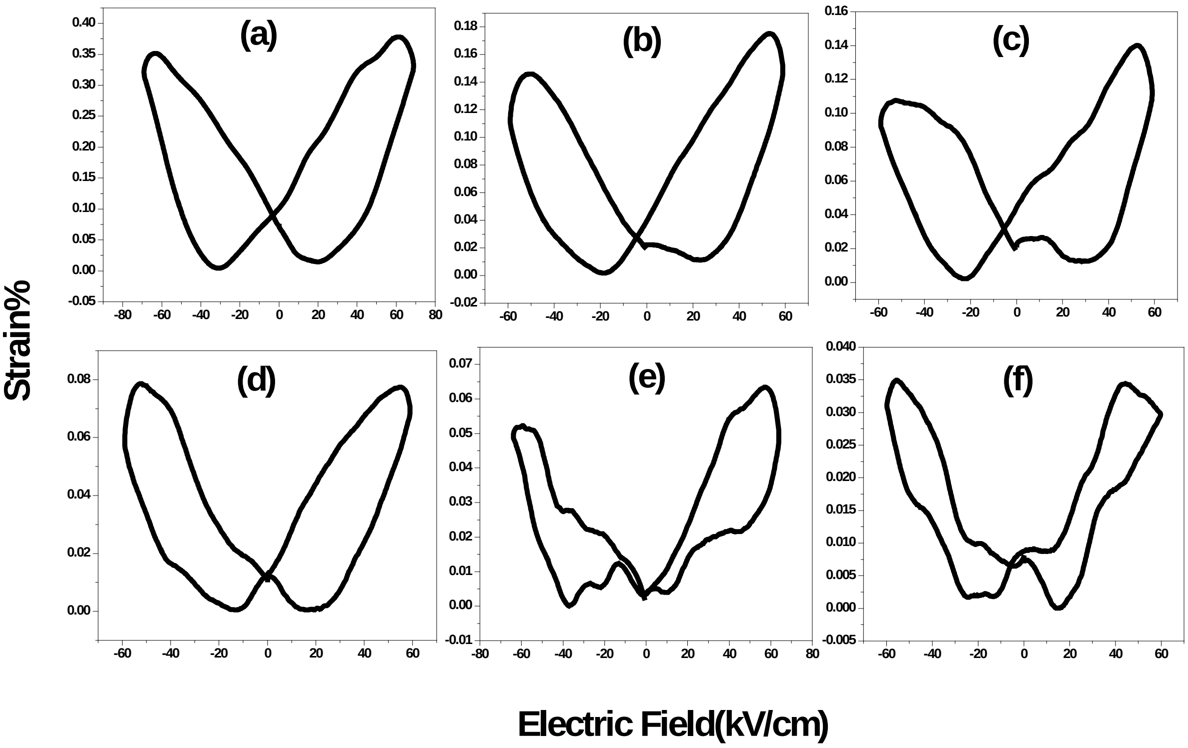

**Fig. 6.10:** Bipolar field-induced strains of (1-ϕ) (NBT-KNN)-ϕ $SB_{ex}T$ ceramics with ϕ (in wt. %) = (a) 0, (b) 2, (c) 4, (d) 8, (e) 12 and (f) 16.

**Table 6.8:** Piezoelectric parameters of (1-ϕ) (NBT-KNN)-ϕ $SB_{ex}T$ (ϕ= 0, 2, 4, 8, 12, 16 wt. %) ceramics.

| **(1-ϕ) (NBT-KNN)-ϕ $SB_{ex}T$** | ϕ = 0 wt. % | ϕ = 2 wt. % | ϕ = 4 wt. % | ϕ = 8 wt. % | ϕ = 12 wt. % | ϕ =16 wt. % |
|---|---|---|---|---|---|---|
| **$k_p$** | 0.12 | 0.10 | 0.08 | - | - | - |
| **$d_{33}$ (pC/N)** | 78 | 52 | 31 | 15 | - | - |
| **Strain%** | 0.29 | 0.15 | 0.11 | 0.08 | 0.05 | 0.03 |

## 6.7 Ferroelectric Study

### 6.7.1 Ferroelectric Study of (1-ϕ) (NBT-BT)-ϕ $SB_{ex}T$ Ceramics

Fig. 6.11 show the P-E hysteresis loops of the (1-ϕ) (NBT-BT)-ϕ$SB_{ex}T$ (where ϕ= 0, 2, 4, 8, 12, 16 wt.%) ceramic samples. The MPB composition of the NBT-BT system exhibits a strong ferroelectric nature with remnant polarization ($P_r$) ~31.71μC/cm$^2$ and coercive field ($E_c$) ~ 40kV/cm. However, as compared to the NBT-BT ceramics, the SB$_{ex}$T incorporated (1-ϕ)(NBT-BT)-ϕSB$_{ex}$T ceramic samples show lowering of the $E_c$ and $P_r$ values. The lowering of $P_r$ value with the incorporation of SB$_{ex}$T in the (1-ϕ) (NBT-BT)-ϕSB$_{ex}$T ceramic samples may be associated with the increase in number of cations [5]. In addition, the drastic decrease in $E_c$ and $P_r$ values accompanied by slightly pinched P–E hysteresis loops with the incorporation of higher content of SB$_{ex}$T in the (1-ϕ) (NBT-BT)-ϕSB$_{ex}$T ceramic samples may also be attributed to the introduction of non-polar and development of secondary phases [26]. For lower content of SB$_{ex}$T (ϕ= 2 and 4 wt. %), $T_d$ shifts towards RT. This shift in $T_d$ can cause the appearance of non-polar phase in these ceramics and the interactions between these polar and non-polar phases may give rise to the deformation of the P–E hysteresis loops [27-30]. Further, the ferroelectric P-E hysteresis loop analysis of the (1-ϕ)(NBT-BT)-ϕSB$_{ex}$T ceramic samples is in good agreement with its piezoelectric behavior. $P_r$ and $E_c$ values of all the (1-ϕ) (NBT-BT)-ϕSB$_{ex}$T ceramic samples are given in Table 6.9.

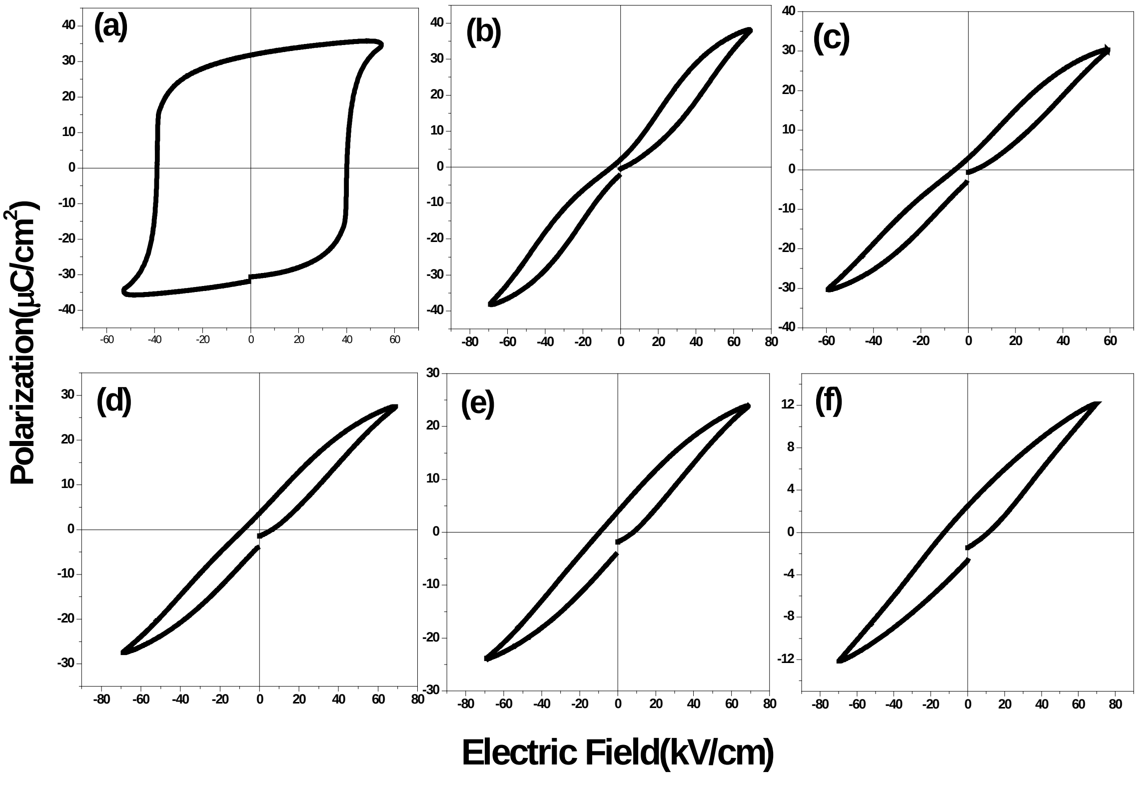

**Fig. 6.11:** P-E hysteresis loops of (1-ϕ) (NBT-BT)-ϕ SB$_{ex}$T ceramics with ϕ (in wt.%) = (a) 0, (b) 2, (c) 4, (d) 8, (e) 12 and (f) 16.

**Table 6.9:** Ferroelectric parameters of (1-ϕ) (NBT-BT)-ϕ $SB_{ex}T$ (ϕ= 0, 2, 4, 8, 12, 16 wt. %) ceramics.

| **(1-ϕ)(NBT-BT)-ϕ$SB_{ex}T$** | ϕ = 0 wt. % | ϕ = 2 wt. % | ϕ = 4 wt. % | ϕ = 8 wt. % | ϕ = 12 wt. % | ϕ = 16 wt. % |
|---|---|---|---|---|---|---|
| **$P_r$ (µC/cm$^2$)** | 31.71 | 1.88 | 3.02 | 3.47 | 3.84 | 2.20 |
| **$E_c$(kV/cm)** | 40.00 | 1.70 | 5.20 | 5.59 | 9.11 | 11.02 |

## 6.7.2 Ferroelectric Study of (1-ϕ) (NBT-KNN)-ϕ $SB_{ex}T$ Ceramics

Fig. 6.12 shows the RT well-developed P–E hysteresis loops of all the (1-ϕ) (NBT-KNN)-ϕ $SB_{ex}T$ (ϕ= 0, 2, 4, 8, 12, 16 wt. %) ceramic composites. Leakage current of a ferroelectric material plays a great impact on its ferroelectric behavior. Development of slimmer P-E loops with the increase of ϕ content can be correlated with the decrease of its leakage current. The ceramic composites with ϕ =16 wt. % have the lowest leakage current in the (1-ϕ)(NBT-KNN)-ϕ $SB_{ex}T$ sample. This can be attributed to the addition of excess $SB_{ex}T$, that might have caused lattice defects which blocked electron transporting, resulting in less electrical conductivity and in turn lower leakage [16]. This is in good agreement with the lower coercive field as shown in Fig 6.12. Moreover, the observed ferroelectric behavior can be attributed to the domain wall motion and structural distortion of the oxygen octahedra in all the studied ceramics. The leakage current, $P_r$, and $E_c$ values of all the (1-ϕ)(NBT-KNN)-ϕ$SB_{ex}T$ ceramic composite samples are given in Table 6.10.

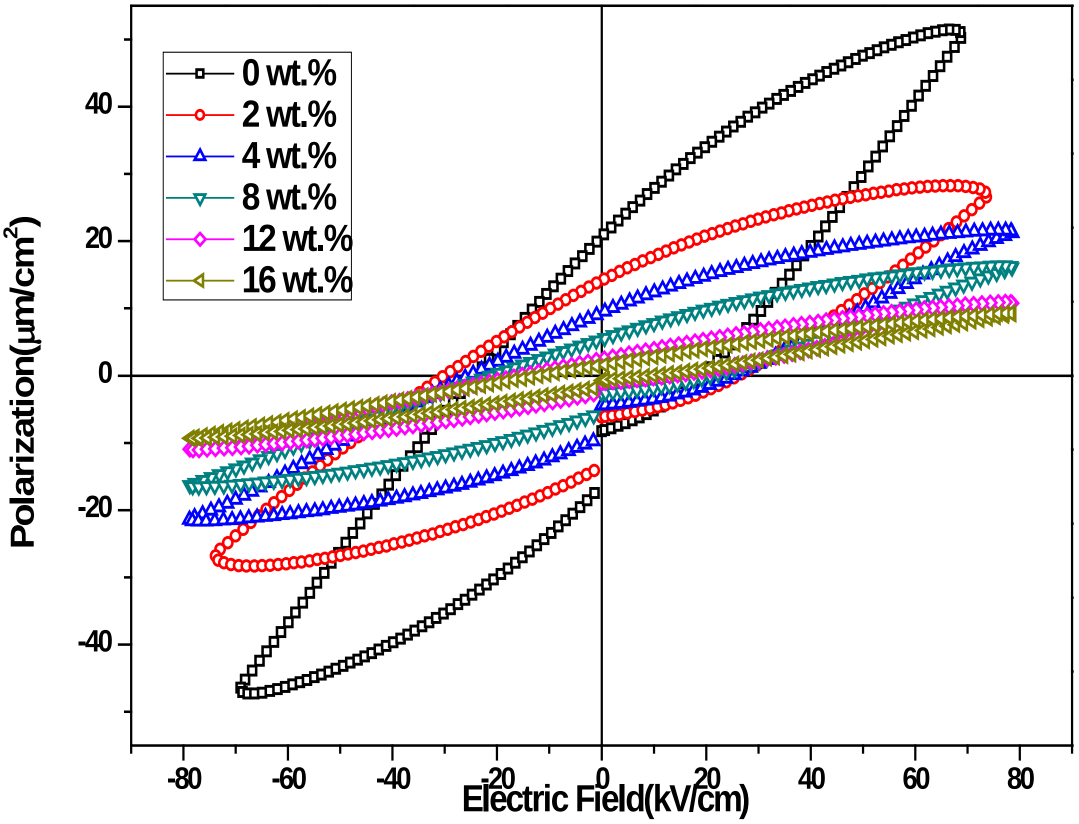

**Fig. 6.12:** P-E hysteresis loops of (1-ϕ) (NBT-KNN)-ϕSB$_{ex}$T (ϕ= 0, 2, 4, 8, 12, 16 wt. %) ceramics.

**Table 6.10:** Ferroelectric parameters of (1-ϕ) (NBT-KNN)-ϕ SB$_{ex}$T (ϕ= 0, 2, 4, 8, 12, 16 wt. %) ceramics.

| **(1-ϕ) (NBT-KNN)-ϕSB$_{ex}$T** | ϕ = 0 wt. % | ϕ = 2 wt. % | ϕ = 4 wt. % | ϕ = 8 wt. % | ϕ = 12 wt. % | ϕ = 16 wt. % |
|---|---|---|---|---|---|---|
| **P$_r$ (μC/cm$^2$)** | 20.61 | 9.64 | 9.54 | 5.64 | 2.60 | 1.44 |
| **E$_c$(kV/cm)** | 19.90 | 27.63 | 25.68 | 24.49 | 18.26 | 10.80 |

## 6.8 Polarization Fatigue Study

### 6.8.1 Polarization Fatigue Study of (1-ϕ) (NBT-BT)-ϕSB$_{ex}$T Ceramics

The fatigue endurance study of the (1-ϕ)(NBT-BT)-ϕSB$_{ex}$T (ϕ= 0, 2, 4, 8, 12, 16 wt. %) ceramic composites was carried out at room temperature by using $10^5$Hz bipolar triangular switching pulses. Fig. 6.13 shows the variation of normalized polarization vs. number of switching cycles (up to $10^9$) of all the (1-ϕ) (NBT-BT)-ϕ SB$_{ex}$T ceramic composite samples. The switched polarization value in the positive and negative applied electric field cycles is denoted by P* and -P* (μC/cm$^2$). The NBT-BT composition near MPB shows degradation of ~ 22.54% in their polarization behavior. From Fig. 6.13 plots, it is observed that the polarization degradation gradually decreases with the increase in SB$_{ex}$T content, which can be related to anti-fatigue behaviour of SB$_{ex}$T system. Since, polarization fatigue, which is related to the leakage current, obstructs the use of ferroelectric materials in memory applications. The studied polarization fatigue characteristics has also supported the leakage current behavior of (1-ϕ)(NBT-BT)-ϕSB$_{ex}$T ceramics. The relative polarization fatigue% values of all the (1-ϕ) (NBT-BT)-ϕSB$_{ex}$T ceramics after $10^9$ switching cycles are listed in Table 6.11. The mechanisms of reduction of polarization fatigue with SB$_{ex}$T incorporation has already been discussed in the following 6.8.3 section.

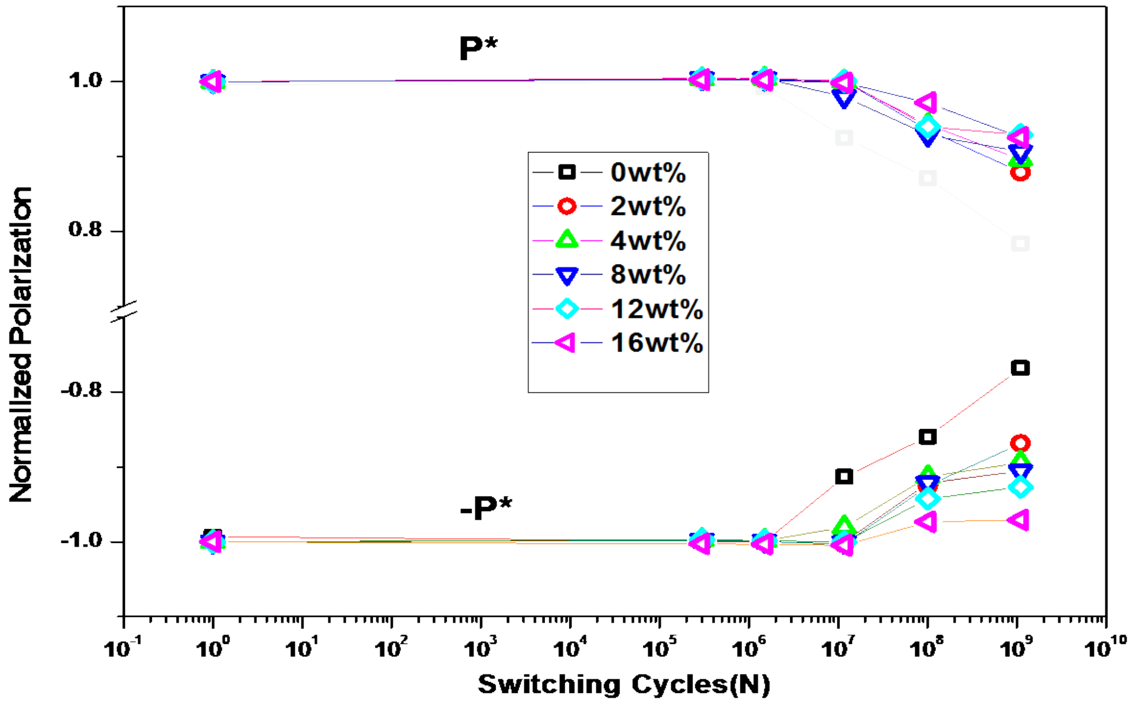

**Fig. 6.13:** Normalized polarization vs. number of cycles plots of (1-ϕ) (NBT-BT)-ϕ SB$_{ex}$T (ϕ= 0, 2, 4, 8, 12, 16 wt. %) ceramics.

**Table 6.11:** Polarization fatigue of (1-ϕ) (NBT-BT)-ϕ $SB_{ex}T$ (ϕ= 0, 2, 4, 8, 12, 16 wt %) ceramics.

| **(1-ϕ) (NBT-BT)- ϕ $SB_{ex}T$** | ϕ = 0 wt. % | ϕ = 2 wt. % | ϕ = 4 wt. % | ϕ = 8 wt. % | ϕ = 12 wt. % | ϕ = 16 wt. % |
|---|---|---|---|---|---|---|
| **Relative polarization fatigue %($10^9$ cycle)** | 22.54 | 13.48 | 11.02 | 9.94 | 8.26 | 5.84 |

## 6.8.2 Polarization Fatigue Study of (1-ϕ)(NBT-KNN)-ϕ$SB_{ex}T$ Ceramics

Fig. 6.14 shows the RT polarization fatigue characteristics of the (1-ϕ)(NBT-KNN)-ϕ$SB_{ex}T$ (ϕ= 0, 2, 4, 8, 12, 16 wt. %) ceramics at 10kHz bipolar triangular switching pulses. Variation of normalized polarization vs. number of cycles (up to $10^9$) of all the (1-ϕ)(NBT-KNN)-ϕ$SB_{ex}T$ ceramic composites is shown in Fig. 6.14. The switching polarizations are observed after 1, 300000, $1.5x10^6$, $1.17x10^7$, 1.11 $x10^8$ and $1.23x10^9$ numbers of the applied electric field cycles. It is observed that the polarization degradation gradually decreases with the increase of $SB_{ex}T$ content in the (1-ϕ)(NBT-KNN)-ϕ$SB_{ex}T$ ceramics. It is well known that the polarization fatigue of a ferroelectric material is strongly related to its leakage current behavior i.e., lower the leakage current, higher is the fatigue-free behavior in the material [31] This also explains the decrease of polarization degradation with the increase of $SB_{ex}T$ content in (1-ϕ)(NBT-KNN)-ϕ$SB_{ex}T$ ceramics. In the $ABO_3$ type of perovskite ferroelectric ceramics, formation of oxygen vacancy types of defects is more pronounced [32]. Therefore, with the increase of $SB_{ex}T$ content in the (1-ϕ) (NBT-KNN)-ϕ$SB_{ex}T$ ceramics, the number of oxygen vacancies decreases [19] and the polarization fatigue resistant increases. The detailed mechanism has been explained in the following section.The relative polarization fatigue% values after $10^9$ cycles of all the (1-ϕ) (NBT-KNN)-ϕ $SB_{ex}T$ ceramics are listed in Table 6.12.

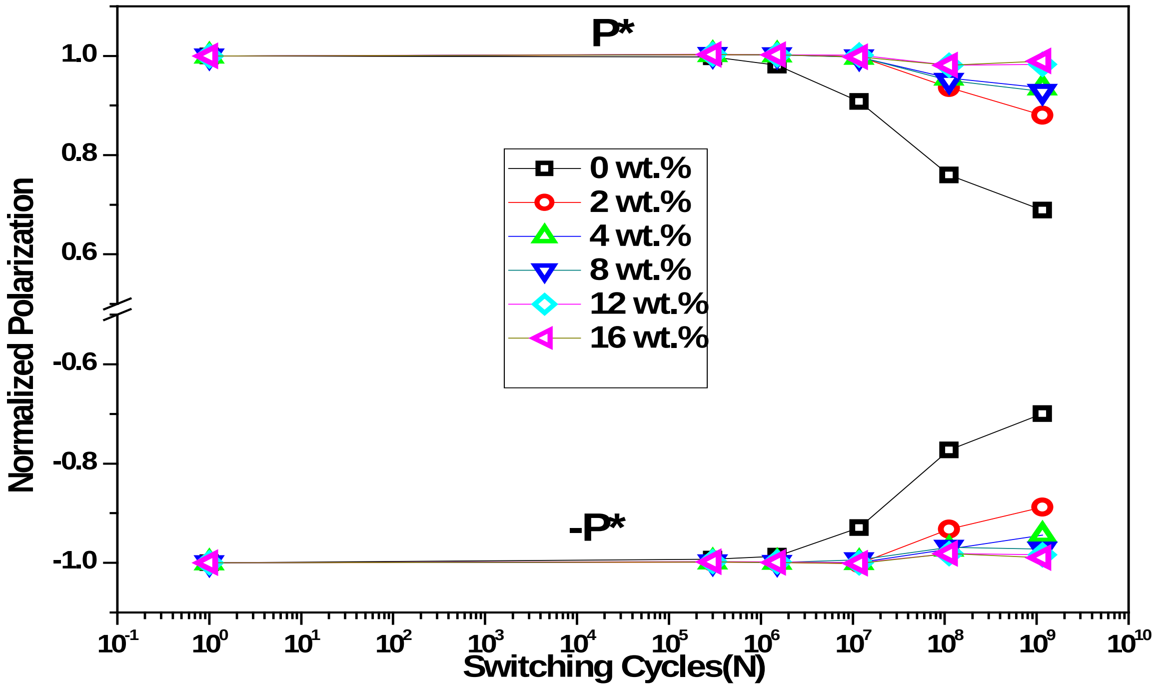

**Fig. 6.14:** Normalized polarization vs. number of cycles plots of (1-ϕ) (NBT-KNN)-ϕ $SB_{ex}T$ (ϕ= 0, 2, 4, 8, 12, 16 wt. %) ceramics.

**Table 6.12:** Polarization fatigue of (1-ϕ) (NBT-KNN)-ϕ $SB_{ex}T$ (ϕ= 0, 2, 4, 8, 12, 16 wt %) ceramics.

| **(1-ϕ) (NBT-KNN)-ϕ $SB_{ex}T$** | ϕ = 0 wt. % | ϕ = 2 wt. % | ϕ = 4 wt. % | ϕ = 8 wt. % | ϕ = 12 wt. % | ϕ = 16 wt. % |
|---|---|---|---|---|---|---|
| **Relative polarization fatigue %($10^9$ cycle)** | 30.57 | 11.57 | 6.0 | 4.98 | 1.66 | 1.05 |

## 6.8.3 Mechanism of Improvement of Electric Fatigue Endurance of the (1-ϕ)(NBT-KNN)-ϕ$SB_{ex}T$ and (1-ϕ) (NBT-BT)-ϕ$SB_{ex}T$ Ceramics

The major contribution to polarization fatigue in normal perovskite ferroelectric materials is related to the oxygen vacancies, created at high processing temperatures [33]. During reorientation of the domains, these oxygen vacancies are generally driven towards domain walls or grain boundaries and captured by space charges [33]. This accumulation of oxygen vacancies at the domain walls and/or at grain boundaries would lead to the pinning of domain walls and development of depolarization field. The depolarization field weakens the applied external electric field and results in effectively less reorientation of domains, which is reflected in the decrease of remnant/saturation polarization after repeated no. of electric field cycles and accounts the polarization fatigue of the ferroelectric material. This type of phenomena is common in perovskite phase ferroelectric systems. Whereas, in layered perovskite ferroelectrics such as in SBT, a specific bismuth oxide layer $(Bi_2O_2)^{2+}$ exists between the oxygen octahedron chains $(SrTa_2O_7)^{2-}$ [34]. With this, the ferroelastic stress, caused by the reorientation of the polarization under applied external electric field can be relieved. Moreover, due to the large lattice space and weak ionic bonds in the $(Bi_2O_2)^{2+}$ layers, the oxygen vacancies can be accommodated in these layers, which restrict the piling of oxygen vacancies near the domain walls [35]. Thus, a weaker depolarization field or less pinning of the domain walls would be present, which accounts the better polarization fatigue endurance of the layered perovskite ferroelectrics. This explains the improvement of polarization fatigue endurance in the $SB_{ex}T$ modified NBT-BT and NBT-KNN ceramics, respectively.

## References

[1] K. Kotani, I. Kawayama, M. Tonouchi, Y. Hotta, H. Tabata, Dielectric and ferroelectric properties of c-axis oriented strontium bismuth tantalate thin films applied transverse electric fields, Journal of Applied Physics, 99 (2006) 124106.

[2] N. Zhang, L. Li, B. Li, D. Guo, Z. Gui, Improvement of electric fatigue properties in PLZT ferroelectric ceramics due to $SrBi_2Ta_2O_9$ incorporation, Materials Science and Engineering: B, 90 (2002) 185-190.

[3] M.S. Anwar, A.A. Khan, K.Y. Park, S.R. Lee, F. Ahmed, B.H. Koo, Influence of Zn on magnetocaloric effect in $(0.95)La_{0.7}Sr_{0.3}MnO_3/Ni_{1-x}Zn_xFe_2O_4$ ceramic composites, Materials Research Bulletin, 69 (2015) 41-45.

[4] I. Coondoo, N. Panwar, A.K. Jha, Effect of sintering temperature on the structural, dielectric and ferroelectric properties of tungsten substituted SBT ceramics, Physica B: Condensed Matter, 406 (2011) 374-381.

[5] K. Ramam, M. Lopez, K. Chandramouli, Dielectric and piezoelectric studies of perovskite–tungsten bronze structured (1− x)PLZT–xPBBiN nanoceramic composites by high-energy mechanical activation technique, Journal of Alloys and Compounds, 488 (2009) 211-216.

[6] L.A. Schmitt, J. Kling, M. Hinterstein, M. Hoelzel, W. Jo, H.J. Kleebe, H. Fuess, Structural investigations on lead-free $Bi_{1/2}Na_{1/2}TiO_3$-based piezoceramics, J Mater Sci, 46 (2011) 4368-4376.

[7] C.C. Wang, C.M. Lei, G.J. Wang, X.H. Sun, T. Li, S.G. Huang, H. Wang, Y.D. Li, Oxygen-vacancy-related dielectric relaxations in $SrTiO_3$ at high temperatures, Journal of Applied Physics, 113 (2013) 094103.

[8] J. S. Kim, B.C. Choi, J. H. Jeong, S. T. Chung, S. Cho, I. W. Kim, Low-Frequency Dielectric Dispersion and Impedance Spectroscopy of lead-free $Na_{0.5}Bi_{0.5}TiO_3$(NBT) Ferroelectric Ceramics, Journal Korean Physical Society 55 (2009) 21.

[9] S.N. Kumar, P. Kumar, D.K. Agrawal, Structural, dielectric and ferroelectric properties of SBN ceramics synthesized by microwave reactive sintering technique, Ceramics International, 38 (2012) 5243-5250.

[10] S.K. Acharya, B.-G. Ahn, C.U. Jung, J.-H. Koh, I.-H. Choi, S.-K. Lee, Effect of Rb doping on ferroelectric and piezoelectric properties of $Bi_{0.5}Na_{0.5}TiO_3$–$BaTiO_3$ thin films, Journal of Alloys and Compounds, 603 (2014) 248-254.

[11] J. Li, P. Li, J. Yu, Study on substitution effect of $Bi_4Ti_3O_{12}$ ferroelectric thin films, in: I. Coondoo (Ed.) Ferroelectrics, In Tech, Croatia, 2010, pp. 119-138.

[12] Q.-Y. Tang, Y.-M. Kan, Y.-G. Li, G.-J. Zhang, P.-L. Wang, Effect of vanadium doping on fabrication and property of $Bi_4Ti_3O_{12}$ ceramics, Scripta materialia, 54 (2006) 2075-2080.

[13] L. Zhang, J. Zhai, W. Mo, X. Yao, The dielectric and leakage current behavior of $CoFe_2O_4$-$BaTiO_3$ composite films prepared by combining method of sol-gel and electrophoretic deposition, Solid State Sciences, 12 (2010) 509-514.

[14] A. Mukherjee, P. Victor, J. Parui, S. Krupanidhi, Leakage current behavior in pulsed laser deposited Ba $(Zr_{0.05}Ti_{0.95})O_3$ thin films, Journal of applied physics, 101 (2007) 034106-034106-034106.

[15] A.R. Chaudhuri, A. Laha, S.B. Krupanidhi, Enhanced ferroelectric properties of vanadium doped bismuth titanate (BTV) thin films grown by pulsed laser ablation technique, Solid State Communications, 133 (2005) 611-614.

[16] J.X. Tang, M.H. Tang, J. Zhang, F. Yang, W.F. Zhao, H.Y. Xu, Z.H. Sun, Y.C. Zhou, $V^{5+}$-doped $Bi_{3.4}Yb_{0.6}Ti_3O_{12}$ fatigue resistant ferroelectric thin films, Materials Letters, 62 (2008) 3189-3191.

[17] T.P.-c. Juan, S.-m. Chen, J.Y.-m. Lee, Temperature dependence of the current conduction mechanisms in ferroelectric $Pb(Zr_{0.53}Ti_{0.47})O3$ thin films, Journal of Applied Physics, 95 (2004) 3120-3125.

[18] S. Swain, P. Kumar, R.B. Choudhary, Electrical and ferroelectric studies of the 2-layered SrBi2Ta2O9 based ceramics, Physica B: Condensed Matter, 477 (2015) 56-63.

[19] X. Tang, L. Hu, J. Yang, L. Chen, J. Dai, W. Song, Z. Yang, X. Zhu, Y. Sun, $BiFeO_3$ thin films prepared on metallic Ni tapes by chemical solution deposition: effects of annealing temperature and a $La_{0.5}Sr_{0.5}TiO_3$ buffer layer on the dielectric, ferroelectric and leakage properties, RSC Advances, 4 (2014) 32738-32743.

[20] L. Pintilie, Charge Transport in Ferroelectric Thin Films, 2011.

[21] S.-T. Chang, J.Y.-m. Lee, Electrical conduction mechanism in high-dielectric-constant $(Ba_{0.5}Sr_{0.5})TiO_3$ thin films, Applied Physics Letters, 80 (2002) 655-657.

[22] W. Krauss, D. Schütz, M. Naderer, D. Orosel, K. Reichmann, BNT-based multilayer device with large and temperature-independent strain made by a water-based preparation process, Journal of the European Ceramic Society, 31 (2011) 1857-1860.

[23] A. Ullah, C.W. Ahn, A. Hussain, S.Y. Lee, J.S. Kim, I.W. Kim, Effect of potassium concentration on the structure and electrical properties of lead-free $Bi_{0.5}(Na,K)_{0.5}TiO_3$–$BiAlO_3$ piezoelectric ceramics, Journal of Alloys and Compounds, 509 (2011) 3148-3154.

[24] D. Fu, M. Endo, H. Taniguchi, T. Taniyama, S.-y. Koshihara, M. Itoh, Piezoelectric properties of lithium modified silver niobate perovskite single crystals, Applied Physics Letters, 92 (2008) 172905.

[25] X. Zheng, J. Liu, J. Peng, X. Liu, Y. Gong, K. Zhou, D. Huang, Effect of potassium content on electrostrictive properties of $Na_{0.5}Bi_{0.5}TiO_3$-based relaxor ferroelectric thin films with morphotropic phase boundary, Thin Solid Films, 548 (2013) 118-124.

[26] J. Shi, H. Fan, X. Liu, A.J. Bell, Large Electrostrictive Strain in $(Bi_{0.5}Na_{0.5})TiO_3$–$BaTiO_3$–$(Sr_{0.7}Bi_{0.2})TiO_3$ Solid Solutions, Journal of the American Ceramic Society, 97 (2014) 848-853.

[27] Y.-Q. Yao, T.-Y. Tseng, C.-C. Chou, H.H.D. Chen, Phase transition and piezoelectric property of $(Bi_{0.5}Na_{0.5})_{0.94}Ba_{0.06}Zr_yTi_{1-y}O_3$(y=0–0.04) ceramics, Journal of Applied Physics, 102 (2007) 094102.

[28] D. Lin, K.W. Kwok, Effect of Li-substitution on piezoelectric and ferroelectric properties of $(Bi_{0.92}Na_{0.92-x}Li_x)_{0.5}Ba_{0.06}Sr_{0.02}TiO_3$ lead-free ceramics, Current Applied Physics, 10 (2010) 1196-1202.

[29] F. Guifen, L. Wenzhong, W. Xiaohong, L. Fei, x. Jianzhong, Phase transition behavior and electromechanical properties of $(Na_{1/2}Bi_{1/2})TiO_3$–$KNbO_3$ lead-free piezoelectric ceramics, Journal of Physics D: Applied Physics, 41 (2008) 035403.

[30] Y. Hiruma, Y. Imai, Y. Watanabe, H. Nagata, T. Takenaka, Large electro strain near the phase transition temperature of $(Bi_{0.5}Na_{0.5})TiO_3$–$SrTiO_3$ ferroelectric ceramics, Applied Physics Letters, 92 (2008) 262904.

[31] H. Du, S. Wohlrab, S. Kaskel, Synthesis, Structure, and Properties of $Bi_{3.25}Pr_{0.75}Ti_{2.97}V_{0.03}O_{12}$ Ferroelectric Ceramics, The Journal of Physical Chemistry C, 111 (2007) 11095-11103.

[32] W.L. Warren, K. Vanheusden, D. Dimos, G.E. Pike, B.A. Tuttle, Oxygen Vacancy Motion in Perovskite Oxides, Journal of the American Ceramic Society, 79 (1996) 536-538.

[33] W.L. Warren, D. Dimos, B.A. Tuttle, G.E. Pike, H.N. AlShareef, Relationships among ferroelectric fatigue, electronic charge trapping, defect-dipoles, and oxygen vacancies in perovskite oxides, Integr. Ferroelectr., 16 (1997) 77-86.

[34] A.D. Rae, J.G. Thompson, R.L. Withers, Structure refinement of commensurately modulated bismuth strontium tantalate, $Bi_2SrTa_2O_9$, Acta Crystallographica Section B, 48 (1992) 418-428.

[35] N. Zhang, L. Li, Z. Gui, Improvement of electric fatigue properties in $Pb_{0.94}La_{0.04}(Zr_{0.70}Ti_{0.30})O_3$ ferroelectric capacitors due to $SrBi_2Nb_2O_9$ incorporation, Materials Research Bulletin, 36 (2001) 2553-2562.

# Chapter 7

## *Conclusions and Future Work*

In the present work, ferroelectric ceramics with NBT-xBT and NBT- xKNN compositions showed an MPB at x=0.07. The ceramics with these compositions were observed to have excellent dielectric, piezoelectric, ferroelectric properties which could be helpful for various device applications. Leakage and polarization fatigue behaviour study is very important for realizing the utility of these materials in various device applications. For this purpose, in the present thesis work, leakage and polarization fatigue study of these systems are carried out and discussed in detail. Next objective of this work was to improve leakage and polarization fatigue behaviour of perovskite based systems. Based on literature, SBT, $SB_{ex}T$, and SBTW (bismuth layered structure ferroelectrics (BLSF) materials), naturally anti-fatigue with low leakage current behaviour, were selected and studied in detail. $SB_{ex}T$ system was selected to further modify the leakage and polarization fatigue behaviour of MPB compositions of NBT-BT and NBT-KNN systems. For this purpose NBT-BT- $SB_{ex}T$ and NBT-KNN- $SB_{ex}T$ composite systems were synthesized and studied in detail. $SB_{ex}T$ phase incorporated NBT-BT and NBT-KNN systems showed improved leakage current density and polarization fatigue behaviour. The major conclusions drawn from the present work and the scope of the related future work are given in this chapter.

## 7.1 Conclusions

### 7.1.1 NBT-xBT and NBT-xKNN Systems:

- Solid solutions of $(1-x)Na_{0.5}Bi_{0.5}TiO_3$-$xBaTiO_3$ (x=0.05, 0.06, 0.07, 0.08) and $(1-x)(Na_{0.5}Bi_{0.5}TiO_3)$-$xK_{0.5}Na_{0.5}NbO_3$ (x=0.05, 0.06, 0.07, 0.08) ceramics near their respective MPBs were synthesized in single perovskite phase by solid-state reaction route.
- In the NBT-xBT system, RT maximum values of $P_r$ ~ 31.71μC/cm$^2$, $\varepsilon_r$ ~2275 (at 1 kHz frequency), $d_{33}$ ~105pC/N, $k_p$ ~ 0.21 and field induced strain% ~ 0.45 were obtained in the x=0.07 composition.
- In the NBT-xKNN system, RT maximum values of $P_r$ ~ 20.61μC/cm$^2$, $\varepsilon_r$ ~ 2787 (at 1 kHz frequency), $d_{33}$ ~78pC/N, $k_p$ ~ 0.12, and maximum induced strain% ~0.36 were obtained in the x=0.07 composition.

- The minimum leakage current density ~$5.72\times10^{-7}$A/cm$^2$ and ~$1.04\times10^{-6}$ A/cm$^2$ were observed in the x=0.07 compositions of the NBT-xBT and NBT-xKNN systems, respectively.
- Polarization fatigue study confirmed the polarization degradation after $10^7$ cycles of all compositions of the NBT-xBT and NBT-xKNN systems.

### 7.1.2 SBT based Systems:

- The 2-layered $SrBi_2Ta_2O_9$/SBT, $Sr_{0.8}Bi_{2.15}Ta_2O_9$/SB$_{ex}$T, and $SrBi_2(Ta_{0.925}W_{0.075})_2O_9$/SBTW BLSF ceramics were successfully synthesized in single phase by the solid-state reaction route.
- Plate-like grains morphology with maximum experimental density ~8.87 g/cc was observed in the SB$_{ex}$T ceramics, sintered at 1200$^o$C/4hr.
- Optimum $\varepsilon_r$ ~1590 at 1 kHz frequency and highest $T_c$ (398$^o$C) were obtained in the SB$_{ex}$T ceramic samples.
- RT lowest leakage current density ~$3.14\times10^{-9}$ A/cm$^2$, maximum $P_r$ ~ 8.07 µC/cm$^2$ with minimum $E_c$ ~ 15.18kV/cm were obtained in the SB$_{ex}$T ceramic samples.
- Polarization fatigue study confirmed negligible polarization degradation even after $10^9$ electric field cycles of all the SBT, SB$_{ex}$T and SBTW ceramics.

### 7.1.3 (1-$\phi$)(NBT-BT)-$\phi$SB$_{ex}$T and (1-$\phi$)(NBT-KNN)-$\phi$SB$_{ex}$T Ceramics:

- (1-$\phi$)(NBT-BT)-$\phi$ SB$_{ex}$T and (1-$\phi$)(NBT-KNN)-$\phi$SB$_{ex}$T ($\phi$= 0, 2, 4, 8, 12, 16 wt. %) ceramic composites were prepared by solid state reaction route.
- XRD studies confirmed the co-existence of respective phases in both the systems.
- SEM study showed the growth of plate-like grains and the dielectric study showed the decrease of $\varepsilon_r$ and tan$\delta$ values with the increase of SB$_{ex}$T content in both the systems.
- Room temperature leakage current density between $10^{-7}$ to $10^{-8}$ A/cm$^2$ (which is one and two order less than that of the MPB compositions of the NBT-xBT and NBT-xKNN systems, respectively) was obtained in both the systems.
- Reduction of maximum induced strain% with the increase of SB$_{ex}$T content was obtained in both the ceramic composite systems.
- Improvement in leakage currents density, fatigue resistance, retention of high $\varepsilon_r$, $P_r$, $d_{33}$ and $k_p$ values in $\phi \leq$ 4wt. % ceramic composites of the (1-$\phi$) (NBT-KNN)-$\phi$SB$_{ex}$T system suggested their usefulness in capacitor, piezoelectric and NVRAM applications.

## 7.2 Recommendations for Future Work

In the present work, $(1-\phi)(NBT\text{-}BT)\text{-}\phi SB_{ex}T$ and $(1-\phi)(NBT\text{-}KNN)\text{-}\phi SB_{ex}T$ ceramic composites were synthesized by solid state reaction route and studied for various structural and electrical properties. Following recommendations are made for the extension of the present work:

- ✓ Thin films and nanoceramics of the best compositions of the $(1-\phi)(NBT\text{-}BT)\text{-}\phi SB_{ex}T$ and $(1-\phi)(NBT\text{-}KNN)\text{-}\phi SB_{ex}T$ systems can be synthesized and studied for various structural and electrical properties.
- ✓ For proper understanding of the grain and grain boundary effects in the $(1-\phi)(NBT\text{-}BT)\text{-}\phi SB_{ex}T$ and $(1-\phi)(NBT\text{-}KNN)\text{-}\phi SB_{ex}T$ ceramic composites, impedance spectroscopic studies can be done.
- ✓ Temperature variation of J-E and P-E loop studies can be carried out to understand the different conduction and FE-AFE transition mechanisms.
- ✓ Fatigue characteristics of the $(1-\phi)(NBT\text{-}BT)\text{-}\phi SB_{ex}T$ and $(1-\phi)(NBT\text{-}KNN)\text{-}\phi SB_{ex}T$ ceramics at different frequency of the applied electric field can be carried out.
- ✓ For proper understanding of the polarization degradation mechanism, the dielectric, piezoelectric and P-E hysteresis loop studies of the best compositions can be carried out after repeated number of electric field cycles.

*************

# Bio-Data of the Author

**Name:** Sridevi Swain

**D.O.B.:** 01-07-1985

**Educational Qualification:**

**Secondary Education:** Jawahar Navodaya Vidyalaya Sarang, Dhenkanal
**Intermediate:** Jawahar Navodaya Vidyalaya Sarang, Dhenkanal
**Int. B.Sc. & B. Ed**: Regional Institute of Education Bhubaneswar
**M.Sc. in Physics**: National Institute of Technology Rourkela
**Ph.D. in Physics**: National Institute of Technology Rourkela

**Publications:**

**1**. **S. Swain**, P. Kumar, D. K. Agrawal, Sonia, Dielectric and ferroelectric study of KNN modified NBT ceramics synthesized by microwave processing technique, ***Ceramics International*** 39 (2013) 3205–3210.

**2. S. Swain,** P. Kumar, Dielectric, ferroelectric and bipolar electric field induced strain properties of MPB composition of NBT-xKNN system, ***Journal of Electroceramics*** 32 1 (2014) 102-107.

**3.** S. K. Kar, **S. Swain**, Sonia, P. Kumar**,** High dielectric constant and low optical band gap studies of La-modified $Ba(Fe_{0.5}Nb_{0.5})O_3$ ceramics, ***Materials Chemistry and Physics*** 155 (2015) 171-177.

**4. S. Swain,** S. K. Kar, P. Kumar, Dielectric, Optical, Piezoelectric and Ferroelectric Studies of NBT-BT Ceramics near MPB, ***Ceramics International*** 41 (2015) 10710–10717**.**

**5. S. Swain,** P. Kumar, R. B. Choudhary**,** Electrical and Ferroelectric Studies of the 2-Layered $SrBi_2Ta_2O_9$ based Ceramics, ***Physica B: Condensed Matter*** 477 (2015) 56–63.

**6. S. Swain,** P. Kumar, Structural, Dielectric and Ferroelectric Study of (1-$\phi$)(NBT-KNN)-$\phi SB_{ex}T$ Ceramics, ***Journal of Physics and Chemistry of Solids*** 98 (2016) 59-64.

**7. S. Swain,** P. Kumar, Synthesis and Characterizations of (1-$\phi$)(NBT-BT)-$\phi SB_{ex}T$ Ceramics for NVRAM Applications, ***Current Applied Physics*** 16 (2016) 1105-1112.

**8. S. Swain,** P. Kumar, Optical, Piezoelectric, Polarization Fatigue and Leakage Current Studies of the NBT-KNN Ceramics near MPB **(Communicated).**

**Permanent Address:** D/O Rabi Narayan Swain
Surapratap pur (Vill./PO)
Dhenkanal (Dist.)
759024, Odisha, India